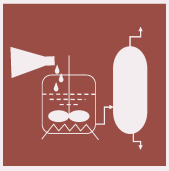

Design and Engineering of Microreactor and Smart-Scaled Flow Processes

Edited by

Volker Hessel

Printed Edition of the Special Issue Published in *Processes*

www.mdpi.com/journal/processes

Volker Hessel (Ed.)

Design and Engineering of Microreactor and Smart-Scaled Flow Processes

This book is a reprint of the special issue that appeared in the online open access journal *Processes* (ISSN 2227-9717) in 2013 (available at: http://www.mdpi.com/journal/processes/special_issues/smart-scaled_flow_processes).

Guest Editor
Volker Hessel
Micro Flow Chemistry and Process Technology
Department of Chemical Engineering and Chemistry
Technische Universiteit Eindhoven
P. O. Box 513, 5600 MB
Eindhoven
The Netherlands

Editorial Office
MDPI AG
Klybeckstrasse 64
Basel, Switzerland

Publisher
Shu-Kun Lin

Senior Assistant Editor
Yurong Zhang

1. Edition 2015

MDPI • Basel • Beijing

ISBN 978-3-03842-039-2

Table of Contents

List of Contributors V

Preface VIII

About the Guest Editor X

Volker Hessel
Special Issue: Design and Engineering of Microreactor and Smart-Scaled Flow Processes
Reprinted from: *Processes* **2015**, *3*(1), 19-22 1
http://www.mdpi.com/2227-9717/3/1/19

Laura Grundemann and Stephan Scholl
Ecological and Economic Assessment of Micro-/Milli-Continuous Campaign Manufacturing: The Case of Writing Ink
Reprinted from: *Processes* **2014**, *2*(1), 238-264 4
http://www.mdpi.com/2227-9717/2/1/238

Dipesh Patel, Suela Kellici and Basudeb Saha
Green Process Engineering as the Key to Future Processes
Reprinted from: *Processes* **2014**, *2*(1), 311-332 31
http://www.mdpi.com/2227-9717/2/1/311

Aikaterini Anastasopoulou, Qi Wang, Volker Hessel and Juergen Lang
Energy Considerations for Plasma-Assisted N-Fixation Reactions
Reprinted from: *Processes* **2014**, *2*(4), 694-710 54
http://www.mdpi.com/2227-9717/2/4/694

Nicolai Krasberg, Lukas Hohmann, Thomas Bieringer, Christian Bramsiepe and Norbert Kockmann
Selection of Technical Reactor Equipment for Modular, Continuous Small-Scale Plants
Reprinted from: *Processes* **2014**, *2*(1), 265-292 71
http://www.mdpi.com/2227-9717/2/1/265

Md. Taifur Rahman and Evgeny V. Rebrov
Microreactors for Gold Nanoparticles Synthesis: From Faraday to Flow
Reprinted from: *Processes* **2014**, *2*(2), 466-493 99
http://www.mdpi.com/2227-9717/2/2/466

Enhong Cao, Ioannis Zuburtikudis, Noor Al-Rifai, Mark Roydhouse and Asterios Gavriilidis
Enhanced Performance of Oxidation of Rosalva (9-decen-1-ol) to Costenal (9-decenal) on Porous Silicon-Supported Silver Catalyst in a Microstructured Reactor
Reprinted from: *Processes* **2014**, *2*(1), 141-157 128
http://www.mdpi.com/2227-9717/2/1/141

Alexander Tollkötter and Norbert Kockmann
Absorption and Chemisorption of Small Levitated Single Bubbles in Aqueous Solutions
Reprinted from: *Processes* **2014**, *2*(1), 200-215 145
http://www.mdpi.com/2227-9717/2/1/200

Michael F. Roberto, Thomas I. Dearing, Charles W. Branham, Olav Bleie and Brian J. Marquardt
Rapid Determination of Optimal Conditions in a Continuous Flow Reactor Using Process Analytical Technology
Reprinted from: *Processes* **2014**, *2*(1), 24-33 161
http://www.mdpi.com/2227-9717/2/1/24

Alejandro A. Munera Parra, Nicolai Antweiler, Rachit Nagpal and David W. Agar
Stability Analysis of Reactive Multiphase Slug Flows in Microchannels
Reprinted from: *Processes* **2014**, *2*(2), 371-391 171
http://www.mdpi.com/2227-9717/2/2/371

Michael Oelgemöller, Sonia Gallagher and Kevin McCarthy
Microflow Photochemistry—Photodecarboxylations in Microformats
Reprinted from: *Processes* **2014**, *2*(1), 158-166 191
http://www.mdpi.com/2227-9717/2/1/158

Nenad Micic, Alan Young, Julien Rosselgong and Christian H. Hornung
Scale-up of the Reversible Addition-Fragmentation Chain Transfer (RAFT) Polymerization Using Continuous Flow Processing
Reprinted from: *Processes* **2014**, *2*(1), 58-70 200
http://www.mdpi.com/2227-9717/2/1/58

Chang-Ho Choi, Brian K. Paul and Chih-Hung Chang
Microreactor-Assisted Solution Deposition for Compound Semiconductor Thin Films
Reprinted from: *Processes* **2014**, *2*(2), 441-465 213
http://www.mdpi.com/2227-9717/2/2/441

List of Contributors

Aikaterini Anastasopoulou: Laboratory of Chemical Reactor Engineering/Micro Flow Chemistry and Process Technology, Department of Chemical Engineering and Chemistry, Eindhoven University of Technology, P.O. Box 513, 5600 MB Eindhoven, The Netherlands

Qi Wang: Laboratory of Chemical Reactor Engineering/Micro Flow Chemistry and Process Technology, Department of Chemical Engineering and Chemistry, Eindhoven University of Technology, P.O. Box 513, 5600 MB Eindhoven, The Netherlands

Juergen Lang: Innovation Management, Verfahrenstechnik & Engineering, Evonik Industries AG, Rodenbacher Chaussee 4, 63457 Hanau-Wolfgang, Germany

Md. Taifur Rahman: School of Chemistry and Chemical Engineering, Queen's University Belfast, Stranmillis Road, Belfast BT9 5AG, UK

Evgeny V. Rebrov: School of Chemistry and Chemical Engineering, Queen's University Belfast, Stranmillis Road, Belfast BT9 5AG, UK

Chang-Ho Choi: School of Chemical, Biological and Environmental Engineering, Oregon State University, Corvallis, OR 97331, USA; Oregon Process Innovation Center/Microproduct Breakthrough Institute, Corvallis, OR 97330, USA

Brian K. Paul: Oregon Process Innovation Center/Microproduct Breakthrough Institute, Corvallis, OR 97330, USA; School of Mechanical, Industrial and Manufacturing Engineering, Oregon State University, Corvallis, OR 97331, USA

Chih-Hung Chang: School of Chemical, Biological and Environmental Engineering, Oregon State University, Corvallis, OR 97331, USA; Oregon Process Innovation Center/Microproduct Breakthrough Institute, Corvallis, OR 97330, USA

Alejandro A. Munera Parra: Laboratory of Chemical Reaction Engineering, Department of Biochemical and Chemical Engineering, Technical University of Dortmund, Dortmund 44227, Germany

Nicolai Antweiler: Laboratory of Chemical Reaction Engineering, Department of Biochemical and Chemical Engineering, Technical University of Dortmund, Dortmund 44227, Germany

Rachit Nagpal: Laboratory of Chemical Reaction Engineering, Department of Biochemical and Chemical Engineering, Technical University of Dortmund, Dortmund 44227, Germany

David W. Agar: Laboratory of Chemical Reaction Engineering, Department of Biochemical and Chemical Engineering, Technical University of Dortmund, Dortmund 44227, Germany

Dipesh Patel: Centre for Green Process Engineering, Department of Applied Sciences, Faculty of Engineering, Sciences and The Built Environment, London South Bank University, 103 Borough Road, London SE1 0AA, UK

Suela Kellici: Centre for Green Process Engineering, Department of Applied Sciences, Faculty of Engineering, Sciences and The Built Environment, London South Bank University, 103 Borough Road, London SE1 0AA, UK

Basudeb Saha: Centre for Green Process Engineering, Department of Applied Sciences, Faculty of Engineering, Sciences and The Built Environment, London South Bank University, 103 Borough Road, London SE1 0AA, UK
Nicolai Krasberg: INVITE GmbH, CHEMPARK, Building W32, D-51368 Leverkusen, Germany
Lukas Hohmann: Laboratory of Equipment Design, BCI, TU Dortmund University, Emil-Figge-Straße 68, D-44227 Dortmund, Germany
Thomas Bieringer: INVITE GmbH, CHEMPARK, Building W32, D-51368 Leverkusen, Germany
Christian Bramsiepe: Laboratory of Plant and Process Design, BCI, TU Dortmund University, Emil-Figge-Straße 70, D-44227 Dortmund, Germany
Norbert Kockmann: Laboratory of Equipment Design, BCI, TU Dortmund University, Emil-Figge-Straße 68, D-44227 Dortmund, Germany
Laura Grundemann: Evonik Industries AG, CREAVIS-Science to Business, Paul-Baumann-Strasse 1, 45764 Marl, Germany
Stephan Scholl: Institut für Chemische und Thermische Verfahrenstechnik, Technische Universität Braunschweig, Langer Kamp 7, 38106 Braunschweig, Germany
Alexander Tollkötter: TU Dortmund University, BCI, Equipment Design, Emil-Figge-Straße 68, D-44227 Dortmund, Germany
Enhong Cao: Department of Chemical Engineering, University College London, Torrington Place, London WC1E 7JE, UK
Ioannis Zuburtikudis: Department of Mechanical and Industrial Design Engineering, T.E.I. of Western Macedonia, Kozani 50100, Greece; Department of Chemical and Petroleum Engineering, United Arab Emirates University, Al Ain, P.O.Box: 15551, UAE
Noor Al-Rifai: Department of Chemical Engineering, University College London, Torrington Place, London WC1E 7JE, UK
Mark Roydhouse: Department of Chemical Engineering, University College London, Torrington Place, London WC1E 7JE, UK
Asterios Gavriilidis: Department of Chemical Engineering, University College London, Torrington Place, London WC1E 7JE, UK
Michael Oelgemöller: James Cook University, School of Pharmacy and Molecular Sciences, Townsville, Queensland 4811, Australia
Sonia Gallagher: Dublin City University, School of Chemical Sciences, Dublin 9, Ireland
Kevin McCarthy: Dublin City University, School of Chemical Sciences, Dublin 9, Ireland
Nenad Micic: CSIRO Materials Science and Engineering, Bayview Avenue, Clayton, VIC 3168, Australia; Chemical Engineering Faculty, Monash University, Wellington Road, Clayton, VIC 3169, Australia
Alan Young: CSIRO Materials Science and Engineering, Bayview Avenue, Clayton, VIC 3168, Australia; Chemical Engineering Faculty, Monash University, Wellington Road, Clayton, VIC 3169, Australia
Julien Rosselgong: CSIRO Materials Science and Engineering, Bayview Avenue, Clayton, VIC 3168, Australia

Christian H. Hornung: CSIRO Materials Science and Engineering, Bayview Avenue, Clayton, VIC 3168, Australia
Michael F. Roberto: Department of Chemistry, University of Washington, 4000 15th Ave NE, Seattle, WA 98105, USA
Thomas I. Dearing: Applied Physics Laboratory, University of Washington, 1013 NE 40th Street, Seattle, WA 98105, USA
Charles W. Branham: Applied Physics Laboratory, University of Washington, 1013 NE 40th Street, Seattle, WA 98105, USA
Olav Bleie: Tel-Tek, Kjølnes Ring 30, Porsgrunn 3918, Norway; Department of Chemistry, University of Bergen, P.O. Box 7800, Bergen NO-5020, Norway
Brian J. Marquardt: Applied Physics Laboratory, University of Washington, 1013 NE 40th Street, Seattle, WA 98105, USA

Preface

The special issue "Design and Engineering of Microreactor and Smart-Scaled Flow Processes" of the journal *Processes* aims to cover recent advances in the development of microreactor and smart-scaled flow processes towards the process level. The special issue is available online at: http://www.mdpi.com/journal/processes/special_issues/smart-scaled_flow_processes.

Small Makes Transfer Faster

Microreactors are small devices with sub-millimeter internals which have superb mass and heat transfer. Initially, they were used for reactions with very high demands on the latter, e.g. very exothermic reactions, gas-liquid reactions with interfacial transport issues, reactions with very fast kinetics which demands even faster mixing, and more. In this way, the processing window was opened widely and, also due to the minute volumes only present in the reaction zone, safe processing under otherwise hazardous conditions was enabled. This includes processing of reactions which are prone to thermal runaway and in the explosive regime. Scale-up of promising reactions and products which was hindered with conventional technology is now possible using the new equipment. This has widened the process development possibilities in chemical industry.

Small Widens Chemistry Options

In the last years, micro process technology was not only used for the very problematic synthetic issues which formerly had a dead-end position in industry's process development. Rather, the scope of chemical reactions to be processed in microreactors was considerably widened by exploring new process conditions with regard to temperature, pressure, concentration, solvents, and more. This is commonly referred to as flow chemistry. This allowed to reduce the processing time-scale for many reactions to the minute range or even below which fits well to the residence times of microreactors. In addition, the process integration of several reactions in one flow to a multi-step synthesis has opened a new door in molecular diversity as well as system and process complexity. The same holds for the combination of reactions and separations in micro-flow. To achieve throughputs relevant for industrial production, smart scale-out to milli-flow units has established and supplemented the numbering-up concept (parallelization of microchannels/-reactors operated under equal conditions).

From Drop-in to End-to-End

A number of review and book compilations as well as journal's special issues reflect the innovations, achievement degree and debottlenecking of such reaction-focused investigations. On a process level, so far it was most often sufficient to use the "drop-in" (retrofit) concept

which especially pharma industry appreciates. The microreactor replaced a conventional (batch) reactor and may be even further implications on the whole process (e.g., downstreamwise) were given on top. Meanwhile and especially with the introduction of the mobile, compact, modular container technology, the focus is much more on the process side. Rather than simple "drop-in" it is aimed at an end-to-end vision of intensified process design. Exactly this is the focus of the current special issue "Design and Engineering of Microreactor and Smart-Scaled Flow Processes" of the journal *Processes*. The selected contributions aim to cover relevant recent advances in the development of microreactor and smart-scaled flow processes towards the process level—in the sense as given above.

Green Engineering in Flow

The special issue-compilation encompasses, among others, end-to-end concepts in plasma-assisted power-to-gas containerized plants, construction methodology for modular containerized plants for fine chemistry/pharma, ecoefficiency analysis for a flow-based pilot plant developed for writing-ink industry and also a helicopter view on Green Engineering as whole, holistic visions in flow-assisted particle synthesis ("from Faraday to Flow"), stability analysis of multiphase flows, scale-up of modern radical polymerizations, dedicated catalyst and photoactivetion studies, and the use of process-analytical technology for monitoring online the flow processing.

In sum, a wide range of facets are offered beyond flow chemistry itself and respective reaction engineering, outlining challenges on the process side and making increasingly evident what is about "Flow Green Engineering".

Prof. Dr. Volker Hessel
Guest Editor

About the Guest Editor

Prof. Dr. Volker Hessel, born 1964, studied chemistry at Mainz University. He got the PhD level in the field of organic chemistry in 1993. Since 1994 he is an employee of the Institut für Mikrotechnik Mainz GmbH. In 1999 he was appointed Head of the Microreaction Technology Department. In 2002, Professor Hessel was appointed Vice Director R&D at IMM and in 2007 as Director R&D at IMM. In 2005, Professor Hessel was appointed as part-time professor at Eindhoven University of Technology, TU/e. He was appointed as honorary professor at the Technical Chemistry Department at Technical University of Darmstadt in 2009 and in 2012 as guest professor at Kunming University of Science and Technology/China. In 2011, he was appointed as full professor for the chair of "Micro Flow Chemistry and Process Technology" at Eindhoven University of Technology, TU/e. Professor Hessel is author or co-author of more than 280 peer-reviewed publications (with 41 extended reviews), 21 book chapters, and 5 books (h-index: 41). He received the AIChE award "Excellence in Process Development Research" in 2007. He received in 2010 the ERC Advanced Grant of EU about "Novel Process Windows". Professor Hessel is an authority in the 35-man teamed Enquete Commission "Future of the Chemistry" of the parliament of Germany's state Nordrhein-Westfalia and is so involved in making strategic recommendations on the future material mix and proper use of resources and reserves. He is in the scientific steering board of the "International Conference on Microreaction Technology" (IMRET). He is Editor-in-Chief of the journal "Green Processing and Synthesis".

Special Issue: Design and Engineering of Microreactor and Smart-Scaled Flow Processes

Volker Hessel

Reprinted from *Processes*. Cite as: Hessel, V. Special Issue: Design and Engineering of Microreactor and Smart-Scaled Flow Processes. *Processes* **2015**, *3*, 19-22.

Reaction-oriented research in flow chemistry and microreactor has been extensively focused upon in special journal issues and books. On a process level, this resembled the "drop-in" (retrofit) concept with the microreactor replacing a conventional (batch) reactor. Meanwhile, with the introduction of the mobile, compact, modular container technology, the focus is more on the process side, including also providing an end-to-end vision of intensified process design. Exactly this is the focus of the current special issue "Design and Engineering of Microreactor and Smart-Scaled Flow Processes" of the journal "*Processes*". This special issue comprises three review papers, five research articles and two communications.

Rahman and Rebrov have presented an overview of the application of microreactors in the synthesis of gold nanoparticles (GNP) [1]. Considering that reactant mixing is one of the most critical factors influencing the GNP synthesis, batch operating conditions commonly pose great limitations to both quality and scalability of the process. In contrast, synthesis in microflow overcomes this constraint and allows to individually affect the diverse elemental steps within GNP synthesis, which provides unique chances in process optimization.

Choi *et al.* have given the state-of-the-art of the microreactor-assisted solution deposition (MASD) technique for fabricating compound semiconductors, as well as instructive insights in scaling-up the MASD process by implementing the numbering-up strategy [2]. Special focus has been given on the application of the MASD in cadmium sulfide (CdS) thin film deposition. The MASD process exhibits advantages over the conventional batch chemical solution method by enabling operation at lower temperature, enhancing reaction selectivity, reducing capital cost and providing perspectives for process scale-up.

The third review by Anastasopoulou *et al.* addresses the energy considerations of N-fixation reactions in non-thermal plasma microreactors [3]. There are three main factors from the process design viewpoint which are delineated and stressed for the plasma-assisted nitric acid and ammonia processes: (a) the incorporation of renewable energy sources (b) the electricity consumption of the plasma reactors and (c) the overall energy performance of the process beyond the concept of the plasma reactors. Optimization of these factors is considered under a holistic viewpoint towards process intensification.

The research articles presented in this special issue outline the applicability of microreactors in a variety of chemical reactions and processes. The selective oxidation of 9-decen-1-ol to 9-decenal has been realized in silicon/glass microreactors under the impact of a specific catalyst [4]. The performance of the studied reaction was tested and evaluated at a given range of temperatures, concentration of

reactants and residence times. The synergetic effect of flow chemistry and catalysis facilitated high reaction conversion and selectivity over a wide range of operating conditions.

Tollkötter and Kockmann have conducted experiments on the physical and reactive absorption of nitrogen and carbon dioxide gas bubbles in aqueous solutions in microflow reactors [5]. The study proved the feasibility of the aforementioned chemical processes in microflow conditions and triggered further research on the inherent mass transfer phenomena.

Grundemann and Scholl have conducted an environmental and economic evaluation of both batch and continuous operating modes for producing writing ink [6]. The analysis results showed clear advantages of the micro-continuous process over the respective batch operation in terms of improved energy efficiency, lower environmental impact and costs associated with human resources.

In addition to that, Patel *et al.* emphasized the role of green process engineering in achieving long-term sustainability [7]. Illustrative examples on the application of green engineering are presented mainly in the areas of environmentally friendly supercritical fluids, catalysts and continuous flow reactors.

Krasberg *et al.* proposed a computer-aided methodology for conceptual design and scale-up of modular continuous processes using the container technology available at the INVITE facility at Bayer Company [8]. In essence, given the process data are known, the methodology enables the selection of the appropriate reactor unit for homogenous liquid phase reactions among various proposed operating alternatives. The computational tool enables the equipment selection not only for one but for multiple operating units. This is likely to fill a profound gap between the conceptual design and industrialization of microreactors.

Roberto *et al.* investigated the incorporation of univariate and multivariate analytical techniques in the operation of continuous flow reactors for rapid monitoring of steady state conditions [9]. For enhanced performance the additional use of process analytical technology (PAT) is proposed resulting to time and cost savings. Parra *et al.* conducted a study on the stability of flow regime in reactive and non-reactive multiphase slug flows in the case of numbered-up microchannel reactor [10]. Experimental results showed fluid maldistrubition and, in turn, the need to incorporate control techniques for ensuring uniform flow patterns.

Oelgemöller *et al.* studied the photodecarboxylation reaction of phthalimides in a microreactor under the effect of UVB light [11]. Photoflow processing is advantageous because of the much enhanced quantum efficiency of the thin liquid layers. Operating under microflow conditions demonstrated better performance in terms of reaction time, yield and conversion as compared to the corresponding batch process.

Micic *et al.* oriented their research in scaling up a lab-scale controlled radical polymerization process under batch and continuous flow conditions [12]. For the batch process, a series of glass vessels were deployed whereas for the continuous operating mode a tubular flow reactor. Based on experiments carried out in both operating modes, the effect of the size and type of reactor on the reaction temperature profile was tested and analyzed accordingly.

The current Special Issue is more than just a flow chemistry or microreactor-based issue which is a format that was manifold provided in the last years. It embraces modern aspects on the process design side. It reflects the increasing technology-readiness level of the technology underneath. Thus,

it gives a relevant further step towards holistic implementation of process intensification into chemical industry. Actual and cutting-edge facets in process design are given, including the modular container and alternative energy concepts which have become central enframing technologies for flow chemistry and microreactors in the last years. Both have significant support from industry, yet nonetheless leave a lot of fundamental questions open thereby pointing to the appropriateness of high-level basic research. The Special Issue aimed to provide platform for both.

References

1. Rahman, M.T.; Rebrov, E.V. Microreactors for Gold Nanoparticles Synthesis: From Faraday to Flow. *Processes* **2014**, *2*, 466–493.
2. Choi, C.-H.; Paul, B.K.; Chang, C.-H. Microreactor-Assisted Solution Deposition for Compound Semiconductor Thin Films. *Processes* **2014**, *2*, 441–465.
3. Anastasopoulou, A.; Wang, Q.; Hessel, V.; Lang, J. Energy Considerations for Plasma-Assisted N-Fixation Reactions. *Processes* **2014**, *2*, 694–710.
4. Cao, E.; Zuburtikudis, I.; Al-Rifai, N.; Roydhouse, M.; Gavriilidis, A. Enhanced Performance of Oxidation of Rosalva (9-decen-1-ol) to Costenal (9-decenal) on Porous Silicon-Supported Silver Catalyst in a Microstructured Reactor. *Processes* **2014**, *2*, 141–157.
5. Tollkötter, A.; Kockmann, N. Absorption and Chemisorption of Small Levitated Single Bubbles in Aqueous Solutions. *Processes* **2014**, *2*, 200–215.
6. Grundemann, L.; Scholl, S. Ecological and Economic Assessment of Micro-/Milli-Continuous Campaign Manufacturing: The Case of Writing Ink. *Processes* **2014**, *2*, 238–264.
7. Patel, D.; Kellici, S.; Saha, B. Green Process Engineering as the Key to Future Processes. *Processes* **2014**, *2*, 311–332.
8. Krasberg, N.; Hohmann, L.; Bieringer, T.; Bramsiepe, C.; Kockmann, N. Selection of Technical Reactor Equipment for Modular, Continuous Small-Scale Plants. *Processes* **2014**, *2*, 265–292.
9. Roberto, M.F.; Dearing, T.I.; Branham, C.W.; Bleie, O.; Marquardt, B.J. Rapid Determination of Optimal Conditions in a Continuous Flow Reactor Using Process Analytical Technology. *Processes* **2014**, *2*, 24–33.
10. Munera Parra, A.A.; Antweiler, N.; Nagpal, R.; Agar, D.W. Stability Analysis of Reactive Multiphase Slug Flows in Microchannels. *Processes* **2014**, *2*, 371–391.
11. Oelgemöller, M.; Gallagher, S.; McCarthy, K. Microflow Photochemistry—Photodecarboxylations in Microformats. *Processes* **2014**, *2*, 158–166.
12. Micic, N.; Young, A.; Rosselgong, J.; Hornung, C.H. Scale-up of the Reversible Addition-Fragmentation Chain Transfer (RAFT) Polymerization Using Continuous Flow Processing. *Processes* **2014**, *2*, 58–70.

Ecological and Economic Assessment of Micro-/Milli-Continuous Campaign Manufacturing: The Case of Writing Ink

Laura Grundemann and Stephan Scholl

Abstract: Many products from the fine chemicals and pharmaceuticals industries are currently manufactured batch-wise in multi-product plants. However, this processing scheme suffers from severe drawbacks, such as a high specific energy demand, cleaning costs and high staff requirements. Transferring batch into continuous campaign productions may overcome these drawbacks. Using the case of writing ink, such a continuous manufacturing scheme was developed employing micro- and milli-structured components in order to intensify certain unit operations. In this paper, an ecological and economic assessment of both production concepts considering all lifecycle stages is presented. The aim of our work is to highlight the advantages and disadvantages of the two multi-product plants and to derive recommendations for the most efficient design and operation of a continuous campaign manufacturing plant. The results show that lower environmental impacts are related to continuous processing, which is due to the option for energy integration in this case. Furthermore, in the economic assessment, continuous processing proved to be economically viable. In this case, reduced staff requirements based on a highly automated manufacturing plant are the key to lower personnel costs. In general, the results emphasize the importance of such micro-/milli-continuous multi-product plants for the future manufacturing of newly developed products in the mentioned industries.

Reprinted from *Processes*. Cite as: Grundemann, L.; Scholl, S. Ecological and Economic Assessment of Micro-/Milli-Continuous Campaign Manufacturing: The Case of Writing Ink. *Processes* **2014**, *2*, 238-264.

1. Introduction

Ecological sound production concepts have become increasingly sought after. This is mainly due to the associated cost savings, as an Internet survey of 177 environmental experts by the Institut der Deutschen Wirtschaft Köln (Cologne Institute for Economic Research) [1] revealed. Batch processing is one of the manufacturing strategies currently reviewed both for the environmental implications and the associated costs [2]. Since the vessels and reactors are mostly used as multi-product plants, their cleaning frequency is high, resulting in a large specific amount of cleaning agents. Further disadvantages of discontinuous processing include high personnel requirements and low repeatability, as well as inhomogeneity in terms of product quality. These variations can lead to up to 20% of the product being discarded as waste, as highlighted in an example of Suzuki-polycondensation producing organic light emitting diode (OLED) colorants [3]. Moreover, batch vessels are often connected to a low surface-to-volume-ratio, which poses a limitation to the heat transfer, resulting in long heating/cooling times and a high specific energy demand. Since heating and cooling periods occur at different time intervals, heat integration can only be realized via

heat pumps or heat reservoirs. Both solutions are technologically complex and, therefore, often not economically viable, according to Schnitzer and Titz [4].

Using continuous instead of batch processing, the mentioned drawbacks may potentially be overcome and more efficient heat integration accomplished. Continuous manufacturing has therefore attracted much attention in the industries largely characterized by batch processing, namely the pharmaceutical and fine chemical sector. A collaboration between Massachusetts Institute of Technology (MIT) and Novartis on the continuous processing of active pharmaceutical ingredients started in 2007 [5] and resulted in the construction of a pilot plant at Novartis's headquarters in 2012 [6]. Yet, in 2010, Stitt and Rooney [7] concluded in their review that only moderate progress to continuous manufacturing had been made despite the economic and operating advantages demonstrated. Nevertheless, continuous processing has been voted the top green engineering research area by an expert group from several pharmaceutical and fine chemicals manufacturers [8], highlighting the importance and potential of the technology.

Merely transferring the protocols from discontinuous to continuous manufacturing does not however necessarily lead to more ecological sound processes, as pointed out by Kralisch *et al*. [9]. When designing continuous processes, it is therefore crucial to review each step in terms of its necessity and conditions, such as pressure, temperatures and concentrations, potentially opening up novel process windows [10]. According to Charpentier [11], also process intensification measures should be considered, which include micro- and milli-structured components.

In order to preserve the flexibility of batch processing for low-volume products, continuous campaign manufacturing schemes should be considered. During one campaign, a single product is synthesized continuously in a multipurpose plant allowing for a high degree of automation. Having reached the desired production quantity, a product change procedure is run during which the plant may be cleaned and prepared for the next campaign. However, open literature information suggests that so far, mainly dedicated continuous manufacturing schemes employing micro- and milli-structured components have been developed. To the best of the authors' knowledge, there are only two exceptions: The first one is a plant that has been developed for the production of two water soluble synthetic polymers in the F^3 factory project [12]. The other one is a multi-purpose lab plant for the production of different writing inks designed by the authors [13,14]. Therein, it was shown that a multi-product continuous plant employing micro- and milli-structured components is technically feasible. However, continuous production requires more elaborate equipment than a batch plant. This leads both to a high environmental impact on the production side of the equipment itself and to high capital investment. Employing only macro-components, a continuous campaign production was deemed economically viable only for production capacities of a few 1000 t per year [15]. More in-depth analysis of multi-purpose production facilities for small production volumes is however highly sought after, according to Schaber *et al*. [16]. This paper addresses this issue by analyzing a continuous campaign production scheme involving a volume of around 150 t/a for a product group of different colored writing inks. In this analysis, the continuous production scheme is compared to the traditional batch process, both in regards to the economic and ecological implications. Special attention was paid to the specific aspects of a multi-product plant: product qualities during the

start-up and shut-down of the plant, the time required for reaching a steady state and the required cleaning procedures.

2. Methods and Assessment Approach

2.1. Case Study of Writing Ink

A product group of writing ink, currently produced batch-wise in jacketed stirred tank reactors, serves as a model system. It is comprised of 5 different colored inks, although only 4 were considered for continuous manufacturing. This is due to one color being a mixture of two others. The recipes differ mainly in the amount and type of pigments and dyes added. The traditional manufacturing scheme utilizes two 1-m^3 stirred vessels in which an aqueous dye solution and a binder mixture as premixes are prepared. The binder solution is then transferred into the dye solution, mixed, heated up to the reaction temperature, maintained for a specific holding time and then cooled. Subsequently, different additives and preservatives are added. This manufacturing scheme suffers from the following drawbacks: Firstly, a high specific amount of cleaning agents is needed to clean the two production vessels after each run. Fouling layers at the vessel walls are removed manually with 1 L of ethanol and 1 L of a 10% aqueous sodium hydroxide solution. Then, the two vessels are flooded twice with water in order to flush the remnants out. Secondly, a high specific energy demand is connected with the two heating steps: Heating of the whole vessel volume is required both for dissolving the powdery reactants during the preparation of the color premixes, as well as for initiating the color reaction. Cooling the vessel to ambient conditions is simply achieved by opening up the vessel lid; thus, heat integration is not realized.

In order to evaluate the technical feasibility of a micro-/milli-continuous campaign manufacturing scheme, a lab plant was set up as shown in Grundemann *et al*. [13,14]:

- Feeding two reactant streams, a color premix and a binder, a maximum flow rate of 13 $L \cdot h^{-1}$ could be achieved.
- A micro-structured mixer and micro-structured heat exchanger were employed.
- The hold-up of the plant was determined as 0.93 L considering all conduits.
- The lab plant was designed in order to allow for the investigation of product change, as well as cleaning procedures.

Adapting the recipe to a continuous processing scheme and employing hot water during the preparation of the color premixes, we could refrain from heating the whole reactor volume during this processing step. In addition, instead of flooding the premix vessels during cleaning, a high pressure cleaning device was employed, reducing the amount of water needed per cycle and vessel. The continuous flow production of different inks in a multi-product plant requires dealing with dynamic events: the start-up and shut-down phases, as well as product change procedures with or without cleaning cycles. During start-up, it is important to follow a strict procedure, described in Table 1, in order to avoid agglomerates and blockages of the two opposing reactant inlet nozzles. The ink produced is fed into a micro-heat exchanger for preheating in counterflow with the reacted ink. At the beginning of the weekly production period lasting for 100 h in total (e.g., Monday, 8:00 h

to Friday, 12:00 h), it takes around 40 min to reach steady state in the micro-heat exchanger. Afterwards, the ink meets the specifications, both in regard to the particle size distribution, as well as the color properties.

The procedure for the product change is determined by the production sequence and the lot size. Ideally, product changes do not involve any cleaning. In this case, a blend of successively produced colors is created. When feeding this blend to the subsequent product drum, whether the color specifications are still met depends on the lot size. We reported that a minimum lot size of 20 times the plant hold-up relating to the product change is sufficient to gain in-spec ink adhering to the optimum production sequence [14]. Therefore, cleaning of the micro-/milli-continuous plant can be curtailed until shut-down at the end of the weekly production period. Maximum contamination levels have also been defined for cleaning procedures in order to ensure that colors produced directly after cleaning procedures are not contaminated by remnants of the previously produced inks. These levels are reached after the exchange of twice the partial plant hold-up relevant for cleaning.

Based on the experimental results obtained on the lab plant scale, a concept for a production plant was developed. This paper describes the results of the process development and assessment using an exemplary production capacity of 30 L h^{-1}. A flowchart of the production plant is presented in the Appendix A. A floor plan was also drawn in order to estimate the required length of the pipes and tubing. Appendix B contains the equipment list of both plants. In contrast to the lab plant, a macro-heat exchanger was included, due to the lower risk of fouling and clogging, as well as the lower investment. Based on the information from the suppliers, the hold-up of the production plant was estimated to be 7.2 L, of which 4.8 L can be accounted for by the macro heat exchanger. As a first estimate during this early project stage, similar residence times, mixing and heat transfer characteristics were assumed for the production plant as experimentally determined for the lab plant. This resulted in the amounts of fluid to be considered during start-up, shut-down and product change as listed in Table 1.

2.2. Ecological Assessment

The ecological study has been conducted with a lifecycle perspective, following the lifecycle assessment (LCA) approach defined in ISO 14040 [17] and ISO 14044 [18]. LCA is a systematic methodology covering the whole lifecycle of a product or process from the cradle to the grave, thereby avoiding a shift of environmental impacts from one lifecycle stage to the next [19]. LCA studies consist of four phases: In the first phase, the goal and scope are defined, including the system boundaries and the functional unit. Secondly, a flow diagram is developed, helping to identify all material and energy flows within the defined system boundaries. These flows are then converted to the functional unit forming the LCA inventory. In the third phase, the potential environmental impacts associated with all flows inside the inventory are assessed. Finally, the results are evaluated to choose the most beneficial product or process.

Table 1. The procedures and amount of fluids to be considered during start-up, shut-down and product change for the drafted continuous multi-product production plant at a volumetric flow rate of 30 L h^{-1}.

Event	Procedure (Based on Experiments with the Lab Plant)	Amount of Fluids (Derived by Extrapolation from the Lab Plant Based on the Relevant Plant Hold-Up)
Start-up at the beginning of the weekly production period	Feeding water with both reactant pumps for 5 min.	2.5 L of water
	Connecting the two reactants step-wise; 5-min waiting period until the second stream is connected; production of agglomerate-laden ink for 10 min.	5 L mixture of water/binder/color premix in total
	Until stationary mode of heat exchanger is achieved after 40 min, the ink does not meet specifications regarding the color value.	20 L of ink
Cleaning during shut-down procedures at the end of the weekly production period	Replacing twice the cleanable plant hold-up.	14.2 L mixture of water and ink
Product change procedure without cleaning	Replacing 20 times the plant hold-up relevant for product changes.	120.9 L product (minimum lot size)

2.2.1. Goal and Scope Definition of the Ecological Assessment

This study aims to derive the potential environmental impacts of both process alternatives to highlight their advantages and disadvantages, as well as to derive recommendations on whether to change the manufacturing scheme. The functional unit was chosen to be a yearly output of 148,200 L of writing ink. This amount is based on a production period of 52 weeks per year, each covering 100 h. Implying a plant occupancy rate of 95% and a production capacity of 30 L h^{-1}, the functional unit was determined. During batch manufacturing, however, up to 2% of the annual output needs to be discarded, due to quality defects. For the continuous campaign production, it is assumed that all fluids arising during start-up, shut-down and product change procedures as listed in Table 1 are also discarded as waste. Both aspects were taken into account by increasing the reactant streams accordingly.

In order to comply with the LCA methodology, the system boundaries encompassed both upstream and disposal stages in addition to the production stage itself, as shown in Figure 1. However, the so-called black-box method proposed by Klöpffer and Grahl [20] was followed. This implies that only those lifecycle and process stages were included that differ between the two process alternatives, minimizing the costs and effort for data collection during process development. The results presented in this paper are therefore only valid for this particular comparative study and do not represent absolute values. Regarding the inputs and outputs of the LCA inventory, the following approach was taken:

- All material and energy flows were considered that differ by more than 2% between the two alternatives. Except for the reactant water, the differences in the amount of the reactants lie below this threshold and their acquisition therefore outside of the system boundaries.
- Manufacturing differently colored inks, the same process steps are performed, adjusting the same process conditions, so that the material flow model is valid for all colors under the assumptions described above. Merely the frequency and type of cleaning cycles of the continuous campaign manufacturing scheme are differing depending on the product sequencing and capacities of the different colors. A sensitivity analysis has been included in the study to evaluate this aspect (see Section 2.3.2.).
- The LCA inventory of both process alternatives excluded all material transports, since reliable data were not available. According to Wernet *et al*. [21], these material transports account for a maximum. of 5% of the environmental impacts, though, and, therefore, play a minor role.

In order to derive the overall material and energy balances of the two process alternatives, process models were set up with the software, Umberto 5.6 [22]. Modeling the traditional batch process, data from the existing plant was used, whereas the production concept presented in Section 2.1 was taken as the data basis for the micro-/milli-continuous campaign manufacturing scheme. For the base scenario, it was assumed that 1 m^3 of a certain color premix is created and consumed for ink production. After having emptied the tank, it is cleaned with a high-pressure cleaner. Furthermore, the binder feed lines are rinsed.

The geographical scope of this study is the writing ink production industry in Germany. In order to include the upstream and disposal stages, generic datasets from the ecoinvent database [24] were used. Where possible, datasets applicable to Germany were selected. In cases in which the origins of the raw materials were unknown, datasets generated for Europe were chosen.

The temporal scope is one year, according to the functional unit. An operational life span of 20 years was, however, chosen for both plants, a time frame which is typical for batch plants in Germany as laid down in a joint report by VDI/VDE (Verein deutscher Ingenieure/Verband der Elektrotechnik Elektronik Informationstechnik) and NAMUR (Normen-Arbeitsgemeinschaft Mess- und Regeltechnik) [25]. Required materials and components for plant maintenance were specified for this time frame. The associated environmental impacts were depreciated on a straight-line basis over the 20 years, so that only the share for one year was taken into consideration during material and flow modeling.

Estimating the potential environmental impacts of the material and energy flows listed in the inventory, the CML (Centrum voor Milieukunde, Universiteit Leiden) 2001 impact assessment method [26] was applied. The environmental impacts were first calculated for all 15 impact categories of the CML 2001 method, as recommended by Azapagic and Perdan [27]. Afterwards, eight categories were chosen for detailed analysis, as well as for an effective comparison and presentation of the results. We refrained from using extra endpoint indicators, since ISO 14044 [17] does not permit their use for comparative analyses. Additionally, Huppes *et al*. [28] stress that the procedure of weighing different impact categories in order to derive an endpoint indicator is still controversial. In this paper, all material and energy flows are combined in so-called modules according

to their function, e.g., “upstream stages of operating supplies”. The respective environmental impacts are therefore also expressed depending on these modules.

Figure 1. System boundaries for the ecological assessment of both process alternatives [23]. The included lifecycle stages and components are shaded in grey.

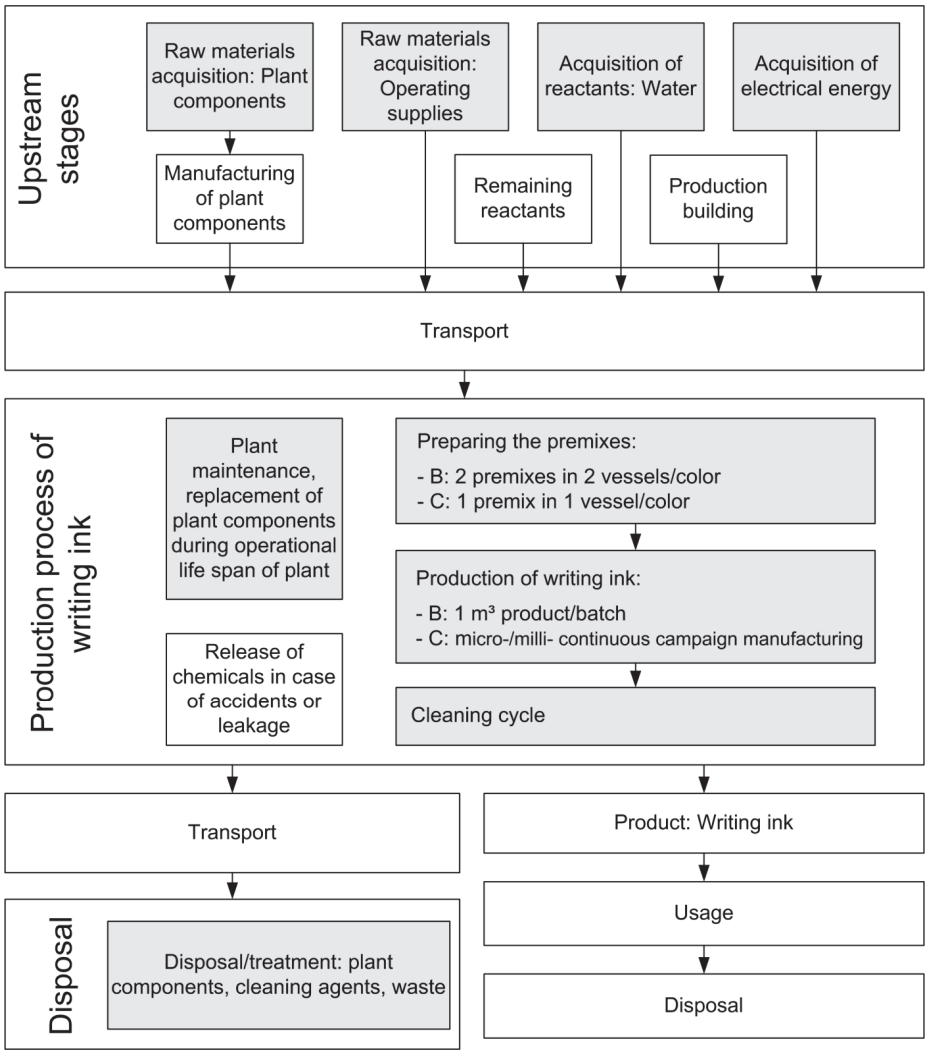

2.2.2. Description of the Sensitivity Analysis: Cleaning Agent Demand of Micro-/Milli-Continuous Campaign Manufacturing

Regarding the cleaning agent demand for continuous production, it was hypothesized in the first approximation that the results from cleaning experiments conducted on the lab plant can be extrapolated to the production plant based on the plant hold-up.

Furthermore, assumptions were made concerning the required amount of cleaning agents for rinsing the color premix vessels and the binder feeding lines. The influence of all these assumptions on the results of the ecological assessment of the micro-/milli-continuous campaign manufacturing was evaluated by means of a sensitivity analysis. All options considered are listed in Table 2.

The case C-2W-1 is similar to the base scenario requiring only one cleaning cycle at the end of the weekly production period, assuming that the minimum production output per color is exceeded

and the optimum production sequence adhered to. However, twice the amount of cleaning agents is used per cycle. C-W-4 describes the production of all four ink colors each week, not adhering to the optimum production sequence or at lower amounts than the minimum production output. Therefore, cleaning of one premix vessel and of the micro-/milli-continuous plant shall be required during each product change procedure. C-EW-1 stands for the option of using 14.2 L of ethylene glycol for discoloring the tubes and rinsing the plant afterwards with three times the amount of water. It is further assumed that 1 L of ethanol is employed for an efficient pre-clean of the color premix vessel walls prior to cleaning the vessel with a high-pressure device. The worst case is represented by the abbreviation C-EW-4, requiring cleaning of the continuous flow plant and of the color premix vessels according to the procedure of C-EW-1, however, increasing the cleaning frequency to four times per week.

Table 2. Options of the sensitivity analysis regarding the required amount of cleaning agents for the micro-/milli-continuous campaign manufacturing.

Name	Assumptions for Cleaning of		
	Micro-/Milli-Continuous Flow Plant	Color Premix Vessel	Binder Feeding Lines
C-Base scenario	14.2 L water, 1× per week	High-pressure cleaner, 135 L/event, after emptying of vessel	10 L/event, after emptying of drum
C-2W-1	28.4 L water, 1× per week	High-pressure cleaner, 270 L/event, after emptying of vessel	20 L/event, after emptying of drum
C-W-4	14.2 L water, 4× per week	High-pressure cleaner, 135 L/event, 4× per week	10 L/event, after emptying of drum
C-EW-1	14.2 L ethylene glycol, 42.6 L water, 1× per week	Preliminary cleaning with 1 L ethanol/event; afterwards, use of high-pressure cleaner, 135 L/event, 1× per week	10 L/event, after emptying of drum
C-EW-4	14.2 L ethylene glycol, 42.6 L water, 4× per week	Preliminary cleaning with 1 L ethanol/event; afterwards, use of high-pressure cleaner, 135 L/event, 4× per week	10 L/event, after emptying of drum

2.3. Economic Assessment

In this section, the methods for the economic assessment will be presented. A cost analysis was chosen as the method, since no data concerning the expected sales was available. Note that the system boundary was conformed to the lifecycle costing approach described in the VDI guideline 2884 [29]. In this study, only those costs are included that are directly related to the two processing methods. According to Klöpffer and Grahl [20], overhead costs are therefore disregarded. The static payback period was added as a further means of assessment.

2.3.1. Goal and Scope Definition of the Economic Assessment

The purpose of this study was to compare the two process alternatives, both in regard to the ecological, as well as the economic implications. Therefore, the assessments were based on the

same material and energy flow balances with identical boundary conditions. In the following, the information given for the ecological assessment in Section 2.2.1. is specified regarding the requirements of the cost analysis.

We aimed at determining the total production costs per year for a capacity of 148.200 L a^{-1} for both alternatives and identifying the main cost factors along the lifecycle. The costs for off-spec batches in the case of the batch plant and waste arising during the start-up and shut-down phases of the continuous process were thus included. The analysis was conducted from the producer's point of view in order to support a decision for or against the transfer of the traditional batch to a novel micro-/milli-continuous campaign manufacturing scheme. This corresponds to a replacement investment. As a second option, it was evaluated whether it is better to invest in either a batch or a continuous campaign plant in the case of a capacity increase to produce special writing inks. Again, the influence of data uncertainties and assumptions made for the continuous process regarding the cleaning frequency was assessed by a sensitivity analysis.

During the production phase, costs arise from the provision of electrical energy, the reactants and operating supplies, the plant operator, personnel for quality control and for maintenance services. These are part of the variable costs and are listed in Appendix C. Analogous to the ecological assessment, changes in deionized water and tap water, respectively, are the only reactants considered due to the minor changes of all other reactants, falling below the threshold value. The assessment is thus again valid for all ink colors. All waste streams are included in the assessment; the disassembly and end-of-life of the plant was, however, excluded, since no reliable data were available. Moreover, all transport was left out of the evaluation.

For both manufacturing schemes, the costs for reactants, operating supplies and electricity were calculated with the yearly amounts resulting from the material and energy flow modeling and their respective prices. Personnel costs were derived from the required work time. During batch operation, an operator without formal vocational training prepares the premixes, dispenses the binder premix to the color premix, is responsible for operating control, filling the ink into drums and cleaning the stirred vessels after each production. On average, 3–7 h are required per batch for the plant operator depending on the amount manufactured, as well as 1 hour for the chemical laboratory assistant. During continuous manufacturing, the following tasks are carried out by the plant operator:

- Premix preparation: The color premixes are prepared taking 1 h on a 1 m^3 scale. As described in Section 2.1, the recipe adaption allows for a simplified preparation procedure. For the base scenario, it is assumed that two color premixes are consumed per weekly production procedure. During reactant mixing, the plant operator is also responsible for supplying new binder drums and for refilling of the preservatives.
- Monitoring of the plant: According to Wichmann [30], the start-up phase of micro-/milli-continuous plants ought to be monitored by an operator, whereas the production phase can be automated. In addition, shut-down and cleaning procedures can also be automated. Therefore, a plant operator needs to be on-site for merely 1 h, observing the start-up.
- Cleaning: After the color premix has been used up, the operator uses a high-pressure cleaner to clean the vessel for 15 min.

In total, a plant operator is required for 3.5 h per week for the continuous manufacturing of a single ink color per week. A trained laborer was included in the calculations for plant control in contrast to an untrained laborer for premix preparation and cleaning. The process control system guarantees that the product specifications are met, rendering any additional quality control in the laboratory superfluous. The costs for maintenance services were added to the variable costs. The costs for equipment exchanged during the 20 years of plant life (see Section 2.2.1.) were calculated based on data from the suppliers. The associated personnel costs were added, assuming that the ratio of wages to material costs is 43.5:56.5, as stated by Kölbel and Schulze [31].

Besides the variable costs, the fixed costs for all plant equipment were determined based on current quotations from existing suppliers; see Appendix B. The costs for construction and assembly of the plants were added. In the case of the batch plant consisting mainly of stirred vessels and equipment made of non-alloy steel, 10% of the investment may be taken on according to Helfrich and Schubert [32]. Due to the more elaborate equipment in the case of the continuous process, the recommendation from Ullrich [33] was accepted, who deems a value of 15% of the investment realistic for the construction and assembly of chemical plants with a heterogeneous composition. Furthermore, costs for the programming of the process control system and the testing of the automatic measurement of the color values arise for continuous manufacturing. These costs were also included based on a supplier's quotation. For both plants, the investment and costs for construction were summed up and depreciated on a straight line basis over 20 years. Depreciation on a straight line basis is customary during pre-calculation, as Ullrich [33] postulates. Other fixed costs, such as taxes and interests, were not included in the cost analysis.

2.3.2. Description of the Sensitivity Analysis: Cleaning Agent Demand of the Micro-/Milli-Continuous Campaign Manufacturing

For sensitivity analysis of the cleaning frequency and, therefore, the cleaning agent demand, the same cases as in the ecological assessment are considered. This sensitivity analysis influenced all cost positions of the variable costs: The type and amount of the cleaning agent is varied for the two cases, C-2W-1 and C-EW-1, which influences the raw material costs, as well as the costs for disposal. In case C-2W-1, the cleaning period of the color premix vessels is duplicated, which increases the labor costs per cleaning cycle accordingly. Furthermore, the energy costs are slightly higher compared to the base scenario of the continuous manufacturing scheme, since the cleaning cycles are lengthened.

In cases C-W-4 and C-EW-4, it is assumed that four cleaning cycles are required for both the continuous flow plant, as well as the color premix vessels, which leads to higher raw material, disposal and personnel costs. Although the share of solvents in the waste is considerably higher than in the other cases, the same disposal costs were applied for all cases, since no other was available. Note that four color premixes shall be prepared in contrast to the cases with only one cleaning cycle. During start-up after cleaning, the same amount of off-spec ink is produced and disposed of as in the C base scenario, leading to higher reactant costs. In order to compensate for this amount of ink, the total production period for the required output is prolonged, which also increases the energy costs.

3. Assessment Results and Discussion

The results of the ecological, as well as the economic assessment will be described in this chapter. The results from both base scenarios, as well as sensitivity analyses will be analyzed and discussed in regard to their significance and validity. Afterwards, conclusions will be drawn with respect to the defined goal of the study.

3.1. Ecological Assessment

3.1.1. Ecological Assessment of the Base Scenarios

The potential environmental impacts of the eight categories chosen for a detailed analysis from the CML 2001 method are presented in this section. Figure 2 gives an overview of the results for the impact categories, global warming potential and land occupation, each related to the values of the base scenario of the batch process. The global warming potential (GWP) associated with continuous manufacturing is decreased by 68% compared to batch processing. In both cases, more than 92% of the GWP are related to the two modules “provision of electrical energy” and “upstream stages of plant equipment”. Each time, the module mentioned first is associated with the highest impact by far. Savings in electrical energy during the continuous production of writing ink are therefore decisive for the GWP reduction. These are realized by eliminating energy-intensive heating periods in the vessels, enabled both by recipe adaption and effective mixing of the reactants in the micro-mixer. Such a recipe adaption seems not feasible for the batch process, since the premixes have been explicitly designed and adjusted to the production conditions in the stirred tank reactors in order to reach the lowest probability of agglomeration. Besides, the cleaning process of the vessels is shortened by employing a high pressure cleaning device, thus reducing the energy demand for cleaning. Heat integration with a heat exchanger leads to a further decrease in comparison with the batch process. The energy demand of the continuous process is therefore mainly influenced by the power of the electrically operated equipment, whereas it is resulting from long heating periods and the associated heat losses to the environment for the batch process. The second most important component is the module “upstream stage of plant equipment” in which a higher GWP value is derived for the continuous rather than for the batch process. This is mainly caused by more elaborate plant equipment and the use of polytetrafluorethylene (PTFE) for tubing and pipes as the highest single value.

Regarding land occupation, the reduction achieved by changing from batch to continuous processing is lower than for the GWP. This fact can be ascribed to the module “upstream stage of plant equipment”, therein to the use of varnished medium-density fiberboards as plant shelves, accounting for around 86% of the category’s value. According to Frühwald *et al*. [34], wood is both used as the raw material for the fiberboards, as well as the energy source for generating the process energy, therefore resulting in significant land occupation.

Figure 2. Comparison of the global warming potential (GWP) and land occupation (LO) of batch and micro-/milli-continuous campaign manufacturing.

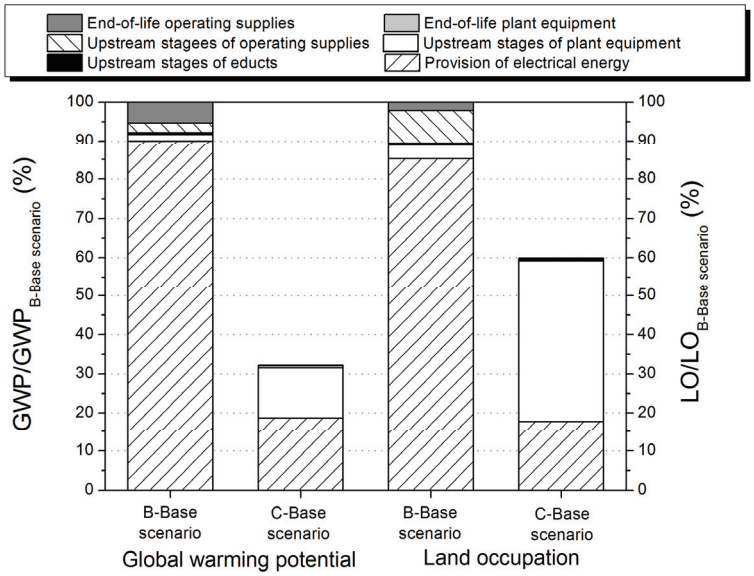

The results of all six toxicity impact categories are illustrated in Figure 3. The values of the continuous process are reduced by 68% to 71% compared to batch manufacturing, with the exception of the human toxicity potential being reduced by only 31%. This lower reduction rate is due to the module "upstream stages of plant equipment" being mainly responsible for this impact category, as well as to the fact that stainless steel is provided in similar amounts for both plants. In all other toxicity categories, the provision of electrical energy causes the highest impacts. These findings support the results of Wernet *et al*. [21], after which generally more than half of the environmental impacts are caused by the energy-related inputs in chemical industries producing organic and inorganic products.

3.1.2. Ecological Assessment of the Sensitivity Analysis

A sensitivity analysis of the cleaning agent demand was conducted in order to examine the reliability of the study. The results of this sensitivity analysis are illustrated in Figure 4. It is evident that the increased amount of water required for cases C-2W-1 and C-W-4 has only minor influences on the impact categories. Decoloring the plant with ethylene glycol and rinsing it afterwards with water at the end of each weekly production period, represented by case C-EW-1, is also ecologically tolerable. However, if this intensive cleaning is required during each of the four cleaning procedures, then the indicator values would be affected very negatively (C-EW-4). In this case, the human toxicity potential is drastically increased and even 1% higher than the equivalent value for batch processing. The deterioration compared to the case C-W-4 with the same cleaning frequency is mainly caused by the calculated amount of ethylene glycol.

Figure 3. Toxicity potentials of batch and micro-/milli-continuous campaign manufacturing. MAETP, marine aquatic eco-toxicity potential; HTP, human toxicity potential; TAETP, terrestrial aquatic eco-toxicity potential; MSETP, marine sediment eco-toxicity potential; FAETP, fresh water aquatic eco-toxicity potential; FSETP, fresh water sediment eco-toxicity potential.

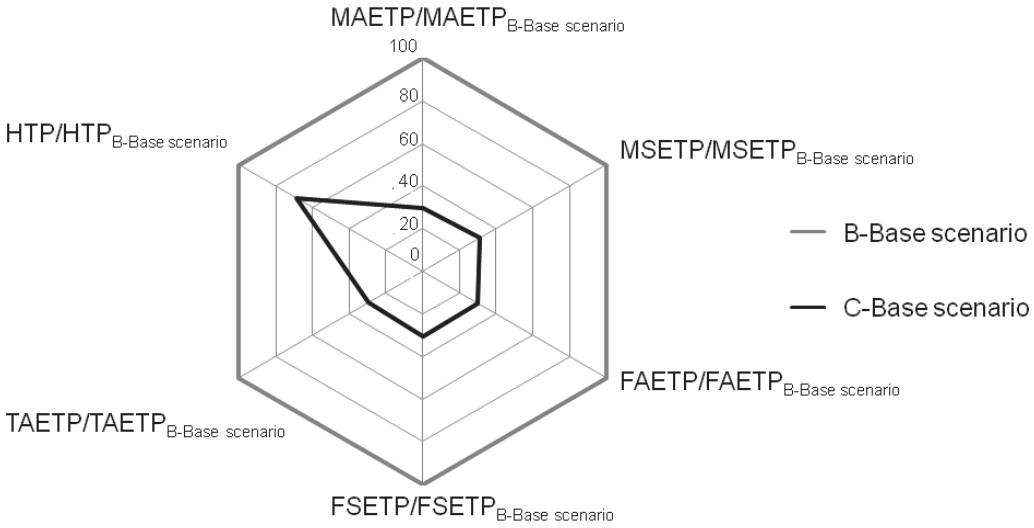

Figure 4. The change in the potential environmental impacts of the continuous process in comparison with the batch production scheme varying the cleaning agent demand.

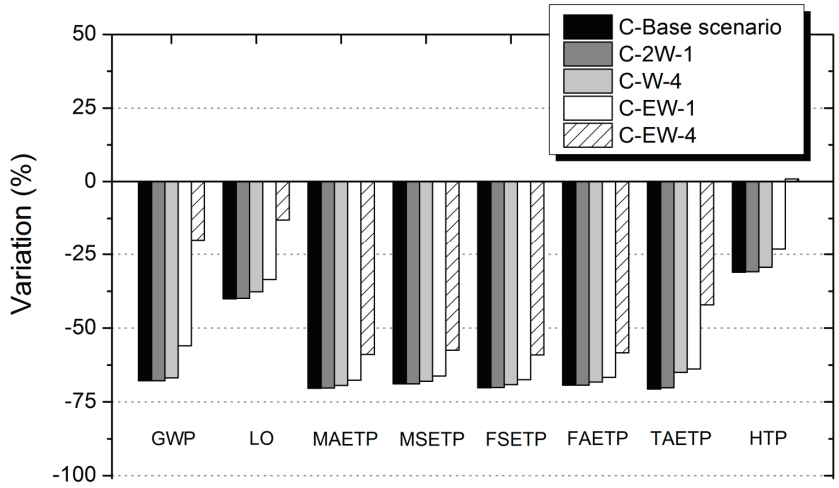

3.1.3. Significance and Validity of the Results of the Ecological Assessment

This study comprises the comparison of the current batch and the novel micro-/milli-continuous campaign manufacturing scheme, whereas an optimized batch process was not included. However, it cannot be ruled out that a fully or partially automated batch plant leads to similar advantages in regard to energy and cleaning agent demand, as well as personnel requirements as the automated continuous plant. Such an optimized batch production may therefore be the subject of future studies, as, for example, described in Oldenburg *et al*. [35].

When discussing the significance and validity of these results, the focus should be mainly on their overall robustness.

That is influenced by data uncertainties during material and energy flow modeling caused both by errors in modeling, as well as by the quality of the data used. Regarding the process models, it should again be stressed that a black-box model was employed. The level of detail of both process models is therefore similar: in both cases, the acquisition of raw materials, as well as the end-of-life stages were included as generic datasets, whereas the ink production was modeled on the basis of measurement results, calculations and assumptions.

The quality of the data used for the modeling of the batch production stage can be graded as 1–2, according to the Pedigree matrix presented by Weidema and Wesnaes [36], wherein 1 is the best and 5 the worst classification. This is due to the fact that the lifecycle inventory is mainly based on primary data, which at the time of the study, was not older than three years. In contrast, the quality of the data used for the continuous process can be rated as 4–5. In this case, the results achieved with the continuous lab plant were extrapolated to the production stage, which then served as a basis for the lifecycle inventory analysis. This approach leads to higher data uncertainties. However, several scenario and sensitivity analysis, described in Grundemann [23], as well as for the cleaning agent demand in this paper, showed that only minor variations in the indicator values are resulting from the plausible scenarios. Additional worst cases helped to allow for the deriving of the recommendations.

It can therefore be concluded that the quality of the model and the data employed are adequate for a solid comparison of the two processing schemes.

3.2. Economic Assessment

3.2.1. Economic Assessment of the Base Scenarios

The total annual production costs to manufacture the desired amount of ink are summarized for both processing alternatives in Table 3. It shows that the fixed costs of the continuous production scheme are almost three times higher than those of the batch production scheme, which is due to the more elaborate plant equipment with more electrically-driven parts and sensors. As a result of this, the costs for maintenance services are also increased.

However, all other variable costs are decreased when transferring the production scheme. This is mainly caused by reducing the labor costs by 84%, realized both during the production itself and the automated quality control. The energy demand and, hence, the energy costs can be lowered by 79%, a similar percentage as the labor costs. However, the energy costs have less influence on the total production costs, because of the lower prices per unit. This effect is even more pronounced for the costs of the operating supplies and their disposal. Transferring a batch to a continuous process would lead to a reduction of both items by 94% to 98%. Since they are associated with a very low price per unit, though they play only a minor role in the cost analysis.

The cost structure is therefore altered by transferring the manufacturing strategy, as Figure 5 illustrates. The largest share of the total production costs per year of the batch plant is related to personnel costs, followed by the costs for electricity, raw materials and disposal. Meanwhile, the

fixed costs account for only 4% of the total production costs per year. For the continuous process, the labor costs still have a very high impact, decreasing, however, by 68% to 30%. Since the total production costs are lower than for the batch process, the share of the fixed costs and those for maintenance rise.

Table 3. Total annual production costs of the base scenarios of the batch production (B base scenario) and the micro-/milli-continuous campaign manufacturing scheme (C base scenario) for a total production output of 148,200 L of writing ink.

	B-Base Scenario	**C-Base Scenario**
Data of both plants		
Investment (€)	21,315	52,018
Costs for construction and assembly of plant (€)	2132	7803
Costs for programming and testing of the process control system (€)	/	6850
Sum of total investment (a)	23,447	66,671
Operational life span (a)	20	20
Recovery value (€)	0	0
Fixed costs (€ a^{-1})		
Depreciation	1172	3334
Variable costs (€ a^{-1})		
Raw materials		
Water for ink production	114	94
Operational supplies (cleaning, start-up)	1855	25
Disposal of waste water and solvents	1478	37
Energy	4319	898
Personnel		
Plant operator	16,235	3263
Chemical laboratory assistant	4025	/
Maintenance services	646	3241
Sum of variable costs	28,672	7558
Total production costs (€ a^{-1})	**29,844**	**10,892**
Specific manufacturing costs (€ L^{-1})	**0.2014**	**0.0735**

Figure 5. The change in the potential environmental impacts of the continuous process varying the cleaning agent demand in comparison with the batch production scheme.

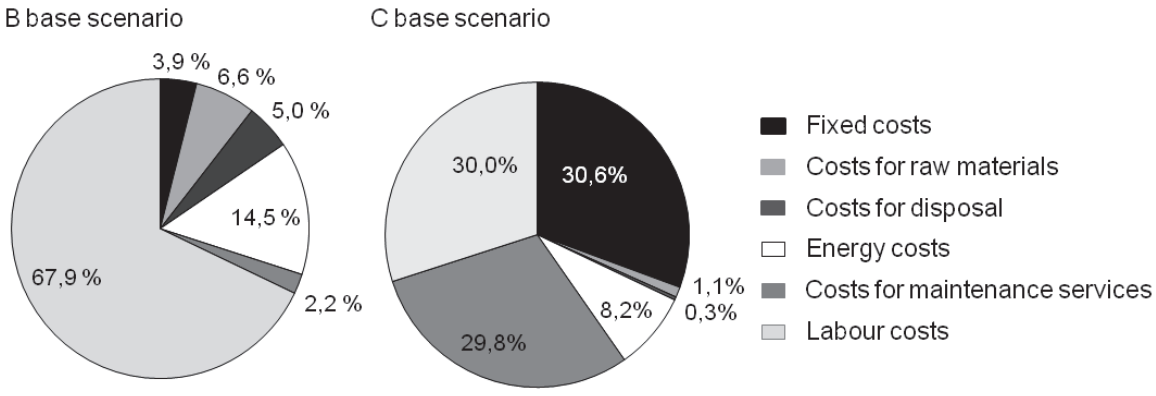

The cost structure, however, is influenced by the system boundaries chosen. If all reactants were included in the calculation of the costs for raw materials, these would dominate the variable costs for both manufacturing strategies. The latter was also found by Krtschil *et al*. [37] for the continuous production of 4-cyanophenylboronic acid with micro-components, as well as by Benaskar *et al*. [38], who have conducted an economic assessment of the Ullmann C–O cross-coupling reaction using both microprocessing and microwave heating. In the case of writing ink, the only reactant included in this study, water, would have the lowest share in the raw material costs, due to its low price.

The comparison of the total production costs per year shows that the cost advantage of the continuous manufacturing scheme is mainly based on lower variable costs. This was predicted by Roberge *et al*. [39] for dedicated micro-/milli-continuous processes. Investing in either a batch or a continuous plant for ink manufacturing, a cost advantage of 18,953 € arises when choosing the continuous instead of the batch regime. Dividing the difference in the total production costs per year of both processes by the cost advantage mentioned according to:

$$t_{P,choice} = \frac{66{,}671\ € - 23{,}447\ €}{18{,}953\ € \ a^{-1}} \quad (1)$$

results in a payback time of 2.3 years. However, if the current batch process is replaced by a new micro-/milli-continuous campaign manufacturing scheme, it is assumed that the batch plant is already written off. Only the variable costs have to be considered in this case. The cost advantage of the continuous processing scheme is reduced to 17,781 €. The payback time then follows from to 3.8 years.

$$t_{P,replacement} = \frac{66{,}671\ €}{17{,}781\ € \ a^{-1}} \quad (2)$$

3.2.2. Economic Assessment of the Sensitivity Analysis

Figure 6 shows that a cost advantage can be realized compared to batch processing for all cases considered. However, this cost advantage strongly depends on the assumptions and the resulting variable costs, as described below.

Using twice the amount of water for cleaning in case C-2W-1 has a negligible impact on the total production costs. Despite their rise by 5.2% compared to the C base scenario, they are still 62% lower than in the batch scenario. The rise mentioned is mainly due to the doubled personnel requirements during the cleaning of the premix vessels. The costs for tap water and its disposal have only a minor impact. The payback time is similar to the C base scenario.

If additional solvents are used for cleaning (C-EW-1), then the total production costs are lowered by 55% compared to the batch scheme. Due to the high costs of ethylene glycol, they are higher than in case C-2W-1; the personnel requirements are, however, equivalent to those of the base scenario. The investment in a new continuous plant is amortized after 2.6 years, whereas exchanging the existing production facilities leads to a payback period of 4.3 years.

Figure 6. Total annual production costs of the batch and the micro-/milli-continuous campaign manufacturing process for writing ink varying the cleaning agent demand.

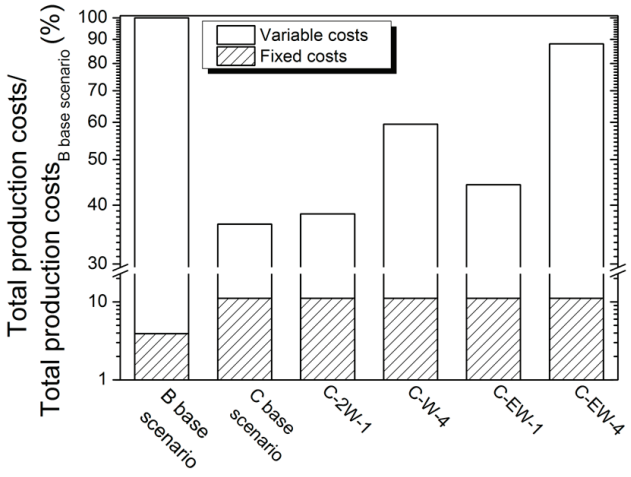

Four cleaning cycles are required per week in C-W-4 with production costs 40% lower than for the batch process. The rise compared with the base scenario is caused by the increased personnel requirements for the separate preparation of four premixes and the on-site control of each of the four start-up phases. As a result of this, the payback period is 3.6 years when investing in a new plant and 6.1 years when exchanging the existing plant. This illustrates that even the production of specialties at low volumes or without adhering to the optimum production sequence is economically viable in the case of a capacity increase or the production of new products.

If, however, four intensive cleaning cycles are required per week, then the total production costs are only 12% lower than those of the batch plant. These high production costs are determined by the high labor costs and the high costs for providing the cleaning agent, ethylene glycol. The low cost advantage compared to batch processing renders this version not economically viable: the payback period in the case of a new investment is increased to 12.2 years and to 28.1 years in the case of a plant exchange.

3.2.3. Significance and Validity of the Results of the Economic Assessment

The economic assessment was based on the comparison of the total production costs per year and the payback periods of both process alternatives. The total production costs were calculated with data from an existing batch plant, however, derived from a production concept of the continuous manufacturing scheme. Again, it is stressed that an optimized batch plant is not considered in this paper. Such an optimization might lead to similar cost advantages, as described here for the continuous manufacturing scheme. In order to calculate the fixed costs, detailed equipment lists served as a basis for specific supplier quotations. The fixed costs are therefore regarded as reliable based on the system boundaries chosen and the assumptions made. The calculation of the variable costs is dependent on the material and energy streams derived by flow modeling and the respective prices per unit. For flow modeling, please refer to the constraints and comments listed in Section

3.1.3. All Prices Employed are Valid for the Specific Production Location

Based on the data basis described, the data quality for the economic assessment of the batch process can be awarded grade 2 following the Pedigree matrix by Ciroth [40], the continuous process, however, only grades 3–4. The grades range from 1 for the best to 5 for the worst data quality. The main influencing factors on the economic viability of the micro-/milli-continuous campaign manufacturing scheme were identified by sensitivity analysis. It was shown that the results are reliable, even when varying critical parameters. Critical limits led to recommendations for an efficient continuous campaign production, as described in the following section.

3.3. Interpretation of All Results and Recommendations

Based on the results of the base scenarios and the sensitivity analysis of the cleaning agent demand of both the ecological, as well as the economic assessment, the following recommendations can be given regarding the operation of a continuous campaign production plant for writing ink:

- If different ink colors are to be produced during one production week, it is advised to adhere to the optimum production sequence, as well as to the minimum production volume of 121 L. In this way, the cleaning frequency can be limited to one cycle at the end of the weekly production period, decreasing the amount of cleaning agents, as well as the disposal effort required and the labor costs associated with it.
- However, if cleaning is required several times a week, due to very tight product specifications, the best option is to use only water (see case C-W-4). It is generally suggested to aim at minimizing the use of ethylene glycol, ethanol or sodium carbonate solution, both from the ecological and economic point of view. Of these three fluids, sodium carbonate solution is the preferred cleaning medium if decoloration is necessary. One cleaning cycle per week using additional solvents to fully clean and decolor the continuous flow plant seems, however, ecologically tolerable and economically viable according to C-EW-1.
- Since the personnel costs are the main influencing factor on the annual production costs, preparing several premixes per week in order to produce various specialties therefore carries weight. It is recommended to prepare at least two premixes in parallel if the type and amount of vessels available permit. Conducting a cost analysis, it is assumed that the same sales can be realized by common inks and special inks of very small production volumes. The additional personnel costs could be taken into consideration during pricing, though.
- From an ecological point of view, the amount of waste should be minimized by its reuse. Particularly, the waste water arising during the cleaning of the premix vessels could be reused as the reactant for the production of the same or similar inks, like is proposed for the waste water of dying processes by Shams-Nateri [41]. The rest of the cleaning agents should, however, be discarded, due to their contamination with a binder, a potential source of agglomerate formation. From an economic point of view, reusing the waste water is not absolutely necessary, due to the low water price, and might even lead to higher labor costs, because of additional handling steps.

4. Conclusions

Based on this study, it can be concluded that a continuous campaign manufacturing scheme is both an ecologically and economically viable alternative to the traditional batch production of writing ink. Lower environmental impacts in all impact categories result from the new production strategy. The key to ecological viability is the reduced energy demand during continuous processing, resulting from more intensive mixing in the micro-mixer, as well as from recipe adaption, thus eliminating the long heating periods in the vessels. The reduced energy demand also outweighs the additional environmental impacts, due to the more elaborate plant equipment. Furthermore, a cost advantage can be realized with the micro-/milli-continuous campaign manufacturing scheme compared to batch processing. In this case, the reduced personnel requirements resulting from a mostly automated production are decisive. Overall, this leads to lower variable costs compared to batch production. The scope of this paper does not include a fully or partially automated batch plant, which might lead to similar advantages in regard to energy demand and personnel requirements. However, intensified heat and mass transfer in micro- and milli-structured components greatly enhances the process repeatability and product quality in comparison with processing in batch vessels. Due to the high investment, continuous campaign production is especially suited for a capacity increase of existing or the introduction of new products.

Acknowledgments

This work has been partially funded by the Deutsche Bundesstiftung Umwelt, Germany, under grant no. AZ 25833 within the funding cluster “Novel Process Windows”. We gratefully acknowledge the financial support.

Nomenclature

a	Year (Latin: annum)
ABS	Acrylonitrile butadiene styrene
B	Batch processing of writing ink
C	Micro-/milli-continuous campaign manufacturing of writing ink
CML	Centrum voor Milieukunde, Universiteit Leiden
EPDM	Ethylene propylene diene monomer
FAETP	Fresh water aquatic eco-toxicity potential
FSETP	Fresh water sediment eco-toxicity potential
FU	Functional unit
GWP	Global warming potential
HTP	Human toxicity potential
LCA	Lifecycle assessment
LO	Land occupation
MAETP	Marine aquatic eco-toxicity potential
MSETP	Marine sediment eco-toxicity potential
NAMUR	Normen-Arbeitsgemeinschaft Mess- und Regeltechnik

OLED	Organic light emitting diode
PET	Polyethylene terephtalate
PTFE	Polytetrafluorethylene
t_P	Payback time in years
TAETP	Terrestrial aquatic eco-toxicity potential
VDI/VDE	Verein deutscher Ingenieure/Verband der Elektrotechnik Elektronik Informationstechnik

Appendix A: Flow Chart of the Continuous Manufacturing Plant

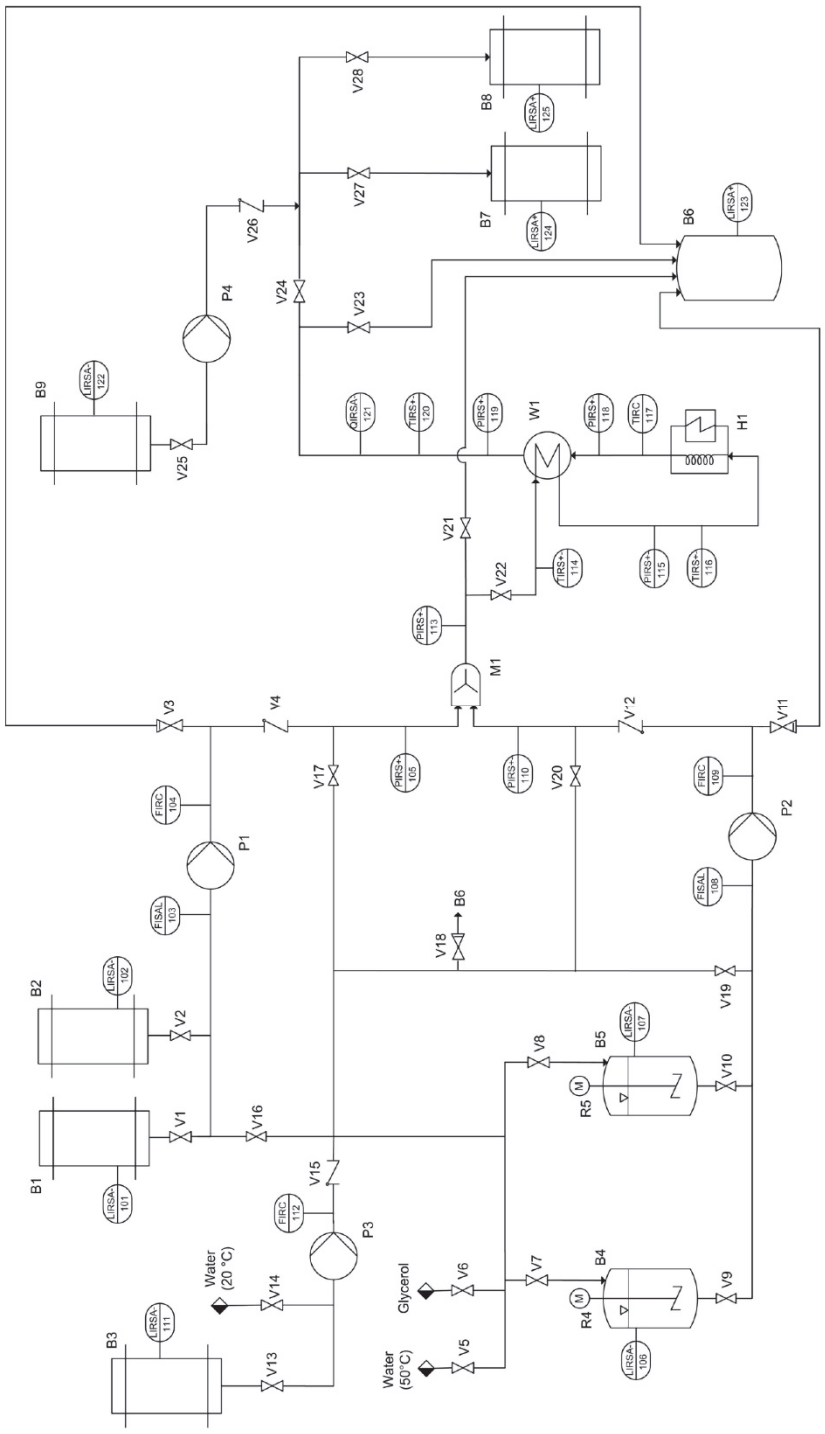

Appendix B: Equipment List and Investment for Both Process Alternatives

Table B-1. Equipment list and costs for the batch plant. PTFE, polytetrafluoroethylene.

Equipment	Supplier and Model	Technical Data, Comments	Main Material	Price/Piece (€)	Amount	Total Costs (€)
Jacketed stirred vessel	HAB Heiland Apparatebau	$V = 1\ m^3$	1.4301	6820	2	13,640
Stirrer	Stelzer SM-63, propeller stirrer	$P_{max} = 2.2$ kW	1.4571	1,940	2	3880
Level sensor	E.L.B. Füllstandsgeräte, magnetic level gauge	PTFE sealing: $T_{max} = 150$ °C	1.4571	1046	2	2,092
Centrifugal pump	Linn-Pumpen T65E with frequency converter VF S11S 2004 PLE-	$\dot{V} = 8–50\ L \cdot min^{-1}$, $P_{max} = 0.45$ kW	1.046	922	1	922
Tube	Haarmann pressure hose	$2 \times l = 1.5$ m, $2 \times l = 4$ m	EPDM	568	1	568
Portable thermometer	Ebro TFX 410	T = −50–300 °C	ABS	213	1	213
Total investment						21,315

Table B-2. Equipment list and costs for the micro-/milli-continuous campaign plant.

Equipment	Code	Supplier and Model	Technical Data, Comments	Main Material	Price/Piece (€)	Amount	Total Costs (€)
Stirred vessel	B4, B5	HAB Heiland Apparatebau	V = 1 m³	1.4301	4140	2	8280
Stirrer	R4, R5	Stelzer SM-63, propeller stirrer	P_{max} = 2.2 kW	1.4571	1940	2	3880
Level sensor	LIRSA-101/2, 106/7, 124/5	Waycon UFP-1600-M18-2P-SA	/	PET	178	6	1068
Tube	/	Haarmann pressure hose	2 × l = 1.5 m, 2 × l = 4 m	EPDM	568	1	568
Pump for feeding of reactants	P1, P2	Knoll MX10S-10/20	$\dot{V}$ = 10–25 L·h^{-1}, P_{max} = 0.37 kW	1.4571	1,868	2	3736
Limit switch	FISAL 103, 108	Infra CS15	/	Brass	94	2	188
Flow meter	FIRC 109	Krohne OPTIMASS 3300 C, MFC 300 C	/	1.4404	3,647	1	3647
Flow meter	FIRC 104	PKP DV01	/	Aluminum	878	1	878
Pressure sensor	PIRS+-	tecsis DD701	Flush-mounted membrane	1.4301	240	6	1440
Mixer	M1	Synthesechemie MicroJetReactor	/	Hastelloy	3190	1	3190
Thermo couple	TIRS+-114, 116, 120	TMH	Type K	2.4816	39	3	117
Heat exchanger	W1	API Schmidt-Bretten SIGMA M 9 NBL	A = 1.7 m²	1.4404	1,100	1	1,100
Thermostat	H1	Fisher Scientific FBH 712	P_{max} = 2.25 kW	1.0037	1344	1	1344
Resistance thermometer	TIRC 117	TMH	Pt100/A	1.4541	82	1	82
Measurement of the color value	QIRSA-121	Premosys PR0126-C4, PR0137, Durchflussküvette	/	Aluminum	1626	1	1626

Table B-2. *Cont.*

Equipment	Code	Supplier and Model	Technical Data, Comments	Main Material	Price/Piece (€)	Amount	Total Costs (€)
Pump for feeding of preservative	P4	Mecorex TL/15E	$\dot{V}$ = 0.36–36 mL h^{-1}, P_{max} = 0.015 kW	1.4301	1340	1	1340
Limit switch	LIRSA 111, 122/3	Honeywell LLE 102000	/	Polysulf.	41	3	123
Centrifugal pump	P3	Linn-Pumpen T 65E, frequency converter VF S11S 2004 PLE-	$\dot{V}$ = 8–50 L h^{1}, P_{max} = 0.45 kW	Cast steel	922	1	922
Flow meter	FIRC 112	PKP DOZ01	/	PTFE	232	1	232
Valves	V1–V28	END Automation, Bürkert: div. models (28 in total)	/	1.4404	2059	1	2059
Fittings	/	Swagelok div.	/	1.4404	2088	1	2088
Tubing	/	Bola div.	d_{in} = 2.4 mm/6 mm/8 mm	PTFE	440	1	440
Suction lance	/	Franck und Warnecke	d_{in} = 8 mm	1.4404	23	2	46
High-pressure cleaning device	/	Nilfisk-Alto Poseidon 2-22XT	$\dot{V}_{max}$ = 9 L min^{-1}, P_{max} = 2.3 kW	Cast steel	577	1	577
Rockwool	/	Rockwool Klimarock KR50	A = 2.5 m^2, λ = 0.04 W $m^{-1} \cdot K^{-1}$	Rockwool	18	1	18
Plant Framework	/	Rose + Krieger profiles, Modulor Medium Density Fibre shelves, Jaera perforated plates made of stainless steel	/	Aluminum	2,948	1	2948
Process control unit	/	Delphin TopMessage device	/	Electronics	9,369	1	9369
Computer, screen, mouse	/	Ateclo including assembly	/	/	653	1	653
Power supply unit	/	Voltcraft FSP 1207	/	Polystyrene	59	1	59
Total investment							52,018

Appendix C: Prices

Table C-1. Adopted prices for operating supplies, reactants and electricity for the cost analysis.

Name	Price	Unit	Comment	Source
Tap water	1.62	€ m^{-3}	City of Peine, 2008	Landesbetrieb für Statistik und Kommunikationstechnologie (LSKN) [42]
Waste water	2.43	€ m^{-3}	City of Peine, 2008	LSKN [42]
Electricity	0.1233	€ kWh^{-1}	Average price without tax for German industries, 2012	Bundesverband der Energieabnehmer e.V. (VEA), Bundesverband der Energie- und Wasserwirtschaft (BDEW) [43]
Deionized water	1.93	€ m^{-3}	Assumption that price is 20% higher than tap water	/
Sodium carbonate	4.02	€ kg^{-1}	Packing unit: 25 kg; quotations from 2012	Each time price average based on three quotations
Ethanol	2.24	€ l^{-1}	Packing unit: 100–190-L drum; quotations from 2012	
Ethylene glycol	2.68	€ L^{-1}	Packing unit: 205–220-L drum; quotations from 2012	

Table C-2. Adopted prices for personnel costs for the cost analysis.

Name	Price	Unit	Comment	Source
Plant operator (unskilled)	15.65	€ h^{-1}	Assumed pay grade: E5, after 6 years	Labor agreement of the chemicals industries in Niedersachsen, Germany. From Wirtschafts- und Sozialwissenschaftliches Institut (WSI) archive [44]
Plant operator	18.61	€ h^{-1}	Assumed pay grade: E7, after 6 years	
Chemical laboratory assistant	27.16	€ h^{-1}	Assumed pay grade: E11, after 6 years	

Conflicts of Interest

The authors declare no conflict of interest.

References

1. Mahammadzadeh, M. Unternehmen investieren in den Umweltschutz. *UmweltMagazin* **2013**, *43*, 36–39.
2. Yue, D.; Fengqi, Y. Sustainable scheduling of batch processes under economic and environmental criteria with MINLP models and algorithms. *Comp. Chem. Eng.* **2013**, *54*, 44–59.
3. Mitropetros, K.; Bazzanella, A. *Leitfaden Mikroverfahrenstechnik: µVTGuide*; Dechema e.V.: Frankfurt, Germany, 2010.
4. Schnitzer, H.; Titz, M. Technology wedges for low carbon-strategies in industry. In *Energy Options Impact on Regional Security*; Barbir, F., Ulgiati, S., Eds.; Springer: Dordrecht, The Netherlands, 2010; pp. 109–122.
5. MIT news. MIT and Novartis in new partnership aimed at transforming pharmaceutical manufacturing. Available online: http://web.mit.edu/newsoffice/2007/novartis-0928.html (accessed on 12 December 2013).
6. MIT news. Continuous drug manufacturing offers speed, lower costs. Available online: http://web.mit.edu/newsoffice/2012/manufacturing-pharmaceuticals-0312.html (accessed on 12 December 2013).
7. Stitt, E.H.; Rooney, D.W. Switching from batch to continuous processing for fine and intermediate-scale chemicals manufacture. In *Novel Concepts in Catalysis and Chemical Reactors: Improving the Efficiency of the Future*; Cybulski, A., Moulijn, J.A., Stankiewicz, A., Eds.; Wiley-VCH: Weinheim, Germany, 2010; pp. 309–330.

8. Jiménez-González, C.; Poechlauer, P.; Broxtermann, Q.B.; Yang, B.S.; am Ende, D.; Baird, J.; Bertsch, C.; Hannah, R.E.; Dell'Orco, P.; Noorman, H.; *et al*. Key green engineering research areas for sustainable manufacturing: A perspective from pharmaceutical and fine chemicals manufacturers. *Org. Proc. Res. Dev.* **2011**, *15*, 900–911.
9. Kralisch, D.; Streckmann, I.; Ott, D.; Krtschil, U.; Santacesaria, E.; di Serio, M.; Russo, V.; de Carlo, L.; Linhart, W.; Christian, E.; *et al*. Transfer of the epoxidation of soybean oil from batch to flow chemistry guided by cost and environmental issues. *ChemSusChem* **2012**, *5*, 300–311.
10. Hessel, V. Novel process windows—Gate to maximizing process intensification via flow chemistry. *Chem. Eng. Technol.* **2009**, *32*, 1655–1681.
11. Charpentier, J.-C. In the frame of globalization and sustainability, process intensification, a path to the future of chemical and process engineering (molecules into money). *Chem. Eng. J.* **2007**, *134*, 84–92.
12. F^3 Factory. Third Newsletter published on 27th August 2012. Available online: http://www.f3factory.com/scripts/pages/en/newsevents/F3_Factory_Newsletter_3.pdf (accessed on 12 December 2013).
13. Grundemann, L.; Fischer, N.; Scholl, S. From macro batch to micro-conti manufacturing: A new eco-friendly production process for writing ink employing micro-process engineering. *Chem. Eng. Technol.* **2009**, *32*, 1748–1756.
14. Grundemann, L.; Gonschorowski, V.; Fischer, N.; Scholl, S. Cleaning waste minimization for multi-product plants: transferring macro batch to micro conti manufacturing. *J. Cleaner Prod.* **2012**, *24*, 92–101.
15. Fürer, S.; Rauch, J.; Sanden, F.J. Konzepte und Technologien für Mehrproduktanlagen. *Chem. Ing. Tech.* **1996**, *68*, 375–381.
16. Schaber, S.D.; Gerogiorgis, D.I.; Ramachandran, R.; Evans, J.M.B.; Barton, P.I.; Trout, B.L. Economic analysis of integrated continuous and batch pharmaceutical manufacturing: a case study. *Ind. Eng. Chem. Res.* **2011**, *50*, 10083–10092.
17. Environmental management—Life cycle assessment—Principles and framework, 2006, ISO 14040:2006.
18. Environmental management—Life cycle assessment—Requirements and guidelines, 2006, ISO 14044:2006.
19. Curran, M.A. Life Cycle Assessment: Principles and Practices. By Scientific Applications International Corporation (SAIC), Contract No. 68-C02–067, Work Assignment 3–15–on behalf of: United States Environmental Protection Agency, National Risk Management Research Laboratory, Cincinnati, OH, USA, 2006. Available online: http://www.epa.gov/nrmrl/std/lca/lca.html (accessed on 12 December 2013).
20. Klöpffer, W.; Grahl, B. *Ökobilanz (LCA): Ein Leitfaden für Ausbildung und Beruf*; Wiley-VCH: Weinheim, Germany, 2009.
21. Wernet, G.; Mutel, C.; Hellweg, S.; Hungerbühler, K. The environmental importance of energy use in chemical production. *J. Ind. Ecol.* **2011**, *15*, 96–107.
22. *Umberto 5.6*; ifu Hamburg: Hamburg, Germany, 2011.

23. Grundemann, L. *Zur Umstellung von Chargenweise Betriebenen Mehrproduktanlagen auf Kontinuierliche Kampagnenfertigung*; Cuivillier: Göttingen, Germany, 2013.
24. *Ecoinvent database v 2.2*; Swiss Centre for Life Cycle Inventories: Zürich, Switzerland, 2010.
25. VDI/VDE, NAMURVDI/VDE-Gesellschaft Mess- und Automatisierungstechnik; NAMUR. Roadmap Prozess-Sensoren 2015+: Technologie-Roadmap für Prozess-Sensoren in der chemisch-pharmazeutischen Industrie, 11/2009. Available online: http://www.vdi.de /fileadmin/vdi_de/redakteur_dateien/gma_dateien/Prozess-Sensoren_2015+.pdf (accessed on 12 December 2013).
26. Guinée, J.B.; Gorrée, M.; Heijungs, R.; Huppes, G.; Klein, R.; de Koning, A.; van Oers, L.; Wegener Sleeswijk, A.; Suh, S.; de Haes, U.H.A.; *et al*. *Handbook on Life Cycle Assessment: Operational Guide to the ISO Standards*; Kluwer Academic Publishers: Dordrecht, The Netherlands, 2002.
27. Azapagic, A.; Perdan, S. Indicators of sustainable development for industry. *Process Saf. Environ.* **2000**, *78*, 243–261.
28. Huppes, G.; van Oers, L.; Pretato, U.; Pennington, D.W. Weighting environmental effects: Analytic survey with operational evaluation methods and a meta-method. *Int. J. Life Cycle Assess.* **2012**, *17*, 876–891.
29. Verein Deutscher Ingenieure. Richtlinie 2884. *Beschaffung, Betrieb und Instandhaltung von Produktionsmitteln unter Anwendung von Life Cycle Costing (LCC)*; Beuth: Berlin, Germany, 2005.
30. Wichmann, M. Field report about MRT pilot-application in specialty & fine chemicals production. In Proceedings of the Symposium: Micro process technologies—From mg to tons, Hannover, Germany, 26 November 2008.
31. Kölbel, H.; Schulze, J. *Projektierung und Vorkalkulation in der Chemischen Industrie*; Springer: Berlin, Germany, 1960.
32. Helfrich, F.; Schubert, W. Ermittlung von Investitionskosten, Einfluss auf die Wirtschaftlichkeitsrechnung. *Chem. Ing. Tech.* **1973**, *65*, 891–897.
33. Ullrich, H. *Wirtschaftliche Planung und Abwicklung verfahrenstechnischer Anlagen*; Vulkan-Verlag: Essen, Germany, 1996.
34. Frühwald, A.; Scharai-Rad, M.; Hasch, J. Ökologische Bewertung von Holzwerkstoffen. Universität Hamburg, Bundesforschungsanstalt für Forst- und Holzwirtschaft Hamburg, 11/2000. Schlussbericht März 2000, ergänzt in den Bereichen Spanplattenrecycling und OSB-Bilanzen. Available online: http://www.Bfafh.de/bibl/pdf/scharai_pub1.pdf (accessed on 12 December 2013).
35. Oldenburg, J.; Schlegel, M.; Cruse, A.; Marquardt, M. Batch process modeling and optimization. In *Batch Processes*; Korovessi, E., Linniger, A.A., Eds.; CRC Press: Boca Raton, FL, USA, 2005; pp. 305–387.
36. Weidema, B.P.; Wesnaes, M.S. Data quality management for life cycle inventories—An example using data quality indicators. *J. Cleaner Prod.* **1996**, *4*, 167–174.

37. Krtschil, U.; Hessel, V.; Kralisch, D.; Kreisel, G.; Küpper, M.; Schenk, R. Cost analysis of a commercial manufacturing process of afine chemical compound using micro process engineering. *Chimia* **2006**, *60*, 611–617.
38. Benaskar, F.; Ben-Abdelmoumen, A.; Patil, N.G.; Rebrov, E.V.; Meuldijk, J.; Hulshof, L.A.; Hessel, V.; Krtschil, U.; Schouten, J.C. Cost analysis for a continuously operated fine chemicals production plant at 10 kg/day using a combination of microprocessing and microwave heating. *J. Flow Chem.* **2011**, *1*, 74–89.
39. Roberge, D.M.; Ducry, L.; Bieler, N.; Cretton, P.; Zimmermann, B. Microreactor technology: A revolution for the fine chemical and pharmaceutical industries? *Chem. Eng. Technol.* **2005**, *28*, 318–323.
40. Ciroth, A. Cost data quality considerations for eco-efficiency measures. *Ecol. Econ.* **2009**, *68*, 1583–1590.
41. Shams-Nateri, A. Reusing wastewater of madder natural dye for wool dyeing. *J. Cleaner Prod.* **2011**, *19*, 775–781.
42. Landesbetrieb für Statistik und Kommunikationstechnologie (LSKN): Trink- und Abwasserentgelte nach Gemeinden. Available online: http://www.lskn.niedersachsen.de (accessed on 12 December 2013).
43. Bundesverband der Energieabnehmer e.V. (VEA); Bundesverband der Energie- und Wasserwirtschaft (BDEW). BDEW-Strompreisanalyse 05/2012: Haushalte und Industrie. Berlin, 04.05.2012. Available online: http://bdew.de/internet.nsf/id/0E5D39E2E798737FC1257A09002D8C9C/$file/120525%20BDEW-Strompreisanalyse%202012%20Chartsatz%20gesamt.pdf (accessed on 12 December 2013).
44. WSI-Tarifarchiv der Hans-Böckler-Stiftung. Tarife in der chemischen Industrie. Available online: http://www.boeckler.de/index_wsi_tarifarchiv.htm (accessed on 12 December 2013).

Green Process Engineering as the Key to Future Processes

Dipesh Patel, Suela Kellici and Basudeb Saha

Abstract: Growing concern for the environment, increasing stringent standards for the release of chemicals into the environment and economic competiveness have led to more environmentally friendly approaches that have resulted in greater pollution prevention via waste reduction and efficiency maximisation. Green process engineering (GPE) is an important tool that could make significant contributions in the drive toward making hazardous and wasteful processes more sustainable for the benefit of the economy, environment and society. This article highlights the guidelines that could be used by scientists and engineers for designing new materials, products, processes and systems. Few examples of current and future applications of GPE, particularly in the areas of biofuels, supercritical fluids, multi-functional reactors and catalytic processes, have been presented.

Reprinted from *Processes*. Cite as: Patel, D.; Kellici, S.; Saha, B. Green Process Engineering as the Key to Future Processes. *Processes* **2014**, *2*, 311-332.

1. Introduction

It is impossible to imagine modern life without the products manufactured by industries. These products are used in everyday aspects of life, including agriculture, construction, transportation, electronics and well-being. However, their productions generate waste, release toxic chemicals, increase greenhouse emissions and greatly affect human health and the environment. As such, these concerns are driving new priorities that have emphasis on being "green", ranging from products to processes and technologies. Engineers and scientists from diverse fields are leading the way to solve these issues and challenges. Thus, green engineering has the capability to support and foster this innovation. One of the goals of the modern green process engineering (GPE) community is to design, develop and commercialise industrial processes that are sustainable and economically feasible, whilst minimizing the impact of chemical processes on human health and the environment. GPE is defined as, "the design, commercialization, and use of processes and products, which are feasible and economical while minimizing (a) generation of pollution at the source and (b) risk to human health and the environment. Green engineering embraces the concept that decisions to protect human health and the environment can have the greatest impact and cost effectiveness when applied early to the design and development phase of a process or product [1]. In the past, the objective of process engineering was to minimise product cost and increase profitability without assessing the long-term impacts on the planet and human health. Hence, engineers and scientists should carefully make technical decisions that could have significant impact on the environment. These decisions can lead us either in the direction of sustainability or contribute further to the growing problems. Hence, there is a greater need for engineers and scientists to come together for a common vision of saving the planet by providing new greener technologies and products in an environmentally friendly manner.

1.1. Issues and Challenges of Green Process Engineering

As we move to 2014, our society is faced with challenges in the sustainability of our current technological and lifestyle systems. There are enormous global environmental concerns, including energy and fuels, food, transportation, construction, water access and use, pollution and ecological destruction. The current and future goals of process engineering are therefore not only to sustain and reduce the cost of products, but simultaneously reduce the impact on the environment and on human health. In other words, today's process engineering has moved towards green process engineering (GPE). As such, the biggest challenge is to find innovative solutions that are based on environmentally benign design and manufacturing, to avoid the generation of waste or pollutants, to keep the product cost affordable with growing demands, to increase the capability of products to be recycled or reused and with the ultimate goal of introducing significant environmental improvements. Most companies are on a sustainability mission, where parameters, such as the utilization of non-depletable resources, the reduction of global-equivalent greenhouse gases emissions and the reduction of energy costs (by utilizing renewable energy resources), are considered important environmental and social targets [2]. However, in terms of fully adopting a sustainable process, there are other factors to be considered, including suitable market conditions, effective economical regulations and social acceptance defined by product demands. To improve industrial sustainability at the process level, the principles of green engineering provide a tangible framework to address the growing concern of human health and the environment and also provide a suitable guide for green process engineering. Its emphasis is on process, system and product optimisation. Anastas and Zimmerman [3] have outlined twelve principles of green engineering that are summarised in Figure 1a. Similarly, at the first conference on "Green Engineering: Defining the Principles" held in Florida in 2003, nine principles of green engineering were developed and are presented in Figure 1b. These principles provide a framework for scientists and engineers to use in designing processes and products within the boundary conditions set by society, business and government, which are guided by important parameters, such as costs, safety, demand, performance and environmental impact [4]. It integrates and couples the most important elements on product optimisation, processes and systems [5].

In 2012, the U.K. Engineering and Physical Sciences Research Council (EPSRC) announced four new engineering projects that aim to help the U.K. in developing lightweight, novel, easily recyclable, with a longer lifetime, materials and clean contaminated land for reclaiming valuable metals [6]. These projects are: (i) CLEVER (Closed Loop Emotionally Valuable E-waste Recovery); (ii) Cleaning Land for Wealth (CL4W); (iii) EXHUME (Efficient X-sector use of Heterogeneous Materials); and (iv) CORE (Creative Outreach for Resource Efficiency).

Thus, as noted, many industrial and academic sectors are considering greener and cleaner alternative routes. Green engineering applications are extremely broad and include almost every industry. These applications can be generally grouped into the following categories: renewable power energy [7], process optimisation [8], environmental monitoring [9] and the development of green products and technologies [2]. In this paper, we will focus on green processes, examine how industry is moving towards this direction and highlight the challenges chemical and process engineers are currently facing. A mini review of a selection of implemented processes, such as the utilization of supercritical fluids,

continuous hydrothermal processes and a few important catalytic processes, that have had direct impact on the field of green engineering are discussed in the following section.

Figure 1. (**a**) The twelve [3] and, (**b**) nine [4] principles of green engineering.

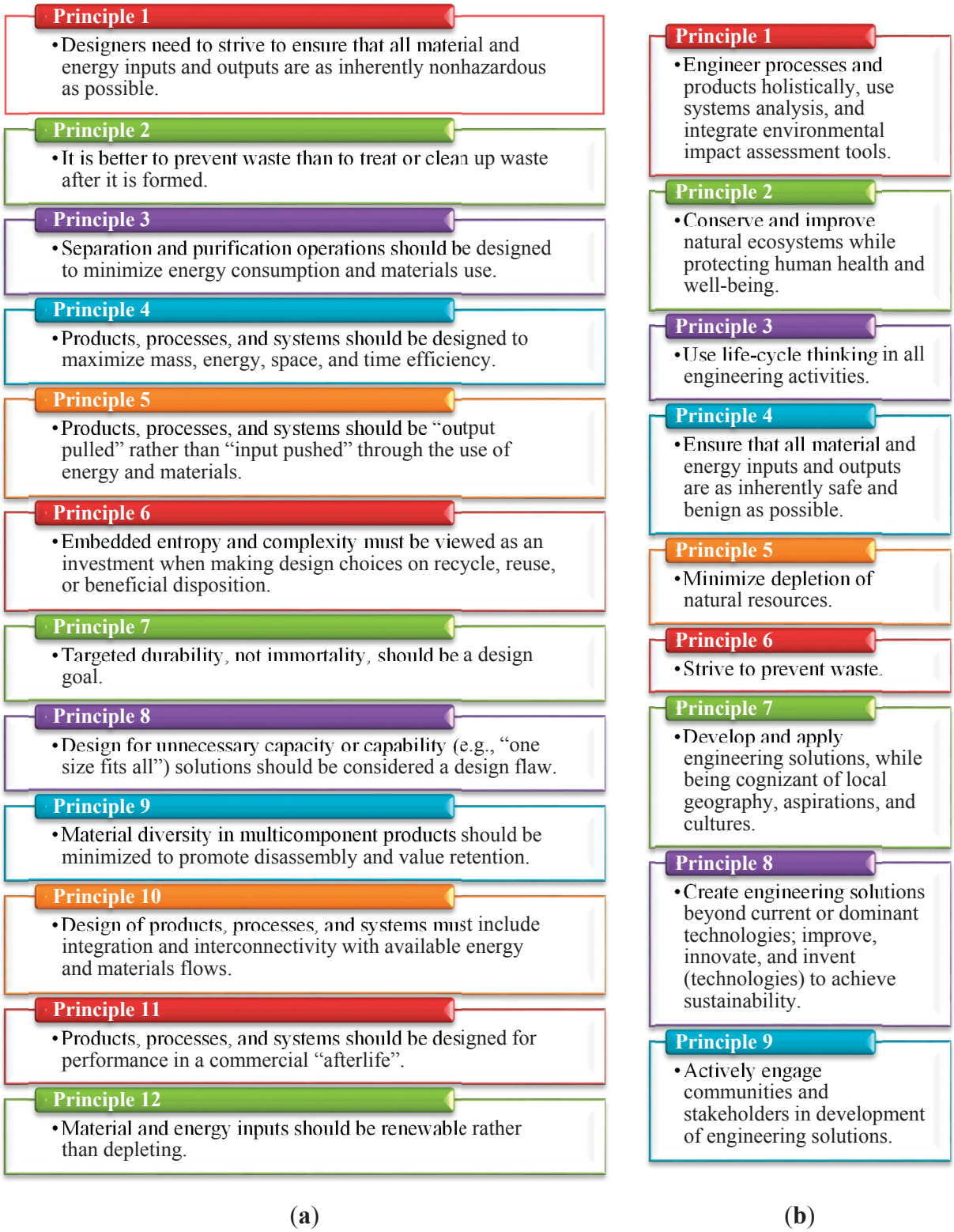

2. Applications of Green Process Engineering (GPE)

2.1. Production of Biodiesel and Biofuels

Currently, the majority of the world's energy is supplied through petrochemical sources, coal and natural gas. However, depleting fossil fuels, increasing energy demand from various sectors, global warming, environmental pollution due to the widespread use of fossil fuels and price fluctuations make petroleum-based energy unreliable. Therefore, it is increasingly necessary to develop renewable energy resources to replace the traditional sources.

Biodiesel has recently attracted enormous interest as an alternative and environmentally friendly fuel source. Biodiesel exhibits characteristics that are similar to traditional diesel fuel. In addition, the flow and combustion properties of biodiesel are similar to petroleum-based diesel [10]. Biodiesels have the following advantages over diesel fuel: they produce less smoke and particulates, have higher cetane numbers, produce lower carbon monoxide and hydrocarbon emissions, are biodegradable and non-toxic and provide better performances in engine lubricity compared to low sulphur diesel fuels. Hence, it could be used as a substitute for diesel fuel.

Abbaszaadeh *et al*. [11] have compared different current biodiesel production technologies, including blending of vegetable oils, micro-emulsions, pyrolysis and transesterification reaction. The preferred method for the production of biodiesel is generally prepared from the transesterification of triglycerides. The most common sources of triglycerides are first generation biofuels, such as edible virgin vegetable oils, and second generation biofuels, such as animal fats and used cooking oil (UCO). Most of the current biodiesel (>95%) is prepared from first generation agricultural crops [12]. The use of food sources for biodiesel production could have serious consequences on the food supply chain. Hence, UCO is considered to be an attractive feedstock for biodiesel production, since it does not put pressure on food supply, helps in recycling the UCO and is significantly cheaper than virgin oils. However, UCO must go through a pre-treatment process before it can be used for the production of biodiesel [13,14]. Alcohols, such as methanol, ethanol and butanol, have been used for the transesterification reaction [15,16]. However, it is considered that short chain alcohols, such as methanol and ethanol, give a stable product and higher conversion, compared to long-chain alcohols [17]. The transesterification reaction can be acid-catalysed [18], alkali-catalysed [19] or enzyme-catalysed [18,20,21]. A number of authors have reported biodiesel production in terms of composition, properties and specification [22], the effect of different catalysts on biodiesel production [23], biodiesel production using enzymatic transesterification [24] and waste cooking oil [25,26].

A comparison of an immobilised enzyme (Novozyme 435) with an ion exchange resin (Purolite D5081) for the pretreatment of used cooking oil (UCO) for biodiesel production was reported by Haigh *et al*. [18]. A 94% conversion of free fatty acids (FFA) was obtained using Purolite D5081 compared to FFA conversion of 90% with Novozyme 435. On the other hand, it was reported that there are side reactions associated with Novozyme 435, which result in the formation of more fatty acid methyl esters (FAME) and FFA. However, it was stated that Novozyme 435 uses a low optimum methanol to FFA ratio of 6.2:1, instead of the very high methanol to FFA ratio, *i.e*., 98:1, required by Purolite D5081 for optimum FFA conversion. Jachuck *et al*. [27] reported an energy

efficient continuous production of biodiesel from methanol and sodium hydroxide using an intensified narrow channel reactor module and canola oil as a feedstock. A triglyceride conversion of 98% was reported within 3 min at 60 °C, 80 psig and 1% catalyst loading.

To eliminate the drawbacks of first and second generation biofuels, including the issue of sustainability, the third generation of biofuels, such as microalgal oil, is regarded as the best route for biodiesel production, as it is independent of food sources [12,28,29]. During the process of photosynthesis, algae efficiently store solar energy and sequester CO_2, easing climate change caused by the emission of greenhouse gases [29]. In addition, algae could grow 7–31 times faster than palm oil plants, and 50% of their weight consists of oil [28]. Pfromm *et al*. [30] studied the economics of biodiesel from algae using the principle of conversion of mass and concluded that algal biodiesel could be produced sustainably with the exception of natural gas to produce nitrogen-based fertiliser in the long term. Overall, the commercialization of algae to biodiesel during initial stages will depend on the support of the government [31,32]. A number of reviews on biodiesel production using microalgae as feedstock has been published [33,34].

A number of publications have reported the production of biodiesel from algal oil using a two-step process, *i.e.*, acid esterification followed by base transesterification. [35,36]. Using a two-step process, a 90.6% yield of biodiesel was achieved at optimum conditions using *Enteromorpha compressa* algal oil [36], while 100% conversion of triacylglycerols (TAG) and FFA was achieved using *Scenedesmus* sp. algal oil [35]. Krohn *et al*. [37] reported the production of biodiesel using a supercritical fixed bed continuous flow process using algae (*N. oculata*) as a feedstock with 85% efficiency. A single-step process of converting wet algal biomass (Inoculum: *Nannochloropsis* sp.) to biodiesel using supercritical methanol was reported by Patil *et al*. [38]. Similarly, a single-step method using a wet lipid extraction procedure (WLEP) was conducted to extract 79% of transesterifiable lipids present in wet algal biomass (84% moisture) via acid and base hydrolysis [39]. The single-step process looks promising, as it eliminates the need for drying and extraction of algal biomass and yields faster reaction times. Martin and Grossman [40] conducted experiments for the production of biodiesel using different technological routes and concluded that for algal oil, the optimised route for biodiesel production is an alkali-catalysed process, while for waste cooking oil, heterogeneous catalysed transesterification is regarded as the optimum process for biodiesel production.

As of now, the production of biodiesel is much less compared to traditional fuels to make a significant impact on the fuel market. In comparison to petroleum-based fuel, biodiesel has poor cold flow properties, therefore, having a tendency to gel or solidify at low temperatures, and possesses low volatility, high pour and cloud points, higher NOx emissions and incomplete combustion. In addition, the cost for biodiesel is not competitive compared to petroleum-based fuel and requires special management for transportation and storage. However, engineers and scientists are putting significant efforts into improving the current technology of biodiesel production, so as to reduce the greenhouse gases and to meet the needs of current and future fuel demands.

2.2. Green Synthesis of Organic Carbonates from Carbon Dioxide

One of the requirements for a sustainable environment in designing a green chemical process is the utilization of renewable raw materials. Carbon dioxide (CO_2) emissions have increased to

unsustainable levels in the atmosphere, which has led to climate change. The reduction of CO_2 emissions has therefore become a global environmental challenge. Organic carbonates, such as propylene carbonate (PC) and dimethyl carbonate (DMC) have been widely used as intermediates in the synthesis of chemicals, pharmaceuticals and fuel additives [41–45]. Organic carbonates are generally synthesised using homogeneous catalysts, toxic raw materials, including phosgene and *iso*-cyanates and solvents [45–50]. Hence, there is an urgent need for an environmentally benign green process for the synthesis of organic carbonates from CO_2 by using a heterogeneous catalyst and eliminating the use of toxic chemicals and solvents. Several methods have been developed to design a stable and reusable heterogeneous system by immobilised or grafted ionic liquids and salts into solid materials, such as polymers [51,52], a molecular sieve MCM-41 (Mobil Composition of Matter No. 41) [53,54], magnesium oxide (MgO) [55,56] and silicon dioxide (SiO_2) [57,58]. These heterogeneous catalysts showed good catalyst activity and selectivity for the cycloaddition reaction of organic carbonate synthesis, but failed in terms of catalyst reusability.

Adeleye *et al*. [59] synthesised PC in a Parr high pressure reactor using several heterogeneous catalysts, including ceria doped zirconia (Ce-Zr-O), lanthanum oxide (La-O), lanthana doped zirconia (La-Zr-O), ceria and lanthana doped zirconia (Ce-La-Zr-O) and zirconium oxide (Zr-O), and without using a solvent. High propylene oxide (PO) conversion and yield of PC were reported at 170 °C, 70 bar CO_2 pressure and 10% catalyst loading using the Ce-La-Zr-O catalyst. Reusability studies revealed that the Ce-La-Zr-O catalyst could be used several times without any significant decrease in PC yield.

Similarly, Saada *et al*. [60] have used heterogeneous catalysts, such as ceria-zirconia doped graphene (Ce-Zr-graphene) catalyst, for the synthesis of DMC from CO_2 in the presence of 1,1,1-trimethoxymethane (TMM) as a dehydrating agent and without using a solvent. The results for the synthesis of PC and DMC look promising as a future greener process. From the environmental, economic and human health point of view, solvent-free heterogeneous catalysis is the process route of the future for eliminating the shortcomings of the current process of organic carbonate synthesis.

2.3. Production of Commercially Important Epoxide Building Blocks

Epoxides are valuable building blocks for organic synthesis, particularly for the production of commercially important products for pharmaceuticals, plastics, fragrances, food additives, paints and adhesives [61–64]. The conventional methods for the industrial production of epoxides employ either stoichiometric peracids or chlorohydrin as an oxygen source. However, both methods have a serious environmental impact, as the former produces an equivalent amount of acid waste, whilst the later yields chlorinated by-products and calcium chloride waste. In addition, there are safety issues associated with the handling and storage of peracids. Hence, there is a strong need for cleaner catalytic epoxidation methods that use safer oxidants and produce little waste.

Over the years, soluble compounds of transition metals have been used as efficient catalysts in alkene epoxidation [65,66]. A notable industrial implementation of homogenous catalysed epoxidation is the Halcon process [67]. However, homogenous catalysed systems suffer from several industrial difficulties, including corrosion, deposition of the catalyst on the wall of the reactor and difficulties in the separation of the catalyst from the reaction mixture, which may lead to product

contamination [68]. As such, alternatives have been considered. These new routes include developing a greener epoxidation process by utilizing a heterogeneous catalyst and a benign oxidant, such as *tert*-butyl hydroperoxide (TBHP), as it is environmentally benign, safer to handle and possesses good solubility in polar solvents. There has been a considerable amount of publications on polymer supported alkene epoxidation catalysts, such as Fe, Ni and Co [69], Ru [70], Ti [71], Mn [72], Mo [73] and Cu [74]. Additionally, polymer supported molybdenum catalysts have been reported to be effective for alkene epoxidation using alkyl hydroperoxide as the oxygen source [75–83].

A number of authors reported a novel and greener solvent-free process for alkene epoxidation using environmentally benign *tert*-butyl hydroperoxide (TBHP) as an oxidant [84,85]. In this process, polybenzimidazole supported molybdenum complex (PBI.Mo) and a polystyrene 2-(aminomethyl) pyridine-supported molybdenum complex (Ps.AMP.Mo) were used as catalysts for the epoxidation of alkenes. During the epoxidation reaction, *tert*-butanol is also formed as a co-product, and hence, this is termed as an atom-efficient process. Furthermore, *tert*-butanol can be efficiently recycled through hydrogenolysis and oxidation [86]. Recently, continuous epoxidation of 1-hexene with TBHP using the Ps.AMP.Mo catalyst has been conducted in an RDC (Reactive Distillation Column) [87,88] and FlowSyn reactor [89,90].

Continuous flow reactions in a FlowSyn reactor (Figure 2) have shown substantial benefits, including increased selectivity, scalability and reproducibility, and therefore, they have enormous potential as a process alternative for carrying out liquid phase chemical reactions [91–94] compared to experiments conducted in a classical batch reactor. The reactor is equipped with a stainless steel column packed with catalyst, two HPLC pumps, a control interface, SquirrelView software and a data logger supplied by Grant Instruments. Recently, epoxidation experiments conducted in a FlowSyn reactor achieved 95% conversion of TBHP and ~82% yield of 4-vinyl-1-cyclohexane 1,2-epoxide at 353 K and a 5:1 feed mole ratio (FMR) using Ps.AMP.Mo catalyst [90].

Figure 2. Continuous FlowSyn flow reactor experimental set-up.

2.4. Green Chemical Processing Using Supercritical CO_2 (SC-CO_2)

A supercritical fluid (SCF) is defined as a material that is used in a state above the critical temperature and critical pressure (Figure 3) where gases and liquids can coexist [95–97]. They exhibit unique

properties that are different from those of either gases or liquids under standard conditions. SCF has a higher diffusion coefficient, lower viscosity (very similar to the gas phase) and lower surface tension than a liquid solvent and improved mass transport properties. SCF properties can be tuned dramatically by small changes in pressure, especially when the critical parameters are being approached [98].

Figure 3. A simplified phase diagram for a pure phase substance illustrating density changes from liquid to gas. P_c and T_c are the critical pressure and temperature, respectively. P_c and T_c are the defining boundaries on a phase diagram for a substance. Beyond these points, the fluid is supercritical, with unique physical and chemical properties between gases and liquids.

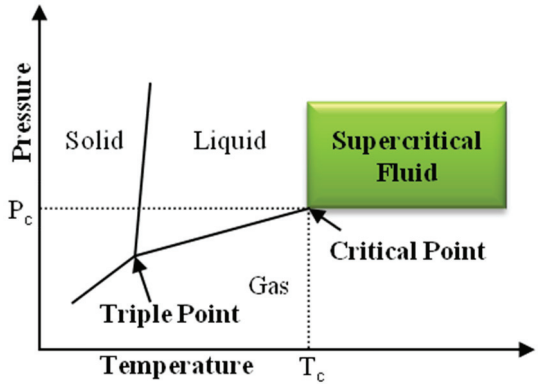

The increased interest in SCFs is driven by the ability to easily modulate their properties (via altering the pressure and temperature) and, more importantly, their potential to substitute toxic organic solvents [95,99] Conventional synthetic processes use volatile organic solvents that are flammable, toxic, generate large amounts of waste and, consequently, are non-sustainable. Dictated by the changes in legislation on waste solvent production and emissions and the significant increased costs of their waste disposal, many industrial sectors have moved towards cleaner and greener chemical manufacturing routes.

The substitution of the organic solvents by SCFs (e.g., carbon dioxide or water) offers significant improvements in the chemical and environmental fields. As such, supercritical carbon dioxide (sc-CO_2) offers relatively low critical parameters (T_c = 31.1 °C, P_c = 7.38 MPa), non-toxicity, non-flammability, recyclability and is a by-product of the industrial synthesis of ammonia [100]. Furthermore, it leaves no residue, as the solvent removal is done easily via the decompression of CO_2. As a result, the number of applications in various areas, including industrial scale-up production, has increased dramatically. These include nutrition, such as coffee bean decaffeination, pharmaceutical and polymer processing [99,101–103] of compounds, such as hyperbranched copolyesters [104], polycarbonates [105] and polyurethane [106], cleaning applications in the area of microelectronics, medical instrumentation and metallic surface cleaning, textile processing and dyeing of natural fibres, such as cotton, cellulose fibres and some synthetic materials [107,108], offering optimisation in the economical, energy reduction and waste aspects of this technology [109,110], chromatography and materials synthesis [111–114], such as metallic Janus silica particles [115], palladium (Pd) nanoparticles [116] or the treatment of $LiFePO_4$ cathode materials [117], in addition to the

fabrication of semiconductor devices [118]. Recent scientific reports have utilised sc-CO_2 for the synthesis of graphene-related materials, including exfoliation of graphite to make graphene [119], polystyrene/functionalised graphene nanocomposite foams [120], platinum (Pt) [121] or platinum-ruthenium/graphene catalysts [122] for methanol oxidation and cell or silver-graphene antibacterial materials [123]. Our group employed an innovative approach for synthesizing graphene-inorganic nanoparticles *via* the utilization of sc-CO_2, which allows us to homogeneously grow and disperse various nanoparticles onto graphene [124,125]. This is because of the high diffusion rates, zero surface tension and low viscosity; the SCF can rapidly transport and homogeneously deposit a range of materials onto a sample matrix very efficiently. In a typical experiment, graphene (synthesised using the chemical exfoliation method), a Pd precursor and the reducing agent were placed in the reactor with sc-CO_2, (as shown in Figure 4), leading to the formation and homogenous dispersion of Pd nanoparticles onto graphene.

Figure 4. A schematic representation for the synthesis of Pd-graphene nanocomposites using sc-CO_2.

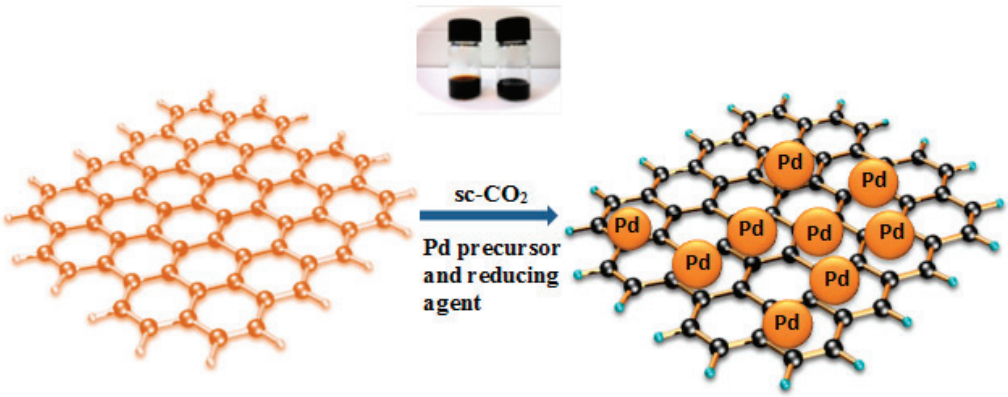

The Pd-graphene ratio was varied, and the properties of the nanocomposites were studied. Atomic force microscopy (AFM) and transmission electron microscopy (TEM) images of homogeneously dispersed Pd nanoparticles onto graphene materials are shown in Figure 5. This is a promising strategy for designing, synthesizing and developing next-generation functional novel nanomaterials with a broad range of applications, where the simplicity of the reactor design offers great possibility for the production of graphene-based nanocomposite materials.

2.5. Continuous Hydrothermal Flow Synthesis (CHFS)

Like sc-CO_2, supercritical water (sc-H_2O) has attracted tremendous interest amongst academia and industry [126]. The critical parameters of sc-H_2O (374 °C and 22.1 MPa) are higher than those for sc-CO_2 (31.1 °C and 7.38 MPa). In the supercritical state, water solvent properties, such as the density, viscosity and dielectric constant, change drastically in comparison to ambient water [95]. Conventionally, due to the high dielectric constant, ambient water easily dissolves polar compounds [127]. However, near the critical phase, the dielectric constant of water is greatly reduced, and therefore, it has the ability to dissolve non-polar compounds. Furthermore, the lower

density and viscosity values of water at its supercritical state mean higher diffusion and, consequently, faster reaction rates, provided that mass transfer is the rate controlling step of the process. The density, viscosity and dielectric constant of sc-H_2O, as with most SCF properties, can be controlled by fine-tuning the pressure and temperature of the fluid. Sc-H_2O with unique tuneable properties provides an excellent medium for the synthesis of various highly crystalline nanoparticles [128].

Figure 5. (**a**) Atomic force microscopy (AFM) images and (**b**) transmission electron microscopy (TEM) images of Pd-graphene nanocomposites.

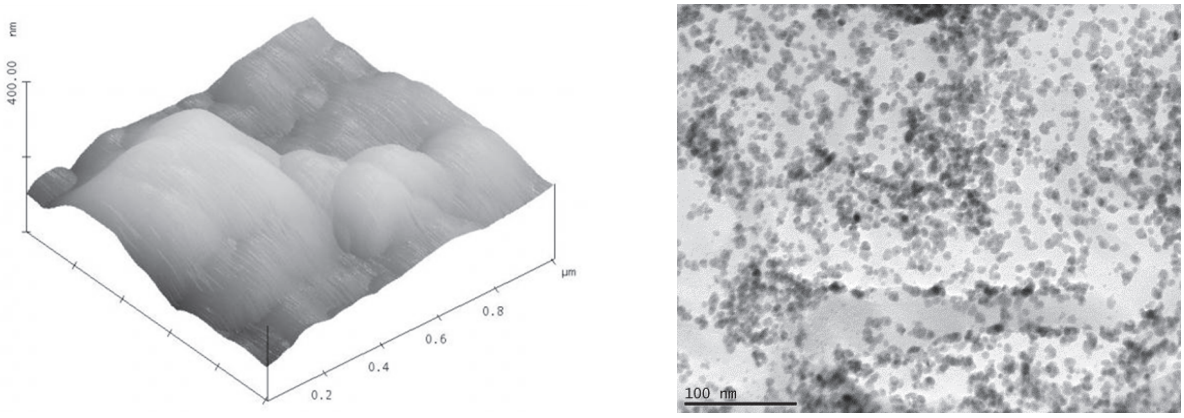

(**a**) (**b**)

In the manufacture of materials, hydrothermal (superheated or sc-H_2O) syntheses can offer many advantages over conventional preparation methods, e.g., lower synthesis temperatures and relatively less processing steps [129–131]. The vast majority of hydrothermal synthesis tends to be conducted in batch reactions, which are time consuming and allow little or no control over the final product properties. Following the pioneering research of the Arai group in Japan [132], continuous hydrothermal flow reactors were developed [133–136]. The process is considered green, since it uses water rather than organic solvents. The basic process involves mixing a flow of superheated or sc-H_2O with a flow of an aqueous solution of metal salts to give the rapid precipitation and growth of well-defined particles [137,138]. The composition and certain particle properties, such as size and morphology can be modulated by controlling the ratios of the metal salt feed, the pressure, the temperature of mixing and the presence of a pH or redox modifiers [131,137,139]. Sc-H_2O provides a rapid nucleating and crystallizing environment within a hydrothermal flow reactor, which facilities the accelerated synthesis of highly crystalline nanomaterials. The mechanism of the production of nanomaterials is generally explained in terms of: (i) the kinetics of the reaction; (ii) the solubility of the metal oxide; and (iii) the hydrodynamics around the mixing point. Near to or in the supercritical conditions, the rate of the hydrothermal reactions increases, and the solvation of metal oxides are extremely low. Consequently, such hydrothermal reactions are associated with high supersaturation levels, very rapid nucleation, high dehydration and low growth rates, which lead to the precipitation of fine particles. Further, the reaction engineering of the reactor, including the shape and the direction of the mixing point, influence the particle size and the particle size distribution of the final product. Commonly, the mixing of water and metal feeds is usually carried out in a tee union mixer. In the nozzle reactor, the water is injected downwards using a pipe-in-pipe design [133,136], whereas the

side injection of water has been reported to produce smaller particles. Recently, a new mixer design was reported, where the metal salt feed and auxiliary were mixed well and then split into two streams before entering the reactor through two inlets, where they meet sc-H_2O, forming nanoparticles [140]. In all cases, the synthesis of uniform reproducible nanoparticles has been successfully achieved. To conclude, continuous hydrothermal synthesis has been proven to be an excellent medium for the synthesis of nanomaterials. In such processes, control over particle properties, such as the size and composition, is easily achievable. Moreover, continuous hydrothermal systems offer the ability to carry out synthesis in a high-throughput mode, enabling the discovery of new materials [139,141,142]. Additionally, large-scale production is also reported [143,144].

2.6. Supercritical Water Oxidation (SCWO) Process

Supercritical water oxidation utilises the unique properties of sc-H_2O, such as the high diffusivity, low density and remarkable mass transport properties, for the destruction of various toxic and hazardous wastes streams, such as paints, oils, pharmaceutical wastes, chemical warfare agents and contaminated soil [145–149]. The addition of an oxidant, such as hydrogen peroxide or oxygen, is often required. The destruction efficiencies of supercritical water oxidation (SCWO) are reported to be very high (99.99%). At supercritical conditions, various organic compounds, such as chlorinated organic compounds or nitro-compounds, are destroyed to more environmentally friendly compounds, such as chloride ions and nitrates, respectively [150]. However, this process is associated with technical drawbacks, such as corrosion and salt precipitation, and, as such, is limited to the selection of a suitable wastewater and correctly designed reactors that satisfy a selection of criteria for successful operation, including an energy recovery system for the economically feasible implementation of this technology [151].

2.7. Green Process Using Biphasic Catalysis

Most of the industrial processes rely on catalysis, such as chemical, pharmaceutics, materials, polymers and energy. In the case of homogeneous catalysts, where the catalyst is in the same phase as the reactants, they offer numerous advantages for optimizing catalytic systems [152]. However, homogeneous catalysts suffer from many drawbacks, including difficulty in separating the catalyst particles after the reaction, which could increase the overall product cost. The concept of biphasic catalysis, which could possess high activity and reusability, has attracted considerable interest [153]. One such example of the biphasic catalytic process is the Ruhrchemie/Rhone-Poulenc commercial process [154]. In a biphasic catalysis system, a homogenous catalyst is modified to dissolve in a particular solvent, e.g., Solvent A, and the reactants are dissolved in another solvent, e.g., Solvent B. During the course of the reaction, the reactants, catalyst and Solvents A and B are vigorously stirred to form a single phase in which the reaction can take place. As soon as the reaction is completed, the reaction mixture is cooled down, resulting in phase separation and can be easily separated by simple decantation. Since the catalyst and product are in separate phases, this helps in removing the catalyst from the reaction mixture, and it could be recycled several times without any problems. Yu *et al*. [155] investigated the oxidation of benzyl alcohol to benzaldehyde with hydrogen peroxide as the oxidant

and metal dodecanesulfonate salts as the catalysts and found that ~100% selectively could be achieved by the principle of biphasic catalysis. Recently, the application of biphasic catalysis for hydrogenation of cinnamaldehyde to hydrocinnamaldehyde has been reported, wherein 100% selectivity of cinnamaldehyde to hydrocinnamaldehyde has been achieved [156].

3. Conclusions

Engineering strategies have a direct significant impact on the environment. These approaches can either add to growing environmental concerns or direct us towards sustainability if the right tools and options are selected. As such, green engineering is an effective approach, which offers guidance and support towards the direction of sustainable processes, products and systems, whilst reducing the risks to humans and the environment. The "greening" of the industry with the introduction of processes that provide adequate environmental protection is a key component for the future sustainable growth of our society. To implement this vision, new approaches have been developed. These include the utilisation of greener supercritical fluids, catalysis, continuous flow processes for the synthesis of a broad range of materials or the conversion of carbon dioxide to a value-added chemical. Overall, the examples represented here aim to be green in terms of processing with cleaner solvents, avoiding multiple step reactions and lowering the energy requirements, in addition to providing materials with improved properties. To conclude, driven by fast developing social and economic factors, the greening of the industry is the key to our future, where the motivation and efforts of chemical and process engineers have introduced attractive and ecological changes via changes in chemical processes. However, there still are challenges ahead, and much has to be achieved for the "greening" of chemical processes.

Acknowledgments

Some of our research activities have been supported by the U.K. Engineering and Physical Sciences Research Council (EPSRC) (grant no. EP/H027653/1), The Royal Society Brian Mercer Feasibility award, Purolite International Ltd., Llantrisant, Wales, U.K. and MEL Chemicals, Manchester, Eng., U.K. We would like to thank David C. Sherrington, Rene Mbeleck, Misbahu Ladan Mohammed, Adegboyega Isaac Adeleye and Rim Saada for their important contributions.

Conflicts of Interest

The authors declare no conflict of interest.

References

1. Website of U.S. Environmental Protection Agency, Washington, D.C. Available online: http://www.epa.gov/oppt/greenengineering/pubs/whats_ge.html (accessed on 3 February 2014).
2. Jenck, J.F.; Agterberg, F.; Droesher, M.J. Products and processes for a sustainable chemical industry: A review of achievements and prospects. *Green Chem.* **2004**, *6*, 544–556.

3. Anastas, P.T.; Zimmerman, J.B. Design through the 12 principles of green engineering. *Environ. Sci. Technol*. **2003**, *37*, 94A–101A.
4. Abraham, M.A.; Nguyen, N. "Green engineering: Defining the principles"—Resdts from the sandestin conference. *Environ. Prog.* **2003**, *22*, 233–236.
5. Patel, D.; Kellici, S.; Saha, B. Some novel aspects of green process engineering. *Chim. Oggi* **2013**, *31*, 57–61.
6. Website of Engineering and Physical Sciences Research Council (EPSRC). Available online: http://www.epsrc.ac.uk/newsevents/news/2012/Pages/greenengineering.aspx (accessed on 3 February 2014).
7. Liu, C.; Li, F.; Ma, L.P.; Cheng, H.M. Advanced materials for energy storage. *Adv. Mater.* **2010**, *22*, E28–E62.
8. Diwekar, U.M. Greener by design. *Environ. Sci. Technol.* **2003**, *37*, 5432–5444.
9. Grimm, N.B.; Faeth, S.H.; Golubiewski, N.E.; Redman, C.L.; Wu, J.G.; Bai, X.M.; Briggs, J.M. Global change and the ecology of cities. *Science* **2008**, *319*, 756–760.
10. Lotero, E.; Liu, Y.J.; Lopez, D.E.; Suwannakarn, K.; Bruce, D.A.; Goodwin, J.G. Synthesis of biodiesel via acid catalysis. *Ind. Eng. Chem. Res*. **2005**, *44*, 5353–5363.
11. Abbaszaadeh, A.; Ghobadian, B.; Omidkhah, M.R.; Najafi, G. Current biodiesel production technologies: A comparative review. *Energy Convers. Manag*. **2012**, *63*, 138–148.
12. Rawat, I.; Kumar, R.R.; Mutanda, T.; Bux, F. Biodiesel from microalgae: A critical evaluation from laboratory to large scale production. *Appl. Energy* **2013**, *103*, 444–467.
13. Abidin, S.Z.; Haigh, K.F.; Saha, B. Esterification of free fatty acids in used cooking oil using ion-exchange resins as catalysts: An efficient pretreatment method for biodiesel feedstock. *Ind. Eng. Chem. Res*. **2012**, *51*, 14653–14664.
14. Haigh, K.F.; Abidin, S.Z.; Saha, B.; Vladisavljević, G.T. Pretreatment of used cooking oil for the preparation of biodiesel using heterogeneous catalysis. *Prog. Colloid Polym. Sci*. **2012**, *139*, 19–22.
15. Demirbaş, A. Biodiesel fuels from vegetable oils via catalytic and non-catalytic supercritical alcohol transesterifications and other methods: A survey. *Energy Convers. Manag.* **2003**, *44*, 2093–2109.
16. Abidin, S.Z.; Vladisavljević, G.; Saha, B. Two-stage esterification-transesterification process for synthesis of biodiesel from used cooking oil (UCO) using novel heterogeneous catalysts. In Proceedings of the 9th World Congress of Chemical Engineering (WCCE9), Seoul, Korea, 18–23 August 2013; Paper number ThO-T409-6, Korean Institute of Chemical Engineers (KIChE): Seoul, Korea, 2013.
17. Dorado, M.P.; Ballesteros, E.; Mittelbach, M.; Lopez, F.J. Kinetic parameters affecting the alkali-catalyzed transesterification process of used olive oil. *Energy Fuels* **2004**, *18*, 1457–1462.
18. Haigh, K.F.; Abidin, S.Z.; Vladisavljević, G.T.; Saha, B. Comparison of Novozyme 435 and Purolite D5081 as heterogeneous catalysts for the pretreatment of used cooking oil for biodiesel production. *Fuel* **2013**, *111*, 186–193.

19. Kim, H.J.; Kang, B.S.; Kim, M.J.; Park, Y.M.; Kim, D.K.; Lee, J.S.; Lee, K.Y. Transesterification of vegetable oil to biodiesel using heterogeneous base catalyst. *Catal. Today* **2004**, *93–95*, 315–320.
20. Du, W.; Xu, Y.Y.; Liu, D.H. Lipase-catalysed transesterification of soya bean oil for biodiesel production during continuous batch operation. *Biotechnol. Appl. Biochem.* **2003**, *38*, 103–106.
21. Haigh, K.F.; Vladisavljević, G.T.; Reynolds, J.C.; Nagy, Z.; Saha, B. Kinetics of the pre-treatment of used cooking oil using Novozyme 435 for biodiesel production. *Chem. Eng. Res. Des*. **2014**, doi:10.1016/j.cherd.2014.01.006.
22. Hoekman, S.K.; Broch, A.; Robbins, C.; Ceniceros, E.; Natarajan, M. Review of biodiesel composition, properties, and specifications. *Renew. Sustain. Energy Rev.* **2012**, *16*, 143–169.
23. Atadashi, I.M.; Aroua, M.K.; Aziz, A.R.A.; Sulaiman, N.M.N. The effects of catalysts in biodiesel production: A review. *J. Ind. Eng. Chem.* **2013**, *19*, 14–26.
24. Gog, A.; Roman, M.; Toşa, M.; Paizs, C.; Irimie, F.D. Biodiesel production using enzymatic transesterification—Current state and perspectives. *Renew. Energy* **2012**, *39*, 10–16.
25. Talebian-Kiakalaieh, A.; Amin, N.A.S.; Mazaheri, H. A review on novel processes of biodiesel production from waste cooking oil. *Appl. Energy* **2013**, *104*, 683–710.
26. Abidin, S.Z.; Patel, D.; Saha, B. Quantitative analysis of fatty acids composition in the used cooking oil (UCO) by gas chromatography-mass spectrometry (GC-MS). *Can. J. Chem. Eng.* **2013**, *91*, 1896–1903.
27. Jachuck, R.; Pherwani, G.; Gorton, S.M. Green engineering: Continuous production of biodiesel using an alkaline catalyst in an intensified narrow channel reactor. *J. Environ. Monit*. **2009**, *11*, 642–647.
28. Demirbaş, A.; Demirbaş, M.F. Importance of algae oil as a source of biodiesel. *Energy Convers. Manag*. **2011**, *52*, 163–170.
29. Blatti, J.L.; Burkart, M.D. Releasing stored solar energy within pond scum: Biodiesel from algal lipids. *J. Chem. Educ*. **2012**, *89*, 239–242.
30. Pfromm, P.H.; Amanor-Boadu, V.; Nelson, R. Sustainability of algae derived biodiesel: A mass balance approach. *Bioresour. Technol*. **2011**, *102*, 1185–1193.
31. Gallagher, B.J. The economics of producing biodiesel from algae. *Renew. Energy* **2011**, *36*, 158–162.
32. Lee, D.H. Algal biodiesel economy and competition among bio-fuels. *Bioresour. Technol*. **2011**, *102*, 43–49.
33. Wiley, P.E.; Campbell, J.E.; Mckuin, B. Production of biodiesel and biogas from algae: A review of process train options. *Water Environ. Res.* **2011**, *83*, 326–338.
34. Halim, R.; Danquah, M.K.; Webley, P.A. Extraction of oil from microalgae for biodiesel production: A review. *Biotechnol. Adv.* **2012**, *30*, 709–732.
35. Chen, L.; Liu, T.Z.; Zhang, W.; Chen, X.L.; Wang, J.F. Biodiesel production from algae oil high in free fatty acids by two-step catalytic conversion. *Bioresour. Technol*. **2012**, *111*, 208–214.

36. Suganya, T.; Gandhi, N.N.; Renganathan, S. Production of algal biodiesel from marine macroalgae Enteromorpha compressa by two step process: Optimization and kinetic study. *Bioresour. Technol*. **2013**, *128*, 392–400.
37. Krohn, B.J.; McNeff, C.V.; Yan, B.W.; Nowlan, D. Production of algae-based biodiesel using the continuous catalytic Mcgyan® process. *Bioresour. Technol*. **2011**, *102*, 94–100.
38. Patil, P.D.; Gude, V.G.; Mannarswamy, A.; Deng, S.G.; Cooke, P.; Munson-McGee, S.; Rhodes, I.; Lammers, P.; Nirmalakhandan, N. Optimization of direct conversion of wet algae to biodiesel under supercritical methanol conditions. *Bioresour. Technol*. **2011**, *102*, 118–122.
39. Sathish, A.; Sims, R.C. Biodiesel from mixed culture algae via a wet lipid extraction procedure. *Bioresour. Technol*. **2012**, *118*, 643–647.
40. Martín, M.; Grossmann, I.E. Simultaneous optimization and heat integration for biodiesel production from cooking oil and algae. *Ind. Eng. Chem. Res.* **2012**, *51*, 7998–8014.
41. Shiels, R.A.; Jones, C.W. Homogeneous and heterogeneous 4-(*N*,*N*-dialkylamino)pyridines as effective single component catalysts in the synthesis of propylene carbonate. *J. Mol. Catal. A Chem*. **2007**, *261*, 160–166.
42. Wang, J.Q.; Yue, X.D.; Cai, F.; He, L.N. Solventless synthesis of cyclic carbonates from carbon dioxide and epoxides catalyzed by silica-supported ionic liquids under supercritical conditions. *Catal. Commun*. **2007**, *8*, 167–172.
43. Verevkin, S.P.; Emel'yanenko, V.N.; Toktonov, A.V.; Chernyak, Y.; Schäffner, B.; Börner, A. Cyclic alkylene carbonates. Experiment and first principle calculations for prediction of thermochemical properties. *J. Chem. Thermodyn*. **2008**, *40*, 1428–1432.
44. Bian, J.; Xiao, M.; Wang, S.J.; Wang, X.J.; Lu, Y.X.; Meng, Y.Z. Highly effective synthesis of dimethyl carbonate from methanol and carbon dioxide using a novel copper-nickel/graphite bimetallic nanocomposite catalyst. *Chem. Eng. J.* **2009**, *147*, 287–296.
45. Ulusoy, M.; Kilic, A.; Durgun, M.; Tasci, Z.; Cetinkaya, B. Silicon containing new salicylaldimine Pd(II) and Co(II) metal complexes as efficient catalysts in transformation of carbon dioxide (CO_2) to cyclic carbonates. *J. Organomet. Chem*. **2011**, *696*, 1372–1379.
46. Bhanage, B.M.; Fujita, S.; Ikushima, Y.; Arai, M. Synthesis of dimethyl carbonate and glycols from carbon dioxide, epoxides, and methanol using heterogeneous basic metal oxide catalysts with high activity and selectivity. *Appl. Catal. A* **2001**, *219*, 259–266.
47. Sun, J.M.; Fujita, S.; Arai, M. Development in the green synthesis of cyclic carbonate from carbon dioxide using ionic liquids. *J. Organomet. Chem*. **2005**, *690*, 3490–3497.
48. Sakakura, T.; Choi, J.C.; Yasuda, H. Transformation of carbon dioxide. *Chem. Rev*. **2007**, *107*, 2365–2387.
49. Dai, W.L.; Chen, L.; Yin, S.F.; Luo, S.L.; Au, C.T. 3-(2-Hydroxyl-ethyl)-1-propylimidazolium bromide immobilized on SBA-15 as efficient catalyst for the synthesis of cyclic carbonates via the coupling of carbon dioxide with epoxides. *Catal. Lett*. **2010**, *135*, 295–304.
50. Song, J.; Zhang, B.; Jiang, T.; Yang, G.; Han, B. Synthesis of cyclic carbonates and dimethyl carbonate using CO_2 as a building block catalyzed by MOF-5/KI and MOF-5/KI/K_2CO_3. *Front. Chem. China* **2011**, *6*, 21–30.

51. Kim, H.S.; Kim, J.J.; Kwon, H.N.; Chung, M.J.; Lee, B.G.; Jang, H.G. Well-defined highly active heterogeneous catalyst system for the coupling reactions of carbon dioxide and epoxides. *J. Catal.* **2002**, *205*, 226–229.
52. Alvaro, M.; Baleizao, C.; Carbonell, E.; El Ghoul, M.; García, H.; Gigante, B. Polymer-bound aluminium salen complex as reusable catalysts for CO_2 Insertion into epoxides. *Tetrahedron* **2005**, *61*, 12131–12139.
53. Yasuda, H.; He, L.N.; Takahashi, T.; Sakakura, T. Non-halogen catalysts for propylene carbonate synthesis from CO_2 under supercritical conditions. *Appl. Catal. A* **2006**, *298*, 177–180.
54. Udayakumar, S.; Park, S.W.; Park, D.W.; Choi, B.S. Immobilization of ionic liquid on hybrid MCM-41 system for the chemical fixation of carbon dioxide on cyclic carbonate. *Catal. Commun.* **2008**, *9*, 1563–1570.
55. Yamaguchi, K.; Ebitani, K.; Yoshida, T.; Yoshida, H.; Kaneda, K. Mg-Al mixed oxides as highly active acid-base catalysts for cycloaddition of carbon dioxide to epoxides. *J. Am. Chem. Soc.* **1999**, *121*, 4526–4527.
56. Barbarini, A.; Maggi, R.; Mazzacani, A.; Mori, G.; Sartori, G.; Sartorio, R. Cycloaddition of CO_2 to epoxides over both homogeneous and silica-supported guanidine catalysts. *Tetrahedron Lett*. **2003**, *44*, 2931–2934.
57. Wang, J.Q.; Kong, D.L.; Chen, J.Y.; Cai, F.; He, L.N. Synthesis of cyclic carbonates from epoxides and carbon dioxide over silica-supported quaternary ammonium salts under supercritical conditions. *J. Mol. Catal. A Chem.* **2006**, *249*, 143–148.
58. Zhang, X.H.; Zhao, N.; Wei, W.; Sun, Y.H. Chemical fixation of carbon dioxide to propylene carbonate over amine-functionalized silica catalysts. *Catal. Today* **2006**, *115*, 102–106.
59. Adeleye, A.I.; Patel, D.; Niyogi, D.; Saha, B. An efficient and greener synthesis of propylene carbonate from carbon dioxide and propylene oxide. Unpublished work (in preparation), 2014.
60. Saada, R.; Kellici, S.; Saha, B. Synthesis of dimethyl carbonate from carbon dioxide and methanol using ceria-zirconia doped graphene catalyst. Unpublished work (in preparation), 2014.
61. Sienel, G.; Rieth, R.; Rowbottom, K.T. Epoxides. In *Ullmann's Encyclopedia of Industrial Chemistry*; Wiley-VCH: Weinheim, Germany, 2000.
62. Bauer, K.; Garbe, D.; Surburg, H. *Common Fragrance and Flavour Materials*, 4th ed.; Wiley-VCH: Weinheim, Germany, 2001; pp. 143–145.
63. Andrei, K.Y. *Aziridines and Epoxides in Organic Synthesis*; Wiley-VCH: Weinheim, Germany, 2006; p. 516.
64. Ambroziak, K.; Mbeleck, R.; He, Y.; Saha, B.; Sherrington, D.C. Investigation of batch alkene epoxidations catalyzed by polymer-supported Mo(VI) complexes. *Ind. Eng. Chem. Res*. **2009**, *48*, 3293–3302.
65. Serafimidou, A.; Stamatis, A.; Louloudi, M. Manganese(II) complexes of imidazole based-acetamide as homogeneous and heterogenised catalysts for alkene epoxidation with H_2O_2. *Catal. Commun*. **2008**, *9*, 35–39.

66. Sözen-Aktaş, P.; Manoury, E.; Demirhan, F.; Poli, R. Molybdenum *versus* tungsten for the epoxidation of cyclooctene catalyzed by [Cp*$_2$M$_2$O$_5$]. *Eur. J. Inorg. Chem*. **2013**, *2013*, 2728–2735.
67. Kollar, J. Epoxidation Process. US Patent 3351635, 7 November 1967.
68. Salavati-Niasari, M.; Esmaeili, E.; Seyghalkar, H.; Bazarganipour, M. Cobalt(II) Schiff base complex on multi-wall carbon nanotubes (MWNTs) by covalently grafted method: Synthesis, characterization and liquid phase epoxidation of cyclohexene by air. *Inorg. Chim. Acta* **2011**, *375*, 11–19.
69. Dell'Anna, M.M.; Mastrorilli, P.; Nobile, C.F.; Suranna, G.P. Epoxidation of olefins catalyzed by polymer-supported metal beta-ketoesterato complexes of iron(III), nickel(II) and cobalt(II). *J. Mol. Catal. A Chem*. **1995**, *103*, 17–22.
70. Antony, R.; Tembe, G.L.; Ravindranathan, M.; Ram, R.N. Polymer supported Ru(III) complexes, synthesis and catalytic activity. *Polymer* **1998**, *39*, 4327–4333.
71. Deleuze, H.; Schultze, X.; Sherrington, D.C. Reactivity of some polymer-supported titanium catalysts in transesterification and epoxidation reactions. *J. Mol. Catal. A Chem*. **2000**, *159*, 257–267.
72. Brulé, E.; de Miguel, Y.R.; Hii, K.K. Chemoselective epoxidation of dienes using polymer-supported manganese porphyrin catalysts. *Tetrahedron* **2004**, *60*, 5913–5918.
73. Grivani, G.; Tangestaninejad, S.; Halili, A. A readily prepared, highly reusable and active polymer-supported molybdenum carbonyl Schiff base complex as epoxidation catalyst. *Inorg. Chem. Commun*. **2007**, *10*, 914–917.
74. Islam, S.M.; Roy, A.S.; Mondal, P.; Mobarok, M.; Roy, B.; Salam, N.; Paul, S.; Mondal, S. Olefin epoxidation with *tert*-butyl hydroperoxide catalyzed by functionalized polymer-supported copper(II) Schiff base complex. *Monat. Chem*. **2012**, *143*, 815–823.
75. Sherrington, D.C. Polymer-supported metal complex alkene epoxidation catalysts. *Catal. Today* **2000**, *57*, 87–104.
76. Mbeleck, R.; Ambroziak, K.; Saha, B.; Sherrington, D.C. Stability and recycling of polymer-supported Mo(VI) alkene epoxidation catalysts. *React. Funct. Polym*. **2007**, *67*, 1448–1457.
77. Tangestaninejad, S.; Mirkhani, V.; Moghadam, M.; Grivani, G. Readily prepared heterogeneous molybdenum-based catalysts as highly recoverable, reusable and active catalysts for alkene epoxidation. *Catal. Commun*. **2007**, *8*, 839–844.
78. Barrio, L.; Campos-Martin, J.M.; de Frutos, M.P.; Fierro, J.L.G. Alkene epoxidation with ethylbenzene hydroperoxides using molybdenum heterogeneous catalysts. *Ind. Eng. Chem. Res*. **2008**, *47*, 8016–8024.
79. Ambroziak, K.; Mbeleck, R.; Saha, B.; Sherrington, D.C. Greener and sustainable method for alkene epoxidations by polymer-supported Mo(VI) catalysts. *Int. J. Chem. React. Eng*. **2010**, *8*, A125:1–A125:13.

80. Mbeleck, R.; Mohammed, M.L.; Ambroziak, K.; Sherrington, D.C.; Saha, B. Cleaner and efficient alkenes/terpenes epoxidation process catalysed by novel polymer-supported Mo(VI) complexes. In Proceedings of the IEX 2012, Cambridge, UK, 19–21 September 2012; Society of Chemical Industry (SCI): London, UK, 2012.
81. Grivani, G.; Akherati, A. Polymer-supported bis (2-hydroxyanyl) acetylacetonato molybdenyl Schiff base catalyst as effective, selective and highly reusable catalyst in epoxidation of alkenes. *Inorg. Chem. Commun*. **2013**, *28*, 90–93.
82. Mohammed, M.L.; Mbeleck, R.; Sherrington, D.C.; Saha, B. Greener and efficient alkene epoxidation process. In Proceedings of the 9th European Congress of Chemical Engineering (ECCE9), Hague, The Netherlands, 21–24 April 2013; Paper number 794, ECCE9-ECAB2 App, MCI-Eurocongress v.o.f.: Amsterdam, The Netherlands, 2013.
83. Mbeleck, R.; Mohammed, M.L.; Sherrington, D.C.; Saha, B. Environmentally benign alkene epoxidation process. In Proceedings of the 9th World Congress of Chemical Engineering (WCCE9), Seoul, Korea, 18–23 August 2013; Paper number FrO-T104-3, Korean Institute of Chemical Engineers (KIChE): Seoul, Korea, 2013.
84. Mohammed, M.L.; Patel, D.; Mbeleck, R.; Niyogi, D.; Sherrington, D.C.; Saha, B. Optimisation of alkene epoxidation catalysed by polymer supported Mo(VI) complexes and application of artificial neural network for prediction of catalytic performances. *Appl. Catal. A* **2013**, *466*, 142–152.
85. Mbeleck, R.; Mohammed, M.L.; Ambroziak, K.; Sherrington, D.C.; Saha, B. Efficient epoxidation of cyclododecene and dodecene catalysed by polybezimidazole-supported Mo(VI) complex. Unpublished work (in preparation), 2014.
86. Oku, N.; Seo, T. Process for Producing Propylene Oxide. U.S. Patent 6646138, 11 November 2003.
87. Saha, B.; Ambroziak, K.; Sherrington, D.C.; Mbeleck, R. Process. Publication Number WO/2011/012869, International Patent Application Number PCT/GB2010/001458. 3 February 2011.
88. Mbeleck, R.; Ambroziak, K.; Sherrington, D.C.; Saha, B. Production of commercially important epoxide building blocks by catalytic distillation. Unpublished work (in preparation), 2015.
89. Saha, B. Continuous clean alkene epoxidation process technology for the production of commercially important epoxide building blocks. In Proceedings of the 3rd International Conference of the Flow Chemistry Society, Munich, Germany, 19–20 March 2013; Select Biosciences Ltd.: Sudbury, UK, 2013.
90. Mohammed, M.L.; Mbeleck, R.; Niyogi, D.; Sherrington, D.C.; Saha, B. Continuous alkene epoxidation process catalysed by polymer supported molybdenum (VI) complex. Unpublished work (in preparation), 2014.
91. Browne, D.L.; Baumann, M.; Harji, B.H.; Baxendale, I.R.; Ley, S.V. A new enabling technology for convenient laboratory scale continuous flow processing at low temperatures. *Org. Lett*. **2011**, *13*, 3312–3315.

92. Kelly, C.B.; Lee, C.; Mercadante, M.A.; Leadbeater, N.E. A continuous-flow approach to palladium-catalyzed alkoxycarbonylation reactions. *Org. Process Res. Dev*. **2011**, *15*, 717–720.
93. Nagy, K.D.; Jensen, K.F. Catalytic processes in small scale flow reactors Status and opportunities. *Chim. Oggi* **2011**, *29*, 18–21.
94. Palde, P.B.; Jamison, T.F. Safe and efficient tetrazole synthesis in a continuous-flow microreactor. *Angew. Chem. Int. Ed*. **2011**, *50*, 3525–3528.
95. Savage, P.E.; Gopalan, S.; Mizan, T.I.; Martino, C.J.; Brock, E.E. Reactions at supercritical conditions: Applications and fundamentals. *AIChE J*. **1995**, *41*, 1723–1778.
96. Darr, J.A.; Poliakoff, M. New directions in inorganic and metal-organic coordination chemistry in supercritical fluids. *Chem. Rev.* **1999**, *99*, 495–541.
97. Darr, J.A.; Kellici, S.; Rehman, I.U. Titania nanospheres from supercritical fluids. *IEE Proc. Nanobiotechnol.* **2005**, *152*, 109–111.
98. Jung, J.; Perrut, M. Particle design using supercritical fluids: Literature and patent survey. *J. Supercrit. Fluids* **2001**, *20*, 179–219.
99. Sheldon, R.A. Green solvents for sustainable organic synthesis: State of the art. *Green Chem.* **2005**, *7*, 267–278.
100. Eckert, C.A.; Knutson, B.L.; Debenedetti, P.G. Supercritical fluids as solvents for chemical and materials processing. *Nature* **1996**, *383*, 313–318.
101. Kendall, J.L.; Canelas, D.A.; Young, J.L.; DeSimone, J.M. Polymerizations in supercritical carbon dioxide. *Chem. Rev.* **1999**, *99*, 543–563.
102. Cooper, A.I. Polymer synthesis and processing using supercritical carbon dioxide. *J. Mater. Chem.* **2000**, *10*, 207–234.
103. Kazarian, S.G. Polymer processing with supercritical fluids. *Polym. Sci. Ser. C* **2000**, *42*, 78–101.
104. Gregorowicz, J.; Wawrzyńska, E.P.; Parzuchowski, P.G.; Fraś, Z.; Rokicki, G.; Wojciechowski, K.; Wieczorek, S.A.; Wiśniewska, A.; Plichta, A.; Dąbrowski, K.; *et al*. Synthesis, characterization, and solubility in supercritical carbon dioxide of hyperbranched copolyesters. *Macromolecules* **2013**, *46*, 7180–7195.
105. Tryznowski, M.; Tomczyk, K.; Fraś, Z.; Gregorowicz, J.; Rokicki, G.; Wawrzyńska, E.; Parzuchowski, P.G. Aliphatic hyperbranched polycarbonates: Synthesis, characterization, and solubility in supercritical carbon dioxide. *Macromolecules* **2012**, *45*, 6819–6829.
106. Smith, C.A.; Cloutet, E.; Tassaing, T.; Cramail, H. Synthesis of polyurethane particles in supercritical carbon dioxide using organocatalysts or organocatalytic surfactants. *Green Chem.* **2013**, *15*, 2769–2776.
107. Mohamed, A.L.; Er-Rafik, M.; Moller, M. Supercritical carbon dioxide assisted silicon based finishing of cellulosic fabric: A novel approach. *Carbohydr. Polym.* **2013**, *98*, 1095–1107.
108. Liu, W.W.; Zhang, B.; Li, Y.Z.; He, Y.M.; Zhang, H.C. An environmentally friendly approach for contaminants removal using supercritical CO_2 for remanufacturing industry. *Appl. Surf. Sci.* **2014**, *292*, 142–148.

109. Matson, D.W.; Fulton, J.L.; Petersen, R.C.; Smith, R.D. Rapid expansion of supercritical fluid solutions: Solute formation of powders, thin films, and fibers. *Ind. Eng. Chem. Res.* **1987**, *26*, 2298–2306.
110. Beckman, E.J. Supercritical and near-critical CO_2 in green chemical synthesis and processing. *J. Supercrit. Fluids* **2004**, *28*, 121–191.
111. Johnston, K.P.; Harrison, K.L.; Clarke, M.J.; Howdle, S.M.; Heitz, M.P.; Bright, F.V.; Carlier, C.; Randolph, T.W. Water-in-carbon dioxide microemulsions: An environment for hydrophiles including proteins. *Science* **1996**, *271*, 624–626.
112. Kellici, S.; Rehman, I.; Darr, J.A. Controlled growth of titania nanospheres in supercritical carbon dioxide using a novel surfactant stabilised precursor. *J. Mater. Chem.* **2006**, *16*, 159–161.
113. Reverchon, E.; Adami, R. Nanomaterials and supercritical fluids. *J. Supercrit. Fluids* **2006**, *37*, 1–22.
114. Poe, D.P.; Veit, D.; Ranger, M.; Kaczmarski, K.; Tarafder, A.; Guiochon, G. Pressure, temperature and density drops along supercritical fluid chromatography columns in different thermal environments. III. Mixtures of carbon dioxide and methanol as the mobile phase. *J. Chromatogr. A* **2014**, *1323*, 143–156.
115. Yang, Q.Y.; de Vries, M.H.; Picchioni, F.; Loos, K. A novel method of preparing metallic Janus silica particles using supercritical carbon dioxide. *Nanoscale* **2013**, *5*, 10420–10427.
116. Yan, K.; Jarvis, C.; Lafleur, T.; Qiao, Y.X.; Xie, X.M. Novel synthesis of Pd nanoparticles for hydrogenation of biomass-derived platform chemicals showing enhanced catalytic performance. *RSC Adv*. **2013**, *3*, 25865–25871.
117. Xie, M.; Zhang, X.X.; Deng, S.X.; Wang, Y.Z.; Wang, H.; Liu, J.B.; Yan, H.; Laakso, J.; Levänen, E. The effects of supercritical carbon dioxide treatment on the morphology and electrochemical performance of $LiFePO_4$ cathode materials. *RSC Adv.* **2013**, *3*, 12786–12793.
118. Romang, A.H.; Watkins, J.J. Supercritical fluids for the fabrication of semiconductor devices: Emerging or missed opportunities? *Chem. Rev.* **2010**, *110*, 459–478.
119. Wang, W.; Wang, Y.; Gao, Y.; Zhao, Y. Control of number of graphene layers using ultrasound in supercritical CO_2 and their application in lithium-ion batteries. *J. Supercrit. Fluids* **2014**, *85*, 95–101.
120. Li, C.Q.; Yang, G.H.; Deng, H.; Wang, K.; Zhang, Q.; Chen, F.; Fu, Q. The preparation and properties of polystyrene/functionalized graphene nanocomposite foams using supercritical carbon dioxide. *Polym. Int.* **2013**, *62*, 1077–1084.
121. Zhao, J.; Zhang, L.Q.; Chen, T.; Yu, H.; Zhang, L.; Xue, H.; Hu, H.Q. Supercritical carbon-dioxide-assisted deposition of Pt nanoparticles on graphene sheets and their application as an electrocatalyst for direct methanol fuel cells. *J. Phys. Chem. C* **2012**, *116*, 21374–21381.
122. Zhao, J.; Zhang, L.; Xue, H.; Wang, Z.B.; Hu, H.Q. Methanol electrocatalytic oxidation on highly dispersed platinum-ruthenium/graphene catalysts prepared in supercritical carbon dioxide-methanol solution. *RSC Adv*. **2012**, *2*, 9651–9659.
123. Nguyen, V.H.; Kim, B.K.; Jo, Y.L.; Shim, J.J. Preparation and antibacterial activity of silver nanoparticles-decorated graphene composites. *J. Supercrit. Fluids* **2012**, *72*, 28–35.

124. Saha, B. The Centre for Green Process Engineering (CGPE) opens with launch event at London South Bank University (LSBU). *Green Process. Synth.* **2013**, *2*, 169–174.
125. Adeleye, A.I.; Kellici, S.; Saha, B. Synthesis of propylene carbonate by graphene-inorganic nanoparticles. Unpublished work (in preparation), 2014.
126. Weingärtner, H.; Franck, E.U. Supercritical water as a solvent. *Angew. Chem. Int. Ed.* **2005**, *44*, 2672–2692.
127. Shaw, R.W.; Brill, T.B.; Clifford, A.A.; Eckert, C.A.; Franck, E.U. Supercritical water—A medium for chemistry. *Chem. Eng. News* **1991**, *69*, 26–39.
128. Byrappa, K.; Adschiri, T. Hydrothermal technology for nanotechnology. *Prog. Cryst. Growth Charact. Mater*. **2007**, *53*, 117–166.
129. Cabañas, A.; Poliakoff, M. The continuous hydrothermal synthesis of nano-particulate ferrites in near critical and supercritical water. *J. Mater. Chem.* **2001**, *11*, 1408–1416.
130. Blood, P.J.; Denyer, J.P.; Azzopardi, B.J.; Poliakoff, M.; Lester, E. A versatile flow visualisation technique for quantifying mixing in a binary system: Application to continuous supercritical water hydrothermal synthesis (SWHS). *Chem. Eng. Sci.* **2004**, *59*, 2853–2861.
131. Chaudhry, A.A.; Haque, S.; Kellici, S.; Boldrin, P.; Rehman, I.; Fazal, A.K.; Darr, J.A. Instant nano-hydroxyapatite: A continuous and rapid hydrothermal synthesis. *Chem. Commun.* **2006**, *21*, 2286–2288.
132. Hakuta, Y.; Adschiri, T.; Suzuki, T.; Chida, T.; Seino, K.; Arai, K. Flow method for rapidly producing barium hexaferrite particles in supercritical water. *J. Am. Ceram. Soc.* **1998**, *81*, 2461–2464.
133. Lester, E.; Blood, P.; Denyer, J.; Giddings, D.; Azzopardi, B.; Poliakoff, M. Reaction engineering: The supercritical water hydrothermal synthesis of nano-particles. *J. Supercrit. Fluids* **2006**, *37*, 209–214.
134. Boldrin, P.; Hebb, A.K.; Chaudhry, A.A.; Otley, L.; Thiebaut, B.; Bishop, P.; Darr, J.A. Direct synthesis of nanosized $NiCo_2O_4$ spinel and related compounds via continuous hydrothermal synthesis methods. *Ind. Eng. Chem. Res.* **2007**, *46*, 4830–4838.
135. Weng, X.; Boldrin, P.; Abrahams, I.; Skinner, S.J.; Darr, J.A. Direct syntheses of mixed ion and electronic conductors $La_4Ni_3O_{10}$ and $La_3Ni_2O_7$ from nanosized coprecipitates. *Chem. Mater.* **2007**, *19*, 4382–4384.
136. Middelkoop, V.; Boldrin, P.; Peel, M.; Buslaps, T.; Barnes, P.; Darr, J.A.; Jacques, S.D.M. Imaging the inside of a continuous nanoceramic synthesizer under supercritical water conditions using high-energy synchrotron X-Radiation. *Chem. Mater.* **2009**, *21*, 2430–2435.
137. Weng, X.L.; Boldrin, P.; Abrahams, I.; Skinner, S.J.; Kellici, S.; Darr, J.A. Direct syntheses of $La_{n+1}Ni_nO_{3n+1}$ phases (n = 1, 2, 3 and ∞) from nanosized co-crystallites. *J. Solid State Chem.* **2008**, *181*, 1123–1132.
138. Lin, T.; Kellici, S.; Gong, K.; Thompson, K.; Evans, J.R.G.; Wang, X.; Darr, J.A. Rapid automated materials synthesis instrument: Exploring the composition and heat-treatment of nanoprecursors toward low temperature red phosphors. *J. Comb. Chem.* **2010**, *12*, 383–392.

139. Zhang, Z.C.; Brown, S.; Goodall, J.B.M.; Weng, X.L.; Thompson, K.; Gong, K.N.; Kellici, S.; Clark, R.J.H.; Evans, J.R.G.; Darr, J.A. Direct continuous hydrothermal synthesis of high surface area nanosized titania. *J. Alloys Compd.* **2009**, *476*, 451–456.
140. Ma, C.Y.; Wang, X.Z.; Tighe, C.J.; Gruar, R.I.; Darr, J.A. Simulation of hydrodynamics and heat transfer in confined jet reactors of different size scales for nanomaterial production. *Comput.-Aided Chem. Eng.* **2012**, *31*, 1236–1240.
141. Weng, X.L.; Cockcroft, J.K.; Hyett, G.; Vickers, M.; Boldrin, P.; Tang, C.C.; Thompson, S.P.; Parker, J.E.; Knowles, J.C.; Rehman, I.; *et al*. High-throughput continuous hydrothermal synthesis of an entire nanoceramic phase diagram. *J. Comb. Chem.* **2009**, *11*, 829–834.
142. Kellici, S.; Gong, K.A.; Lin, T.A.; Brown, S.; Clark, R.J.H.; Vickers, M.; Cockcroft, J.K.; Middelkoop, V.; Barnes, P.; Perkins, J.M.; *et al*. High-throughput continuous hydrothermal flow synthesis of Zn-Ce oxides: Unprecedented solubility of Zn in the nanoparticle fluorite lattice. *Philos. T. R. Soc. A* **2010**, *368*, 4331–4349.
143. Gruar, R.I.; Tighe, C.J.; Muir, J.; Kittler, J.T.; Wodjak, M.; Kenyon, A.J.; Darr, J.A. Continuous hydrothermal synthesis of surface-functionalised nanophosphors for biological imaging. *RSC Adv.* **2012**, *2*, 10037–10047.
144. Gruar, R.I.; Tighe, C.J.; Darr, J.A.; Scaling-up a confined jet reactor for the continuous hydrothermal manufacture of nanomaterials. *Ind. Eng. Chem. Res.* **2013**, *52*, 5270–5281.
145. Hawthorne, S.B.; Yang, Y.; Miller, D.J. Extraction of organic pollutants from environmental solids with sub- and supercritical water. *Anal. Chem.* **1994**, *66*, 2912–2920.
146. Gloyna, E.F.; Li, L.X. Supercritical water oxidation research and development update. *Environ. Prog.* **1995**, *14*, 182–192.
147. Cabeza, P.; Bermejo, M.D.; Jiménez, C.; Cocero, M.J. Experimental study of the supercritical water oxidation of recalcitrant compounds under hydrothermal flames using tubular reactors. *Water Res*. **2011**, *45*, 2485–2495.
148. Jimenez-Espadafor, F.; Portela, J.R.; Vadillo, V.; Sánchez-Oneto, J.; Villanueva, J.A.B.; García, M.T.; de la Ossa, E.J.M. Supercritical water oxidation of oily wastes at pilot plant: Simulation for energy recovery. *Ind. Eng. Chem. Res*. **2011**, *50*, 775–784.
149. Zhao, Q.C.; Dong, X.; Zhou, M.H.; Wang, J.C. Dioxin destruction by supercritical water oxidation. *Adv. Mater. Res*. **2013**, *864–867*, 1709–1712.
150. Kritzer, P.; Dinjus, E. An assessment of supercritical water oxidation (SCWO): Existing problems, possible solutions and new reactor concepts. *Chem. Eng. J.* **2001**, *83*, 207–214.
151. Vadillo, V.; Sánchez-Oneto, J.; Portela, J.R.; de la Ossa, E.J.M. Problems in supercritical water oxidation process and proposed solutions. *Ind. Eng. Chem. Res.* **2013**, *52*, 7617−7629.
152. Baker, R.T.; Tumas, W. Homogeneous catalysis—Toward greener chemistry. *Science* **1999**, *284*, 1477–1479.
153. Jutz, F.; Andanson, J.M.; Baiker, A. Ionic liquids and dense carbon dioxide: A beneficial biphasic system for catalysis. *Chem. Rev*. **2011**, *111*, 322–353.
154. Kohlpaintner, C.W.; Fischer, R.W.; Cornils, B. Aqueous biphasic catalysis: Ruhrchemie/Rhone-Poulenc oxo process. *Appl. Catal., A* **2001**, *221*, 219–225.

155. Yu, Y.Y.; Lu, B.; Wang, X.G.; Zhao, J.X.; Wang, X.Z.; Cai, Q.H. Highly selective oxidation of benzyl alcohol to benzaldehyde with hydrogen peroxide by biphasic catalysis. *Chem. Eng. J.* **2010**, *162*, 738–742.
156. Mao, H.; Yu, H.; Chen, J.; Liao, X.P. Biphasic catalysis using amphiphilic polyphenols-chelated noble metals as highly active and selective catalysts. *Sci. Rep.* **2013**, *3*, A2226:1–A2226:5.

Energy Considerations for Plasma-Assisted N-Fixation Reactions

Aikaterini Anastasopoulou, Qi Wang, Volker Hessel and Juergen Lang

Abstract: In a time of increasing concerns about the immense energy consumption and poor environmental performance of contemporary processes in the chemical industry, there is great need to develop novel sustainable technologies that enhance energy efficiency. There is abundant chemical literature on process innovations (laboratory-scale) around the plasma reactor itself, which, naturally, is the essential part to be intensified to achieve a satisfactory process. In essence, a plasma process needs attention beyond reaction engineering towards the process integration side and also with strong electrical engineering focus. In this mini-review, we have detailed our future focus on the process and energy intensification of plasma-based N-fixation. Three focal points are mainly stressed throughout the review: (I) the integration of renewable energy; (II) the power supply system of plasma reactors and (III) process design of industrial plasma-assisted nitrogen fixation. These different enabling strategies will be set in a holistic and synergetic picture so as to improve process performance.

Reprinted from *Processes*. Cite as: Anastasopoulou, A.; Wang, Q.; Hessel, V.; Lang, J. Energy Considerations for Plasma-Assisted N-Fixation Reactions. *Processes* **2014**, *2*, 694-710.

1. Introduction

Nitrogen fixation is indisputably one of the most important chemical processes for both biological and industrial applications. It is a reaction of vital importance as it converts atmospheric nitrogen into ammonia or other useful nitrogen compounds that can be directly absorbed by living organisms as nutrients. It also plays an integral part in the nitrogen cycle and, thereby, in the conservation of all ecosystems. However, apart from its natural importance, fixed nitrogen, and more precisely ammonia, is a fundamental component of fertilizers and other chemicals, and is primarily manufactured via the Haber-Bosch process. It is the second largest commodity in the global chemicals industry and almost 80% of its production is utilized in the manufacture of fertilizer [1]. It is worth mentioning that, in 2011, the world ammonia market exceeded 120 million tons, whereas it is expected to reach up to 160 million tons by the end of 2020 [2].

From an energy point of view, industrial ammonia synthesis is the most energy intensive chemical process, consuming approximately 36.6 GJ/ton NH_3 for natural gas feedstock and achieving an energy efficiency of about 60% [3–6]. For heavier hydrocarbon feedstock, the specific energy consumption can increase considerably, reaching a value up to 169 GJ/t NH_3 for coal gasification. In addition to that, the environmental performance of current state-of–the-art industrial nitrogen fixation processes is relatively poor, being characterized by high carbon dioxide (CO_2) and nitrous oxide (N_2O) emissions. In particular, a typical natural gas-based ammonia plant utilizing steam reforming process, generates emissions of 1.15–1.30 kg·CO_2/kg NH_3, while for partial oxidation, they reach up to 2–2.6 kg·CO_2/kg NH_3 [7]. Additionally, nitric acid plants employing non-selective catalytic

reduction technology and operating under medium pressure, emit an average amount of 7 kg N_2O/ton HNO_3, whereas for low and high pressure conditions, emissions reach an average value of 5 and 9 kg N_2O/ton HNO_3, respectively [8].

Considering the increasing demand of fertilizers, the high energy intensity and environmental concerns triggered by industrial nitrogen fixation, the need to develop and integrate more sustainable processes becomes imperative. A preliminary contribution in that direction has been made by plasma technology which is perceived to be a promising novel approach for improving process environmental and energy efficiency. In terms of nitrogen fixation, there is literature documented on its synthesis in different plasma reactors under varied operating conditions. Ammonia synthesis has been realized in a dielectric barrier discharge reactor under N_2/H_2 feed flow rate of 0.73 L/min, operating temperature of 80 °C and 1 bar pressure [9]. The maximum production efficiency of 1.83 g/kWh has been achieved for an applied power of 57.2 W and NH_3 concentration of 1400 ppm [9]. Furthermore, the synthesis of nitric oxide has also been studied in a microwave discharge plasma reactor for a nitrogen feed with 35% O_2 content at a flow rate of 22 Nl/h, an operating pressure of 50 torr and an applied power of 10 W [10]. Under these conditions and the incorporation of MoO_3 catalyst, an energy consumption of 28 MJ/kg NO has been reported, which equals to 35% energy improvement compared to experimental results without the use of catalyst [10].

The research mentioned above serves as illustrative example of the synthesis of ammonia and nitric oxide via non-thermal plasma technology. Non-thermal plasma reactors are linked to relatively high reaction selectivity and energy efficiency due to the fact that the supplied electrical power is channeled predominately to excite electrons rather than heat the bulk volume of the plasma gas [11,12]. In addition to this, non-thermal plasmas generated at atmospheric pressure and temperature demonstrate clear advantages of low operational costs [13]. However, when it comes to industrial application it becomes necessary to adopt a holistic design approach and consider a scale-up process and its optimization with respect to the energy efficiency, environmental and economic performance. This particular point is initiated in the context of the "Microwave, Ultrasonic and Plasma assisted Syntheses" (MAPSYN) Project which focuses on the sustainable process intensification of nitrogen-fixation reactions and selective hydrogenations reinforced by plasma and microwaves/ultrasound technology respectively [14,15]. In principle, the project aims to overcome the energy and environmental challenges related to the massive production of industrially-fixed nitrogen by developing flexible "small-scale processes", which will incorporate the advantages of the aforementioned alternative energy sources in novel plasma reactors. A typical example illustrating the applicability of this concept is the technology of a vehicle on-board ammonia production from water and nitrogen carried out in a Dielectric Barrier Discharge (DBD) plasma reactor at a variety of operating conditions [16].

2. Methodology-Approach

As it can be deduced from the previous discussion, the initial conceptualization of industrial plasma-assisted nitrogen fixation requires certain design considerations that will lead to an energy efficient and sustainable chemical process. In order to realize this, the process design model of ammonia and nitric acid synthesis—incorporating the nitric oxide generation as a reaction

intermediate—will be developed for both conventional and plasma-assisted production pathways. Simulating the selected plasma-assisted processes in the Aspen Plus software tool (Aspen Technology, Inc.: Burlington, MA, USA) is likely to facilitate the energy efficiency benchmarking and optimization procedure with the corresponding conventional industrial operations.

The simulation model of the scaled-up plasma ammonia and nitric acid will primarily satisfy the prerequisites of a typical medium-scale ammonia and nitric acid plant with respect to the feedstock properties and flow rate, as well as, the type of upstream and downstream activities. However, at a later stage when the simulation optimization for the given plasma-assisted processes has been achieved, certain design modifications will be incorporated related to the capacity/capability of upstream and downstream activities based on different supply chains scenarios, the hydrogen production source, as well as, the power supply system of plasma reactors. These considerations, as shown in Figure 1, will be briefly discussed below with the view to providing a general overview of the upcoming energy challenges associated with the design and integration of plasma technology to conventional-established chemical processes.

Figure 1. Focus areas of energy considerations for plasma-assisted nitrogen fixation.

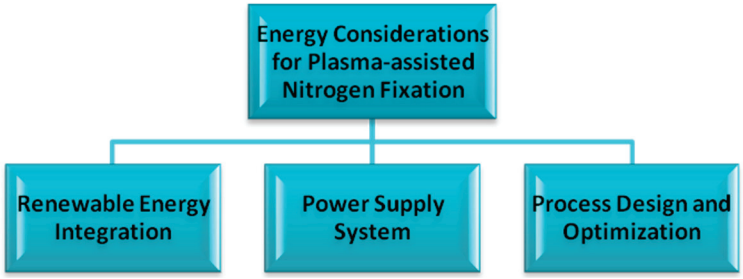

2.1. Integration of Renewable Energy Sources

Almost 97% of the energy requirements of a typical ammonia plant is associated with hydrogen generation via natural gas steam reforming [3]. This fact indicates the necessity to consider renewable energy sources as an alternative electricity power supply system and hydrogen production source. In essence, numerous researchers have conducted detailed studies on the electricity generation via solar and wind energy, as well as hydropower energy [13,17–20]. Case studies on ammonia production via alternative energy sources will be presented below.

Ammonia synthesis via alternative energy sources has been conceptualized for both electricity and hydrogen production based on different technologies as shown in Figure 2 [13]. Although methane steam reforming is a more economically and energy efficient production technique of hydrogen, compared to hydrolysis or air separation, the latter can be proved feasible, if combined with renewable sources what have higher or comparable electricity generation efficiency as the conventional one. For example, the efficiency of electricity generation by hydro, wind and solar can reach up to 95%, 35% and 23%, respectively, whereas natural gas turbine and steam turbine coal-fired power plants have efficiencies of 39% and 47%, correspondingly [21]. These facts, in combination with the following case studies, provide some promising industrial perspectives of the renewable energy sources that will be thoroughly investigated in the content of the MAPSYN project.

Figure 2. Ammonia synthesis based on different hydrogen sources. Reprinted with permission from [13]. Copyright 2008, Iowa State University.

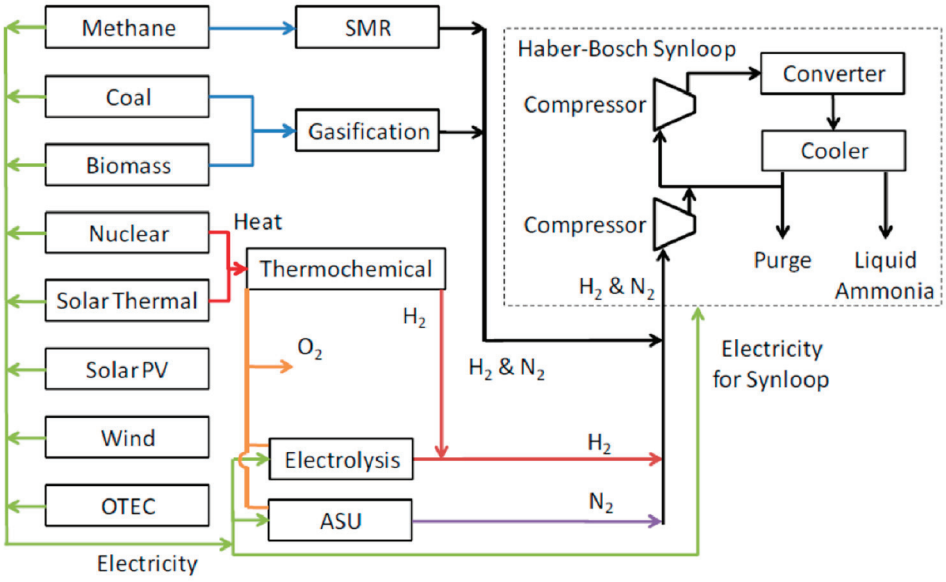

Avery *et al.* extended the existing knowledge on Ocean Thermal Energy Conversion (OTEC) technology by proposing the design of a 325 MWe plant-ship generating 1000 tons of ammonia per day [22,23]. The plant would basically exploit the temperature gradient between the surface and deep ocean water to generate electric power onboard which would be used, in turn, for ammonia synthesis and other energy-demanding operations. As it can be clearly deduced from the Figure 3, the majority of the OTEC power is allocated to hydrogen and nitrogen production via water electrolysis and air liquefaction, respectively, whereas the rest covers propulsion and other related needs.

Figure 3. Ammonia plantship powered by OTEC. Reprinted with permission from [23]. Copyright 1985, International Association for Hydrogen Energy.

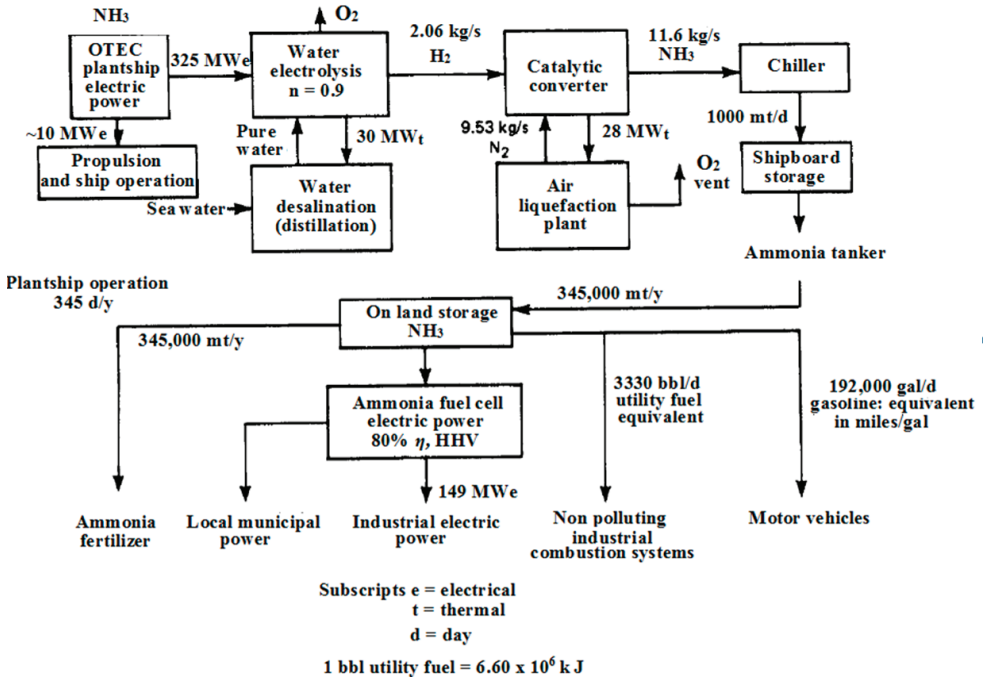

An effort towards commercialization has been made by the University of Minnesota (West Central Research and Outreach Center), which inaugurated the operation of the first wind-powered ammonia pilot plant in 2013 (Figure 4). Early-bird results from plant performance testing demonstrated an energy consumption of 60 GJ/ton NH_3 [24]. Although, the value is relatively higher than the conventional ammonia production by steam reforming, the environmental impact of the process is considerably lower as less fossil fuels are utilized for electricity generation. It is also worth mentioning that the plant undergoes optimization and new plants are likely to achieve an energy consumption of 8 MWh/ton NH_3 where average consumption for conventional synthesis route is 12 MWh/ton NH_3 [25].

Figure 4. Ammonia pilot plant powered by wind in Minnesota. Reprinted with permission from [17]. Copyright 2013, University of Minnesota.

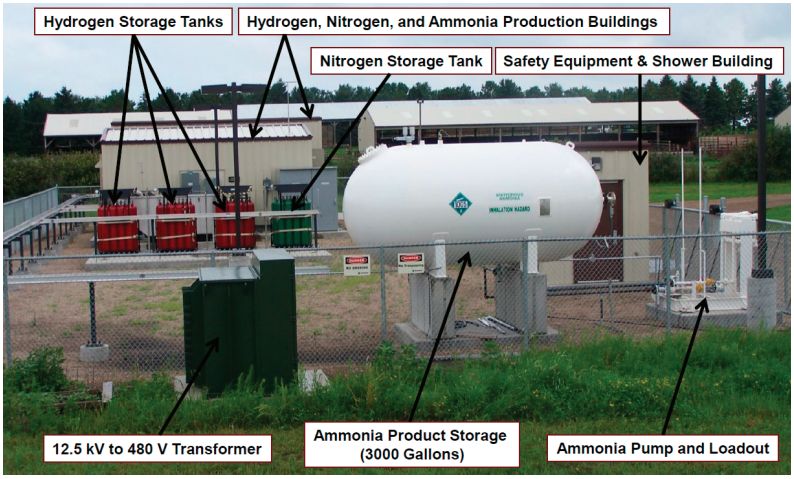

As can be deduced from the above case studies, the integration of alternative energy in plasma-assisted nitrogen fixation can be feasible and sustainable, provided the optimum plant design with respect to the location of the resources has been selected. This is likely to facilitate and maximize the resource utilization and, also, reduce the overall energy costs and the environmental footprint of the given processes. In essence, in the framework of the MAPSYN project, different scenarios for certain alternative energy sources will be developed and optimized based on discrete criteria, such as location, capacity, desired design, operational flexibility, *etc*. A detailed report on this topic will be provided at a later stage, when research has demonstrated progress enough to generate concrete results.

2.2. Power Supply System of Plasma Reactors

Regarding the energy consumption of plasma-assisted nitrogen fixation, all the reported literature focuses mainly on the performance of the plasma reactors rather than the efficiency of the applied power supply system. In the case of plasma processing, the term efficiency implies the real amount of power transferred in the discharge plasma, as compared to what is generated. This has become a focus area of many researchers who have stressed the importance of the power supply system in the overall energy consumption of plasma reactors [26–31]. Especially for DBD plasma reactors that will be also utilized in the MAPSYN project, there is reported literature on the principle of

impedance matching as a way to enhance the overall electrical performance of both the plasma reactor and power generator systems. To exemplify, two case studies will be provided below, illustrating the practical application of the aforementioned principle in reducing DBD impedance.

Prior to the citation of two illustrative examples that focus on the impedance matching in DBD reactors, it would be wise to explain the principle of impedance matching. As seen in Figure 5, in a simple electrical circuit, the power generator (E_G) is meant to provide power to a load resistance (R_L) [32]. However, due to the internal resistance of the source (R_G), a considerable amount of the generated power is wasted as heat whenever the circuit is closed. This actually implies that less power will be always transferred to the load compared to the generated one. In order to minimize this effect and maximize the power transfer to the load, the optimal position, as depicted in the Figure 6, should be achieved where the internal impedance is equal to the load impedance. In that case, the maximum power transfer is achieved with a power transfer efficiency of 50%, which implies that half of the generated power is dissipated by the R_L, whereas the other half is allocated to heat losses induced by the R_G [32]. The process of reducing load impedance and making it equal to the internal impedance is called impedance matching and is accomplished by adding a proper matching network/component between R_G and R_L, as will be described in the following case studies.

Singh and Roy have highlighted the phenomenon of power reflection due to the capacitive behavior of a DBD plasma actuator and, also, the importance of impedance matching for an optimum performance [33]. For that reason, their focus has been placed on integrating a resistance-inductor (RL) or resistance-inductor-capacitor (RLC) circuit between the power generator and plasma actuator, with a view to reducing the capacitive reactance of the latter and, hence, enhancing power transfer in the plasma. Initially, the equivalent circuit of the actuator and the matching component has been designed as shown in the Figure 7, with the plasma actuator being simulated by a group of capacitors, inductor and resistance. On this circuit diagram, the influence of the applied frequency on the equivalent resistance and reactance has been examined for the three following cases: (I) System of DBD actuator circuit without any matching network (II) System of DBD actuator circuit with an RL matching component and (III) System of DBD actuator circuit with an RLC matching component. Given that the values of the C_P, L_P, C_{dv} and C_d are 1 nF, 1 pH, 1 pF and 1 Pf, respectively, and the resistance r_p varies between 0.1, 1, and 10 ohm, the stand-alone DBD actuator system demonstrates negative reactance at low applied frequencies. On the other hand, by adding an RL circuit with R_m = 0.1 ohm and L_m = 0.1 pH in parallel to the actuator the equivalent reactance becomes positive and the resistance remains constant at a value of 0.1 ohm. Under these conditions impedance matching is facilitated by a recommended power generator of low output impedance, around 0.1 ohm [33].

The third examined case involves the integration of an LRC circuit in parallel to the actuator with R_m = 0.1 ohm, L_m = 100 μH and Cm = 100 μF. As Figure 8 depicts, the equivalent resistance of the circuit is 10 ohm and the reactance fluctuates between of −0.5 and +0.5 Ω. This operating regime promotes rather a higher resistance power supply than the one proposed for the RL matching network.

Figure 5. Typical electrical circuit consisting of power generator and a load. Reprinted with permission from [32]. Copyright 2001, Jaycar Electronics Group.

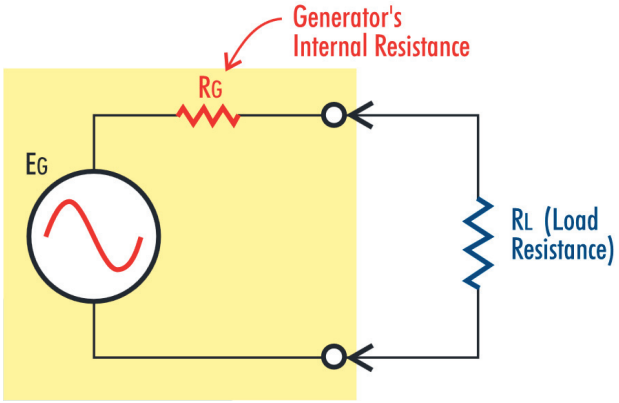

Figure 6. Relationship of power delivery with varying load resistance. Reprinted with permission from [32]. Copyright 2001, Jaycar Electronics Group.

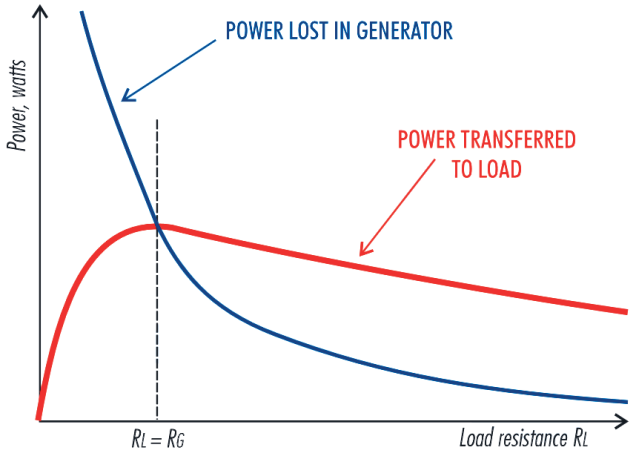

Figure 7. Equivalent electrical circuit of a DBD reactor incorporating an impedance matching component. Reprinted with permission from [33]. Copyright 2007, AIP Publishing LLC.

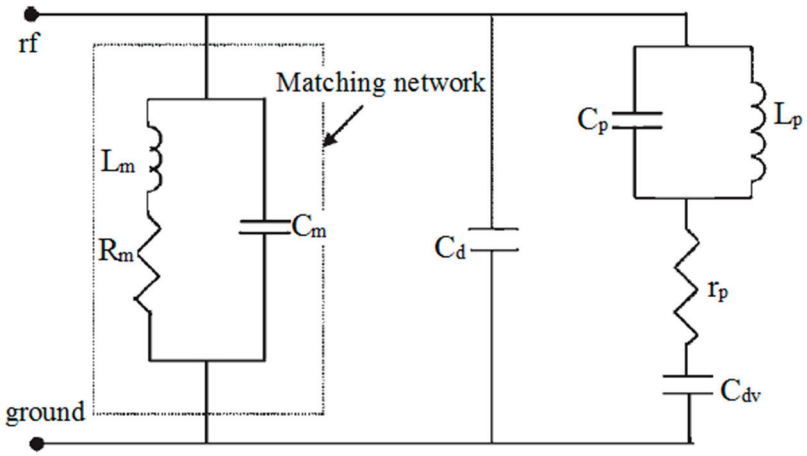

Figure 8. Effect of applied frequency on the resistance and reactance of the plasma reactor system under the effect of (**a**) an inductor-resistor (LR) matching component and (**b**) an inductor-resistor-capacitor (LRC) impedance matching component. Reprinted with permission from [33]. Copyright 2007, AIP Publishing LLC.

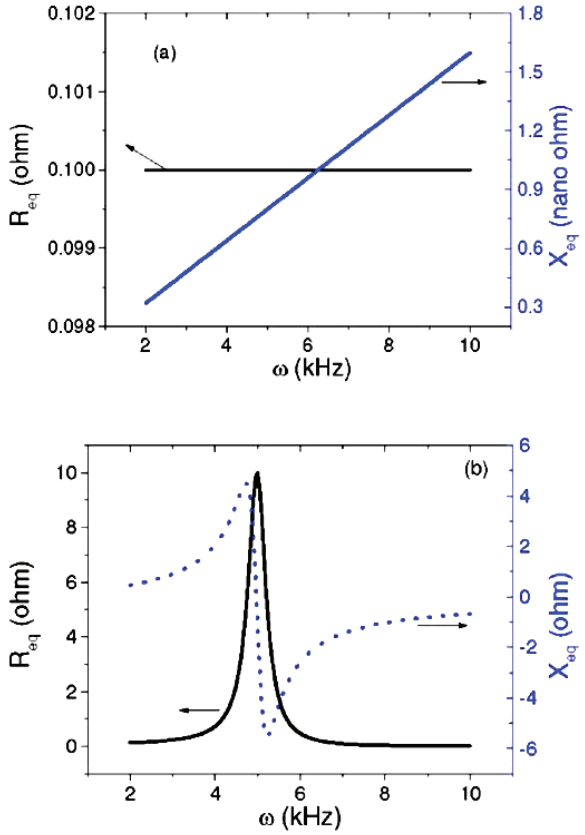

In addition to the previous case study, Zito *et al.* have also investigated the effect of impedance properties on the power delivery in a DBD plasma actuator and proposed a matching network [34]. In specific, the first part of their research includes the examination of power transfer with respect to the applied voltage and current. The generated graphic plots demonstrated periodically positive and negative values of power transfer. The negative values indicate the reactive impedance of the DBD actuator. To address this point, they proceeded with the design of the equivalent electrical circuit of the plasma actuator system in parallel with an LRC matching circuit. The actuator is modeled with a resistance and a capacitor of 5 pF in parallel under an applied frequency of 14 kHz. Depending on these parameters, a pair of values for the capacitor and inductor of the matching network has been estimated and ranged between 0 to 1 mF and 25.8 H to 130 nH, respectively [34].

As discussed above, the impedance of the plasma reactor has been simulated as an electrical equivalent circuit with known values for the related resistances, capacitors and inductors. In literature various electrical models-circuits have been reported for both DBD and Gliding arc reactors based on different assumptions and configurations [26–28,35–42]. To elaborate, in the case of a DBD reactor, Barrientos *et al.* have represented dielectric layers by an ideal capacitor and plasma discharges by a variable resistance and a current source controlled by a voltage source (Figure 9) [43]. On the other hand, Liu and Neiger have used only a variable capacitor so as to avoid the unknown

discharge dependent non-linear variable R(t) (Figure 10) [44]. In addition to the configuration of the equivalent circuit, measuring the external applied voltage and current applying basic electrical formulas, such as the Ohm's law and Kirchoff's law, enables the estimation of the displacement current Iv,g(t) and conduction discharge current Ip,g(t) [44], as well as, the determination of the optimal operating conditions [43]. In the case of a Gliding arc reactor, Diatczyk and Stryczewska *et al.* have applied the Cassie-Mayr model to simulate the Gliding arc with the electrical arc generated in the circuit breakers [28,45]. In particular, the Cassie model, assuming power losses caused by convection, estimates arc conductance as a function of a constant electric arc voltage and time constant value at maximum current [46,47]. On the contrary, the Mayr model assumes power loses caused by thermal conduction and proposes an equation where arc conductance is estimated as a function of the power losses and a time constant value at zero current [46,47]. Although the Cassie and Mayr models are usually applied at low and high-range currents, respectively, in complex problems, they are both combined to a hybrid model with certain parameters being modified so as to cover all possible operating conditions [41]. Generally, for the MAPSYN plasma reactors, the applicability of these electrical models will be critically tested and compared with experimental results so as to facilitate a robust approach to the aforementioned impedance matching problem.

Figure 9. Electrical model of DBD reactor. Reprinted with permission from [43]. Copyright 2006, IOP Publishing.

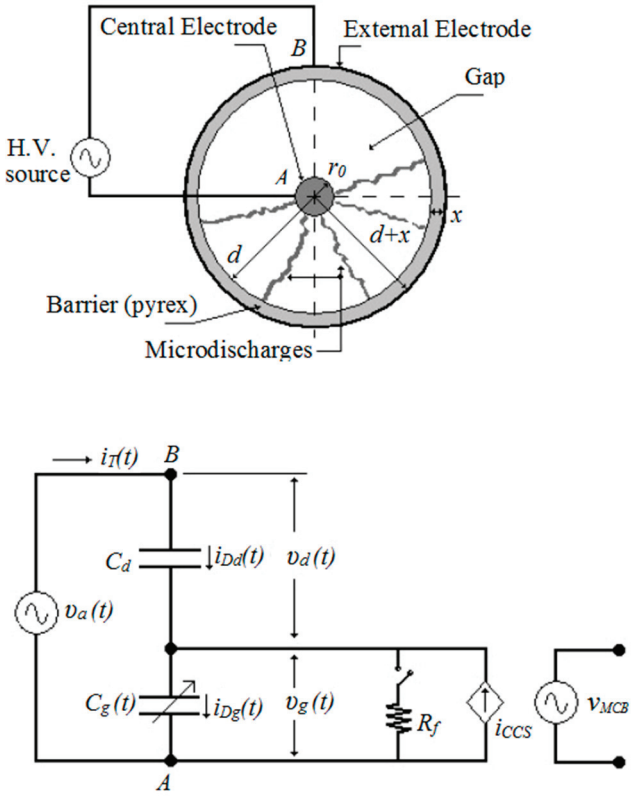

As can be concluded from the above discussions, the importance of impedance matching is apparent throughout many related research papers. The applied methodology behind this electrical principle is overall the same in all cases and entails the understanding of key electrical characteristics of

plasma reactors, the impedance modeling (equivalent circuit modeling) and the proper selection of a matching network that will reduce load reactance and increase power transfer. However, although DBD reactors have received intense attention in terms of optimization of their power supply system, until now, there is no relevant literature reported on plasma-assisted ammonia and nitric oxide in DBD and Gliding arc reactors. This fact triggers the necessity to examine its applicability in this project with a view to designing an efficient power supply system for future industrial applications. As the Dielectric Barrier Discharge (DBD) and Gliding Arc (GA) reactors will be used in the context of the MAPSYN project, studying and comprehending the behavior of key electrical parameters are likely to yield new insights into minimizing power losses and maximizing power transfer to plasma discharge. The existing knowledge gap is intended to be narrowed by conducting both systematic and methodical experimental and simulation studies on the dynamic behavior of the power supply system of plasma reactors.

Figure 10. (**a**) The DBD electrode layout and (**b**) the equivalent circuit. Reprinted with permission from [44]. Copyright 2003, IOP Publishing.

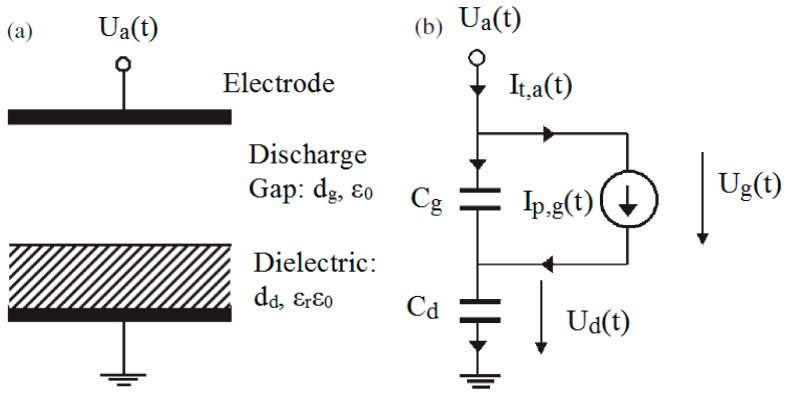

2.3. Synthesis Loop and Downstream Activities

A critical part in the energy optimization of the plasma-assisted nitrogen fixation processes is the ASPEN design and simulation of the synthesis loop, or more precisely the reactor scheme itself. The performance of the plasma reactor will closely influence the capability of the relevant upstream and downstream activities. To elaborate, as shown in Figure 11, the synthesis gas (nitrogen/hydrogen feed), which is obtained from the methanation section at a temperature of 280 °C and pressure of 26.5 bar, undergoes further compression to approximately 300 bar prior to entering the ammonia synthesis loop [48]. The generated ammonia exits the synthesis loop at a temperature around 440 °C and pressure of 284 bar and, then, is directed to the refrigeration system with starting operating conditions of 15 °C and 275 bar. Upon the same design concept and feedstock properties, replacing the conventional ammonia converters in the synthesis loop with a single or a series of plasma reactor operating at 1 bar and 25 °C is likely to reduce energy costs at a first stage, as the compression and preheat requirements of the reactor feed will be remarkably lower. However, this point alone is not able to provide a clear view of the process energy efficiency, since it should be considered in combination with the electricity consumption of plasma reactor, which will play a contributory role and request considerable attention in terms of its optimization.

In addition to the power consumption of the plasma reactor, the ammonia conversion rate will also influence the overall energy savings. The maximum conversion rate for plasma-assisted ammonia synthesis in DBD reactor reported in literature is 12.6% (under 180 °C and 1 bar) compared to 24% of the conventional one [49]. This implies a re-conceptualization of the established downstream processes for the reason that more quantity of unreacted reactants will be recycled in the synthesis loop and, thereby, larger heat transfer areas of the heat exchangers and higher capacity of compressors and flash tanks will be required [50].

Figure 11. Schematic overview of ammonia synthesis process. Adapted with permission from [51]. Copyright 2006, Wiley-VCH Verlag GmbH & Co. KGaA.

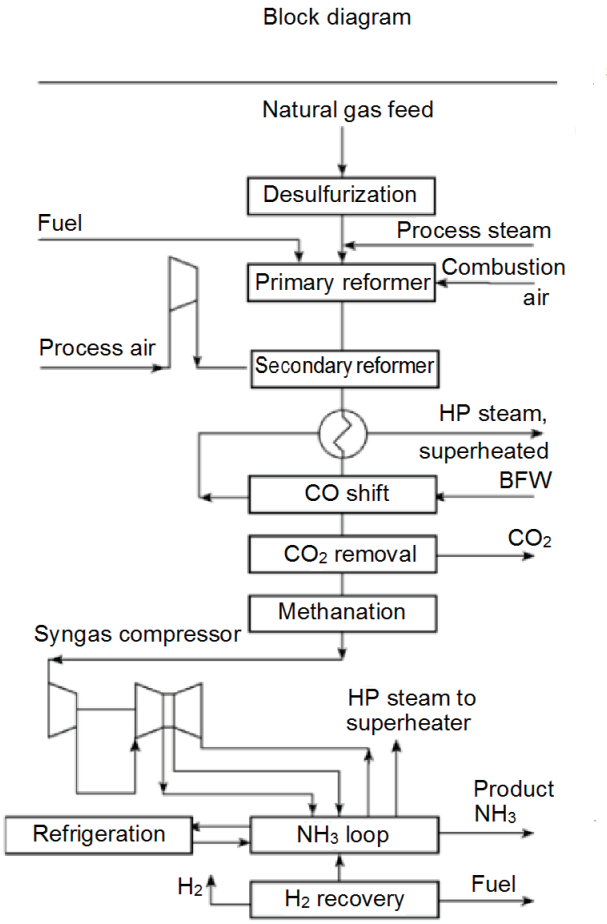

On the other hand, nitric acid synthesis is energy efficient and is consolidated upon three major reactions: (a) ammonia combustion, (b) oxidation of nitric oxide, and (c) absorption of nitric oxide in water (Figure 12) [52]. The process demonstrates a net energy export of approximately 1.6 GJ/t HNO_3. attributed to the heat recovery from the absorption tail gases and the exothermic oxidation of ammonia which takes place at temperatures and pressures between 840–950 °C and 1–8 bar, respectively [53]. The NO gas generated by ammonia combustion is cooled to 20–30 °C and driven to the absorption column where its oxidation and absorption in water will take place. Based on these operating conditions and assuming the replacement of the ammonia oxidation by a plasma-assisted nitric oxide process operating at ambient temperature and pressure, the energy profile of the entire

process seems to drastically change, as the nitric oxide reaction is highly endothermic and the NO conversion rate is still lower than the conventional one. Although energy savings from avoiding cooling the plasma-produced NO for the absorption section seem to dominate at a first stage, the lower conversion will lead to a redesign of the downstream activities and, thereby, to a different energy profile for the plasma process as compared to the conventional one. Consequently, a pinch analysis will be conducted for the optimal ASPEN design model of the plasma-assisted nitric acid synthesis so as to minimize energy consumption and to enable a complete benchmark with the conventional route.

In both cases of plasma-assisted nitrogen fixation, the initial ASPEN model will be established and optimized based on the conventional operating conditions. However, after completing this step, different design scenarios that enhance the energy performance of plasma-assisted nitrogen fixation will be applied since the final aim of the MAPSYN project is not to achieve comparable industrial production capacities, but to develop processes performing at a maximum efficiency based on their inherent characteristics and operational requirements.

Figure 12. Process flow diagram of dual pressure nitric acid synthesis. Reprinted with permission from [53]. Copyright 2001, Umweltbundesamt-Federal Environment Agency Austria.

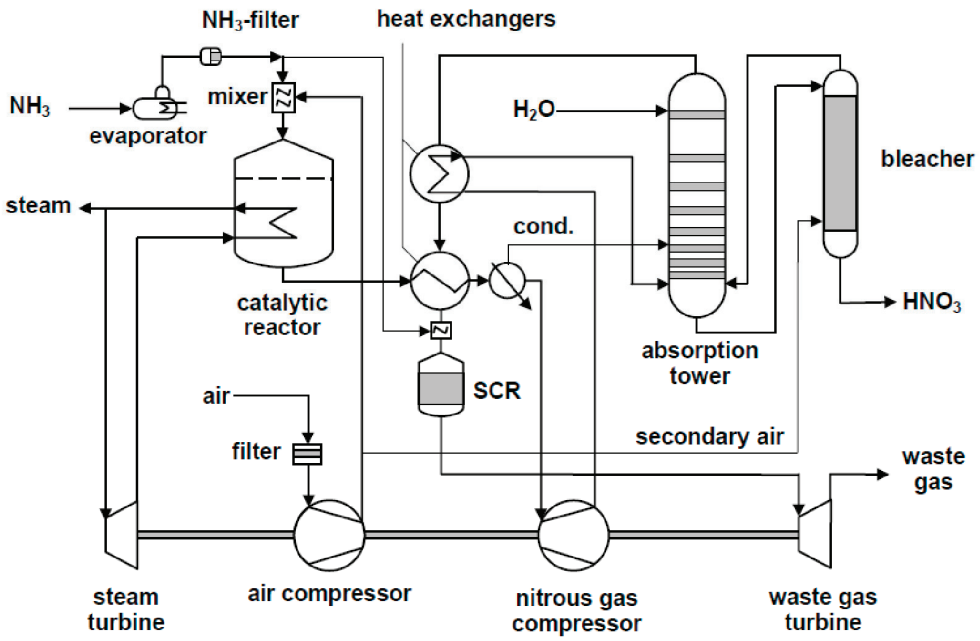

3. Conclusions

As it can be concluded from the above, there are three major design parameters that will play a critical role in the energy performance of plasma-assisted nitrogen fixation: (I) the integration of renewable energy; (II) the power supply system of plasma reactors; and (III) process design of industrial plasma-assisted nitrogen fixation. The integration of renewable energy sources is one of the most influential factors in enhancing the sustainability profile of the selected processes. Valid scenarios, for example, for the utilization of solar and wind energy will be developed and incorporated in

the process design and the corresponding energy footprint will be monitored. In addition to that, the power supply system of the plasma reactors will also become a subject of profound research. The reason for this lies in the fact that studies towards the improvement of the power delivery efficiency in the discharge plasma have been intensely identified in literature with the majority of them employing the impedance matching theory. The underlying principle of this impedance matching will be applied and tested in the plasma reactors of the MAPSYN project with a view to minimizing power losses and maximizing power delivery in plasma discharge.

Regarding the initial industrial design of the plasma-assisted ammonia and nitric acid syntheses, although it will generally follow the conventional corresponding production routes, the synthesis and downstream activities will still be subject to re-conceptualization with respect to the capability, equipment size, *etc*. Finally, the proposed design for the selected processes will be subjected to a multi-criteria optimization procedure with the ultimate aim of attaining long-term economic feasibility and sustainability.

Acknowledgments

This research is kindly funded by the EU project MAPSYN: Microwave, Acoustic and Plasma SYNtheses, under grant agreement no. CP-IP 309376 of the European Community's Seventh Framework Program.

Author Contributions

Volker Hessel and Qi Wang developed the conceptual idea and defined the topic of the review paper. All authors contributed to the manuscript drafting. Aikaterini Anastasopoulou detailed the concept with the concrete contents and coordinated the writing. She also contributed to the revision of the manuscript.

Conflicts of Interest

The authors declare no conflict of interest.

References

1. Willem, E.J.; Sutton, M.A.; Galloway, J.; Klimont, Z.; Winiwarter, W. How a Century of Ammonia Synthesis Changed the World. *Nat. Geosci.* **2008**, *1*, 636–639.
2. Companies and Markets. Ammonia Global Market to 2020. Available online: http://www.companiesandmarkets.com/Market/Chemicals/Market-Research/Ammonia-Global-Market-to-2020/RPT1145125 (accessed on 21 February 2014).
3. Rafiqul, I.; Weber, C.; Lehmann, B.; Voss, A. Energy Efficiency Improvements in Ammonia Production—Perspectives and Uncertainties. *Energy* **2005**, *30*, 2487–2504.
4. International Energy Agency (IEA). *Tracking Industrial Energy Efficiency and CO_2 Emissions*; IEA Publications: Paris, France, 2007; p. 324.

5. Feibelman, P.J.; Stumpf, R. Comments on Potential Roles of Ammonia in a Hydrogen Economy—A Study of Issues Related to the Use of Ammonia for On-Board Vehicular Hydrogen Storage. Available online: http://www.sandia.gov/surface_science/pjf/On_NH3_roles_in_H2_economy.pdf (accessed on 21 February 2014).
6. Lan, R.; Tao, S. Direct Ammonia Alkaline Anion-Exchange Membrane Fuel Cells. *Electrochem. Solid-State Lett.* **2010**, *13*, B83–B86.
7. European Fertilizer Manufacturers Association (EFMA). *Best Available Techniques for Pollution Prevention and Control in the European Fertilizer Industry. Booklet No. 1 of 8: Production of Ammonia*; EFMA: Brussels, Belgium, 2000.
8. Kool, A.; Marinussen, M.; Blonk, H.; Consultants, B. *LCI Data for the Calculation Tool Feedprint for Greenhouse Gas Emissions of Feed Production and utilization.GHG Emissions of N, P and K Fertilizer Production*; Blonk Consultants: Gouda, The Netherlands, 2012; p. 15.
9. Bai, M.; Zhang, Z.; Bai, X.; Bai, M.; Ning, W. Plasma Synthesis of Ammonia with a Microgap Dielectric Barrier Discharge at Ambient Pressure. *IEEE Trans. Plasma Sci.* **2003**, *31*, 1285–1291.
10. Mutel, B.; Dessaux, O.; Goudmand, P. Energy Cost Improvement of the Nitrogen Oxides Synthesis in a Low Pressure Plasma. *Rev. Phys. Appl.* **1984**, *19*, 461–464.
11. Fridman, A.; Cho, Y.-I. *Transport Phenomena in Plasma-Advances in Heat Transfe*; Academic Press, Elsevier: Waltham, MA, USA, 2007; Volume 1, pp. 1–4.
12. Pekárek, S. Non-Thermal Plasma Ozone Generation. *Acta Polytech.* **2003**, *43*, 47–51.
13. Bartels, J.R. A Feasibility Study of Implementing an Ammonia Economy. Master's Thesis, Iowa State University, Ames, IA, USA, 2008.
14. Hessel, V.; Anastasopoulou, A.; Wang, Q.; Kolb, G.; Lang, J. Energy, Catalyst and Reactor Considerations for (near)-Industrial Plasma Processing and Learning for Nitrogen-Fixation Reactions. *Catal. Today* **2013**, *211*, 9–28.
15. Hessel, V.; Cravotto, G.; Fitzpatrick, P.; Patil, B.S.; Lang, J.; Bonrath, W. Industrial applications of plasma, microwave and ultrasound techniques: Nitrogen-fixation and hydrogenation reactions. *Chem. Eng. Process.* **2013**, *71*, 19–30.
16. Gieshoff, J.; Lang, J. Process for the Plasma-Catalytic Production of Ammonia. U.S. Patent 6471932B1, 29 October 2002.
17. Tallaksen, J.; Reese, M. Ammonia Production Using Wind Energy. Available online: http://nh3fuel.files.wordpress.com/2013/10/nh3fcx-joel-tallaksen.pdf (accessed on 21 February 2014).
18. Dugger, G.; Francis, E. Design of an Ocean Thermal Energy Plant Ship to Produce Ammonia via Hydrogen. *Int. J. Hydrog. Energy* **1977**, *2*, 231–249.
19. Lu, X.; McElroy, M.B.; Kiviluoma, J. Global Potential for Wind-Generated Electricity. *Proc. Natl. Acad. Sci. USA* **2009**, *106*, 10933–10938.
20. Alosaimy, A.S.; Hamed, A.M.; Balabel, A.; Mahrous, A. Experimental Investigation of Solar Hydrogen Production Unit in Taif, Saudi Arabia. *Int. J. Adv. Sci. Tech. Res.* **2013**, *6*, 61–73.
21. Union of the Electric Industry-EURELECTRIC & VGB PowerTech. *Efficiency in Electric Generation*; Union of the Electricity Industry-EURELECTRIC & VGB: Brussels, Belgium, 2003.

22. Waid, R.L. The Mini-Otec Test. In Proceedings of the OCEANS '79: Fifth Annual Combined Conference, San Diego, CA, USA, 17–19 September 1979; pp. 548–552.
23. Avery, W.H.; Richards, D.; Dugger, G.L. Hydrogen Generation by OTEC Electrolysis, and Economical Energy Transfer to World Markets via Ammonia and Methanol. *Int. J. Hydrog. Energy* **1985**, *10*, 727–736.
24. NH_3 Fuel Association. Ammonia Production Using Wind Energy. Available online: http://nh3fuelassociation.org/2013/08/28/ammonia-production-using-wind-energy/ (accessed on 21 February 2014).
25. Ammonia Industry. Ammonia Plants: Morris, MN—University of Minnesota. Available online: http://ammoniaindustry.com/morris-mn-university-of-minnesota/ (accessed on 23 June 2014).
26. Chen, Z. Impedance Matching for One Atmosphere Uniform Glow Discharge Plasma (OAUGDP) Reactors. *IEEE Trans. Plasma Sci.* **2002**, *30*, 1922–1930.
27. Spiliopoulos, N.; Mataras, D.; Rapakoulias, D.E. Power Dissipation and Impedance Measurements in Radio-Frequency Discharges. *J. Vac. Sci. Technol. A* **1996**, *14*, 2757–2765.
28. Diatczyk, J.; Komarzyniec, G.; Stryczewska, H.D. Power Consumption of Gliding Arc Discharge Plasma Reactor a B. *Int. J. Plasma Environ. Sci. Technol.* **2011**, *5*, 12–16.
29. Holub, M.; Kalisiak, S.; Jakubowski, T.; Balcerak, M. Power Electronic Supply Systems for Non-Thermal Plasma Sources. In Proceedings of the XVIII International Conference on Gas Discharge and Their Applications (GD2010), Greifswald, Germany, 5–10 September 2010.
30. Sheykhrajeh, S.Z. Flexible High Voltage Pulsed Power Supply for Plasma Applications. Ph.D. Thesis, Queensland University of Technology, Brisbane, QLD, Australia, 2011.
31. Van Dijk, J.; Kroesen, G.M.W.; Bogaerts, A. Plasma Modelling and Numerical Simulation. *J. Phys. D* **2009**, *42*, 190301.
32. Jaycar Electronics Group. Impedance Matching : A primer. Available online: http://www.jaycar.com.au/images_uploaded/impmatch.pdf (accessed on 21 February 2014).
33. Singh, K.P.; Roy, S. Impedance Matching for an Asymmetric Dielectric Barrier Discharge Plasma Actuator. *Appl. Phys. Lett.* **2007**, *91*, 081504.
34. Zito, J.C.; Arnold, D.P.; Duscher, R.J.; Roy, S. Investigation of Impedance Characteristics and Power Delivery for Dielectric Barrier Discharge Plasma Actuators. In Proceedings of the 48th AIAA Aerospace Sciences Meeting Including the New Horizons Forum and Aerospace Exposition, Orlnado, FL, USA, 4–7 January 2010; pp. 1–17.
35. Kriegseis, J.; Grundmann, S.; Tropea, C. Power Consumption, Discharge Capacitance and Light Emission as Measures for Thrust Production of Dielectric Barrier Discharge Plasma Actuators. *J. Appl. Phys.* **2011**, *110*, 013305.
36. Ebato, S.; Ogino, Y.; Ohnishi, N. Computational Study of Discharge Processes in DBD Plasma Actuators. *J. Space Technol. Sci.* **2011**, *25*, 19–33.
37. Kriegseis, J.; Möller, B.; Grundmann, S.; Tropea, C. Capacitance and Power Consumption Quantification of Dielectric Barrier Discharge (DBD) Plasma Actuators. *J. Electrost.* **2011**, *69*, 302–312.

38. Pipa, A.V.; Koskulics, J.; Brandenburg, R.; Hoder, T. The Simplest Equivalent Circuit of a Pulsed Dielectric Barrier Discharge and the Determination of the Gas Gap Charge Transfer. *Rev. Sci. Instrum.* **2012**, *83*, 115112.
39. Tran, N.D.; Sasaki, T.; Kikuchi, T.; Harada, N. Optimization Input Power to Obtain the Stable Annealing Conditions of a Plasma Annealing System at Atmospheric Pressure. *J. Plasma Fusion Res. Ser.* **2010**, *9*, 503–508.
40. Dai, J.; Hao, R.; You, X.; Sun, H.; Huang, X.; Li, Y. Modeling of Plasma Arc for the High Power Arc Heater in MATLAB. In Proceedings of the 5th IEEE Conference on Industrial Electronics and Applications, Taichung, Taiwan, 15–17 June 2010; pp. 463–468.
41. Tseng, K.-J.; Wang, Y.; Vilathgamuwa, D.M. An Experimentally Verified Hybrid Cassie-Mayr Electric Arc Model for Power Electronics Simulations. *IEEE Trans. Power Electron.* **1997**, *12*, 429–436.
42. Jaroszyński, L.; Stryczewska, H.D. Computer Simulation of the Electric Discharge in Glidarc Plasma Reactor. In Proceedings of the 3rd International Conference: Electromagnetic devices and processes in environment protection ELMECO-3, Naleczow, Poland, 4–6 June 2000.
43. Valdivia-Barrientos, R.; Pacheco-Sotelo, J.; Pacheco-Pacheco, M.; Benítez-Read, J.S.; López-Callejas, R. Analysis and Electrical Modelling of a Cylindrical DBD Configuration at Different Operating Frequencies. *Plasma Sourc. Sci. Technol.* **2006**, *15*, 237–245.
44. Liu, S.; Neiger, M. Electrical Modelling of Homogeneous Dielectric Barrier Discharges under an Arbitrary Excitation Voltage. *J. Phys. D Appl. Phys.* **2003**, *36*, 3144–3150.
45. Stryczewska, H.D.; Janowski, T.; Jaroszyński, L. Mathematical Model of the Non-Thermal Plasma Reactor. In Proceedings of the IV International Workshop on Advanced Plasma Tools and Process Engineering, Millbrae, CA, USA, 26–27 May 1998.
46. Gustavsson, N. Evaluation and Simulation of Black-Box Arc Models for High Voltage Circuit-Breakers. Master's Thesis, Linkoping University, Linkoping, Sweden, 2004.
47. Nitu, S.; Nitu, C.; Mihalache, C.; Anghelita, P.; Pavelescu, D. Comparison between Model and Experiment in Studying the Electric Arc. *J. Optoelectron. Adv. Mater.* **2008**, *10*, 1192–1196.
48. Russamee, N. Simulation and Design of Ammonia Process from Natural Gas Reforming. Master's Thesis, Kasetsart University, Bangkok, Thailand, 2009.
49. Ruan, R.; Deng, S.; Le, Z.; Chen, P. Non-Thermal Plasma Synthesis of Ammonia. WO Patent, 2009025835 A1, 26 February 2009.
50. Thyssenkrupp Uhde. Ammonia. Available online: http://www.thyssenkrupp-uhde-asia-pacific.com/fileadmin/documents/brochures/0a2d5391-b166-484d-847d-3cbfd941f06b.pdf (accessed on 21 February 2014).
51. Appl, M. Ammonia. In *Ullmann's Encyclopedia of Industrial Chemistry*; Wiley-VCH Verlag GmbH & Co. KGaA: Weinheim, Germany, 2006; p. 85.

52. Thyssenkrupp Uhde. Nitric acid. Available online: http://www.thyssenkrupp-uhde-asia-pacific.com/fileadmin/documents/brochures/cc0d66ab-c015-4512-8c70-1dd5d2917b9e.pdf (accessed on 21 February 2014).
53. Wiesenberger, H. *State-of-the-Art for the Production of Nitric Acid with Regard to the IPCC Directive*; Umweltbundesamt-Federal Environment Agency Austria: Vienna, Austria, 2001; p. 66.

Selection of Technical Reactor Equipment for Modular, Continuous Small-Scale Plants

Nicolai Krasberg, Lukas Hohmann, Thomas Bieringer, Christian Bramsiepe and Norbert Kockmann

Abstract: Fast process development, flexible production and the utilization of advanced process conditions are the main goals of modular and continuous small-scale plants (MCSPs). A configurable layout of the modules and the use of predefined equipment enable a quick and reliable conceptual process development and scale-up of continuous processes. Therefore, a computer-assisted selection methodology was developed and is presented, which allows the quick selection of plug flow reactor equipment for homogeneous liquid phase reactions. It identifies a favorable technical apparatus and the configuration in the early stages of process development. This can lead to the effective planning and guiding of scale-up experiments and closes the gap between lab and process development.

Reprinted from *Processes*. Cite as: Krasberg, N.; Hohmann, L.; Bieringer, T.; Bramsiepe, C.; Kockmann, N. Selection of Technical Reactor Equipment for Modular, Continuous Small-Scale Plants. *Processes* **2014**, *2*, 265-292.

1. Introduction

In recent public funding projects (e.g., F^3 Factory [1], CoPIRIDE [2]), the first examples of modular and continuously operated small-scale plants (MCSPs) have been evaluated and confirmed to be beneficial in a technical and economical manner [3,4]. The presented prototypes represent first-of-its-kind plants and demonstrate the general feasibility of the technology. To fully exploit the potential of MCSPs, the entire development chain, starting with the chemical process development and conceptual process design to engineering and construction, has to be supplemented with innovative methodologies. These should take into account the main drivers for the utilization of future production concepts. For some products, "time-to-process" is of great importance for enabling market entry. This can be true for products with a short product lifespan in volatile markets, as described by I.V. Gürsel *et al*. [5]. Other products, like high value pharmaceutical drugs, benefit from continuous processing and fast process development by using the same MCSP for the early supply of kilogram-samples for clinical trials and for later market entry. MCSPs also provide a flexible platform concept [6] for the production of different lot sizes of highly customized products. Due to continuous processing, lot size can be adapted by the campaign runtime. A range of similar products (e.g., polymers of different molecular weight distribution), which are adapted to exactly meet customer needs, can be realized by utilizing the ability to reconfigure single modules within MCSPs. Singh *et al*. [7] describe a process reconfiguration strategy for substrate adoption that could be applied here. Furthermore, the compact framework of an MCSP provides an ideal infrastructure for the implementation of milli- and micro-structured equipment, enabling the integration of process-intensified equipment into a production environment. The technology offers

access to new synthesis routes and process windows that are not suitable for classical batch operation or that provide better product quality than conventional processing [8,9].

In order to meet the named requirements for a shortened development time and increased plant flexibility, and additionally, enabling the use of modern process equipment, the concept of modular process development [10] utilizing predefined and intensified equipment will be addressed in this article. A methodology for the selection of technical reactors in the early stages of conceptual process design is presented exemplarily, which aims at supporting the data acquisition for reaction systems and process scale-up. By identifying the most critical technical parameters and promising reactor technologies in the early stages of development, the steering of lab development and scale-up can be facilitated. The methodology aims at choosing the optimal solution out of commercially available equipment rather than engineering new, highly optimized equipment. These already existing and tested devices often have inherent numbering-up/scale-up concepts available, which can be combined with a modularized plant framework to simplify and speed up implementation into MCSP.

2. Modular Plant Design and Predefined Equipment

The term plant modularization is widely used within literature, describing different possible layers for the implementation of modularity in plant engineering and construction [4,11–13]. Hence, for the MCSP, the applied definition of modularity shall be specified in this chapter. According to Figure 1, multiple MCSPs can be integrated into one backbone facility to provide the needed technical and logistic infrastructure for the processes and to reduce the overhead operation expenditures (e.g., staff, logistics, storage and civil engineering). The backbone facility can be a greenfield solution or likewise integrated into an existing (batch) facility.

Figure 1. Hierarchical structure of the physical elements within modular and continuously operated small-scale plant (MCSP) planning.

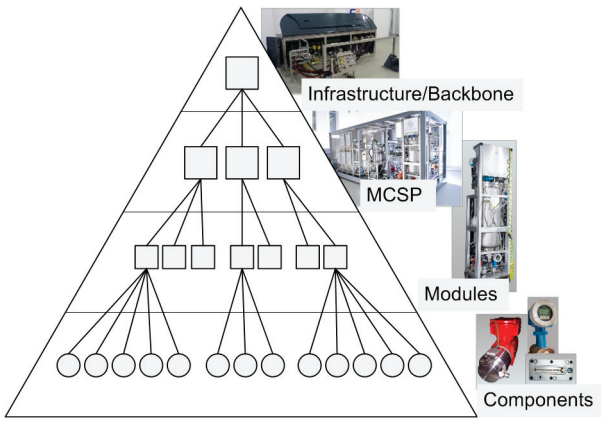

Individual MCSPs can be fitted into ISO transport containers if the preassembly of the plant, location flexibility and an easy process redesign are of some importance. The container framework also provides all the needed process utilities, the overall process control and a grid for the positioning of process modules within its compact footprint.

2.1. Modular Equipment

These two top layers are not regarded as modular. The modular design is applied to the next layer of the plant. Functional units of the process are clustered into modules, where one module consists of the main equipment, which provides the desired unit operation together with all needed peripheral components (e.g., pumps, heat-exchangers, piping, process control components). To be compatible with one another, the construction of each module follows certain design rules. Each module is constructed into a transportable skid in which the footprint of the skid is a multiple of a discrete grid size, which gives flexibility for the arrangement and rotation of adjacent modules. To enable fluidic and electrical connections, predefined compartments, as well as standards for the final interconnection of the modules are specified, and near-field process control systems are provided, which can be connected to the overall process control system.

The main and peripheral equipment within the modules are described in detail at the component layer. The single components are combined to achieve a desired module operation window defined by technical parameters (e.g., ranges for temperature, pressure, flow rates, material grades). Thereby, within one module, some components are exchangeable to adapt different operation conditions. Especially for the main equipment, a certain free space inside each module is reserved during the initial planning, which offers the possibility of integrating various equipment into the same base module, in order to facilitate the reuse of already planned modules.

In addition to these physical properties of a module, a documentation package containing all necessary documents for planning, construction and operation is generated for each module. Besides typical engineering documents (e.g., P&ID, instrument datasheets), it also includes templates for the process control system, a safety and reliability assessment, a list of possible configuration alternatives and simulation models, which describe the resulting operation window. A corresponding definition of module planning documentation is also described by Bramsiepe *et al*. [10].

As a result of the described modularity, different possibilities for the reuse of information and equipment can be utilized to speed up the “time-to-process”. If process specifications for a given task fit into an already existing module (referred to as the “base module”), it can be reused without modification. Furthermore, the reproduction of an existing base module from a documentation package without major modifications is possible, which enables savings in the development and construction time and expenditures. If no existing or planned module meets the specification of an actual process task, a new module has to be designed. Therefore, the documentation package of the best fitting base module is reused by specifying different components where necessary. The method presented in the following aims at supporting the selection of the main equipment within a base module by using predefined process equipment.

2.2. Predefined Equipment

The above-mentioned concept of a configurable base modules can be applied for several unit operations within the MCSP. Especially for the reaction steps of a process, it is augmented by a broad variety of commercially available technical reactors for continuous processing, including intensive mixing, heat exchange and residence time applications. If the peripheral equipment of a

reaction module is chosen carefully, it can be used for a wide range of applications within a defined process task (e.g., reaction systems defined by a phase system). For basic operation conditions (e.g., temperature, pressure, volumetric flow rate, viscosity), a range of one or two magnitudes for each parameter is achievable using the same peripheral equipment. All other operation parameters (e.g., residence time, mixing intensity, heat removal) are only dependent on the main apparatus of the module, which can be chosen arbitrarily within the geometrical boundaries of the base module.

In a classic continuously operated, large-scale plant, the reactor is often intensively optimized and individually designed for a particular application and operating point. Numerous reactor design methods, like heuristic approaches, dynamic optimization approaches, attainable region methods, rigorous optimization approaches (e.g., superstructures) and the systematic staging approach, are presented in the literature, as reviewed by Peschel *et al*., and present a rigorous multi-step optimization approach [14]. A recent method presented by Patel *et al*. [15] adopts a modular approach for tubular reactor design. These methods show an increasing mathematical complexity during the last five decades and usually aim at designing strongly optimized, but individually constructed reactors. To achieve this, a broad variety of process information (especially a mathematical description of the reaction kinetics) is required.

In contrast to this, the approach presented here aims at supporting the early process development and scale-up from lab to productive environment. Hence, it has to deal with increasing system knowledge starting with rudimentary information to support early lab development. To further decrease the development time, the usage of predefined equipment is intended. Predefined equipment can be represented either by an apparatus being already in stock from a former process (reutilization) or by a commercially available standard apparatus. This also affects the design procedure, due to the fact that the geometries of the available reactors are already fixed. Instead of designing an optimized new piece of equipment, an existing apparatus has to be identified from a database, sufficiently approximating an optimal reactor for the process. Some manufacturers already provide a systematic scale-up or sizing approach for their own equipment, which can also be regarded in the selection process. This can address the parallel or serial connection of basic reactor elements or system-inherent scale-up strategies, as reported by Roberge and Kockmann *et al*. [6,16–18], to select the right equipment to meet the process requirements. The selection of equipment from a fixed set of devices and their interconnection allows for a quicker engineering and construction compared to designing specialized equipment. Otherwise, an increased willingness to compromise with respect to the optimal technical process is needed. If a predefined reactor is chosen, for example, the device throughput and mean residence time cannot be chosen independently. For many reactions, the method presented in the following chapter can nonetheless lead to a sophisticated technical solution.

3. Selection of Predefined Plug Flow Reactor Equipment

The methodology will focus on the selection of plug flow reactor equipment, which is suited to operate homogeneous liquid-phase reactions in an MCSP. As a result, favorable technical reactor designs are suggested. Experimental validation and further specifications of the equipment (e.g., material grade, chemical resistance, safety installations) have to be considered subsequently.

The reactor selection methodology presented in this paper requires data from different origins to decide about the technical ability of the reactor system and to identify the most promising ones. From the chemical process development, basic information about the chemistry of the process (stoichiometry, stoichiometric ratio, solvent system, reaction temperature), the mean physical properties of the reacting fluid (density, viscosity, heat capacity, molar masses), the chemical properties of the system (heat of reaction/adiabatic temperature rise, operation temperature interval, reaction kinetics) and the desired reactor concept [19] (plug flow or total back-mixing in the reactor) can be gained. The conceptual process design and the process flowsheet provide information about the state of the feed stream (mass flow rate, composition, temperature, pressure) and give general targets for the outlet stream (targeted conversion/yield). An equipment database provides information about the available predefined reactor systems. For each reactor system, a dataset consisting of geometry information (length, diameter, volume), the allowed operation conditions (feasible operation pressure or temperature), and specific correlations (pressure drop, heat transfer) is stored in the database (*cf*. Table 1).

The database information for process and equipment can be accessed and processed by a user-guided software tool. Suited mathematical models are used to calculate the characteristics of the investigated process simultaneously in various reactor systems. The characteristics can be compared with boundary values connected to the apparatuses or the reacting fluid, which must not be violated. As characteristics, the mechanical and thermal stability of the reactor in operation, a sufficient initial mixing of the reactants in the reactor and the thermal stress to the reacting fluid has to be analyzed. Such a technical boundary will be called the "technical criterion" in the following. Further "performance indicators", like the high conversion of the reactants, the high selectivity to the desired product(s), the moderate operation conditions (low required inlet pressure, ambient required temperature of the heat transfer medium), favorable flow conditions and, especially in case of the MCSP, a sufficiently low space demand of the main reactor equipment in the reactor module, can be used to revise and rate the technical ability of the reactor systems. Beside all these aspects ensuring the technical ability of a certain reactor system, investment costs and the time required for delivery and construction have to be considered, too. The reuse of an already existing reactor module might be of economic advantage over purchasing new (optimized) systems, due to the time-saving aspect. Operating costs are assumed to be less depending on the choice of the main equipment. Thus, operating costs will not be analyzed in detail here, although it might be generally favored to choose a reactor, operating at moderate conditions as mentioned above, resulting in lower energy demand.

3.1. Availability of Process Data

The full range of process information mentioned above is often not available from the start of the process development for a new fine chemical/pharmaceutical product. Especially measuring the kinetics of the reaction are often more complex and time-consuming, compared to physical properties and other chemical properties. Thus, the reactor selection methodology presented here is divided into two parts. The first part works without exact kinetic information. In the second part, reaction kinetics data are used to deeply analyze the pieces of equipment being preselected in the first part.

Table 1. Stepwise methodology to preselect standardized technical plug flow reactor systems from a database.

Level of Detail	Technical Criterion	Process Data Needed	Equipment Data Needed	Operation Data Available
no reaction kinetics required	presettings and prerequisites	reaction stoichiometry molar masses mass flow rate inlet composition inlet temperature required outlet pressure	database of existing and/or commercially available and/or promising new plug flow reactor systems	
	1. residence time *performance indicator*	allowable residence time interval reaction timescale A/B/C [20] mean density of reacting fluid	internal volume of the reactor	(adapted) volumetric flow rate mean residence time
	2. operating pressure *technical criterion*	mean viscosity of reacting fluid	hydraulic diameter channel length channel cross-section area pressure drop correlation	flow velocity Reynolds number pressure drop
	3. operating temperatures *technical criterion*	allowable temperature interval of reacting fluid mean heat capacity of reacting fluid mean heat conductivity of reacting fluid adiabatic temperature rise	Nusselt number correlation (internal heat transfer) external heat transfer estimation heat conductivity (wall material) wall thickness max./min. operating temperature	heat transmission coefficient characteristic temperature difference to heat transfer fluid (HTF)
reaction kinetics required	4. kinetics of mixing and reaction *technical criterion*	kinetic constant at reaction temperature reaction order		time constant of mixing time constant of reaction
	5. safety and hotspot formation *technical criterion*	pre-exponential factor (Arrhenius) energy of activation		safety margin to runaway regime concentration and temperature profile in reactor (hotspot temperature) conversion, yield

3.2. Reliability of Equipment Data

From the equipment point of view, basic information about all mentioned areas (geometries, operation limits, important transport correlations) has to be available to include a reactor system into the database and to consider its application in the MCSP. The reliability of these data depends on the way it was gained. Geometry information taken from detailed mechanical drawings of the reactor or empirical correlations fitted to experimental data will be more accurate than rough assumptions based on catalogues of the equipment manufacturers or literature correlations being suitable for similar channel geometries.

Thus, the reactor systems being implemented in the equipment database use datasets of diverse reliability. The comparison of the results of different reactor systems has to be executed with appropriate caution. A demand for simple, but reliable and experimentally validated, operating correlations (pressure drop, heat transfer and mixing behavior) for predefined reactor equipment can be stated. One the one hand, that information can be gained from operational experience, using the equipment in an MCSP. On the other hand, an intensified cooperation of equipment manufactures and equipment operators is needed.

3.3. Stepwise Reactor Selection Methodology

The methodology of selecting technically suited, predefined plug flow reactor equipment from a database will be described in more detail in the following. An overview about the stepwise procedure is presented in Table 1. Each step requires more data of the particular process and of the predefined equipment. Due to the fact that process data has to be gained during process development (see Chapter 3.1), the order of selection steps is adjusted to an increasing demand of process data and to its expected availability during the approaching process development project. If, e.g., viscosity and heat capacity data of the reacting fluid is unavailable for a new process in an early stage of the process development, suitable reactor setups can already be preselected from the equipment database, based on throughput and mean residence time only.

Before utilizing the reactor selection methodology, a reactor database and basic information about the feed stream to the reactor have to be provided (see Table 1, presettings and prerequisites). The computer-aided execution of the reactor selection methodology allows for the simultaneous analysis of multiple reactor systems. Exclusion of reactor systems due to technical reasons is the main focus of each step of the reactor selection methodology. In addition, further operation data (e.g., flow velocity, Reynolds number, heat transmission coefficient) is gained for every reactor being analyzed (see Table 1).

3.3.1. Step 1: Residence Time (Performance Indicator)

Residence time is an important factor to successfully perform a chemical reaction. In case of insufficient time for the reaction progress (residence time), the conversion/yield will be less than expected. This is often undesired, according to the productivity of the process. In addition, it can cause safety issues if unconverted reagents leave the reactor and react uncontrolled in a downstream part of the process [21]. Excessive residence time can promote undesired slow side/subsequent

reactions, too. In contrast to batch operations, where the operating time is a degree of freedom to control the progress of reaction (conversion), the mean residence time of each plug flow reactor, i, is defined by the volumetric flow rate and the active volume of the certain reactor, i (Equation (1)).

$$\tau_i = \frac{V_i}{\dot{V}_{design}} \tag{1}$$

In order to decide whether a predefined reactor system, i, from the database is suitable for the process or not, the mean residence time of the reactor has to fit in the space of an interval of allowable minimal/maximal residence time of the process (Equation (2)).

$$\tau_{min} \leq \tau_i \leq \tau_{max} \tag{2}$$

In the early steps of process development, the allowable interval can be estimated utilizing semi-quantitative experience from the laboratory, e.g., analyzing the outlet compositions of continuously run experiments at different flow rates or analyzing concentration profiles from batch experiments at a defined reaction temperature. Later on, the chosen interval can be validated using reaction kinetics to simulate the concentration profile in the technical reactor. This residence time interval indicates no technical operating limitation of the reactor, but a window in which the reaction is desired to be operated. Reactor systems missing the residence time interval narrowly should not be excluded directly. If the process flow rate is variable within some percent $\pm f$, the flow rate of those reactors can be adapted (Equation (3)).

$$\dot{V}_i = \begin{cases} \frac{V_i}{\tau_{min}}, & \tau_i < \tau_{min} \ \wedge \ \frac{V_i}{\tau_{min}} \geq \dot{V}_{design}(100\% - f) \\ \frac{V_i}{\tau_{max}}, & \tau_i > \tau_{max} \ \wedge \ \frac{V_i}{\tau_{max}} \leq \dot{V}_{design}(100\% + f) \end{cases} \tag{3}$$

If an adaption of the flow rate is not feasible for a certain reactor system, it will be excluded and not further investigated henceforth.

3.3.2. Step 2: Operating Pressure (Technical Criterion)

The highest pressure in a liquid-phase plug flow reactor is expected at the inlet (Equation (4)), whereas the outlet pressure (reaction pressure p_R) is defined by the laboratory development. It can be elevated from atmospheric pressure, e.g., to suppress the vaporization/desorption of one or more components from the reacting fluid.

$$p_{in,i} = p_R + \Delta p_i \tag{4}$$

The pressure drop depends on the particular reactor system (channel geometry, volumetric flow rate) and the properties of the reacting fluid (density, viscosity). It has to be estimated by suitable pressure drop correlations, which have to be present in the reactor database. The inlet pressure has to be compared to the allowable maximal pressure inside the complete reactor module, which is defined by the particular reactor itself, fittings, piping, gaskets, instruments or the pumping systems available in the reactor module (Equation (5)). It must not be violated.

$$p_{in,i} < \min\left(p_{max,1}, \dots, p_{max,n}\right)_i \tag{5}$$

3.3.3. Step 3: Operating Temperatures (Technical Criterion)

Temperature management is a key issue for processing chemical reactions at a technical scale. This paper is focused on reactors being cooled or heated fluidically. Allowable minimal and maximal temperatures of the reacting fluid (e.g., freezing point, boiling point, decomposition temperature) and of the equipment (e.g., of reactor, fittings, piping, gaskets, instruments) can be defined. These limits must not be violated either by the temperature of the reacting fluid or by the temperature of the heat transfer fluid (HTF). The heat transfer coefficient describing the internal heat transfer from the reacting fluid to the wall can be calculated by suitable Nusselt number correlations for each reactor, which have to be present in the reactor database. Often, the contributions of conduction through the wall material and of the heat transfer from the wall to the HTF cannot be calculated exactly. The contributions can be either neglected (assuming good conduction and heat transfer to the HTF), or an assumption is made that the contributions to heat conduction and external heat transfer are a multiple, $C_{R_{th},i}$, of the internal heat transfer resistance (Equation (6)) [17].

$$\frac{1}{k_{h,i}} = \frac{1}{\alpha_{i,i}} + R_{th,i} = \frac{1 + C_{R_{th},i}}{\alpha_{i,i}} \tag{6}$$

A simplified black-box energy balancing model has been developed in order to compare the heat transfer abilities of different reactors. The flow conditions being defined before and the specific surface area of each reactor are included in the model. The model copes without a mathematical description of the reaction kinetics, but uses information about the heat of the reaction, respectively the adiabatic temperature rise that is accessible by reaction calorimetry. The aim of the black-box model is to calculate a characteristic temperature difference to the HTF at which the total heat of the reaction (complete conversion assumed) can be transferred to the HTF (Equation (7)).

Therefore, the outlet temperature of the reactor will be equal to its inlet temperature. The temperature of the heat transfer medium is assumed to be constant along the reactor.

$$k_{h,i} a_i V_i \Delta T_{HTF,i} = c_{A,in} \dot{V}_i (-\Delta H_R) \qquad \boldsymbol{\Delta T_{HTF,i}} = \boldsymbol{T_R - T_{HTF,i}} = \frac{\boldsymbol{(-\Delta H_R)}}{\boldsymbol{\overline{\rho}\,\overline{c}_p \Delta T_{ad}}} \tag{7}$$

The process temperatures, T_R and $T_{HTF,i}$, can be compared to the temperature limits being defined before, to decide whether the reactor is technically suitable or not (Equation (8), technical criterion).

$$\begin{aligned} \max\left(T_R, T_{HTF,i}\right) &< \min\left(T_{max,1}, \dots, T_{max,n}\right)_i \\ \min\left(T_R, T_{HTF,i}\right) &> \max\left(T_{min,1}, \dots, T_{min,n}\right)_i \end{aligned} \tag{8}$$

In addition, the reactor enabling the lowest characteristic temperature difference according to amount $\left|\Delta T_{HTF,i}\right|$ is most suitable with respect to heat transfer. Thereby, technically suitable reactors can be compared to each other (performance indicator).

3.3.4. Step 4: Kinetics of Mixing and Reaction (Technical Criterion)

In technical systems, sufficient mixing of the reactants has to be ensured by the reactor system itself or by a mixing unit connected upstream of or within the residence time channel. In order to roughly check the mixing properties of the different reactor systems at chosen operation conditions, a short-cut method based on characteristic time scales is applied to the reactor selection method. From this step on, information about the reaction kinetics is necessary.

Therefore, the characteristic time constant of the reaction (Equation (9)) has to be compared to the characteristic time constant of micromixing by engulfment (Equation (10)), which is dominating in a small-scale channel flow [22]. The time constant of the reaction is equal to the reaction half-life in the case of a second order reaction. The time constant of micromixing depends on the mean kinematic viscosity of the reacting fluid and on the energy dissipation rate of the reactor, which can be calculated by means of the pressure drop (Equation (11)).

$$t_R = \frac{1}{k(T_R) \cdot c_{A0}^{m-1}} \tag{9}$$

$$t_{E,i} = \frac{1}{0{,}058}\left(\frac{\bar{\nu}}{\epsilon_i}\right)^{1/2} \tag{10}$$

$$\epsilon_i = \frac{\Delta p_i \dot{V}_i}{\bar{\rho} V_i} \tag{11}$$

Comparing these two characteristic time constants to the mean residence time of the reactor (see Step 1), two different regimes can be distinguished:

- a reaction-dominated regime ($t_{E,i} < t_R < \tau_i$)
- a mixing-dominated regime ($t_R < t_{E,i} < \tau_i$)

In both cases, the dominating phenomenon proceeds faster than the mean residence time of the reactor. Thus, sufficient progress of the reaction at the reactor outlet can be assumed. In the case the residence time is shorter than the characteristic time constant of the reaction ($\tau_i \leq t_R$), the lower boundary, τ_{min}, of the residence time interval (see Step 1) should be revised. If the process is dominated by mixing ($t_R < t_{E,i}$), but the mixing will not be completed in the reactor ($\tau_i < t_{E,i}$), it can be advantageous to implement a mixing unit upstream of the reactor. This decision on the case is regarded as a ‘technical criterion’.

Moreover, controlling the residence time distribution (RTD) behavior of a continuous technical plug flow reactor is of high importance. A majority of reactions generally benefits from a well-defined and narrow RTD. A high local reactant concentration level is favored to accelerate the reaction kinetics and to suppress side/subsequent reactions. Exceptions (e.g., autocatalytic reactions) are described in Levenspiel’s textbook [19]. Modern flow reactors are designed to provide intensified radial mixing, resulting in a concentration profile close to ideal plug flow behavior, even in the laminar flow regime. This is often achieved by the milli- or even micro-structured channel geometries (short diffusion lengths) and can be further optimized by the curved channel flow (Dean vortices) or split-and-recombine techniques, like static mixers.

Above all, it appears difficult to quantitatively predict the plug flow behavior of most technical reactor systems, taking the geometries, fluid properties and process flow rate into account. Elaborate experimental characterization or CFD flow simulation for each reactor system would be necessary to create short-cut models, being comparable to the model of Taylor and Aris [23,24] for straight pipe flow, to estimate the Bodenstein number of modern flow reactors. Therefore, the approach presented in this paper roughly assumes that the RTD of the analyzed reactors is sufficiently close to the ideal plug flow. Defining a standardized methodology to estimate the RTD of various technical reactor systems and their combinations in an MCSP will be a challenging goal for future research.

3.3.5. Step 5: Safety and Hotspot Formation (Technical Criterion)

In the last step of the reactor selection methodology, the mathematical description of the reaction kinetics is used to evaluate the dynamic heat release/heat demand of the reaction. This step is important, especially for highly exothermal reactions, which might cause a safety issue, due to a reaction runaway. Additionally, decomposition of one or more components of the reacting fluid or undesired reactions might occur if elevated temperatures appear at the hotspot in the reactor.

Two methods are implemented in this step of the methodology. Firstly, a safety screening by the use of the short-cut criterion developed by Barkelew for the zeroth-order reaction and extended by Renken for positive order reactions [25]. Thus, unsafe reactor setups can be eliminated before a simulation of the axial concentration and temperature profiles is carried out to calculate the output conversion and the hotspot temperature of the reactor. The inlet temperature and the temperature of the heat transfer medium is set to the value of T_R for both calculation steps.

For applying the Barkelew-Renken (BR) criterion (Equation (12)), the energy of activation of the reaction is used to calculate the heat production potential of the reaction (Equation (13)). By the characteristic time constant of the reaction (Equation (9)) and the characteristic time constant of cooling (Equation (14)), the cooling intensity can be defined (Equation (15)). The constant, b, depends to the reaction order and was defined by means of numeric analysis [25].

$$\frac{N_i}{S'} \geq \exp(1) - \frac{b}{\sqrt{S'}} \tag{12}$$

$$S' = \Delta T_{ad} \frac{E_a}{R(T_R + 273{,}15\ K)^2} \tag{13}$$

$$t_{c,i} = \frac{\bar{\rho}\bar{c}_p}{k_{h,i} a_i V_i} \tag{14}$$

$$N_i = \frac{t_R}{t_{c,i}} \tag{15}$$

In the case of violating the BR criterion, the reactor operates in a window of parametric sensitivity. Small deviations in reaction temperature lead to a strong increase of the hotspot temperature in the reactor or even to a complete runaway of the reaction. Thus, reactor systems violating the BR criterion will be excluded from the list of technically able reactor systems (technical criterion).

The resulting technically applicable reactor systems will be simulated by a simplified axial reactor model. Therefore, the balances for all components, j (Equation (16)), and the coupled energy balance (Equation (17)) of each reactor system, i, have to be solved numerically. Ideal plug flow behavior in the reactors is assumed for the differential modelling.

$$\frac{\partial c_{j,i}}{\partial z} = \frac{1}{\bar{u}_i}\left[\sum_r \upsilon_{j,r} r_{r,i}\left(T_i, c_{1,i}, \dots\right)\right] \qquad (16)$$

$$c_{j,i}(z=0) = c_{j,in,i}$$

$$\frac{\partial T_i}{\partial z} = \frac{1}{\bar{\rho}\bar{c}_p\bar{u}_i}\left[-k_{h,i}a_i(T_i - T_R) + \sum_r (\Delta H_r) r_{r,i}\left(T_i, c_{1,i}, \dots\right)\right] \qquad (17)$$

$$T_i(z=0) = T_R$$

From the resulting axial temperature profile, the hotspot temperature, $T_{HS,i}$, can be derived. This temperature can be significantly higher than the temperatures regarded in Step 3 using the black-box model. Thus, the criterion of Step 3 has to be adapted and checked again (Equation (18), technical criterion).

$$T_{HS,i} < \min\left(T_{max,1}, \dots, T_{max,n}\right)_i \qquad (18)$$

As a result, the simulation conversion and yield at the reactor outlet can be gained. Based on this information, promising reactors can be compared and further optimized.

3.4. Scale-Up and Numbering-Up Concepts

As mentioned above, some commercially available reactor systems have system-inherent numbering-up concepts available. Even if the geometries (volume) of a pre-defined reactor element are fixed, parallel and/or in series, the interconnection of multiple reactor elements is an opportunity to increase the volume/residence time and the free cross-section area of the reactor system, being passed through by the reacting fluid flow. Thus, the interconnection of multiple equal reactor elements represents a degree of freedom for designing the reactor concept for the particular process, considering predefined equipment.

To consider interconnection concepts in the reactor selection methodology presented above, an interconnection matrix is automatically gained for each reactor system in the reactor database (Figure 2). Database information about the available, single reactor elements correspond, e.g., to the number of reactor elements in stock and ready for use, or to the number of reactors fitting into a basic reactor module, due to the outer dimensions of the main apparatus. These database entries can be individually adapted to the particular project. Parallel interconnection can be prohibited from the beginning, e.g., if maldistribution [26] is an issue.

Figure 2. Interconnection matrix for different reactor systems exemplarily having five single reactor elements available.

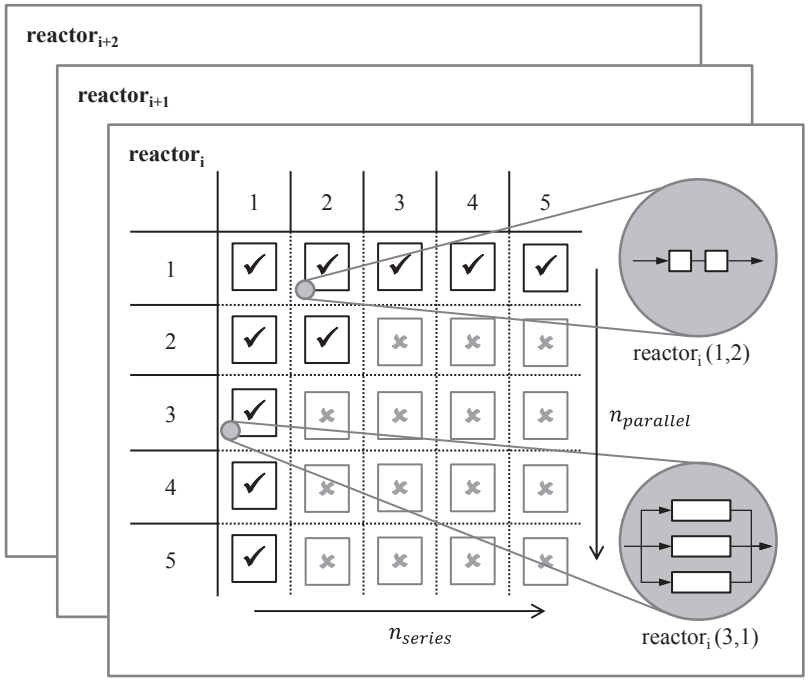

Each valid entry in the interconnection matrix represents one possible interconnection of reactor elements, which has to be analyzed by the criteria described above. Thereby, the most promising setup of each reactor system can be identified.

System-inherent scale-up concepts, like reactor systems of different scales (lab, pilot, production scale; see Chapter 2.1), can be regarded by the selection methodology, too. To do so, a database entry has to be implemented for every scale of the reactor system.

4. Application Example: Reactor Selection Methodology

In order to demonstrate the stepwise approach of the presented reactor selection methodology, a simplified example based on a well-known reaction from the literature—synthesis of the ionic liquid (IL), ethylmethylimidazole ethyl sulfate [EMIM][EtSO4] (Figure 3) [27,28]—will be presented in the following chapter. The reactor technology for this reaction has already been intensively investigated and optimized [29,30]. In this chapter, the presented methodology will be used to select a promising setup of predefined reactors, being comparable to the optimized and experimentally validated reactor concepts from literature.

Figure 3. Alkylation of 1-methylimidazol (MIM) with diethyl sulfate (DES) to ethylmethylimidazole ethyl sulfate ([EMIM][EtSO4]) [28].

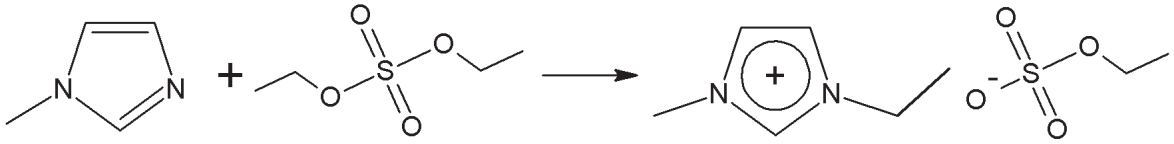

ILs are organic salts with a low melting point and, thus, are often liquid at room temperature. They are known as innovative solvents with beneficial attributes (negligible vapor pressure, designable molecule structure) over conventional solvents and are thus promising for use in chemical processes [31]. For this example, an MCSP process will be assumed, using [EMIM][$EtSO_4$] as a solvent for a reaction step. In continuous operation (24/7), a leaching of the IL takes place, and thus, an amount of 300 g/h of IL has to be provided to restore the losses. A continuous synthesis of the [EMIM][$EtSO_4$] inside the MCSP shall be investigated, designing the reactor with existing, predefined equipment.

The synthesis reaction of [EMIM][$EtSO_4$] is a highly exothermal ($\Delta T_{ad} \approx 165.4$ °C) and fast reaction. The reaction half-life of the pseudo-second order reaction (*i.e.*, first order for both reactants) represents $t_R = 20\,min$ at a reaction temperature of $T_R = 20\,°C$ and $t_R = 3\,min$ at a reaction temperature of $T_R = 35\,°C$ [28]. Thus, the reaction can be categorized as a Type B/C reaction, according to the nomenclature established by Roberge *et al*. [20], and thus, the heat of the reaction will be released fast. In order to achieve the desired product quality, the temperature of the reacting fluid has to be kept below 100 °C [28]. The reactants are sensitive to water and cannot be diluted with other solvents, so the reaction is carried out in the bulk phase [32].

For this example, four different reactor systems will be considered: helically coiled, tubular reactors (CT) made of standard tubing with 3, 6 and 8 mm outer diameters and an SMX-type static mixer reactor (SMX) with an 8-mm outer diameter (Table 2). For design parameters, which could not be estimated from the literature, adequate assumptions (*, Table 2) were made. For demonstration purposes, the described devices only represent a small fraction of reactors available in the database. Intensive mixers, continuous stirred-tank reactor or plate reactors, are not presented here.

Each element of the CT provides a tube length of 4.75 m and consists of 15 coils (0.1 m coil diameter) and a straight inlet/outlet tube of a 2 cm length (Figure 4, Table 2). Due to the centrifugal forces developing in the coils at Dean numbers ≥5 [33], a secondary flow pattern is fully established, leading to increased radial mixing and, thus, to an improved plug flow [34]. Each SMX reactor element provides a length of 1.5 m in a straight tube (Table 2). The structured packing of the SMX static mixer intensively increases radial mixing (plug flow) and heat transfer compared to an empty tube [35,36].

Five elements of each reactor system are assumed to be in stock and can be used for a fast construction of the reactor module. A flow micromixer will be implemented in any case, initially mixing the reactants before entering the CT or SMX reactor, as proposed by Renken *et al*. [29] for this reaction (Figure 5). The residence time of the micromixer is assumed to be less than one second, so the reaction inside the micromixer will be neglected.

The process presettings and constraints (Table 3) being provided by the conceptual process design and the laboratory development and the physical/chemical properties of the reacting system are taken from the literature [28,42,43]. All physical properties of the reacting fluid were assumed to be constant at temperature T_R. Adequate assumptions (*, Table 3) according to the actual operating conditions (throughput, temperature pressure) were made.

Table 2. Simplified reactor database for coiled tube (CT) and static mixer reactors (SMX) (* assumption for demonstration purpose).

Data Type	Symbol	Unit	CT3	CT6	CT8	SMX8	Comments/Source
geometries	d_a	mm	3.0	6.0	8.0	8.0	
	d_i	mm	1.4	4.4	6.0	6.0	standard tubing
	s	mm	0.8	0.8	1.0	1.0	
	L_0	m	4.75	4.75	4.75	1.50	*
	ε	-	1.00	1.00	1.00	0.67	only SMX [37]
	D_{coil}	mm	100.0	100.0	100.0	-	*
	h_{coil}	mm	6.0	12.0	16.0	-	*, $h_{coil} = 2d_a$
	d_h	mm	1.4	4.4	6.0	1.5	CT: $d_h = d_i$, SMX: $d_h = 0{,}25\ d_i$ [38]
	$A_{free,0}$	mm²	1.54	15.2	28.3	18.9	$A_{free,0} = \frac{\pi}{4} d_i^2 L_0 \varepsilon_p$
	V_0	ml	7.3	72.2	134.3	28.4	$V_0 = A_{free,0} L_0$
	a	$m^2 \cdot m^{-3}$	2861	909	667	996	$a = \pi d_i L_0 / V_0$
allowed operation conditions	p_{min}	barg	−1	−1	−1	−1	*
	p_{max}	barg	670	310	310	310	standard tubing
	T_{min}	°C	−20	−20	−20	−20	*
	T_{max}	°C	200	200	200	200	*
correlations	$\zeta(Re)$	-		[39]		[38]	
	$Nu(Re, Pr)$	-		[40]		[41]	

Figure 4. Helically coiled tubular reactor (**CT6**).

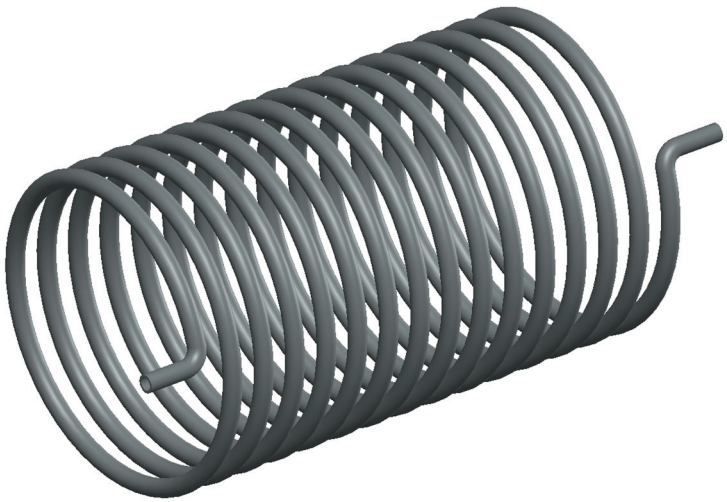

Figure 5. Flowsheet of the example process plant: micromixer to initially mix the reactants; **CT** or **SMX** reactor for the main conversion.

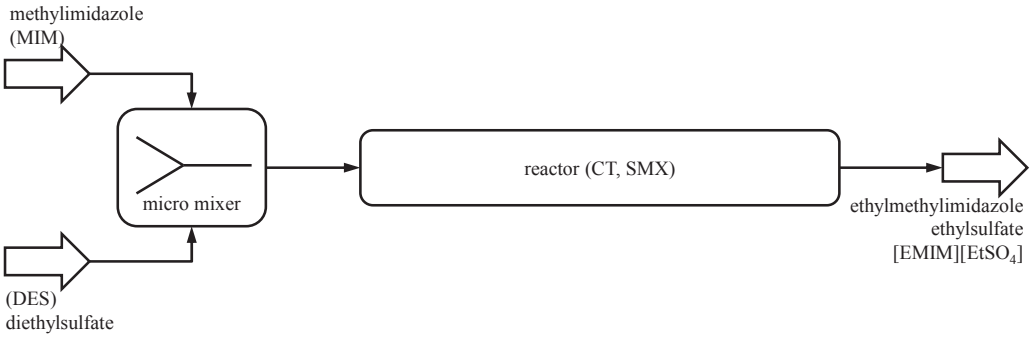

Table 3. Presettings and constraints (* assumption for demonstration purpose).

Symbol	Unit	Value	Comments/Source
$\dot{m}$	kg·h^{-1}	0.30	*, ~4.6 mL·min^{-1}
$\pm f$	%	5	*
c_{MIM}	mol·L^{-1}	4.80	[28]
c_{DES}	mol·L^{-1}	4.73	[28]
T_R	°C	24	*, adapted to experimental data [28]
T_{min}	°C	−6	crystallization of MIM [44]
T_{max}	°C	100	undesired thermal decomposition of the IL [28]
p_R	barg	0	*
τ_{design}	min	38	[28]
τ_{min}	min	30	*, conversion too low below
τ_{max}	min	→ ∞	*, high residence times needed to reach ambient conversion (second-order reaction), no long-term side/subsequent reactions known
X_{design}	%	→100	*

In order to calculate the heat transmission coefficients, contributions to external heat transfer were neglected for all reactor systems. The heat conductivity of the wall material was set to 15 W m^{-1}·K^{-1}, being adequate for high quality steel tubing.

Based on these data and assumptions, a complete pass through the reactor selection methodology and a simple by-hand optimization, utilizing the computer-aided execution of the reactor selection methodology, will be presented in the following.

4.1. Example: Step 1, Residence Time (Performance Indicator)

The residence time criterion (see Chapter 3.3.1) is checked for all reactor systems and their respective setups. All setups of the **CT3** reactor system provide less residence time than required. The maximal residence time provided by the setups using five elements in series or in parallel

interconnection represents 8 min, which is significantly lower than τ_{min} (Table 3). Therefore, **CT3** will be excluded completely from the following selection steps.

The coiled tube reactor systems with larger diameters—**CT6** and **CT8**—provide more residence time and are feasible according to the residence time criterion in the majority, except the respective single element setups (Table 4 and Table 5). In the case of **CT6**, the single element setup (1,1) has to be excluded. The flow rate of the setup, **CT8** (1,1), has to be reduced according to Equation (3), to reach τ_{min}.

Table 4. Results for CT6 after residence time criterion.

Symbol	Unit	(1,1)	(1,2)	(1,3)	(1,4)	(1,5)	(2,1)	(2,2)	(3,1)	(4,1)	(5,1)
$\dot{V}_{CT6}(n_p, n_s)$	mL·min^{-1}	4.6	4.6	4.6	4.6	4.6	4.6	4.6	4.6	4.6	4.6
$\tau_{CT6}(n_p, n_s)$	min	16	32	48	64	80	32	64	48	64	80
feasibility		×	✓	✓	✓	✓	✓	✓	✓	✓	✓

Table 5. Results for CT8 after residence time criterion.

Symbol	Unit	(1,1)	(1,2)	(1,3)	(1,4)	(1,5)	(2,1)	(2,2)	(3,1)	(4,1)	(5,1)
$\dot{V}_{CT8}(n_p, n_s)$	mL·min^{-1}	4.5	4.6	4.6	4.6	4.6	4.6	4.6	4.6	4.6	4.6
$\tau_{CT8}(n_p, n_s)$	min	30	59	89	118	148	59	118	89	118	148
feasibility		✓	✓	✓	✓	✓	✓	✓	✓	✓	✓

The volume of one **SMX8** element is much lower compared to **CT8** and **CT6**, due to the porosity of the static mixer and the shorter tube length. Thus, only the largest setups, **SMX8** (1,5) and **SMX8** (5,1), provide enough residence time. All other setups will be excluded from the following steps of the reactor selection methodology (Table 6).

Table 6. Results for SMX8 after the residence time criterion.

Symbol	Unit	(1,1)	(1,2)	(1,3)	(1,4)	(1,5)	(2,1)	(2,2)	(3,1)	(4,1)	(5,1)
$\dot{V}_{SMX8}(n_p, n_s)$	mL·min^{-1}	4.6	4.6	4.6	4.6	4.6	4.6	4.6	4.6	4.6	4.6
$\tau_{SMX8}(n_p, n_s)$	min	6	13	19	25	31	13	25	19	25	31
feasibility		×	×	×	×	✓	×	×	×	×	✓

4.2. Example: Step 2, Operating Pressure (Technical Criterion)

The low volumetric flow rate of 4.6 mL·min^{-1} leads to low flow velocities and corresponding Reynolds numbers in the channels of the remaining reactor setup. Combined with a moderate dynamic viscosity of about 0.1 Pa·s of the reacting fluid [42], the pressure drop in all remaining reactor setups is below 1 bar. Thus, safety issues due to high pressure or difficulties operating the reactor systems with standardized pumps of the MCSP reactor module are not expected here. All setups remain feasible according to this step.

The pressure drop in the **CT6** setups ranges from 12–218 mbar, corresponding to flow velocities of 1.0–5.0 mm·s^{-1} and Reynolds numbers of 0.05–0.24. In the **CT8** setups, the pressure drop

ranges from 4–64 mbar, corresponding to flow velocities of 0.5–2.7 mm·s^{-1} and Reynolds numbers of 0.03–0.17. The pressure drop in the **SMX8** setups ranges from 27–683 mbar, corresponding to flow velocities of 0.8–4.0 mm·s^{-1} and static mixer Reynolds numbers [38] of 0.01–0.06.

4.3. Example: Step 3, Operating Temperatures (Technical Criterion)

The adiabatic temperature rise of the reaction is high, but the heat transfer abilities of all remaining reactor setups appear to be sufficient to remove the heat of the reaction according to the simplified black-box model (Equation (7)). All reactor systems provide high specific surface areas and can, therefore, achieve ambient heat transfer rates, although the flow regime in the channels is laminar, and the resulting heat transfer coefficients appear quiet low. Comparing all setups using five elements, the setups (1,5) show superior heat transfer abilities over the respective setup (5,1), due to the higher flow velocity/Reynolds number and resulting heat transfer coefficient in the single channel setup. This results in a lower necessary characteristic temperature difference to the HTF for the setup (1,5) compared to setup (5,1) (Table 7).

Table 7. Heat transfer area, heat transmission coefficients and characteristic temperature differences to the heat transfer fluid (HTF) for the selected setups.

Symbol	Value	CT6 (1,5)	CT6 (5,1)	CT8 (1,5)	CT8 (5,1)	SMX8 (1,5)	SMX8 (5,1)
$a_i V$	m^2	0.33		0.45		0.14	
k_h	W·m^{-2}·K^{-1}	168	158	121	115	363	364
ΔT_{HTM}	K	0.8	3.5	0.7	3.5	0.7	4.8

In the case of a process development project, where a mathematical description of the reaction kinetics is not available in the early state of the project, the setups **CT6** (1,5), **CT8** (1,5) and **SMX8** (1,5) are most promising for the temperature sensitive IL synthesis reaction, due to their superior heat transfer abilities and high residence time compared to other setups and because of their technical feasibility compared to the **CT3** reactor system (Chapter 4.1). Thus, experimental validation should focus on these preselected reactor systems.

4.4. Example: Step 4, Kinetics of Mixing and Reaction (Technical Criterion)

The IL synthesis reaction was characterized as a Type B/C reaction (see Chapter 4.) due to the characteristic timescale of the reaction. Thus, the reaction progress will be dominated by the intrinsic reaction kinetics. Assuming sufficient initial mixing of the reactants by use of the micromixer connected upstream of the residence time channels (Figure 5), mixing in the reactors needs not to be investigated in more detail and is therefore neglected here.

4.5. Example: Step 5, Safety and Hotspot Formation (Technical Criterion)

Controlling the temperature profile inside the reactor is most challenging, producing [EMIM][EtSO$_4$]. The reaction rate is fast enough that the dynamic heat release can accelerate the reaction kinetics significantly. This can lead to a distinct hotspot formation, ending up in a

complete runaway of the reaction, where an almost adiabatic temperature rise might occur. Temperatures over 100 °C lead to a degraded product quality.

The dynamic heat release is investigated by the BR criterion (Equation (12)). The results for single channel setups (Figure 6) show that **CT8** operates in the region of parametric sensitivity at $T_R = 24\,°C$ and has to be excluded. The operation of **CT6** and **SMX8** is safe according to the BR criterion. Parallel channel setups show a worse stability behavior, compared to the single channel setups, due to their lower heat transmission coefficients (Table 7). Nonetheless, all remaining setups of **CT6** and **SMX8** can be operated safely according to the BR criterion.

Figure 6. Stability analysis of the [EMIM][EtSO4] synthesis according to the Barkelew–Renken (BR) approach. Unstable operation (•) and stable operation (∘) at $T_R = 24\,°C$, for reactor setups $(1,n_s)$ of **CT6** (——), **CT8** (– –) and **SMX8** (-----) and BR stability (····).

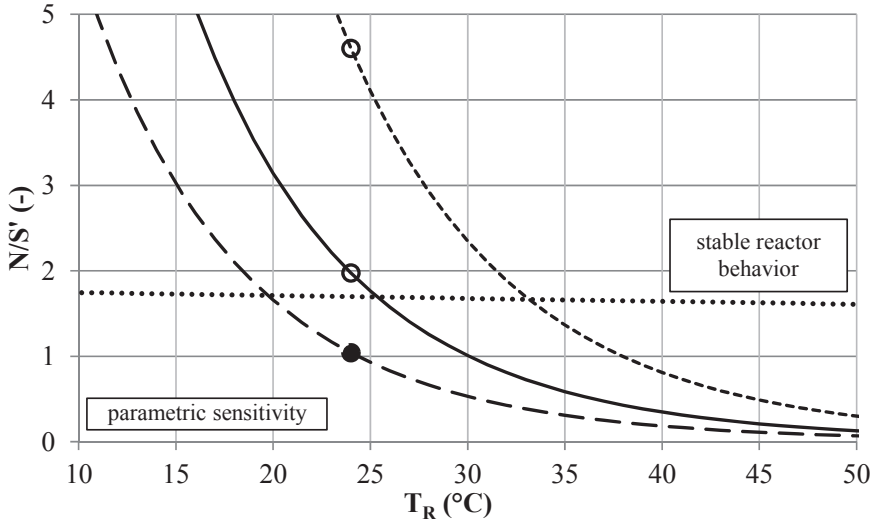

Finally, the reactor simulation (Equations (16) and (17)) is carried out for all remaining setups. The resulting yields of [EMIM][EtSO4] and the hotspot temperatures are presented in Table 8 for the **CT6** and in Table 9 for the **SMX8** reactor systems.

Table 8. Results for CT6 after reactor simulation.

Symbol	Unit	(1,2)	(1,3)	(1,4)	(1,5)	(2,1)	(2,2)	(3,1)	(4,1)	(5,1)
$T_{HS,CT6}$	°C	31.0	31.0	31.0	31.0	31.5	31.5	31.7	31.9	32.0
$Y_{[EMIM][EtSO_4],CT6}$	%	76.2	82.3	85.9	88.3	76.4	86.0	82.4	86.0	88.4
overall feasibility		✓	✓	✓	✓	✓	✓	✓	✓	✓

Table 9. Results for SMX8 after reactor simulation.

Symbol	Unit	(1,5)	(5,1)
$T_{HS,SMX8}$	°C	26.1	27.1
$Y_{[EMIM][EtSO_4],SMX8}$	%	73.9	74.5
overall feasibility		✓	✓

Comparing setups with equal numbers of reactor elements (equal residence time), the resulting yields of the single-channel setups are marginally lower than the yields of multi-channel setups. This is also a result of the lower heat transfer abilities of the multi-channel setups. The hotspot temperature is slightly higher and, therefore, the reaction kinetic is more accelerated in the hotspot region. For a technical realization, the single channel setups will be favored compared to multi-channel designs, due to their higher thermal stability and due to a generally lower tending to maldistribution and blocking effects in long-term operation [26]. Thus, **CT6** (1,5) and **SMX8** (1,5) appear most promising according to this first analysis utilizing the reactor selection methodology. Temperature and yield profiles of both setups are presented in Figure 7. The **SMX8** (1,5) shows a significantly lower hotspot temperature (safer operation), but a limited residence time, resulting from the limited number of reactor elements. Therefore, **CT6** (1,5) achieves a higher yield.

Figure 7. Simulated axial yield of [EMIM]EtSO4] for $T_R = 24$ °C in reactor setups **CT6** (1,5) (∘) and **SMX8** (1,5) (×) and corresponding temperature profile in reactor setups **CT6** (1,5) (•) and **SMX8** (1,5) (■).

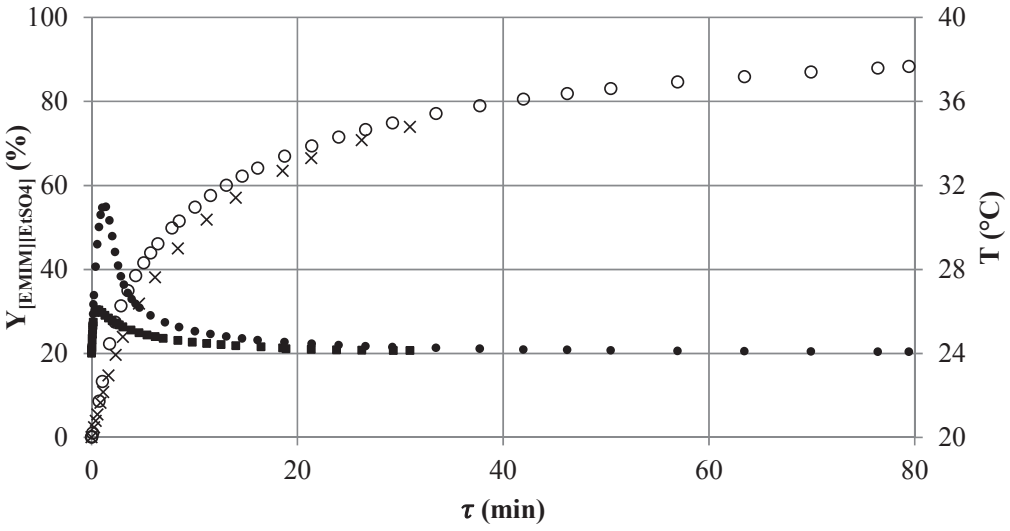

4.6. Optimization Study

Although the most promising setups were identified by the first run of the reactor selection methodology, the attained results are not satisfying. Both setups reach [EMIM][EtSO4] yields of less than 90%. Therefore, more than 10% of the unreacted educts leave the reactors.

Behind the hotspot, the reaction rate (slope of the yield profile) significantly decreases, due to the strong concentration dependence of the second order reaction, and a high additional residence

time is needed to further increase the conversion and yield. Three elements of the **SMX8** ($\tau_{SMX8\,(1,3)} = 19\,min$) are sufficient to reach a yield of 63% and to bring the temperature of the reacting fluid closely back to T_R. The outlet conditions of **SMX8** (1,3) can be used now for a second run of the reactor selection methodology at elevated temperature T_R to again an increase in the reaction rate. A stability analysis for the changed inlet conditions (Figure 8) assists the choosing of the reaction temperature of $T_R = 40$ °C.

Figure 8. Stability analysis of the [EMIM][$EtSO_4$] synthesis according to the BR approach. Unstable operation (•) and stable operation (∘) at $T_R = 40$ °C and initial conversion of 63.4%, for reactor setups **CT6** (——), **CT8** (– –) and **SMX8** (-----) and BR stability (····).

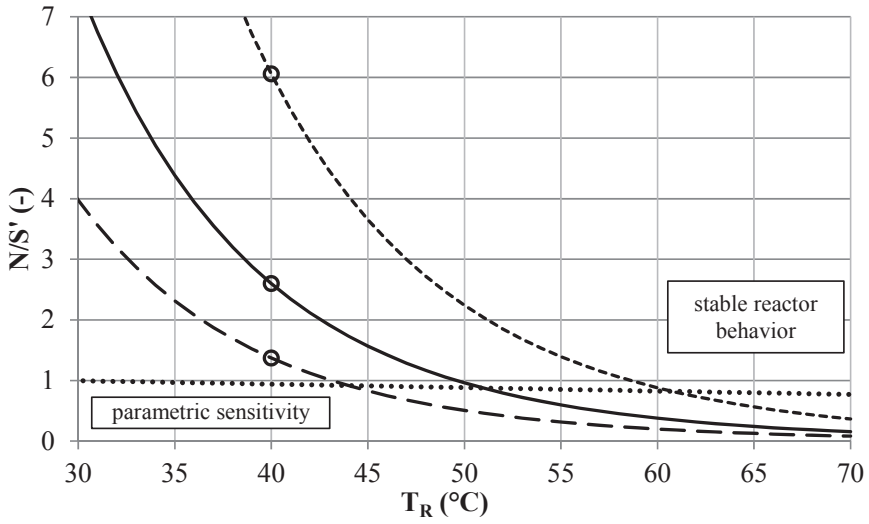

According to the second run of the reactor selection methodology, a **CT8** (1,2) setup is sufficient to reach a conversion of about 98% when being placed downstream of the **SMX8** (1,3) setup (Figure 9). The use of compact **CT** reactors might be favored over using straight tube **SMX** reactors in the MCSP environment, considering the space demand of the systems.

4.7. Conclusion to the Example

The presented reactor selection methodology provides a fast (short-cut) approach to quantitatively identify promising reactor concepts based on predefined available reactor systems in the early stages of process development. Remarkably, two of three reactor configurations that are most promising after Step 3 (low demand of data) remain favored after the whole procedure. Depending on the currently available data, the most promising setups after any step of the methodology can be preferentially used for experimental analysis, validation and/or optimization. Therefore, the reactor selection methodology contributes to the effective guiding and planning of the laboratory development and to the fastening of the whole process development of the MCSP processes. Furthermore, the model equations of the reactor selection methodology clearly define the demand of the data needed for an early start-up of the process development. Thus, missing information can be gained systematically.

Figure 9. Simulated axial yield profile of [EMIM][$EtSO_4$] in reactor setup **SMX**8 (1,3) (×) followed by **CT8** (1,2) (∘) connected in series and the corresponding temperature profile in the reactor setup **SMX** (1,3) (■) ($T_R = 24$ °C) followed by **CT8** (1,2) (•) ($T_R = 40$ °C).

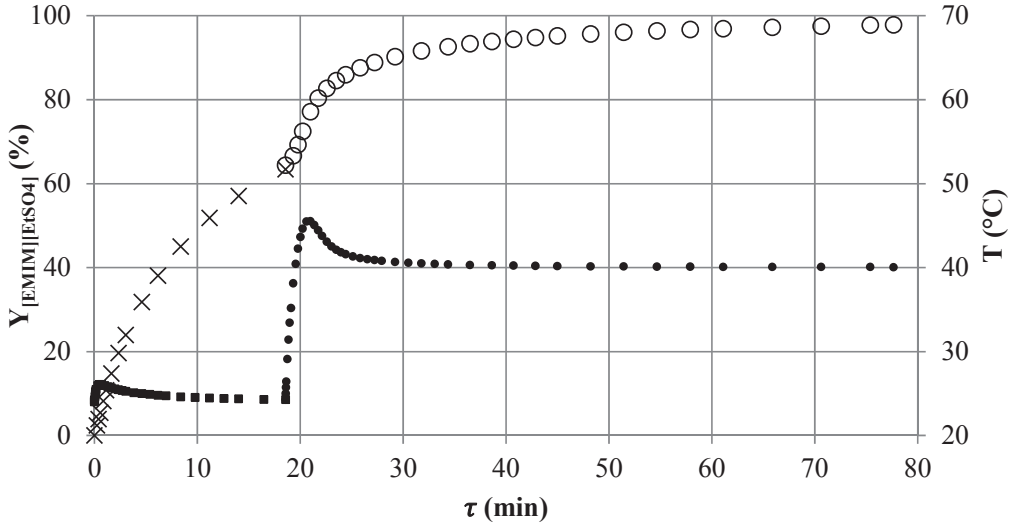

By computer-aided execution of the methodology, even a large number of different reactor systems/configurations can be screened in few minutes of computing. Therefore, a simple optimization study of the promising reactor systems can be carried out, resulting in a technically suitable setup. This setup will not be optimal by means of mathematical optimization, but might be technically sufficient, if a fast "time-to-process" and the use of predefined equipment is the key issue.

Alternatively, the results gained by the reactor selection methodology can be used as initial values/benchmark for more detailed mathematical optimization considering, e.g., multi-injection concepts [30] or, as mentioned before, for a systematical experimental validation.

5. Conclusions and Outlook

The modular approach of MCSP offers an opportunity for the quick realization and flexible design of future production plants. One key aspect is to establish a concept for the reuse of process and engineering knowledge throughout the process development chain and adjacent projects. The definition of reusable basic modules and associated documentation packages simplifies engineering and saves time during the construction phase. By using already tested and validated designs for the peripheral devices, as well as the predefined main apparatus, quick implementation in a production environment can be reached.

The scale-up of continuous processes into an MCSP requires a detailed calculation of all relevant physical and technical phenomena. This calculation process is significantly simplified using the presented computer-aided methodology for homogeneous liquid phase reactions and reactor systems. It allows fast and quantitative generation and rating of process alternatives based on predefined apparatuses. Once the needed process data are obtained, the generation of results can be realized within a few minutes. This is enabled by a database of quantitative calculation methods for each available apparatus, preserving the knowledge between different projects. Through a

five-step selection methodology, all infeasible apparatuses are rejected from the selection process, if technical process requirements cannot be fulfilled. The remaining reactor setups are characterized by several performance indicators to assist the further selection process. The stepwise calculation method can be used in the early process development phase, even if the necessary process dataset is incomplete.

Furthermore, the utilization of the tool already in laboratory development phase can help to identify critical scale-up parameters and essential lab data. The importance of each calculation step strongly depends on the dominating physical phenomena within the specific process. Based on datasets for equipment of different production capacities (lab, pilot, production) and different dominating phenomena (mixing intensity, heat transfer, residence time), suitable devices for lab investigations can be easily identified. This can lead to an effective planning and guiding of scale-up experiments and closes the usual gaps between lab and process development. After the successful selection of a preferred main apparatus and its configuration, the modular design of the MCSP enables the easy integration of the predefined equipment.

So far, the reactor selection tool only enables the selection of a reactor for one desired operation point. To further strengthen the methodology, an automated flexibility assessment for the equipment is developed to evaluate multiple possible operation points. By now, this can be archived via manual parameter variation (sensitivity analysis). Furthermore, detailed data (heat transfer, back mixing and pressure drop) are needed to quantify and reliably predict the performance, especially of process-intensified milli- or micro-structured equipment.

The presented computer-aided methodology is currently utilized to optimize existing and new MCSP processes for continuous operation at the INVITE research center in Leverkusen, Germany. Operational experience and measurement data from the investigated devices will be used to validate the database content. Further steps are to implement multiphase systems into the methodology and to elaborate a similar approach for downstream unit operations.

Acknowledgments

The research leading to these results has received funding from the European Community's Seventh Framework Programme FP7/2007–2013 under grant agreement no. 228867. The authors gratefully acknowledge the contributions of Christoph Fleischer and Bojan Brötz to the presented work.

Nomenclature

$\boldsymbol{a}$	specific surface area, $m^2 \cdot m^{-3}$
$\boldsymbol{A_{free}}$	free cross-sectional area, mm^2
$\boldsymbol{b}$	model parameter (BR), -
$\boldsymbol{c}$	concentration, $mol \cdot m^{-3}$
$\boldsymbol{\bar{c}_p}$	mean heat capacity of the reacting fluid, $J \cdot kg^{-1} \cdot K^{-1}$
$\boldsymbol{C_{R_{th}}}$	model parameter (heat transfer), -
$\boldsymbol{d_a}$	outer tube diameter, mm
$\boldsymbol{d_h}$	hydraulic diameter, mm

$\boldsymbol{d_i}$	inner tube diameter, mm
$\boldsymbol{D_{coil}}$	diameter of helically coiled tubing, mm
$\boldsymbol{f}$	flexibility in the process flow rate, %
$\boldsymbol{h_{coil}}$	pitch of helically coiled tubing, mm
$\boldsymbol{\Delta H_R}$	heat of reaction, $J \cdot mol^{-1}$
$\boldsymbol{k(T)}$	reaction rate constant, $s^{-1} \cdot (m^3 \cdot mol^{-1})^{m-1}$
$\boldsymbol{k_h}$	heat transmission coefficient, $W \cdot m^{-2} \cdot K^{-1}$
$\boldsymbol{L}$	channel length, m
$\boldsymbol{m}$	reaction order, -
$\boldsymbol{\dot{m}}$	mass flow rate, $kg \cdot s^{-1}$
$\boldsymbol{N}$	cooling intensity, -
$\boldsymbol{p}$	pressure, barg
$\boldsymbol{\Delta p}$	pressure drop, bar
$\boldsymbol{R}$	ideal gas constant, $J \cdot mol^{-1} \cdot K^{-1}$
$\boldsymbol{R_{th}}$	heat transfer resistance (wall/external), $m^2 \cdot K \cdot W^{-1}$
$\boldsymbol{s}$	wall thickness, mm
$\boldsymbol{S'}$	heat production potential, -
$\boldsymbol{t_c}$	time constant of cooling, s
$\boldsymbol{t_E}$	time constant of micromixing by engulfment, s
$\boldsymbol{t_R}$	time constant of the reaction, s
$\boldsymbol{T}$	temperature, °C
$\boldsymbol{\Delta T}$	temperature difference, K
$\boldsymbol{\bar{u}}$	mean channel flow velocity, $m \cdot s^{-1}$
$\boldsymbol{V}$	reactor volume, mL
$\boldsymbol{\dot{V}}$	volumetric flow rate, $m^3 \cdot s^{-1}$
$\boldsymbol{X}$	conversion, %
$\boldsymbol{Y}$	yield, %
$\boldsymbol{z}$	axial coordinate, m

Greek symbols

$\boldsymbol{\alpha_i}$	heat transfer coefficient (internal), $W \cdot m^{-2} \cdot K^{-1}$
$\boldsymbol{\zeta}$	pressure drop coefficient, -
$\boldsymbol{\epsilon}$	energy dissipation rate, $W \cdot kg^{-1}$
$\boldsymbol{\varepsilon}$	porosity, -
$\boldsymbol{\bar{\lambda}}$	mean heat conductivity, $W \cdot m^{-1} \cdot K^{-1}$
$\boldsymbol{\bar{\nu}}$	mean kinematic viscosity, $m^2 \cdot s^{-1}$
$\boldsymbol{\bar{\rho}}$	mean density of the reacting fluid, $kg \cdot m^{-3}$
$\boldsymbol{\tau}$	mean residence time, s

Indices and abbreviations

$\boldsymbol{0}$	single reactor element
$\boldsymbol{ad}$	adiabatic
$\boldsymbol{A}$	limiting component

$\boldsymbol{BR}$	Barkelew–Renken criterion
$\boldsymbol{CFD}$	computational fluid dynamic
$\boldsymbol{CT}$	helically coiled tubular reactor
$\boldsymbol{design}$	preset by conceptual design/process flowsheet
$\boldsymbol{DES}$	Diethyl sulfate
$\boldsymbol{HS}$	hot spot
$\boldsymbol{HTF}$	heat transfer fluid
$\boldsymbol{i}$	reactor $\boldsymbol{i = 1}$, ...
$\boldsymbol{in}$	reactor inlet
$\boldsymbol{j}$	component $\boldsymbol{j = 1}$, ...
$\boldsymbol{min}$	lower allowable boundary
$\boldsymbol{max}$	upper allowable boundary
$\boldsymbol{MCSP}$	modular and continuously operated small scale plant
$\boldsymbol{MIM}$	1-Methylimidazole
P&ID	Piping and instrumentation diagram
$\boldsymbol{r}$	reaction $\boldsymbol{r = 1}$, ...
$\boldsymbol{R}$	design set point for the reaction
$\boldsymbol{RTD}$	residence time distribution
$\boldsymbol{SMX}$	static mixer (SMX)-type reactor

Dimensionless numbers

$\boldsymbol{Nu = \frac{\alpha d_h}{\bar{\lambda}}}$	Nusselt number, -
$\boldsymbol{Pr = \frac{\bar{c}_p \bar{\nu}}{\bar{\rho}\bar{\lambda}}}$	Prandtl number, -
$\boldsymbol{Re = \frac{\bar{u} d_h}{\bar{\nu}}}$	Reynolds number, -

Conflicts of Interest

The authors declare of no conflict of interests.

References

1. Buchholz, S. Future manufacturing approaches in the chemical and pharmaceutical industry. *Chem. Eng. Process.* **2010**, *10*, 993–995.
2. Löb, P. EU FP7 Project CoPIRIDE—Towards new production and factory concepts for a sustainable and competitive European chemical industry. *Green Process. Synth.* **2013**, *5*, 379–380.
3. Bieringer, T.; Buchholz, S.; Kockmann, N. Future production concepts in the chemical industry: Modular-Small-Scale-Continuous. *Chem. Eng. Technol.* **2013**, *36*, 1–12.
4. Seifert, T.; Sievers, S.; Bramsiepe, C.; Schembecker, G. Small scale, modular and continuous: A new approach in plant design. *Chem. Eng. Process.* **2012**, *52*, 140–150.

5. Gürsel, I.V.; Hessel, V.; Wang, Q.; Noël, T.; Lang, J. Window of opportunity—Potential of increase in profitability using modular compact plants and micro-reactor based flow processing. *Green Process. Synth.* **2012**, *4*, 315-336.
6. Kockmann, N. Scale-up-fähiges equipment für die prozessentwicklung. *CIT* **2012**, *5*, 646–659.
7. Singh, R.; Rozada-Sanchez, R.; Wrate, T.; Muller, F.; Gernaey, K.V.; Gani, R.; Woodley, J.M. A retrofit strategy to achieve "Fast, Flexible, Future (F3)" pharmaceutical production processes. In *Computer Aided Chemical Engineering*; Pistikopoulos, E.N., Georgiadis, M.C., Kokossis, A.C., Eds.; Elsevier: Amsterdam, The Netherlands; Boston, MA, USA, 2011; Volume 29, pp. 291–295.
8. Hessel, V.; Cortese, B.; de Croon, M.H.J.M. Novel process windows—Concept, proposition and evaluation methodology, and intensified superheated processing. *Chem. Eng. Sci.* **2011**, *7*, 1426–1448.
9. Hessel, V.; Kralisch, D.; Kockmann, N.; Noël, T.; Wang, Q. Novel process windows for enabling, accelerating, and uplifting flow chemistry. *ChemSusChem* **2013**, *5*, 746–789.
10. Bramsiepe, C.; Kussi, J.S.; Schembecker, G. Schneller zur produktion. *CT* **2011**, *3*, 50–52.
11. Wiendahl, H.-P. *Planung Modularer Fabriken*; Hanser: München, Germany, 2005.
12. Dercks, B.; Grünewald, M. Modularisierung von mikrotrennapparaten als scale-up-methode am beispiel der mikrodestillation. *CIT* **2011**, *7*, 1115–1119.
13. Hady, Ł.; Wozny, G. Multikriterielle aspekte der modularisierung bei der planung verfahrenstechnischer anlagen. *CIT* **2012**, *5*, 597–614.
14. Peschel, A.; Karst, F.; Freund, H.; Sundmacher, K. Analysis and optimal design of an ethylene oxide reactor. *Chem. Eng. Sci.* **2011**, *24*, 6453–6469.
15. Patel, M.P.; Shah, N.; Ashe, R. Robust optimisation methodology for the process synthesis of continuous technologies. In *Computer Aided Chemical Engineering*; Pistikopoulos, E.N., Georgiadis, M.C., Kokossis, A.C., Eds.; Elsevier: Amsterdam, The Netherlands; Boston, MA, USA, 2011; Volume 29, pp. 351–355.
16. Roberge, D.M.; Gottsponer, M.; Eyholzer, M.; Kockmann, N. Industrial design, scale-up, and use of microreactors. *Chim. Oggi* **2009**, *4*, 8–11.
17. Kockmann, N.; Roberge, D.M. Scale-up concept for modular microstructured reactors based on mixing, heat transfer, and reactor safety. *Chem. Eng. Process.* **2011**, *10*, 1017–1026.
18. Kockmann, N.; Gottsponer, M.; Roberge, D.M. Scale-up concept of single-channel microreactors from process development to industrial production. *Chem. Eng. J.* **2011**, *2–3*, 718–726.
19. Levenspiel, O. *Chemical Reaction Engineering*, 3rd ed.; Wiley: New York, NY, USA, 1999.
20. Roberge, D.M.; Ducry, L.; Bieler, N.; Cretton, P.; Zimmermann, B. Microreactor technology: A revolution for the fine chemical and pharmaceutical industries? *Chem. Eng. Technol.* **2005**, *3*, 318–323.
21. Kockmann, N. Sicherheitsaspekte bei der Prozessentwicklung und kleinmengenproduktion mit mikroreaktoren. *CIT* **2012**, *5*, 715–726.
22. Bałdyga, J.; Bourne, J.R. *Turbulent Mixing and Chemical Reactions*; Wiley: New York, NY, USA, 1999.

23. Taylor, G. The dispersion of matter in turbulent flow through a pipe. *Proc. R. Soc. Lond. Ser. A* **1954**, *223*, 446–468.
24. Aris, R. On the dispersion of a solute in a fluid flowing through a tube. *Proc. R. Soc. Lond. Ser. A* **1956**, *235*, 67–77.
25. Baerns, M.; Renken, A. Chemische Reaktionstechnik. In *Winnacker/Küchler: Chemische Technik*, 5th ed.; Dittmeyer, R., Keim, W., Kreysa, G., Oberholz, A., Eds.; Wiley-VCH: Weinheim, Germany, 2004; pp. 453–643.
26. Kockmann, N. Transport Phenomena in Micro Process Engineering; Springer: Berlin, Germany, 2008.
27. Große Böwing, A.; Jess, A.; Wasserscheid, P. Kinetik und reaktionstechnik der synthese ionischer flüssigkeiten. *CIT* **2005**, *9*, 1430–1439.
28. Große Böwing, A.; Jess, A. Kinetics and reactor design aspects of the synthesis of ionic liquids—Experimental and theoretical studies for ethylmethylimidazole ethylsulfate. *Chem. Eng. Sci.* **2007**, *6*, 1760–1769.
29. Renken, A.; Hessel, V.; Löb, P.; Miszczuk, R.; Uerdingen, M.; Kiwi-Minsker, L. Ionic liquid synthesis in a microstructured reactor for process intensification. *Chem. Eng. Process.* **2007**, *9*, 840–845.
30. Haber, J.; Kashid, M.N.; Renken, A.; Kiwi-Minsker, L. Heat management in single and multi-injection microstructured reactors: Scaling effects, stability analysis, and role of mixing. ind. *Eng. Chem. Res.* **2011**, *4*, 1474–1489.
31. Wilkes, J.S.; Wasserscheid, P.; Welton, T. 1 Introduction. In *Ionic Liquids in Synthesis*, 2nd ed.; Wasserscheid, P., Welton, T., Eds.; Wiley-VCH: Weinheim, Germany, 2008; pp. 1–6.
32. Gordon, C.M.; Muldoon, M.J. 2 Synthesis and Purification. In *Ionic Liquids in Synthesis*, 2nd ed.; Wasserscheid, P., Welton, T., Eds.; Wiley-VCH: Weinheim, Germany, 2008; pp. 7–25.
33. Saxena, A.K.; Nigam, K.D.P. Coiled configuration for flow inversion and its effect on residence time distribution. *AIChE J.* **1984**, *30*, 363–368.
34. Castelain, C.; Mokrani, A.; Legentilhomme, P.; Peerhossaini, H. Residence time distribution in twisted pipe flows: helically coiled system and chaotic system. *Exp. Fluids* **1997**, *5*, 359–368.
35. Pahl, M.H.; Muschelknautz, E. Statische Mischer und ihre Anwendung. *CIT* **1980**, *4*, 285–291.
36. Hirschberg, S.; Koubek, R.; Moser, F.; Schöck, J. An improvement of the Sulzer SMX™ static mixer significantly reducing the pressure drop. *Chem. Eng. Res. Des.* **2009**, *4*, 524–532.
37. Theron, F.; le Sauze, N. Comparison between three static mixers for emulsification in turbulent flow. *Int. J. Multiphase Flow* **2011**, *5*, 488–500.
38. Kraume, M. *Mischen und Rühren*; Wiley-VCH: Weinheim, Germany, 2003.
39. Kast, W. Druckverlust in durchströmten Rohren. In *VDI-Wärmeatlas*, 10th ed.; Kabelac, S., Gnielinski, V., Kind, M., Martin, H., Mewes, D., Schaber, K., Stephan, P., Eds.; Springer-Verlag: Berlin/Heidelberg, Germany, 2006; pp. Lab1–Lab5.
40. Gnielinski, V. Wärmeübergang bei Strömung durch Rohrwendeln. In *VDI-Wärmeatlas*, 10th ed.; Kabelac, S., Gnielinski, V., Kind, M., Martin, H., Mewes, D., Schaber, K., Stephan, P., Eds.; Springer-Verlag: Berlin/Heidelberg, Germany, 2006; pp. Gc1–Gc2.

41. Kalbitz, H.; Bohnet, M. Einfluß statischer mischer auf den wärmeübergang und den druckverlust in rohrwärmeaustauschern. *CIT* **1991**, *3*, 270–271.
42. Fröba, A.P.; Kremer, H.; Leipertz, A. Density, refractive index, interfacial tension, and viscosity of ionic liquids [EMIM][EtSO4], [EMIM][NTf2], [EMIM][N(CN)2], and [OMA][NTf2] in dependence on temperature at atmospheric pressure. *J. Phys. Chem. B* **2008**, *39*, 12420–12430.
43. Rausch, M.H.; Krzeminski, K.; Assenbaum, D.; Wasserscheid, P.; Leipertz, A.; Fröba, A.P. Messung und vorhersage der wärmeleitfähigkeit von ionischen flüssigkeiten. *CIT* **2011**, *9*, 1510–1514.
44. Data from SRC PhysProp Database (1-Methylimidazole). Available online: http://esc.syrres.com/fatepointer/webprop.asp?CAS=616477 (accessed on 10 December 2013).

Microreactors for Gold Nanoparticles Synthesis: From Faraday to Flow

Md. Taifur Rahman and Evgeny V. Rebrov

Abstract: The seminal work of Michael Faraday in 1850s transmuted the "Alchemy of gold" into a fascinating scientific endeavor over the millennia, particularly in the past half century. Gold nanoparticles (GNPs) arguably hold the central position of nanosciences due to their intriguing size-and-shape dependent physicochemical properties, non-toxicity, and ease of functionalization and potential for wide range of applications. The core chemistry involved in the syntheses is essentially not very different from what Michael Faraday resorted to: transforming ions into metallic gold using mild reducing agents. However, the process of such reduction and outcome (shapes and sizes) are intricately dependent on basic operational parameters such as sequence of addition and efficiency of mixing of the reagents. Hence, irreproducibility in synthesis and maintaining batch-to-batch quality are major obstacles in this seemingly straightforward process, which poses challenges in scaling-up. Microreactors, by the virtue of excellent control over reagent mixing in space and time within narrow channel networks, opened a new horizon of possibilities to tackle such problems to produce GNPs in more reliable, reproducible and scalable ways. In this review, we will delineate the state-of-the-art of GNPs synthesis using microreactors and will discuss in length how such "flask-to-chip" paradigm shift may revolutionize the very concept of nanosyntheses.

Reprinted from *Processes*. Cite as: Md. Rahman, T.; Rebrov, E.V. Microreactors for Gold Nanoparticles Synthesis: From Faraday to Flow. *Processes* **2014**, *2*, 466-493.

1. Introduction: Gold Nanomaterials—Syntheses and Applications

Gold is one of the most important elements in the human civilization. In early human societies, gold was a symbol of power and wealth, and was used as ornaments for both living and the dead. Gold has been, ever since the very dawn of commerce, a reliable and universal means of financial transactions and reserve. Hence, the desire and dream of "transmuting anything into gold" paved the way for alchemy, which is the predecessor of modern Chemistry. Rather unknowingly, non-bulk form of gold had also been a part of humanity from the time of antiquity. Colloidal gold dispersed in glass or ceramics produce hues of red or green, which were used to decorate and color Roman cage-cups, or diatretum. One famous example is the Lycurgus cup, dating from the 4th century A.D., made from nanogold-infested glass, now preserved in the British Museum in London.

Although widely used throughout the history for decorative purposes and as medicines [1,2], the nature of colloidal gold was investigated only sporadically [3]: In 1676, a German chemist, Johann Kunckels, inferred that non-bulk gold exists in infinitesimal state that is not visible to human eyes. It was Michael Faraday who pioneered the first systematic synthesis of gold nanoparticles using phosphorous-based reducing agents. He is widely credited for insightful and for the "first"

scientific discussion on size dependent optical properties and their coagulation behavior of colloidal gold [4].

Rapid growth in interests about colloidal gold was sparked by the availability of electron microscopes that enabled direct visualization of the nanoparticles [5,6]. Over the past two decades, tremendous effort was dedicated to synthesize and optimize a wide class of GNPs possessing a broad spectrum of geometry, size, chemistry and functionality. This paved the way for applications of GNPs in heterogeneous catalysis, bio-imaging, medicines, optics, analytical sciences, sensing, *etc*. [7–17]. Because of widespread applications of GNPs in different branches of sciences and technologies, need for establishing reliable supply chains for such materials is becoming ever more important, hence the involved chemical processes are of utmost importance.

2. Mechanism and Challenges in Metallic Nanoparticles Synthesis

Interestingly, typical GNPs synthesis protocols adapted by most leading research groups are as simple as Michael Faraday's experiments in the 1850s: reduction of gold ions (usually Au(III) salts) in a solution using reducing agents. However straightforward the synthesis may appear, the underlying mechanisms of the elementary processes involved in the formation of metallic colloids from homogeneous mixture of ionic precursors (gold ions and reducing molecules/ions) are rather complex. Formation of such materials from homogeneous state involves several interconnected and interrelated steps: (1) species undergoing reduction leading to supersaturation for metallic atoms in the reaction volume; (2) formation of nuclei from these insoluble metal atoms either by diffusive growth or aggregation; and (3) growth of the nuclei into the final nanostructure by diffusion of atom/ions to the nuclei surface and on-surface deposition/auto-catalytic reduction via electron transfer from the reducing agent [18,19].

The intrinsic kinetics of these elementary steps rather than the thermodynamics defines the outcome of the reactions. Mixing of gold ions with reducing agent is of vital importance, because any inhomogeneity in the mixing will generate concentration gradients in the reaction volume. As such, inhomogeneity would cause random nucleation producing nuclei with variable sizes that would grow into final nanoparticles having poor size distribution. In addition, if the nucleation step is not complete before the growth starts, then there will be a competition for gold ions between two parallel processes: new nucleation and growth of the present nuclei; which is responsible for polydispersity in size and shape. Even if the nucleation is performed properly, homogeneous supply of gold ions to the surface is required for the controlled diffusive growth. Hence, nucleation and growth steps should be separated in time to facilitate monodisperse GNP production. Such a scenario is not often achievable in reproducible manner in conventional stirred reactors (typically flasks). Usually characteristic mixing time is relatively long as compared to nucleation time in conventional reactors. This results in variation of local temperature, pH or reactant concentrations that contribute to polydispersity and poor batch-to-batch reproducibility. All these factors underscore the necessity for an alternative platform for synthesis of these nanomaterials, which is not only reliable and reproducible but also robust enough for scalable production of various types of gold nanoparticles.

3. Scope of the Review

Over the past decade microreaction technology evolved as a miniaturized version of flow reactors [20–22]. Unlike conventional continuous stirred tank reactors (CSTR), mixing between two or more reacting fluids takes place within tens of micrometers length. Hence, complete mixing between reactants occurs in micro-to-millisecond time scale. Due to the small dimensions of the mixing and reaction region, unprecedented control over mass-and-heat transport and reaction time is possible. Initial success of implementing microreaction technology in organic synthesis prompted several groups to resort to microfluidic reactors to circumvent challenges (vide infra) associated with nanomaterials synthesis. There are several recent reviews covering the use of microfluidic reactors for the synthesis of nanoparticles of different kinds [23–26]. Here an overview is provided on how flow synthesis methods leveraged for a wide variety of GNPs possessing superior quality compared to the products obtained from batch processes. Scaling up approaches will also be discussed.

4. Synthesis of Colloidal Gold Nanoparticles in Microreactors

Wagner *et al*. were the first to report synthesis of gold nanoparticles in a microreactor [27]. They used a microfluidic chip fabricated from Pyrex glass by wet etching method. The chip consisted of two micromixers and a residence time unit (Figure 1). In the first micromixer, a solution of ascorbic acid, acting as a reducing agent, was mixed with preformed gold seeds of 12 nm in diameter. This mixture was guided through a serpentine channel to complete mixing. Then, reduction of the gold ions onto the good seeds started in the second micromixer with a volume of 2.3 μL where a solution of chloroauric acid was added to the flow to keep the total flow rate in the range of 5–50 μL/min. The reaction mixture was collected from the reactor outlet via a PTFE tube and analyzed by spectroscopic and microscopic methods.

The channel walls were negatively charged at the pH of 10, used in all experiments. When citrate ions were used as capping agent, the surface of gold nanoparticles was also negatively charged. Therefore electrostatic repulsion prevented seed deposition onto the inner channel walls. However, when the seeds were grown in the presence of ascorbic acid, significant gold deposition on the walls was observed. This undesirable deposition was reduced by increasing the seed to gold ion ratio in the solution. At the 1:1 molar ratio, gold particles with a size of 24 nm were obtained, albeit with poor monodispersity. The size was further controlled by varying the respective flow rates of the reactants and/or the reducing agents.

Figure 1. Microfluidic device for GNP synthesis. Adapted from Ref. [27] (with permission from Elsevier Ltd.

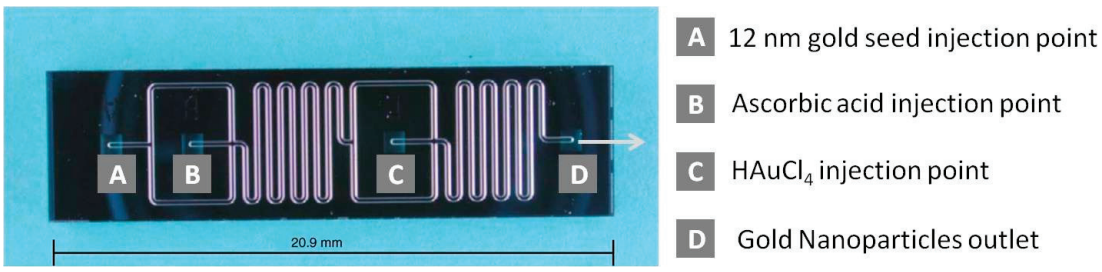

In the absence of seeds in the synthesis with ascorbic acid, both high pH of the reaction mixture and highly hydrophobic surface of the inner reactor walls prevented the nanoparticle deposition onto the inner walls of a pyrex/silicone microreactor [28]. A principle of split-and-recombine mixing was utilized in this microreactor. The hydrophobic surface was created by modification with perfluorosilane and polyvinylpyrrolidone (PVP) was used as capping agent. As the flow rate increased, the mean diameter of the gold nanoparticles decreased, while the total number of nanoparticles increased. It has been shown that there exists a range of flow rates, where axial dispersion effects can be neglected leading to improved control over mixing. The obtained gold nanoparticles showed better distribution, which was twice as narrow in comparison to those obtained in the conventional reactor and in the microreactor with a substantial degree of backmixing observed at low flow rates. In a follow up work, controlled accumulation of the discrete nanoparticles into larger clusters of micrometer size was demonstrated in the channels of 180 × 200 μm^2 made in a glass chip [29]. In this reactor, a solution of reducing agents (ascorbic acid and iron(II) sulfate) was mixed with polyvinyl alcohol in the first mixer. Then, a sodium metasilicate solution was introduced in the second mixer and gold ions were injected in the third mixer. Reduction of gold ions into colloidal gold in the presence of polymer and electrolytes facilitated the clustering of gold nanoparticles into larger clusters. Small GNPs with a diameter of 3–5 nm were obtained when sodium borohydride was used as reducing agent [30]. The size can further be fine-tuned by controlling the concentration (via dilution by introducing diluents water stream) of the gold ions and borohydride. Thus, the authors were able to control the cluster size between 3 nm up to micrometer size by varying the respective flow rates and concentration.

Ultra-small gold clusters with a diameter of 1 nm are an important class of gold nanomaterials with regards to their high catalytic activity in many organic reactions [31]. Synthesis of such gold clusters is a difficult task in conventional stirred reactors due to pure control of mixing. Deviations of the local concentration of reactants, particularly strong reducing agents like sodium borohydride, influence the kinetics of the cluster formation and are detrimental to the size distribution. Tsunoyama *et al*. presented a microfluidic method to produce ultra-small PVP-stabilized gold nanoparticles using a SIMM-V2 micromixer (IMM, Figure 2A) [32]. In this micromixer, the total flow of $HAuCl_4$ gold precursor, PVP and an aqueous solution of sodium borohydride was split in a multitude of parallel substreams with a thickness below 100 μm. This reduced characteristic diffusion time from several minutes to a few seconds. Moreover, it was speculated that microbubbles, which were formed due to the decomposition of borohydride, assisted in breaking the lamellar structure into smaller fragments, further accelerating the mass-transport. Sub 2 nm gold nanoparticles were produced with a monodispersity of 14% from a 10 mM Au precursor solution at a relatively low PVP:Au molar ratio of 40:1 Figure 2B). It should be noted that larger and polydisperse PVP-protected Au clusters were produced in a conventional reactor, when similar concentrations of reactants were used (Figure 2C). The activity of Au clusters in oxidation of 4-hydroxybenzyl alcohol was 50% greater than that with Au clusters produced by classical batch protocol demonstrating the advantages of monodispersed Au nanoparticles in structure sensitive reactions.

Figure 2. (**A**) Multilamination and mixing of gold precursors (Au ions and PVP) with reducing agent (sodium borohydride and PVP); (**B**,**C**) TEM photographs of produced GNPs with size distribution (insets) for microfluidic and batch processes, respectively. Adapted from Ref. [32] (with permission from American Chemical Society).

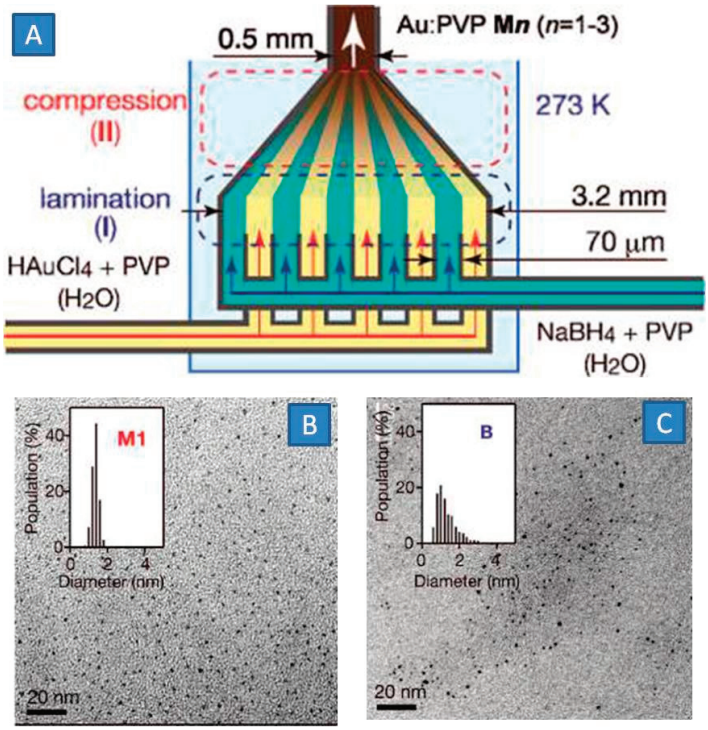

The SIMM-V2 micromixer in combination with a microreactor was employed to examine the dependence of the particles size on the reactant flow rates [33]. The authors used $HAuCl_4$ as gold source, while ascorbic acid and PVP were used as reducing agent and surfactant, respectively. They obtained a set of GNPs with different sizes in the range from 1.7 to 33 nm by varying the flow rate from 7.5 to 0.1 mL/min. The characteristic half time of ascorbic acid mediated reduction of gold ions was found to be 31 ms. Still, this is much shorter as compared to the characteristic diffusion time of at least several seconds. As the diffusion time approaches the characteristic reaction time, it enables to decouple the nucleation and growth steps, which in turn provides better degree of control over the particle size via variation of the residence time. The authors did not observe deposition of on the inner metal walls of the micromixer at high flow rates.

5. Effect of pH

Ishizaka *et al*. adjusted the pH of a gold precursor solution with addition of an aqueous sodium hydroxide solution in a Teflon mixer connected to a capillary [34]. This solution was then mixed with glucose acting as reducing agent. As the hydroxide flow rate decreased, the pH of the resulting solution decreased too yielding non-spherical GNPs as detected by a blue shift in the light absorption (Figure 3). At a pH of 6.9, star-like GNPs were obtained solely in the microreactor, while in their batch system this morphology could not be obtained at the same reaction conditions.

Figure 3. Upper panel: Microfluidic pH Control of Gold solution with NaOH and then online reduction with glucose. Lower panel: GNP samples of wide UV absorption characteristics (depending on shape); TEM photograph of star-like GNP (while line at the bottom left of TEM photo corresponds to scale bar, in addition to the bottom right side, unaltered from the original image). Adapted from Ref. [34] (with permission from Elsevier Ltd.).

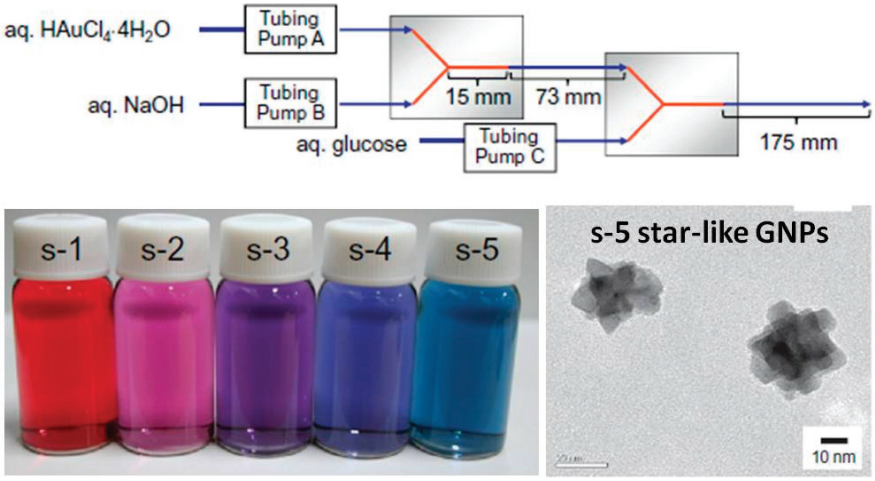

It is known that the reducing potential of ascorbic acid depends on the pH of the solution. At pH below 4.1, ascorbic acid exists in the protonated form, $AscH_2$. As the pH increases, it transforms into ascorbate, $AscH^-$, while at pH above 11.6 it is completely deprotonated to form, Asc^{2-}. Such speciation of ascorbic acid at different pH alters its reducing power. The control of the initial pH of the ascorbic acid solution increased the isolation of spherical GNPs, with high monodispersity [35]. Au nanoparticles with average diameter of 18, 10 and 7 nm, with narrow relative polydispersity indices of 0.4, 0.3 and 0.2 were obtained from a $HAuCl_4$/ascorbic acid mixture at a pH of 10.2, 10.7 and 11.1, other parameters being the same. The initial pH was adjusted with a sodium hydroxide solution. A microfluidic mixer was operated at Reynolds number of 2000, enabling intense mixing between ascorbic acid and gold precursors.

6. Transient Operation

A pulsed dosage of 0.5 µL of a 1 mM Au(III) solution (every 2 s) to a continuous flow of a 1.5 mM sodium borohydride solution was proposed by Pedro *et al*. [36]. The two solutions were mixed in a flow-focusing T-junction connected to a three-dimensional serpentine channel network (Figure 4A,B). This enabled controlled and homogeneous formation of the gold seed/nuclei due to the creation of supersaturated zones in each dosed volume of gold ions. The entire microreactor was made by low-temperature co-fired ceramic technology (LTCC). Highly reproducible 2.7 nm GNPs with high monodispersity were obtained in at least 10 consecutive runs (Figure 4C,D).

Figure 4. (**A**) Microfluidic device made by low-temperature co-fired ceramic technology LTCC; (**B**) Micromixer and 3-D serpentine residence time unit enabling efficient mixing; (**C**) Reproducibility between several runs of experiment; (**D**) TEM photograph: Size-distribution of GNPs in the form of histogram is provided in the inset; mean average diameter is 2.7 nm for the Mercaptoundecanoic acid MUA modified gold nanoparticles. Adapted from Ref. [36] (with permission from IOP Publishing Ltd.).

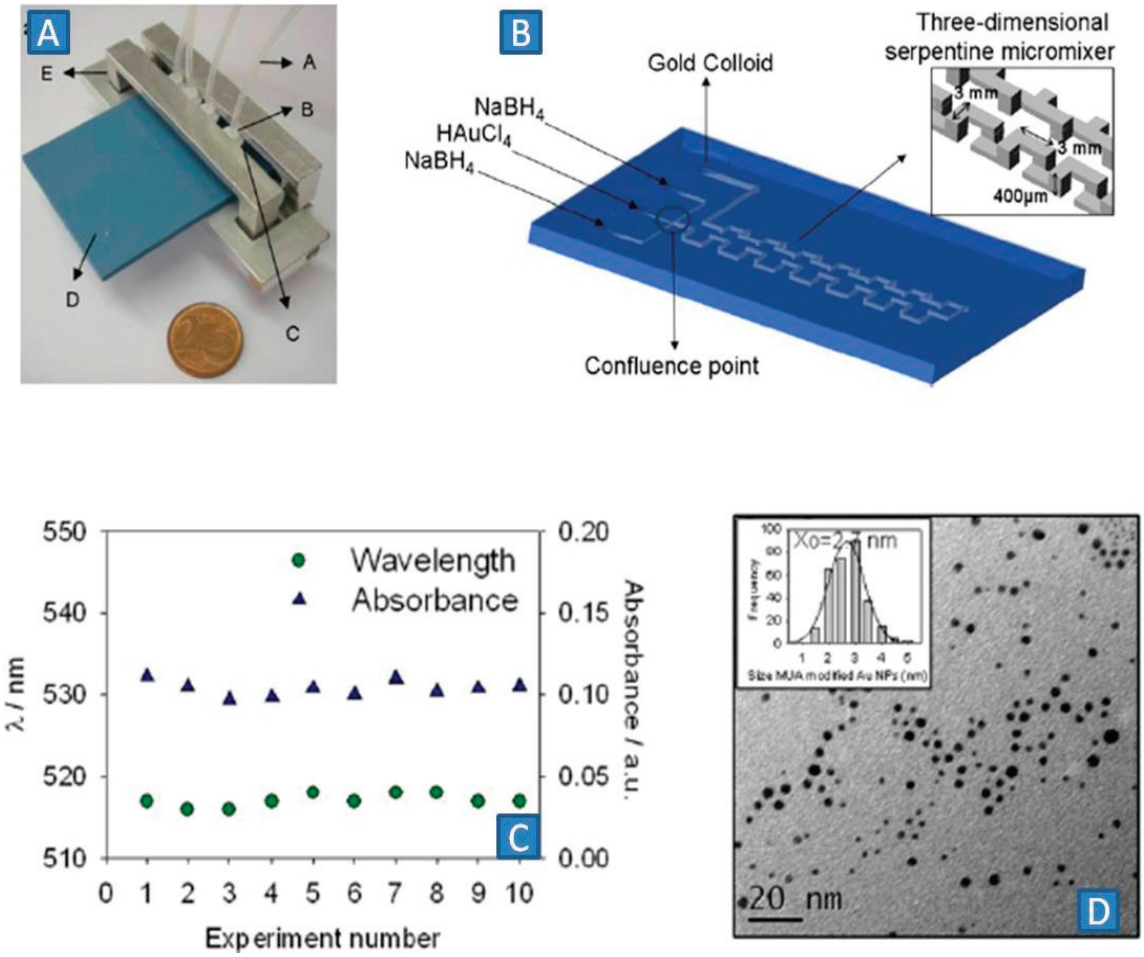

Ultra-small Au nanoparticles can also be obtained by rapid heating and quench in a microreactor system [37]. In this method, the Au ions are reduced with a sodium citrate solution at elevated temperature, just below the boiling point of the solvent, yielding a multitude of nuclei that needs to be immediately cooled to arrest further growth. A T-mixer was connected to a 1.5 m fused silica capillary with a diameter of 200 µm maintained at 100 °C (Figure 5A). The outlet flow was rapidly cooled to quench the reaction. With a residence time of 35 s, gold nanoparticles with an average diameter of 2 nm were produced at a citrate: Au molar ratio of 3.5 (Au 5.4 mM), while the synthesis in batch gave a polydispersed mixture of gold nanoparticles under similar reaction conditions. Different particle sizes in the range of 1.5–3.0 nm were obtained by varying the residence time in the microreactor (Figure 5B). Thus, fast heating enabled to obtain ultra-small GNPs even with classical synthesis methods.

Figure 5. (**A**) T-mixer and Fused Silica capillary microreactor; (**B**) GNP Size variation and size distribution by tuning residence time. Adapted from Ref. [37] (with permission from Royal Society of Chemistry).

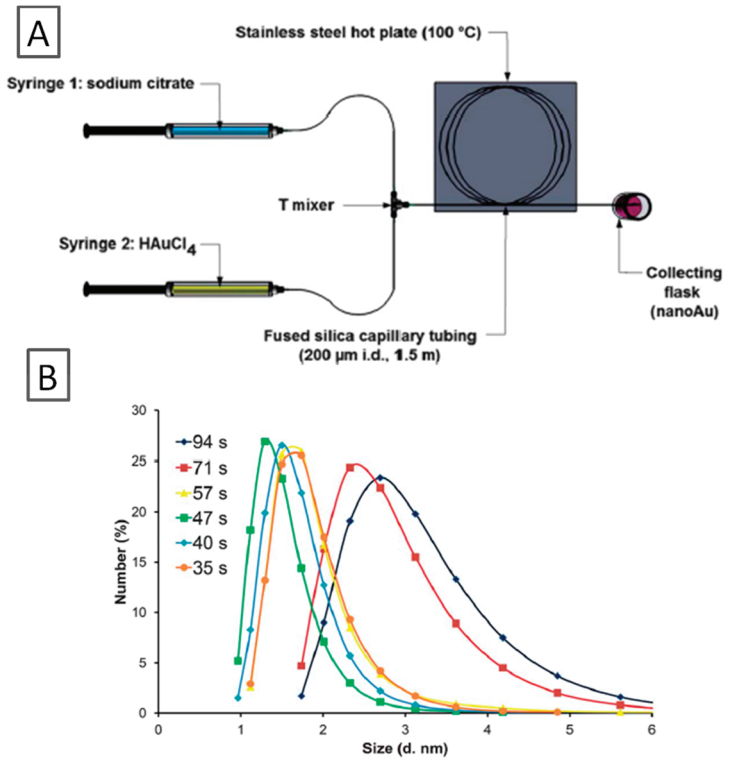

7. Surfactant Stabilized Gold Nanoparticles

While many reports are devoted towards preparing water-dispersible GNPs colloids in microfluidic reactors, less attention was given to organically-capped hydrophobic gold nanoparticles which are also an important class of GNPs. Sugie *et al*. reported reduction of $HAuCl_4$ in tetrahydrofuran (THF) solvent inside a Y-mixer/PTFE microreactor assembly maintained at constant temperature (25–60 °C) using organosilanes (RSiH) as reducing agents and alkyl thiol (RSH) as capping agent [38]. The effect of the residence time and temperatures was studied. As the residence time increased from 12 to 94 min, the size of the GNPs increased from 4.3 to 8.7 nm. The nature of the reducing agent did not alter the size of GNPs when the flow rate and temperature were kept constant. A benchmark experiment in the batch mode at 60 °C produced insoluble precipitates manifesting uncontrolled growth.

8. Development of Time Resolved Analysis Techniques to Monitor Reaction Kinetics

It is generally considered that the kinetics of nucleation and growth is coupled and in most cases extremely fast. Hence, monitoring the nucleation and growth processes in real-time is even more challenging than harnessing such processes to produce GNPs in size/shape-controlled manner. Krishna *et al*. presented a fluidic method to examine the real-time nucleation and growth kinetics by employing on-line X-ray absorption spectroscopy (XAS) [39]. This method provides kinetic profiles of the nucleation and growth of gold nanoparticles on the channel surface. To obtain time resolved information about the growth of gold nanoparticles, an X-ray beam with a size of 50 × 50 μm^2 was

directed via a micromixer where a $HAuCl_4$ solution was contacted with a meso-2,3-dimercapto succinic acid solution at relatively low Re numbers (Figure 6). In such conditions, a gold-thiol species was formed and deposited onto the inner channel surface. Then, a sodium borohydride solution was fed through the microchannel to reduce the Au-Thiol species o colloidal GNPs. The latter step was monitored with XAS at 5 ms intervals at different locations of the channel.

Figure 6. Upper panel: Microfluidic device for *in-situ* monitoring of GNP growth kinetics with an X-Ray probe, Lower panel: time-resolved deposition of gold nanoparticles and aggregation along the microfluidic channel at different positions. Adapted from Ref. [39] (with permission from American Chemical Society).

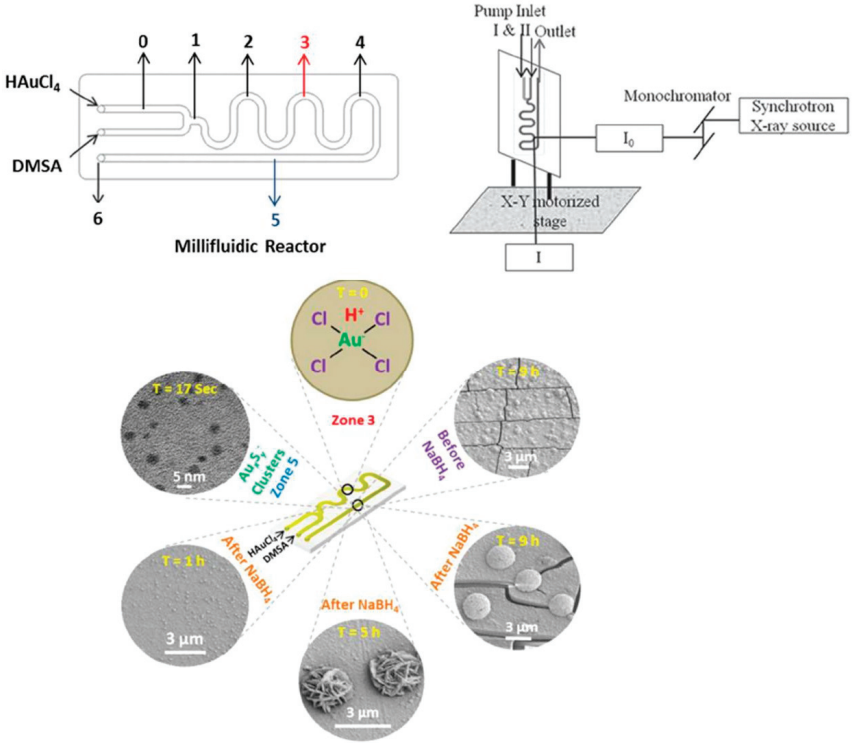

9. Synthesis of Composite GNPs

Au-Metal Composites

During the last fifteen years, core-shell nanoparticles have been intensively studied for their potential to have specific optical, electronic, magnetic and catalytic properties. Several research groups have employed microfluidic reactors for the synthesis of complex gold nanoparticles, such as Au-Ag (gold-silver) composites, core-shell (Au/Ag or Au/Silica), gold nanorods, *etc*. [8,40–47]. Due their tunable optical and chemical properties, these materials hold large promises in optics, analytical and biosciences as imaging and therapeutic agents. The choice of noble-metal (Au) core is motivated by the strong optical responses resulting from the well-known surface plasmon resonance, thus allowing construction of efficient probes for surface enhanced Raman scattering. However, those properties require suppression by use of surface encapsulation of the tendency of the nanoparticles to aggregate. Moreover, the use of dielectric materials such as metal oxides for the shell coating can

allow further tuning of those properties. As a consequence, optimization of this tailoring requires a precise control of the chemical composition, the structure and dimensions of the shells. Although such chemically and structurally delicate nano-motifs can be synthesized in flask reactors, however reliable and scalable means to fabricate such materials are highly challenging. Hence, microreactors are envisaged as a robust means to produce such materials in a reliable and scalable fashion.

It should be noted that the rate of the gold reduction step is much higher than that of silver reduction, therefore it is of importance the presence of the silver ions in the vicinity of the gold seeds in order to make core-shell particles. The microfluidic synthesis of Au-Ag core-shell nanoparticles was realized in a Statmix 7 (IPHT Jena) glass/Si/glass split-and-recombine microreactor to ensure multilamination of fluid segments for better mixing via rapid interdiffusion between adjacent laminar layers (Figure 7) [48]. In the first micromixer, an Au(III) aqueous solution was mixed with ascorbic acid to generate gold nuclei. These nuclei act as seeds/core to catalyze the growth of the silver shell onto the gold core once a stream of silver nitrate solution was introduced in the second micrometer. At a low flow rate of 25 µL/min, the rate of diffusion of ascorbic acid into silver-rich laminar layers was relatively slow. As a result, only gold colloids were formed. As the flow rate increased towards the 42–58 µL/min range, proper multi-stacking of lamellas containing Au-ascorbic acid and the Ag salt was realized. This enhanced diffusion of the silver ions to the gold seeds yielding predominantly the Au-Ag nanoparticles. In the intermediate flow regime (42–50 µL/min), both Au-Ag and Au particles were formed. This work demonstrated the importance of mixing and precise control of the reaction time for the synthesis of complex composite materials of desired/tunable chemical composition.

Figure 7. Upper panel: Schematic of Au-Ag core-shell synthesis in microreactor and possible products. Lower panel: Multilamination and mixing efficiency at different flow rates (**A**: typical flow rate 42–58 µL/min, while **B**: 25 µL/min). Adapted from Ref. [48] (with permission from Wiley-VCH).

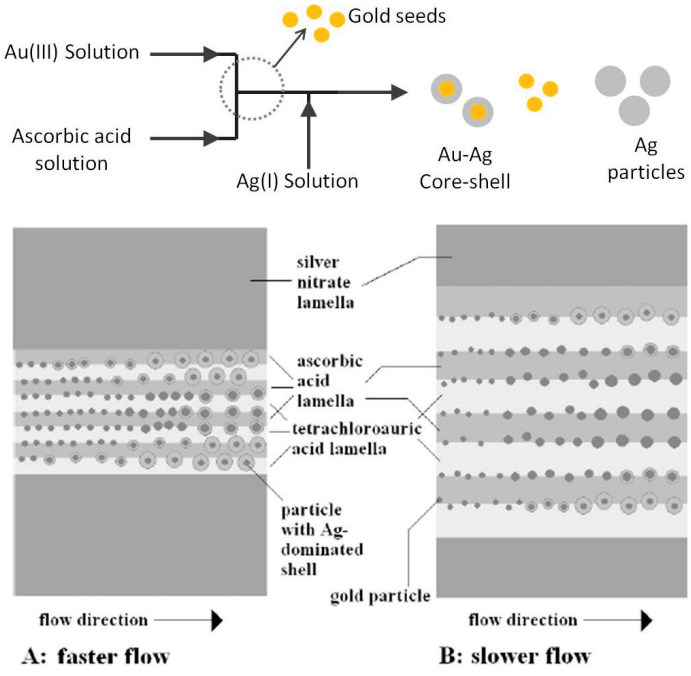

Au-Ag alloy nanocomposites were prepared in a PTFE capillary microreactor with a diameter of 750 μm in a single step (Figure 8) [49]. A preformed solution of silver nitrate, gold chloride, oleylamine and octadecene (Au^{3+}/Ag^{+} = 20) was fed to the microreactor maintained at 140 °C. At this temperature, fast nucleation of gold into the primary core materials was completed prior to thermally assisted diffusion-reduction of Ag inside the Au cores. As the residence time increased from 30 to 320 s, more silver ions diffused towards the gold seeds. As a result, the silver content in the Au-Ag alloy increased commensurately. Highly monodisperse and composition-defined Au-Ag alloy particles with an average diameter of 2.7 nm were produced at a residence time of 3 min. Similar reaction conditions in a batch reactor required longer reaction time and produced Au-Ag nanoparticles with large size distribution.

Figure 8. Schematics of mechanism for Au-Ag alloy synthesis. Change of product composition (colloidal Ag or Au and Au-Ag ally) with residence time inside the microreactor (variation of plasmonic absorption with residence time is shown in the UV-Vis trace of (a)). Adapted from Ref. [49] (with permission from Elsevier Ltd.).

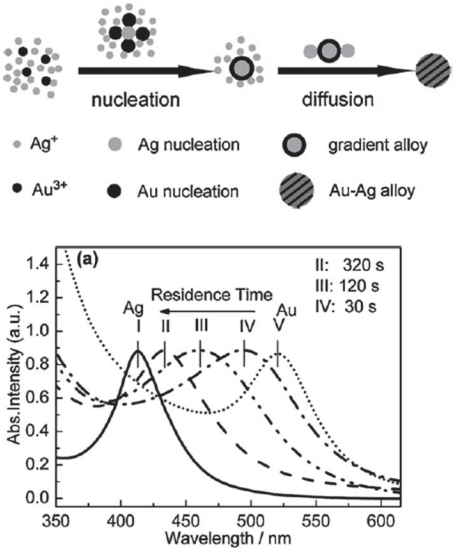

10. Au-Metal Oxide Composites

A uniform gold shell onto dielectric cores such as silica particles exhibits much more pronounced plasmonic properties, which can be utilized in a number of optical and biological applications [41,45]. Such materials sparked intense interests in fundamental and applied research [43]. The thickness of the Au shell and the extent of Au coverage on the silica core dramatically affects the resulting plasmonic behavior. Several groups developed chemical methods to achieve such variation through controlling the reactions. The basic chemistry to form SiO_2@Au nanomaterials involves several steps (Figure 9). It starts with the formation of silica nanoparticles by the Stöber method [50], followed by the functionalization of silica surface with amine containing silane species. The surface becomes positively charged, allowing adsorption of preformed gold seeds. In the last step, the reduction of exogenously added gold ions onto these seeds occurs to form a complete gold shell onto the silica core. Recently, the SiO_2@Au nanomaterials were produced in a Teflon millireactor with a

diameter of 1.3 mm by Gomez *et al*. [51]. The amino-functionalized silica particles were obtained by reaction between an ethanol solution of silica precursor (tetraethyl orthosilicate and 3-aminopropyltriethoxy silane) with an ammonia solution in the flow reactor at 40 °C with a residence time of 30 min. After off-line separation, it was observed a rather big distribution in particle size due to laminar flow and large variation in residence time in the microreactor operated in the laminar regime. In the second step, another microreactor was employed to attach gold seeds (2–4 nm) onto the silica particles. The obtained Au-seeded silica colloids were further treated with a gold salt solution in the presence of formaldehyde as reducing agent. The authors noticed poor attachment of the gold seeds onto the amino-silica cores. As a result, substantial amount of free colloidal gold apart from gold-silica core-shell materials was also observed in the final product, which would require additional purification step. This observation manifests in the necessity of a cleaner process for such materials synthesis, which is often accompanied by undesired side-reactions (here the free colloidal gold formation).

Figure 9. (**a**) Chemical steps for silica particles synthesis, amino functionalization, seeding with Au and the Au shell formation by chemical reduction of gold; (**b**) Microfluidic setup for core-shell synthesis; (**c**) Interdigitated micromixer for mixing of reagents for core-shell synthesis. Adapted from Ref. [51] (with permission from Royal Society of Chemistry).

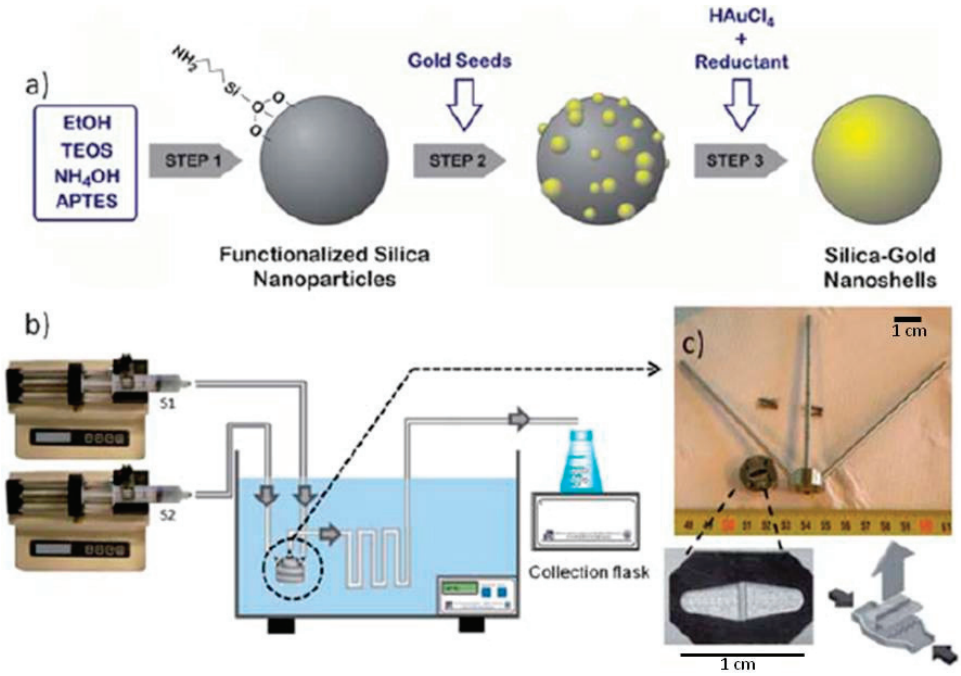

11. Au Nanorods

Gold nanorods (GNRs) is another class of gold nanoparticles, which show surface plasmon behavior [8]. In particular, they can support a longitudinal surface plasmon, which results in suspensions of them having a strong extinction peak in the upper visible or near-infrared parts of the spectrum. The position of this peak can be readily tuned by controlling the shape of the rods. In addition, the surface of the nanorods can be functionalized by a very wide variety of molecules. This has led to

interest in their use as selective biomarkers in biodiagnostics or for selective targeting in photothermal therapeutics [46,47,52,53]. Typical gold nanorods are 30–50 nm long and 5–10 nm wide. The plasmon of nanorods splits into two modes of surface electron oscillation: (1) along the long axis, longitudinal (light absorption beyond 600 nm up to near infrared region) and (2) along the short axis which is typically in the range of spherical gold nanoparticles *i.e.*, 520–530 nm). Longitudinal plasmon can be tuned by controlling the anisotropic growth of gold seeds along the longer axis.

Typically, chemistry of GNRs formation involves templated growth of small gold seeds (1–3 nm) with a growth solution: a mixture of gold salt, ascorbic acid reductant, templating agent CTAB and a small amount of silver nitrate in water. Boleininger *et al*. reported the first GNRs synthesis in a PVC microreactor connected to a three-way valve and a 7-port manifold (Upchurch Scientific) [52]. The authors were able to produce GNRs with different aspect ratio by changing the ratio between the preformed gold seeds solution and the growth solution. In-situ monitoring of the GNRs formation was performed with an optical probe in the downstream part of the microreactor. The effect of the reaction temperature and reactant concentrations was systematically studied. Since preformed seeds for GNRs are not stable over a period of several hours, only freshly prepared seeds can serve as reliable core materials for their growth into monodisperse GNRs. In this way, Bullen *et al*. modified this synthesis by employing a sequentially rotating tube processor (RTP) connected to a microfluidic chip to perform sequential operations of seed formation and growth of seeds into GNRs (Figure 10) [53]. A stable continuous operation for 19 days was demonstrated, which would be hampered had they used presynthesized seeds. Spectral data for all the samples collected over 19 days of operation demonstrate the robustness of the system to produce high quality of gold nanorods having reproducible quality and least by-products (spherical or irregular-shaped gold nanoparticles) as evident from the TEM picture.

Figure 10. (**A**) Injection of reagents into Rotating Tube processor (RTP) and Residence Time Unit fitted with an on-line UV monitoring system; (**B**) UV-Vis Spectrum of Gold Nanorods produced over 19 days; (**C**) TEM photographs of the produced GNRs. Adapted from Ref. [53] (with permission from Royal society of Chemistry).

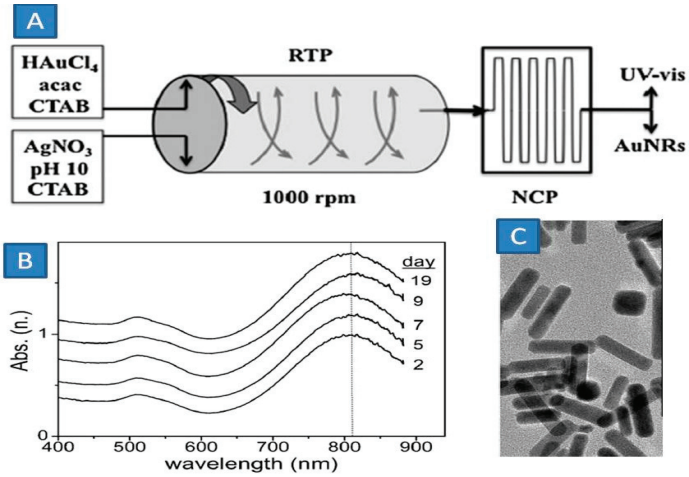

In the "seedless" method, a gold precursor solution ($HAuCl_4$, CTAB, acetylacetone) and a reactant mixture (CTAB, pH 10 carbonate buffer and $AgNO_3$) were fed into the RTP (30 cm × 6 cm, rotating at 1000 rpm). The centrifugal force of the RTP generated a dynamic thin film (300 μm) on the inner wall of the reactor facilitating the Au-seed formation in 30 s. These seeds subsequently grew to nanorods of 24.2 nm × 6.6 nm in the microfluidic chip. Typically, the control of shape and size of anisotropic gold nanoparticles is accomplished by adjusting the concentration of shape modulating agents: silver and CTAB capping agents. By varying the silver concentrations in the second feed, the authors were able to control the aspect ratio of the produced rods. Although, such capping agents enable synthesis of high quality GNRs, both Ag and CTAB exhibit *in vivo* cytotoxicity, limiting their direct use in biological systems.

In an attempt to create a CTAB and Ag-free variant of anisotropic GNRs synthesis, Sebastian *et al*. presented a Y-mixer connected to a 760 μm i.d.; internal diameter PTFE microreactor for continuous flow synthesis of biocompatible GNRs using amino acid (Lysine) instead of CTAB [54]. The presence of two amino groups in Lysine molecule serves a dual purpose of capping and bridging, which is essential for anisotropic growth of gold particles. A premixed solution of gold salt, potassium carbonate and Lysine was contacted for 10 min with sodium borohydride solution in the microreactor placed in an ultrasonic bath (Figure 11). GNRs are obtained with high monodispersity with microreactor (Figure 11B,C,E) while GNPs with irregular shapes and polydispersity were obtained in benchmark experiments in a batch reactor (Figure 11A,D). Fast mixing between the reactants is attributed to such pronounced difference between conventional and flow reactors. The produced GNRs were biocompatible and exhibited strong absorption in the near-infrared range. These GNRs were successfully used in photothermal optical coherence tomography (OCT) of human breast tissue.

So far, we considered syntheses under single-phase conditions, via controlled mixing and reactions between two or more miscible reagent solutions. This protocol is simple and easily adaptable to different microfluidic set-ups. However, there are several drawbacks associated with single-phase materials synthesis: (1) due to axial diffusion in laminar flow, there exists wide distribution in the residence time (Figure 12A,C), which contributes to polydisperse and intractable mixture of several products and by products [55,56]; (2) mixing occurs solely by diffusion, which requires micromachining of additional structural elements (e.g., pin-fin or split-and-recombine) with lithographic techniques to induce convective flux to assist mixing (Hydrodynamics and reaction studies in a layered herringbone channel [57]; (3) deposition of gold nanoparticles occurs onto the inner reactor walls. The deposit serves as nucleation sites hence depleting feed stock in an unproductive way. The reactor becomes unusable at longer reaction times, which impedes the utility of the reactor for long-term use. Passivation of the channel surface with hydrophobic functional groups was proposed as a possible remedy; however, such methods are not generic for all materials used for microfluidic device fabrication. Specifically, while PDMS is the most widely used materials for microfluidic reactor fabrication, unfortunately PDMS is unsuitable for such chemical passivation.

Figure 11. Upper panel: Schematic of Microfluidic setup for CATB and Ag-free Gold Nanorods synthesis. Lower panel: (**A**) Irregular-shaped Gold Nanoparticles from Batch experiments; (**B**) Gold nanorods from microfluidic experiment; (**C**) Absorption spectra of GNP produced in batch and continuous microfluidic device; (**D**) Size distribution of GNPs from batch reactor; (**E**) Size distribution of GNRs from microfluidic device. Adapted from Ref. [54] (with permission from Royal society of Chemistry).

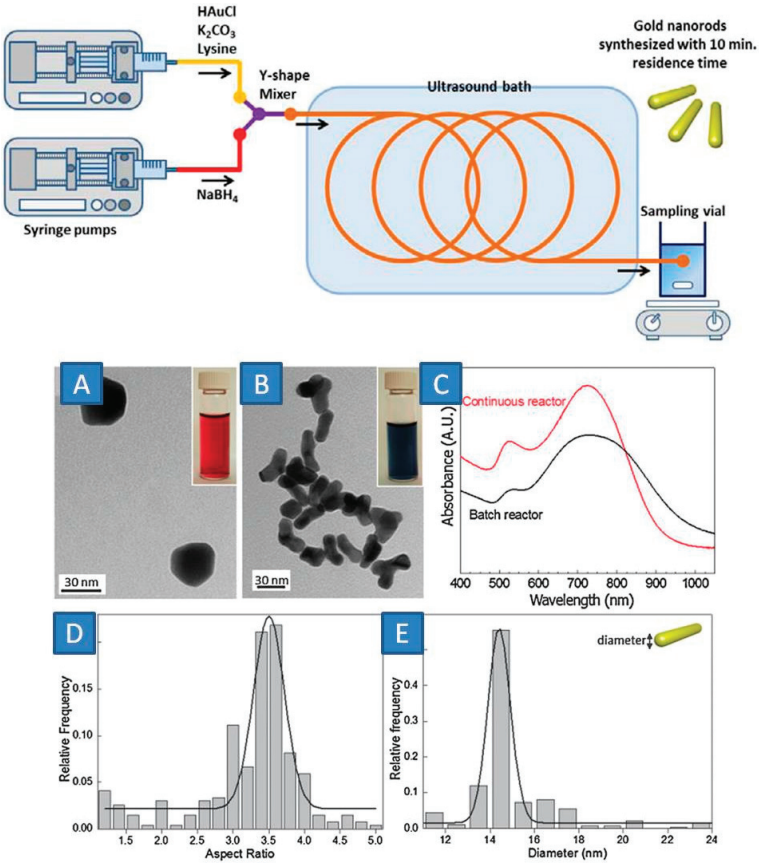

Figure 12. Cartoons for liquid flow pattern and velocity dispersion in liquid elements for (**A**) one-phase laminar flow, (**B**) water-in-oil droplet flow. Residence time distribution in (**C**) laminar flow and (**D**) droplet flow regimes. Adapted from Ref. [55] (with permission from Wiley-VCH).

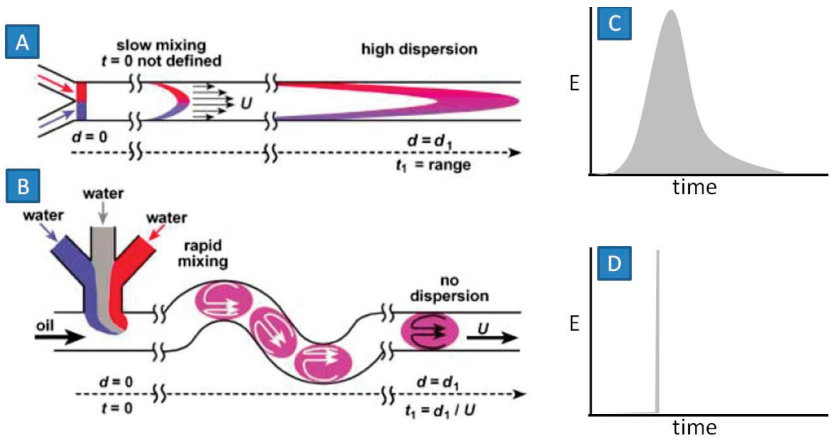

12. Multiphase Flow Operation

Two Phase Segmented Flow

Multiphase flows are created when two of more partially or immiscible fluids are brought in contact. Multiphase flow operation provides several mechanisms for enhancing and extending the performance of single phase microfluidic systems [58,59]. The long diffusion times and dispersion limitations often associated with single-phase flow can be reduced or eliminated by adding a second, immiscible, fluid stream that enhances mixing via transverse convection by inducing a recirculation motion in the liquid. The multiphase flow prevents direct contact between a liquid containing GNPs and the inner microchannel walls and thereby eliminates undesired clogging of channels due to deposition of material on wall surfaces.

In many multiphase operations, reagents containing aqueous streams are pumped inside the microfluidic mixing port/junction and are segmented into small droplets or slugs by introducing an immiscible, non-reacting fluid (gas or oil) [60]. Such droplets/slugs translate through the channel. Due to internal circulation inside these liquid segments, intense inter-phase mixing becomes possible in addition to molecular diffusion. Hence, excellent mixing is accomplished in the segmented flow, which produces a very narrow residence time distribution profile. Moreover, droplets/slugs are produced in high frequency and fidelity in terms of their content concentrations, volume where all droplets act as identical reaction flasks, which are essential to reduce polydispersity and in many cases require minimal/no post-purification operation. All these beneficial attributes of multi-phase microfluidics enabled synthesis of nanoparticles of superior quality and wide chemical-structural diversity [23–25,61]. In the following section, we discuss recent advances in multiphase microfluidics for gold nanoparticles synthesis.

Anisotropic gold nanoparticles, namely gold nanorods, Au-silica core-shell nanomaterials and ultra-small gold nanoparticles were synthesized by Duraiswamy and Khan in segmented flow operation in PDMS-made (Polydimethyloxysiloxane) microchannels [62]. They demonstrated that precise and rapid micromixing within droplets furnished high quality GNRs. Three separate streams containing (1) preformed gold seeds denoted as S (<2 nm); (2) mixture of Au^{3+}, Ag^{+} and CTAB (R1) and (3) ascorbic acid solution (R2) were premixed in a micromixer and then fed into the second micromixer where Taylor flow was created by addition of a silicone oil stream (Figure 13 panel: 1 and 2). Due to intense recirculation inside each droplet, the growth of seeds into rods occurred in a reproducible way, which in turn produced monodisperse GNRs, with insignificant amount of by-products (irregular colloidal gold). By manipulating silver content in the droplets, GNRs of different aspect ratios were produced (Figure 13; panel 3). The reactor was used for 12 h without any channel fouling.

Figure 13. (**1**) Aqueous reagents dispensing in microfluidic channel as water-in-oil droplets; (**2**) Schematic of Microfluidic set-up; (**3**) TEM photographs of produced GNRs of different aspect ratios [decreasing aspect ratios in the order from (**a**) to (**d**)]. Adapted from Ref. [62] (with permission from Wiley-VCH).

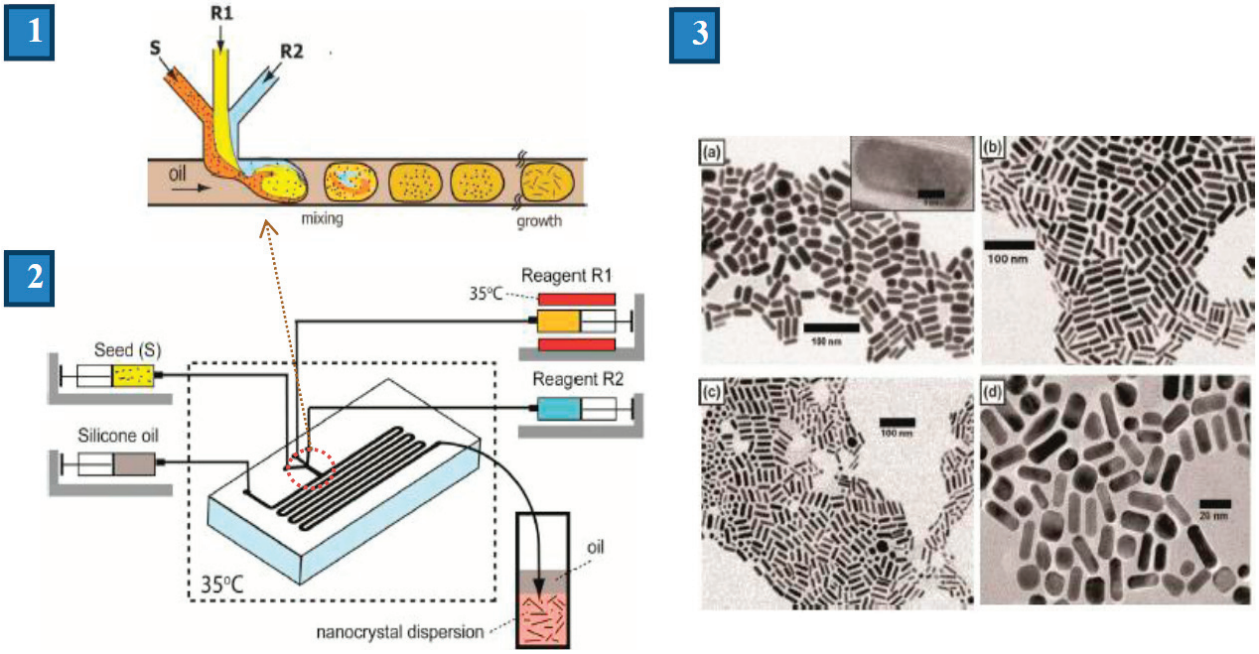

In GNRs synthesis, reliable and continuous supply of stabilized ultra-small gold nanoparticles (or seeds) is of importance to realize a reliable production facility. As discussed in the first part of this review, several authors attempted microfluidic synthesis of ultra-small GNPs using a strong reducing agent, sodium borohydride. However, sodium borohydride is known to decompose in water and produce hydrogen gas bubbles. Generation of additional gas phase in single phase operation may enhance convective mixing between liquid elements, however in a rather irregular manner [32]. Such unpredictable and irregular mixing between liquid reactants would make the process unreliable for sustained and reproducible synthesis. Saif *et al*. suggested to use gas-liquid flow in which nitrogen bubbles were introduced to absorb hydrogen released from the sodium borohydride solution (Figure 14A,B) [63]. In this system, hydrogen gas forming in the aqueous phase rapidly diffuse into the intervening nitrogen bubbles due to large concentration gradient and intense vortex in the liquid slugs. Thereby, hydrogen concentration in the aqueous phase was kept well below the saturation point to suppress nucleation and micro bubbles formation inside the aqueous slugs. A diffusion model was developed which showed that the hydrogen concentration in liquid remained below the solubility threshold of 0.9 mM. In that way, the process was run for 8 h. Spherical gold nanocrystals of below 5 nm in size were produced (Figure 14C). These seeds were successfully used to produce high quality GNRs in batch synthesis. This work envisages that a full continuous process of seed formation and subsequent use in GNRs synthesis would be possible without any flow mal-distribution by $NaBH_4$ decomposition.

Figure 14. (**A**) Schematic of gas-liquid segmented flow generation and hydrogen gas dissolution from aqueous slugs into gas bubbles; (**B**) Microscopic photograph of gas-liquid segmented flow; (**C**) Microfluidic set-up for <5 nm gold seed formation by gas-liquid segmentation and hydrogen-gas trapping. Adapted from Ref. [63] (with permission from Royal Society of Chemistry).

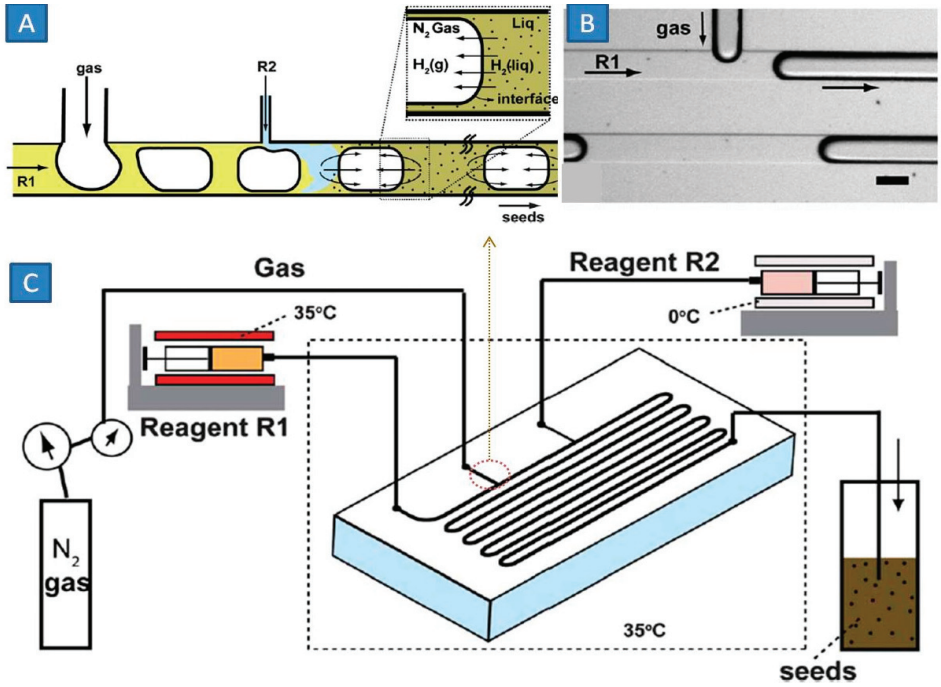

In a similar way, Jensen *et al*. created slugs of aqueous phase containing gold precursor and sodium borohydride solution inside a silicone-pyrex chip by adding either silicone oil, toluene or air as immiscible fluid (Figure 15) [64]. The mixing zone was kept at room temperature while the reaction zone (100 µL volume, either hydrophilic or hydrophobic walls) was kept at 100 °C. In the hydrophilic channel network, continuous aqueous slugs were created inside the channel by introducing the immiscible fluid. In this case, all aqueous slugs were connected to each other by a thin film. The length of the aqueous slugs had pronounced effect on the product size and polydispersity. Short slugs in toluene produced smaller particles of 3.8 ± 0.3 nm at a residence time of 10 s while longer slugs gave larger particles of 4.9 ± 3.0 nm with significant polydispersity at a residence time of 40 s. The relative slip velocity between continuous phase and aqueous slugs determined the internal mixing within the slugs and polydispersity. They observed that higher slip velocity produced narrow particle size distribution, while lower slip velocity lead to poor mixing and wide particle size distribution. The authors derived a relationship between the slug length and the particle size (and polydispersity) in terms of inter-slug mass transfer, which is a function of the slug length.

In the hydrophobic channel network, the droplets of aqueous phase were separated from each other by the continuous organic (or air) phase. They showed that axial dispersion was drastically reduced.

Figure 15. (**a**) Schematic of segmented flow generation in a hydrophilic channel; (**b**) photograph of aqueous slugs in toluene (aqueous slugs are dyed with fluorescein for better visualization); (**c**) microchip with cold (for mixing) and hot zones (for reaction). Adapted from Ref. [64] (with permission from American Chemical Society).

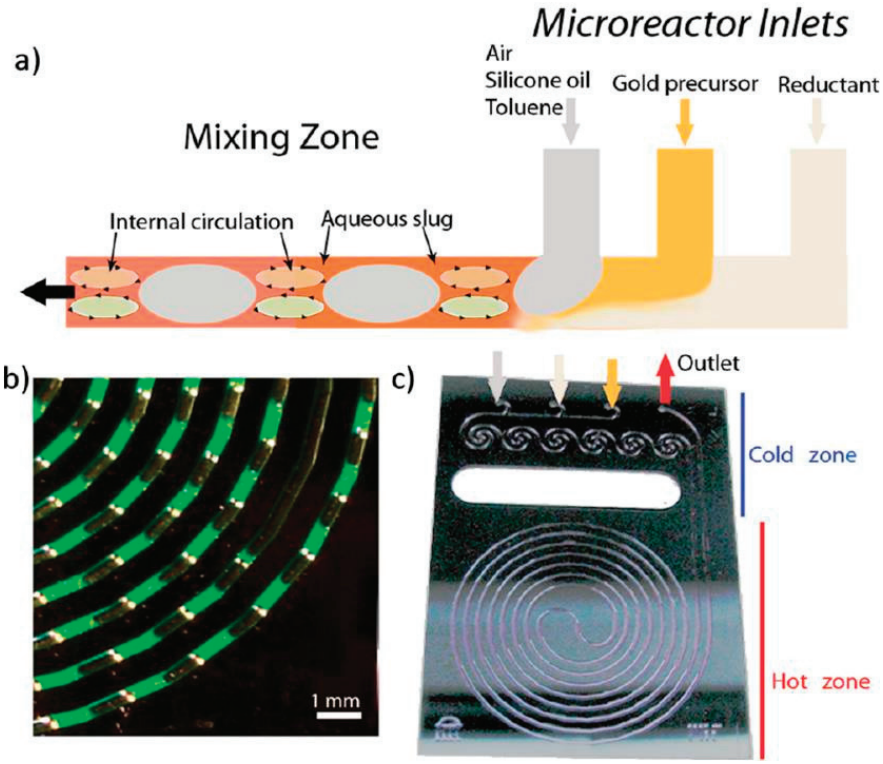

13. Three Phase Segmented Flow

Three phase segmented flow of inert gas, reactant containing aqueous droplets dispersed in a continuous oil phase was employed inside a microchannel by Duraiswamy *et al*. to produce SiO_2@Au core-shell materials with variable plasmonic behavior (600–900 nm in absorption spectrum) [65] (Figure 16). In this approach, inlet clogging due to particle deposition was avoided and droplet coalescence was considerably reduced. The gold coverage onto the silica particles was controlled by the inlet flow rates. Moreover, uncontrolled formation of free gold outside the surface of seeded-silica particles was largely avoided, which enabled pure batches of core-shell materials of varying plasmonic signatures.

In majority of work, liquid-based *i.e.*, aqueous solutions of reducing agents such as ascorbic acid, trisodium citrate, sodium borohydride *etc*. are used in redox-based nanomaterials syntheses. Carbon monoxide or hydrogen are cleaner variants of the reducing agents and can be separated from the reaction mixture by mere exposing to ambient atmosphere. Several groups utilized gaseous reactants in nanomaterials synthesis [66–68], including gold nanoshell synthesis [69]. As the size of GNPs depends on kinetics on nucleation and growth, any inhomogeneity during gas-liquid mass-transport would render the synthesis unreliable and irreproducible. Multiphase microchemical systems take advantage of the large interfacial areas. Carbon monoxide was used as reducing agent to produce SiO_2@Au nanomaterials in a PDMS-membrane microreactor by Rahman *et al*. (Figure 17A) [70].

In this way, CO was dissolved inside the aqueous droplets without forming any gas bubbles. (Figure 17B,C). Depending on the residence time of aqueous droplets (1–70 s), the flow rate of CO across the membrane was adjusted to control the rate of gold deposition onto the silica core. In this way, SiO_2@Au nanomaterials with variable gold coverage and impressively high purity (free from colloidal gold) were produced (Figure 17D). Rapid quenching of the gold deposition was possible by eliminating gas/liquid contact in the downstream section.

Figure 16. (**1**) Microfluidic formation of gas-aqueous foam in continuous oil; (**2**) Panel showing TEM photographs of (**a**) gold-seeded silica particles, (**b**) small gold island on silica, (**c**) dense gold islands on silica, (**d**) fully developed gold shell on silica spheres, (**e**) inset showing UV-Vis absorption of the particles (**a**)–(**d**). Adapted from Ref. [65] (with permission from American Chemical Society).

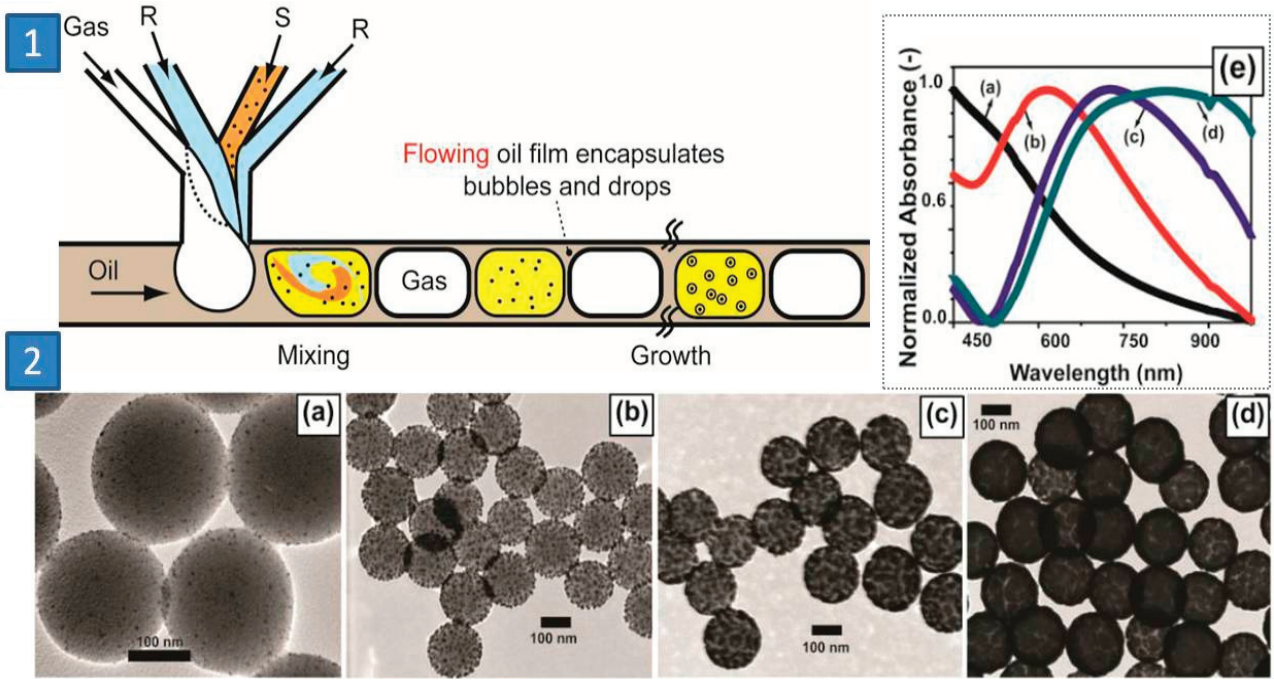

14. Application of Ionic Liquids

Recently, ionic liquids (IL) are considered as an alternative reaction medium for nanoparticles synthesis, given their unique molecular nature, polarity and ability to stabilize nanoparticles via numerous modes of interactions [71–73]. Ionic liquids may serve a dual purpose as a solvent and molecular/colloidal stabilizer, however GNPs synthesis in IL is challenging in terms of size distribution, presumably due to poor mass transport in viscous ionic liquids.

Figure 17. (**A**) Microfluidic set-up for water-oil droplet formation; Schematic (**B**) and microscopic photograph (**C**) of gas-liquid contacting across the membrane; (**D**) Core-shell formation with variable gold coverage (**a**–**d**). Adapted from Ref. [70] (with permission from Royal Society of Chemistry).

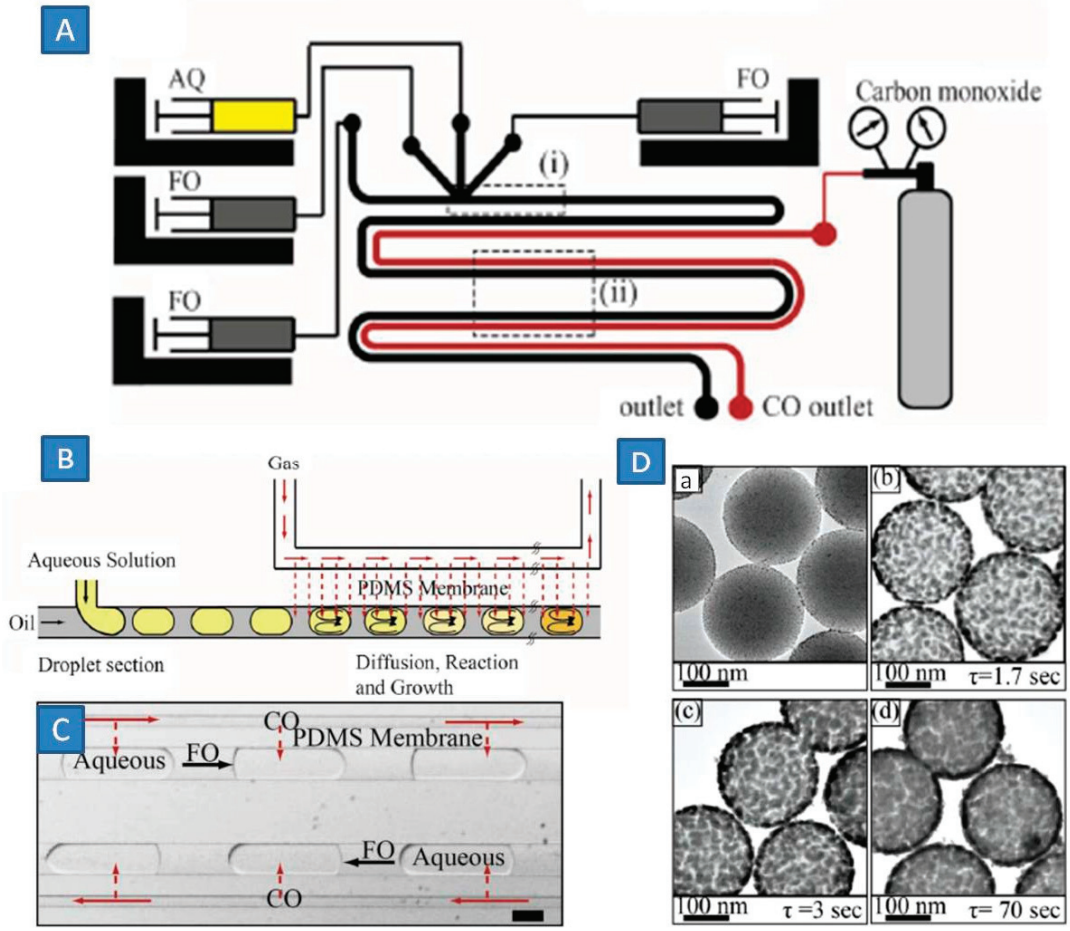

Lazarus *et al*. leveraged the beneficial attributes of both ionic liquids and microreactors for the synthesis of GNPs [74]. The authors used a flow-focusing microfluidic protocol where in the mixing zone a stream of butyl methylimidazolium tetrafluoroborate (BMIM-BF_4) was injected between the two reactant streams ($HAuCl_4$/1-methylimidazole and $NaBH_4$ in BMIM-BF_4) to allow fast mixing (Figure 18A). As this stream arrived at a flow-focusing cross-junction, two oil streams were fed orthogonal to the IL streams. At oil flow rates below 3000 μL h^{-1}, the middle IL stream maintained co-parallel flow with the flanking oil streams (inset A in Figure 18), while above this threshold value, droplets of IL were formed (Inset B in Figure 18). Fast and homogeneous mixing enable rapid nucleation burst, and ensure monodispersity in the final fully grown GNPs. The liquid mixture was quenched at the outlet with ethanol to separate the produced GNPs and analyzed by spectroscopic and microscopic methods. The best quality GNPs in terms of polydispersity (12%), size and roundedness of the GNPs was achieved from the droplet protocol. The mean particle diameter was 4.38 ± 0.53 nm having spherical features. The roundness, defined as (4 × particle area)/(π × (major axis length)^2), below 0.85 was observed only in 15% particles. UV-vis spectra of suspensions exhibited narrow surface plasmon bands cantered at 518.5 nm, typical of non-agglomerated GNPs. With the parallel

flow protocol, the GNPs were of inferior structural features compared to droplet protocol. The mean diameter was 5.65 ± 1.03 nm with a polydispersity index of 18.2%. The roundness below 0.85 was observed in 23% particles. Intriguingly, thinning of the innermost lamella (IL liquid) by increasing the oil flow rate showed tendency of the GNPs to become more monodispersed compared to the case when the inert oil phase was completely excluded. Understandably, mixing within droplets is most efficient due to intense vortex generation, while interdiffusion between liquid streams become progressively limited as the characteristic dimension of the lamella becomes larger. In all cases, the synthesis was completed in 19 s. A benchmarking experiment in the batch requires at least 1 min. The obtained nanoparticles were significantly spheroidal with 28% having a roundness less than 0.85. The mean diameter was larger than that in the flow synthesis (6.25 ± 1.29 nm; polydispersity: 20.6%).

Figure 18. Schematic of the PDMS device (3 × 5 cm) with flow focusing geometry. channel widths and depths are 600 µm and 95 µm (flow-focusing region width: 400 µm), respectively, with a total channel volume of 7.6 µm. Inset **A**: parallel flow of IL and inert Oil at Oil flow rates below 3000 µL h^{-1}, inset **B**: IL droplet formation at Oil flow rates beyond 3000 µL h^{-1}. Adapted from Ref. [74] (with permission from Royal Society of Chemistry).

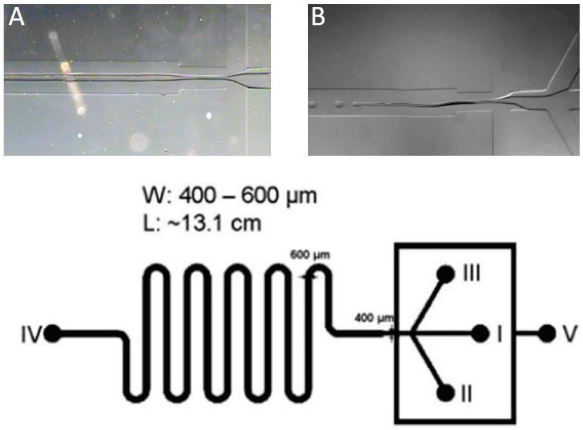

Larazus *et al*. later reported the use of ionic liquid variant of sodium borohydride, namely, 1-butyl-1-methylimidazolium borohydride (BMIM BH_4), to increase the solubility of reducing agent in butyl methylimidazolium bis-triflamide ionic liquid (BMIM NTf_2) in the synthesis of GNPs in a fluorinated PDMS channel [75]. The dispersed phase contained the IL reducing agent and gold ions while a fluorocarbon oil was continuous phase. At low ionic liquid/oil flow ratios of 0.05–0.25, droplets were formed immediately at the junction location. In comparison to batch conditions their microfluidic method produced GNPs of smaller size and higher monodispersity.

15. Scale-Up of GNP Synthesis Using Flow-Chemistry

Only few reports emerged that tackles the scale-up issue associated with complex gold nanoparticles production. Gomez *et al*. presented the first example of continuous synthesis of hollow GNPs in a flow reactor composed of T-pieces for mixing and a 1.6 mm diameter PTFE tube as

residence time unit at two different scales corresponding to production rates of 0.2 and 2.0 mmol Au/min [76]. Hollow GNPs exhibit plasmonic behavior, where the ratio of particle diameter to the thickness of the shell determines the surface plasmon resonance (SPR) peak position and their uniformity determines the SPR bandwidth. At first, a cobalt solution was mixed with sodium borohydride in the first T-junction which produced cobalt nanospheres within 180 s of reaction time (Figure 19). This step was diffusion limited, and the reaction time was set slightly higher than the diffusive mixing time of 160 s. In the second mixer, a gold precursor was introduced which was reduced at the surface of cobalt particles which in turn was dissolved out after being oxidized. In the scale-up process, a stream of oxygen was introduced in the 3rd mixing port to facilitate this galvanic dissolution process to form completely Co free hollow GNPs. *In-situ* functionalization of hollow GNPs with thiolated polyethylene glycols was demonstrated to enhance the biocompatibility. An integrated continuous UV sterilization step facilitated the on-site *in vivo* use of the as-synthesized materials. Such integration of continuous production and downstream processing in a millireactor holds promises for scaling up of "ready-to-use" nanoparticles production.

Figure 19. Microfluidic schematic of hollow gold nanoparticles in a multi-step approach with average reaction time for each step. Insets are TEM photographs of the corresponding nanoparticles formed throughout the process at different stages. Adapted from Ref. [76] (with permission from Royal Society of Chemistry).

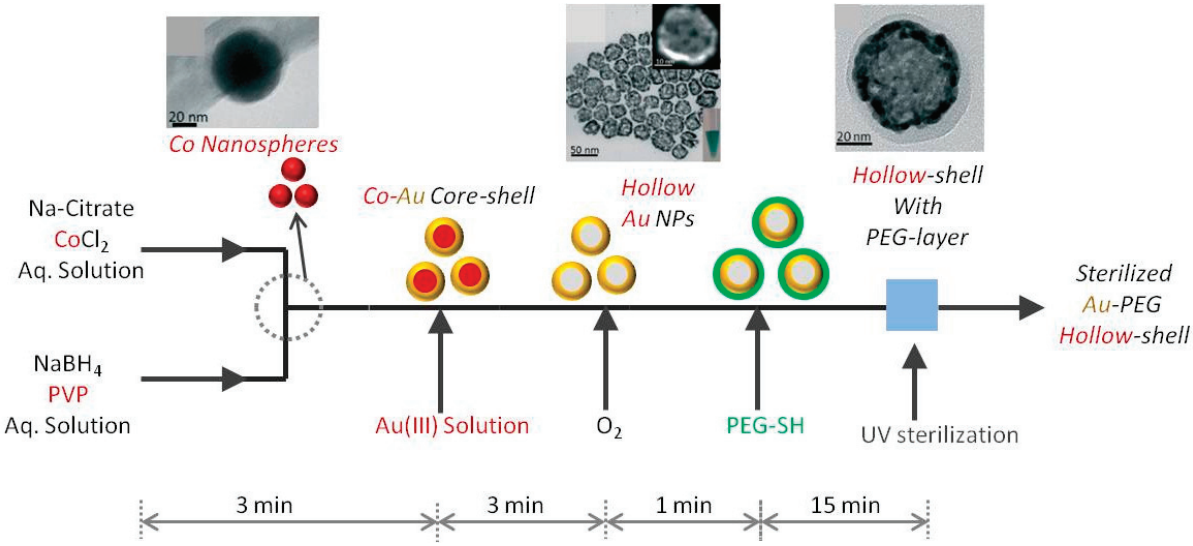

Lohse *et al*. scaled up the microfluidic synthesis to produce 10 L of suspension of GNRs with aspect ratio 2 in three consecutive runs amounting to a total of 1.0 g of product [77]. The product yield and quality showed improvement in regards to monodispersity when compared to the synthesis in a batch system. This clearly shows superiority of microfluidic synthesis over conventional bath synthesis that typically produces 50 mg of GNPs. This was possible using 5–10 fold higher concentrations of reactants in the flow system. Off-the shelf materials were used to construct the fluidic reactor, namely from TYGON polyvinyl tubing as the reactor and polyethylene connectors as mixing ports. In the first step, CTAB-stabilized spherical GNPs were sued via rapid reduction of gold with $NaBH_4$ was conducted in the flow reactor that produces GNPs that would be used as seed

elements in the GNRs synthesis. In the second stage, these seeds were mixed with a growth solution containing (gold salt, CTAB, silver nitrate and ascorbic acid) to generate the rods of tight batch-quality (in terms of desired shape-size and avoidance of undesired by-products). By changing concentrations GNRs with different length (and aspect ratios were obtained. They produce a wide range of plasmonic bands up to near infrared region (Figure 20).

Figure 20. (**A**) UV-Vis spectrum of GNRs of various aspect ratios; (**B**) TEM Photographs of GNRs, inset showing the simple T-junction used as micromixer in this work [variable aspect ratios of the produces gold nanorods are shown in (i)-(v)]. Adapted from Ref. [77] (with permission from American Chemical Society).

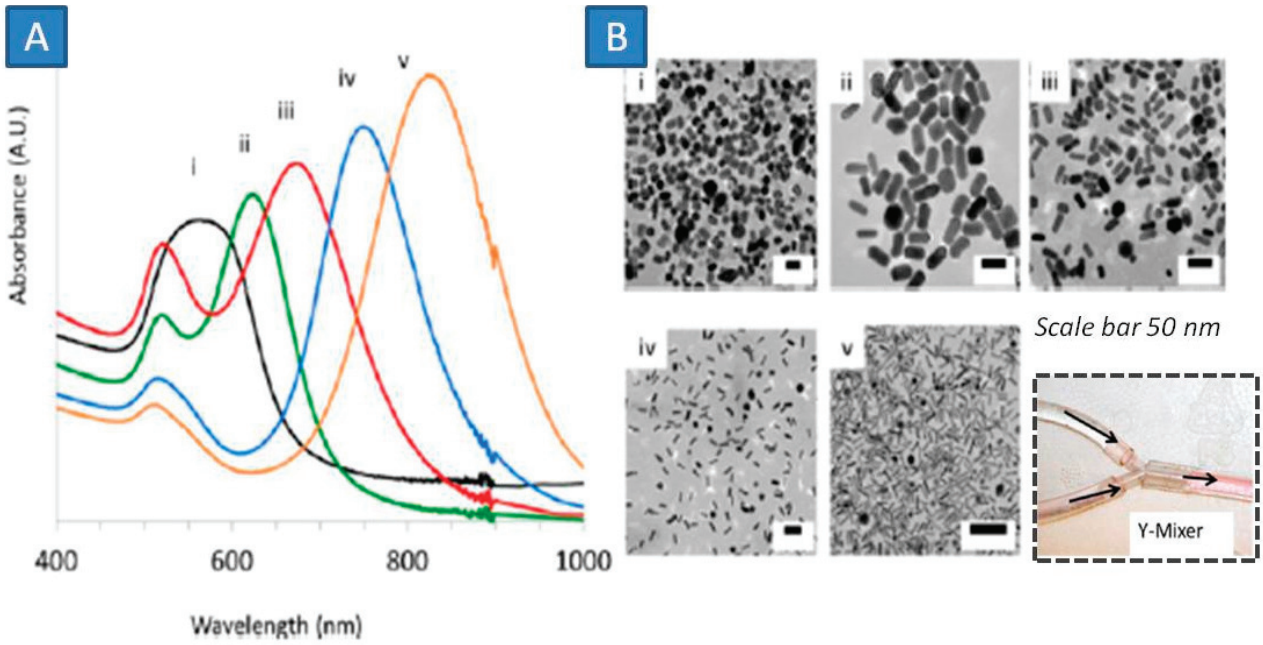

16. Concluding Remarks

Multiphase microreactors have proven particularly promising in the synthesis of complex Au nanoparticles with high monodispersity within short timescales. The precise manipulation of bubbles, droplets or immiscible fluid streams in microfluidic chips is usually achieved by elaborate chip designs that address fluid-fluid hydrodynamics under laminar flow conditions and fluid-solid interactions in microchannels. Such conditions enable fast heating and quenching of reaction mixture under well-defined hydrodynamic conditions. Scale-up is a necessary step when going from mg/day to g/day production rate. The scale-up of multiphase flow remains a major challenge in current microfluidic applications. It often requires application of on-line measurement techniques to monitor the slug lengths, and other dynamic parameters such as flow reversals in order to provide fast feedback to a process control system.

Gas-liquid-liquid three-phase flow in microfluidic systems still remains as a less explored area and has received growing interests in recent years due to its important implications for the synthesis of gold nanoparticles. The use of an inert gas to break up an otherwise liquid-liquid segmented or parallel flow in microchannels yields a better quality of obtained nanomaterials. Hydrodynamics of

three phase (gas-liquid-liquid) flow is not yet fully understood. There exist a rather limited number of publications dealing with the design and operation of three-phase flow in microchannels, however the microfluidic systems being far from fully optimized. This is largely due to the current inadequate understanding on the underlying hydrodynamics. The fundamental laws governing the three-phase generation and flow in microchannels are not yet understood due to their complex nature. The influence of flow rate on the size of bubbles or droplets produced under a three-phase flow has been revealed with some empirical correlations. However, the influence of other parameters, such as fluid properties and the geometry of inlet mixer, were rarely taken into account.

The large interfacial areas associated with multiphase microflows provide efficient mass transfer between immiscible fluids. This opens up new perspective to replace aggressive reducing agent with reactive gases, which would allow making a step forward towards green process engineering.

Acknowledgments

The financial support provided by the European Research Council (ERC) project 279867, is gratefully acknowledged. We thank Yanging Jing for help in the literature survey.

Conflicts of Interest

The authors declare no conflict of interest.

References

1. Huaizhi, Z.; Yuantao, N. China's Ancient Gold Drugs. *Gold Bull.* **2001**, *34*, 24–29.
2. Brown, C.L.; Whitehouse, M.W.; Agarwal, D.S.; Tupe, S.G.; Paknikar, K.M.; Teiknik, E.R.T. Nanogoldpharmaceutics. *Gold Bull.* **2007**, *40*, 245–250.
3. Daniel, M.-C.; Astruc, D. Gold Nanoparticles: Assembly, Supramolecular Chemistry, Quantum-Size-Related Properties, and Applications Toward Biology, Catalysis, and Nanotechnology. *Chem. Rev.* **2004**, *104*, 293–346.
4. Faraday, M. The Bakerian Lecture: Experimental Relations of Gold (and Other Metals) to Light. *Philos. Trans. R. Soc. Lond.* **1857**, *147*, 145–181.
5. Turkevich, J.; Hillier, J. Electron Microscopy of Colloidal Systems. *Anal. Chem.* **1949**, *21*, 475–485.
6. Turkevich, J.; Stevenson, P.C.; Hillier, J. A study of Nucleation and Growth Processes in the Synthesis of Colloidal Gold. *Discuss. Faraday Soc.* **1951**, *11*, 55–75.
7. Boisselier, E.; Astruc, D. Gold Nanoparticles in Nanomedicine: Preparations, Imaging, Diagnostics, Therapies and Toxicity. *Chem. Soc. Rev.* **2009**, *38*, 1759–1782.
8. Chen, H.; Shao, L.; Li, Q.; Wang, J. Gold Nanorods and Their Plasmonic Properties. *Chem. Soc. Rev.* **2013**, *42*, 2679–2724.
9. Cobley, C.M.; Chen, J.; Cho, E.C.; Wang, L.V.; Xia, Y. Gold Nanostructures: A Class of Multifunctional Materials for Biomedical Applications. *Chem. Soc. Rev.* **2011**, *40*, 44–56.
10. Corma, A.; Garcia, H. Supported Gold Nanoparticles as Catalysts for Organic Reactions. *Chem. Soc. Rev.* **2008**, *37*, 2096–2126.

11. Doane, T.L.; Burda, C. The Unique Role of Nanoparticles in Nanomedicine: Imaging, Drug Delivery and Therapy. *Chem. Soc. Rev.* **2012**, *41*, 2885–2911.
12. Dreaden, E.C.; Alkilany, A.M.; Huang, X.; Murphy, C.J.; el-Sayed, M.A. The Golden Age: Gold Nanoparticles for Biomedicine. *Chem. Soc. Rev.* **2012**, *41*, 2740–2779.
13. Eustis, S.; El-Sayed, M.A. Why Gold Nanoparticles Are More Precious Than Pretty Gold: Noble Metal Surface Plasmon Resonance and Its Enhancement of the Radiative and Nonradiative Properties of Nanocrystals of Different Shapes. *Chem. Soc. Rev.* **2006**, *35*, 209–217.
14. Hutchings, G.J.; Brust, M.; Schmidbaur, H. Gold—An Introductory Perspective. *Chem. Soc. Rev.* **2008**, *37*, 1759–1765.
15. Lee, D.-E.; Koo, H.; Sun, I.-C.; Ryu, J.H.; Kim, K.; Kwon, I.C. Multifunctional Nanoparticles for Multimodal Imaging and Theragnosis. *Chem. Soc. Rev.* **2012**, *41*, 2656–2672.
16. Li, G.; Jin, R. Atomically Precise Gold Nanoclusters as New Model Catalysts. *Acc. Chem. Res.* **2013**, *46*, 1749–1758.
17. Llevot, A.; Astruc, D. Applications of Vectorized Gold Nanoparticles to the Diagnosis and Therapy of Cancer. *Chem. Soc. Rev.* **2012**, *41*, 242–257.
18. La Mer V.K.; Dinegar, H. Theory, Production and Mechanism of Formation of Monodisperse Hydrosols. *J. Am. Chem. Soc.* **1950**, *72*, 4847–4854.
19. Polte, J.; Tuaev, X.; Wuithschick, M.; Fischer, A.; Thuenemann, A.F.; Rademann, K.; Kraehnert, R.; Emmerling, F. Formation Mechanism of Colloidal Silver Nanoparticles: Analogies and Differences to the Growth of Gold Nanoparticles. *ACS Nano* **2012**, *6*, 5791–5802.
20. Hessel, V.; Hardt, S.; Löwe, H. *Chemical Micro-Process Engineering*; Wiley-VCH: Weinhein, Germany, 2004.
21. Reschetilowski, W. *Microreactors in Preparative Chemistry*; Wiley-VCH: Weinhein, Germany, 2013.
22. Wirth, T. *Microreactors in Organic Chemistry and Catalysis*; Wiley-VCH: Weinhein, Germany, 2013.
23. Abou-Hassan, A.; Sandre, O.; Cabuil, V. Microfluidics in Inorganic Chemistry. *Angew. Chem. Int. Ed. Engl.* **2010**, *49*, 6268–6286.
24. Marre, S.; Jensen, K.F. Synthesis of Micro and Nanostructures in Microfluidic Systems. *Chem. Soc. Rev.* **2010**, *39*, 1183–1202.
25. Song, Y.; Hormes, J.; Kumar, C.S.S.R. Microfluidic Synthesis of Nanomaterials. *Small* **2008**, *4*, 698–711.
26. Navin, C.V.; Krishna, K.S.; Theegala, C.S.; Kumar, C.S.S.R. Lab-on-a-Chip Devices for Gold Nanoparticle Synthesis and Their Role as a Catalyst Support for Continuous Flow Catalysis. *Nanotechnol. Rev.* **2013**, doi:10.1515/ntrev-2013-0028.
27. Wagner, J.; Kirner, T.; Mayer, G.; Albert, J.; Köhler, J. Generation of Metal Nanoparticles in a Microchannel Reactor. *Chem. Eng. J.* **2004**, *101*, 251–260.
28. Wagner, J.; Köhler, J.M. Continuous Synthesis of Gold Nanoparticles in a Microreactor. *Nano Lett.* **2005**, *5*, 685–691.

29. Köhler, J.M.; Wagner, J.; Albert, J. Formation of Isolated and Clustered Au Nanoparticles in the Presence of Polyelectrolyte Molecules Using a Flow-through Si-Chip Reactor. *J. Mater. Chem.* **2005**, *15*, 1924–1930.
30. Wagner, J.; Tshikhudo, T.; Kohler, J. Microfluidic Generation of Metal Nanoparticles by Borohydride Reduction. *Chem. Eng. J.* **2008**, *135*, S104–S109.
31. Haruta, M.; Yamada, N.; Kobayashi, T.; Iijima, S. Gold Catalysts Prepared by Co-Precipitation for Low-Temperature Oxidation of Hydrogen and of Carbon Monoxide, *J. Catal*. **1989**, *115*, 301–309.
32. Tsunoyama, H.; Ichikuni, N.; Tsukuda, T. Microfluidic Synthesis and Catalytic Application of PVP-Stabilized, Approximately 1 nm Gold Clusters. *Langmuir* **2008**, *24*, 11327–11330.
33. Luty-Błocho, M.; Fitzner, K.; Hessel, V.; Löb, P.; Maskos, M.; Metzke, D.; Pacławski, K.; Wojnicki, M. Synthesis of Gold Nanoparticles in an Interdigital Micromixer Using Ascorbic Acid and Sodium Borohydride as Reducers. *Chem. Eng. J.* **2011**, *171*, 279–290.
34. Ishizaka, T.; Ishigaki, A.; Kawanami, H.; Suzuki, A.; Suzuki, T.M. Dynamic Control of Gold Nanoparticle Morphology in a Microchannel Flow Reactor by Glucose Reduction in Aqueous Sodium Hydroxide Solution. *J. Colloid Interface Sci.* **2012**, *367*, 135–138.
35. Jun, H.; Fabienne, T.; Florent, M.; Coulon, P.; Nicolas, M.; Olivier, S. Understanding of the Size Control of Biocompatible Gold Nanoparticles in Millifluidic Channels. *Langmuir* **2012**, *28*, 15966–15974.
36. Gómez-de Pedro, S.; Puyol, M.; Alonso-Chamarro, J. Continuous Flow Synthesis of Nanoparticles Using Ceramic Microfluidic Devices. *Nanotechnology* **2010**, *21*, 415603.
37. Ftouni, J.; Penhoat, M.; Addad, A.; Payen, E.; Rolando, C.; Girardon, J.-S. Highly Controlled Synthesis of Nanometric Gold Particles by Citrate Reduction using the Short Mixing, Heating and Quenching Times Achievable in a Microfluidic Device. *Nanoscale* **2012**, *4*, 4450–4454.
38. Sugie, A.; Song, H.; Horie, T.; Ohmura, N.; Kanie, K.; Muramatsu, A.; Mori, A. Synthesis of Thiol-Capped Gold Nanoparticle with a Flow System Using Organosilane as a Reducing Agent. *Tetrahedron Lett.* **2012**, *53*, 4457–4459.
39. Krishna, K.S.; Navin, C.V.; Biswas, S.; Singh, V.; Ham, K.; Bovenkamp, G.L.; Theegala, C.S.; Miller, T.; Spivey, J.J.; Kumar, C.S.S.R. Millifluidics for Time-Resolved Mapping of the Growth of Gold Nanostructures. *J. Am. Chem. Soc.* **2013**, *135*, 5450–5456.
40. Cortie, M.B.; McDonagh, A.M. Synthesis and Optical Properties of Hybrid and Alloy Plasmonic Nanoparticles. *Chem. Rev.* **2011**, *111*, 3713–3735.
41. Ghosh Chaudhuri, R.; Paria, S. Core/shell Nanoparticles: Classes, Properties, Synthesis Mechanisms, Characterization, and Applications. *Chem. Rev.* **2012**, *112*, 2373–2433.
42. Grzelczak, M.; Pérez-Juste, J.; Mulvaney, P.; Liz-Marzán, L.M. Shape Control in Gold Nanoparticle Synthesis. *Chem. Soc. Rev.* **2008**, *37*, 1783–1791.
43. Halas, N.J.; Lal, S.; Link, S.; Chang, W.-S.; Natelson, D.; Hafner, J.H.; Nordlander, P. A Plethora of Plasmonics from the Laboratory for Nanophotonics at Rice University. *Adv. Mater.* **2012**, *24*, 4842–4877.

44. Hu, M.; Chen, J.; Li, Z.-Y.; Au, L.; Hartland, G.V.; Li, X.; Marquez, M.; Xia, Y. Gold Nanostructures: Engineering Their Plasmonic Properties for Biomedical Applications. *Chem. Soc. Rev.* **2006**, *35*, 1084–1094.
45. Schärtl, W. Current Directions in Core-Shell Nanoparticle Design. *Nanoscale* **2010**, *2*, 829–843.
46. Vigderman, L.; Khanal, B.P.; Zubarev, E.R. Functional Gold Nanorods: Synthesis, Self-Assembly, and Sensing Applications. *Adv. Mater.* **2012**, *24*, 4811–4841.
47. Huang, X.; Neretina, S.; el-Sayed, M. Gold Nanorods: From Synthesis and Properties to Biological and Biomedical Applications. *Adv. Mater.* **2009**, *21*, 4880–4910.
48. Köhler, J.M.; Held, M.; Hübner, U.; Wagner, J. Formation of Au/Ag Nanoparticles in a Two Step Micro Flow-Through Process. *Chem. Eng. Technol.* **2007**, *30*, 347–354.
49. Sun, L.; Luan, W.; Shan, Y.; Tu, S. One-Step Synthesis of Monodisperse Au–Ag Alloy Nanoparticles in a Microreaction System. *Chem. Eng. J.* **2012**, *189–190*, 451–455.
50. Stöber, W.; Fink, A.; Bohn, E. Controlled Growth of Monodisperse Silica Spheres in the Micron Size Range. *J. Colloid Interface Sci*. **1968**, *26*, 62–69.
51. Gomez, L.; Arruebo, M.; Sebastian, V.; Gutierrez, L.; Santamaria, J. Facile Synthesis of SiO_2–Au Nanoshells in a Three-Stage Microfluidic System. *J. Mater. Chem.* **2012**, *22*, 21420.
52. Boleininger, J.; Kurz, A.; Reuss, V.; Sönnichsen, C. Microfluidic Continuous Flow Synthesis of Rod-Shaped Gold and Silver Nanocrystals. *Phys. Chem. Chem. Phys.* **2006**, *8*, 3824.
53. Bullen, C.; Latter, M.J.; D'Alonzo, N.J.; Willis, G.J.; Raston, C.L. A Seedless Approach to Continuous Flow Synthesis of Gold Nanorods. *Chem. Commun. (Camb.).* **2011**, *47*, 4123–4125.
54. Sebastián, V.; Lee, S.-K.; Zhou, C.; Kraus, M.F.; Fujimoto, J.G.; Jensen, K.F. One-Step Continuous Synthesis of Biocompatible Gold Nanorods for Optical Coherence Tomography. *Chem. Commun. (Camb.).* **2012**, *48*, 6654–6656.
55. Song, H.; Tice, J.D.; Ismagilov, R.F. A Microfluidic System for Controlling Reaction Networks in Time. *Angew. Chem. Int. Ed*. **2003**, *42*, 767–772.
56. Yen, B.K.H.; Günther, A.; Schmidt, M.A.; Jensen, K.F.; Bawendi, M.G. A Microfabricated Gas-Liquid Segmented Flow Reactor for High-Temperature Synthesis: The Case of CdSe Quantum Dots. *Angew. Chem. Int. Ed. Engl.* **2005**, *44*, 5447–5451.
57. Cantu-Perez, A.; Barrass, S.; Gavriilidis, A. Hydrodynamics and reaction studies in a layered herringbone channel. *Chem. Eng. J*. **2011**, *167*, 657–665.
58. Theberge, A.B.; Courtois, F.; Schaerli, Y.; Fischlechner, M.; Abell, C.; Hollfelder, F.; Huck, W.T.S. Microdroplets in Microfluidics: An Evolving Platform for Discoveries in Chemistry and Biology. *Angew. Chem. Int. Ed.* **2010**, *49*, 5846–5868.
59. Teh, S.-Y.; Lin, R.; Hung, L.-H.; Lee, A.P. Droplet Microfluidics. *Lab Chip* **2008**, *8*, 198–220.
60. Baroud, C.N.; Gallaire, F.; Dangla, R. Dynamics of Microfluidic Droplets. *Lab Chip* **2010**, *10*, 2032–2045.
61. Krishna, K.S.; Li, Y.; Li, S.; Kumar, C.S.S.R. Lab-on-a-Chip Synthesis of Inorganic Nanomaterials and Quantum Dots for Biomedical Applications. *Adv. Drug Deliv. Rev.* **2013**, *65*, 1470–1495.
62. Duraiswamy, S.; Khan, S.A. Droplet-Based Microfluidic Synthesis of Anisotropic Metal Nanocrystals. *Small* **2009**, *5*, 2828–2834.

63. Khan, S.A.; Duraiswamy, S. Controlling Bubbles Using Bubbles—Microfluidic Synthesis of Ultra-Small Gold Nanocrystals with Gas-Evolving Reducing Agents. *Lab Chip* **2012**, *12*, 1807–1812.
64. Cabeza, V.S.; Kuhn, S.; Kulkarni, A.A.; Jensen, K.F. Size-Controlled Flow Synthesis of Gold Nanoparticles Using a Segmented Flow Micro Fluidic Platform. *Langmuir* **2012**, *28*, 7007–7013.
65. Duraiswamy, S.; Khan, S.A. Plasmonic Nanoshell Synthesis in Microfluidic Composite Foams. *Nano Lett.* **2010**, *10*, 3757–3763.
66. Huang, X.; Tang, S.; Mu, X.; Dai, Y.; Chen, G.; Zhou, Z.; Ruan, F.; Yang, Z.; Zheng, N. Freestanding Palladium Nanosheets with Plasmonic and Catalytic Properties. *Nat. Nanotechnol.* **2011**, *6*, 28–32.
67. Kang, Y.; Ye, X.; Murray, C.B. Size- and Shape-Selective Synthesis of Metal Nanocrystals and Nanowires Using CO as a Reducing Agent. *Angew. Chem. Int. Ed. Engl.* **2010**, *49*, 6156–6159.
68. Wu, B.; Zheng, N.; Fu, G. Small Molecules Control the Formation of Pt Nanocrystals: A Key Role of Carbon Monoxide in the Synthesis of Pt Nanocubes. *Chem. Commun. (Camb).* **2011**, *47*, 1039–1041.
69. Brinson, B.E.; Lassiter, J.B.; Levin, C.S.; Bardhan, R.; Mirin, N.; Halas, N.J. Nanoshells Made Easy: Improving Au Layer Growth on Nanoparticle Surfaces. *Langmuir* **2008**, *24*, 14166–14171.
70. Rahman, M.T.; Krishnamurthy, P.G.; Parthiban, P.; Jain, A.; Park, C.P.; Kim, D.-P.; Khan, S.A. Dynamically Tunable Nanoparticle Engineering Enabled by Short Contact-Time Microfluidic Synthesis with a Reactive Gas. *RSC Adv.* **2013**, *3*, 2897–2900.
71. Dahl, J.A.; Maddux, B.L.S.; Hutchison, J.E. Toward Greener Nanosynthesis. *Chem. Rev.* **2007**, *107*, 2228–2269.
72. Dupont, J.; Scholten, J.D. On the Structural and Surface Properties of Transition-Metal Nanoparticles in Ionic Liquids. *Chem. Soc. Rev.* **2010**, *39*, 1780–1804.
73. Torimoto, T.; Tsuda, T.; Okazaki, K.; Kuwabata, S. New Frontiers in Materials Science Opened by Ionic Liquids. *Adv. Mater.* **2010**, *22*, 1196–1221.
74. Lazarus, L.L.; Yang, A.S.-J.; Chu, S.; Brutchey, R.L.; Malmstadt, N. Flow-Focused Synthesis of Monodisperse Gold Nanoparticles Using Ionic Liquids on a Microfluidic Platform. *Lab Chip* **2010**, *10*, 3377–3379.
75. Lazarus, L.L.; Riche, C.T.; Marin, B.C.; Gupta, M.; Malmstadt, N.; Brutchey, R.L. Two-Phase Micro Fl Uidic Droplet Flows of Ionic Liquids for the Synthesis of Gold and Silver Nanoparticles. *ACS Appl. Mater. Interfaces* **2012**, *4*, 3077–3083.
76. Gomez, L.; Sebastian, V.; Irusta, S.; Ibarra, A.; Arruebo, M.; Santamaria, J. Scaled-up Production of Plasmonic Nanoparticles Using Microfluidics: From Metal Precursors to Functionalized and Sterilized Nanoparticles. *Lab Chip* **2014**, *14*, 325–332.
77. Lohse, S.E.; Eller, J.R.; Sivapalan, S.T.; Plews, M.R.; Murphy, C.J. A Simple Milli-Fluidic Benchtop Reactor System for the High-Throughput Synthesis and Functionalization of Gold Nanoparticles with Different Sizes and Shapes. *ACS Nano* **2013**, *7*, 4135–4150.

Enhanced Performance of Oxidation of Rosalva (9-decen-1-ol) to Costenal (9-decenal) on Porous Silicon-Supported Silver Catalyst in a Microstructured Reactor

Enhong Cao, Ioannis Zuburtikudis, Noor Al-Rifai, Mark Roydhouse and Asterios Gavriilidis

Abstract: The use of metal-assisted HF chemical etching as a convenient technique to produce a few microns thick porous layer in silicon microchannels was demonstrated. Gas phase selective oxidation of rosalva to its aldehyde (costenal) was performed in glass/silicon microstructured reactors at temperatures of 375–475 °C on silver catalyst which was deposited on both porous and flat silicon surface by sputter-coating. The effects of temperature (375–475 °C), rosalva concentration (1.17%–3.43%), O_2 to rosalva ratio (0.5–20) and residence time on the reaction were investigated. The reactivity of rosalva on the porous silicon supported silver was 5.7–6.4 times higher than on the thin film silver catalyst at 450 °C. Furthermore, activation energy for the porous silicon supported silver was lower. Isothermal conditions in the microreactors allowed high conversion and selectivity to be achieved in a wide range of temperature and oxygen concentration. At typical reaction conditions (1.75% rosalva, O_2/rosalva = 3, residence time 18 ms and 450 °C), conversion of 97% and selectivity of 95% to costenal was achieved, corresponding to a turnover frequency of 268 h^{-1}.

Reprinted from *Processes*. Cite as: Cao, E.; Zuburtikudis, I.; al-Rifai, N.; Roydhouse, M.; Gavriilidis, A. Enhanced Performance of Oxidation of Rosalva (9-decen-1-ol) to Costenal (9-decenal) on Porous Silicon-Supported Silver Catalyst in a Microstructured Reactor. *Processes* **2014**, *2*, 141-157.

1. Introduction

Catalytic selective oxidation of alcohols is a fundamental process in synthetic chemistry as carbonyl compounds have widespread applications in the flavor, pharmaceutical, agrochemical, and fragrance industries [1,2]. Oxidation of alcohols by using air or molecular oxygen has been proposed as a green methodology to replace traditional stoichiometric inorganic oxidants such as K_2CrO_7 and $KMnO_4$, where the dispersal of unwanted by-products and the heavy metal waste represents a huge impact on the environment [3]. The oxidation of alcohols on metal catalyst with molecular oxygen can be performed in the liquid phase or in the gas phase, depending on the thermal stability and volatility of reagents and products. Gas phase oxidation of alcohols with air or oxygen represents an attractive route for the industrial production of carbonyl compounds, but successful industrial application rely on the catalyst to provide high reactivity and selectivity and the reactor design to prevent the degradation of reactants and products at high reaction temperature. Considerable research has been carried out on development of metals or supported metal catalysts for gas phase oxidation of a wide range of alcohols [4–9]. The gas phase oxidation for simple alcohols is well established on the industrial scale (e.g., methanol oxidation to formaldehyde on silver catalyst). In the BASF process for citral synthesis, isoprenol is converted to isoprenal on a supported silver

catalyst at 500 °C with a residence time of about 0.001 s [10]. These examples show that such reactions can be carried out in catalytic reactors provided that very short residence time and fast quenching after reaction can be achieved.

The application of microreaction technology to catalytic oxidation reactions is proving to be beneficial due to the ability to circumvent problems such as high exothermicity and poor control of reaction conditions, commonly associated with catalytic oxidation reactions [11]. The large surface area to volume ratio inherent to microreactors allows even highly exothermic reactions to be performed isothermally, resulting in higher selectivity and minimum waste. The small inventories of catalyst and reactants in a microreactor result in a process requiring only a few milligrams of catalyst and allowing operation within the flammability limits. In our previous research, oxidative dehydrogenation of prenol (3-methyl-2-buten-1-ol) to the corresponding aldehyde was performed in a silicon-glass microreactor on silver catalyst with high selectivity [12]. The silver catalyst was incorporated into the reaction channel by sputtering deposition. In this way, the thin film can only provide limited surface area for catalytic reactions. To generate high surface area in thin films, various methods have been reported. These include sol-gel coating [13,14], anodic oxidation of silicon [15], and more recently, growing nanoparticles and nanosprings on surfaces [16]. With silicon-glass microstructured reactors, the formation of porous silicon in reaction channels is a convenient method to increase surface area. Porous silicon is an important material for the semiconductor industry [17]. It has various applications in chemical devices, such as a high surface area support for chemical and biological applications [18,19], as porous membrane for small fuel cells [20] and as a stationary phase in liquid chromatography chips [21,22]. Various methods have been developed to fabricate porous silicon structures such as reactive ion etching, electrochemical etching (anodic oxidation), and metal-assisted chemical etching [23]. Among these methods, metal-assisted chemical etching provides a low temperature, simple and cost effective method for fabricating various silicon nano- and micro-structures in a controllable way over large areas [17,23,24].

Costenal (9-decenal) has an extremely powerful aldehydic **olfactive note** and is used in flavors and fine fragrances. It can be prepared from rosalva (9-decen-1-ol) via a Swern oxidation [25] or other liquid phase oxidation methods which involve many reaction steps and product purification processes [26–28]. Gas phase selective oxidation of rosalva could be a useful route for preparing the corresponding aldehyde but little investigative work has been done. Gallezot *et al.* [29] reported the gas phase oxidation of rosalva over Ag/SiC catalyst in a laboratory scale reactor at 450 °C. The highest costenal yield of 51% was obtained at conversion of 70% with a contact time of 28 ms. In this paper, we report the investigation of the gas phase rosalva oxidation on silver catalyst in microstructured reactors. Metal-assisted HF/H_2O_2 chemical etching was used to produce porous silicon in the microreactor channel where catalytic reaction takes place in order to increase the available surface area. Enhanced performance of the reaction on the porous silicon supported silver catalyst was demonstrated.

2. Experimental

2.1. Preparation of Microstructured Reactors

A silicon-glass microstructured reactor was prepared in four steps: Silicon etching, formation of porous silicon in the reaction channel, deposition of silver catalyst on the porous silicon and covering the silicon microreactor with a glass wafer through anodic bonding. A schematic illustration of the fabrication process is shown in Figure 1.

Figure 1. Schematic illustration of the microreactor fabrication process: (**a**) photolithography and deep reactive ion etching, (**b**) porous silicon formation and (**c**) catalyst deposition and glass bonding.

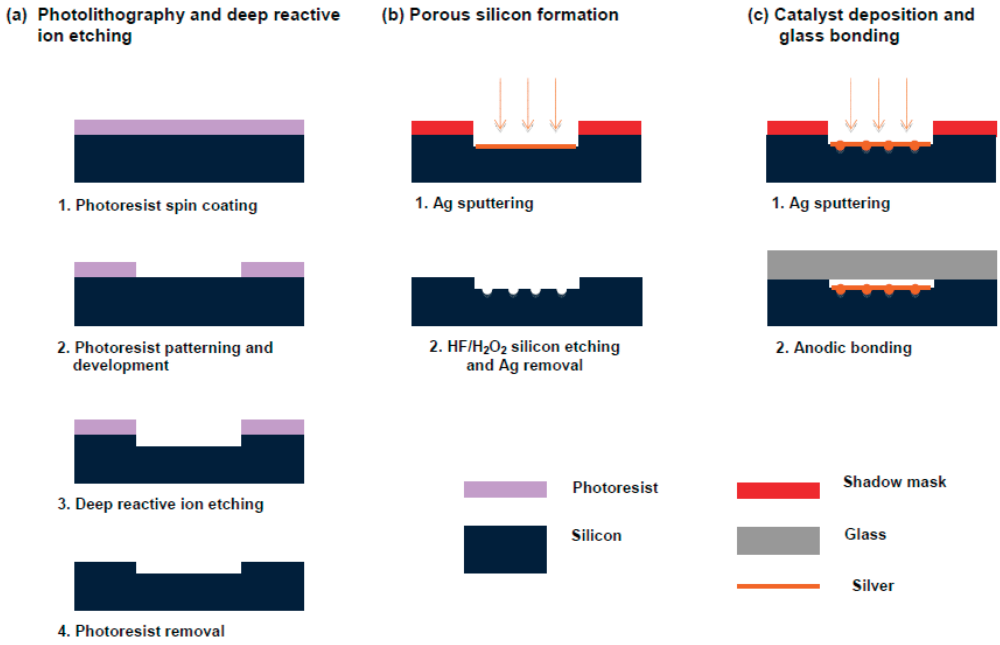

The microreactor, which contains a wide reaction channel (6 mm) with a channel depth of 0.12 mm, as shown in Figure 2a, was fabricated on a 4" silicon wafer (n<100>, 0–10 Ω cm, 0.525 mm thick) using photolithography and deep reactive ion etching (DRIE) (STS ASE; Oxford Instruments, Oxfordshire, UK). The procedure has been described elsewhere [30]. After DRIE, the wafer was diced using an automated precision dicing saw (Disco DADS 3230; Disco Corporation, Tokyo, Japan) and five microreactors were obtained from each 4" silicon wafer.

Figure 2. Microstructured reactor (**a**) without and (**b**) with silver catalyst and glass cover.

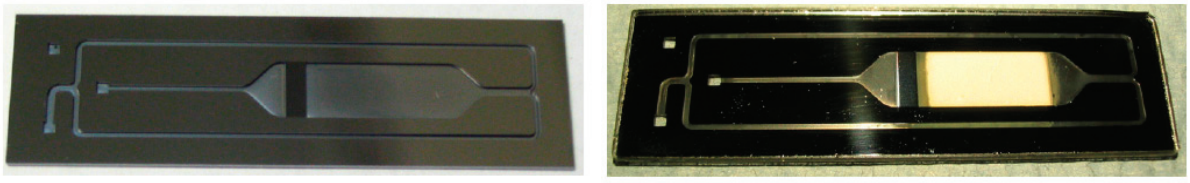

(a) **(b)**

2.1.1. Porous Silicon Formation

The porous silicon structures were formed in the reaction channel by a metal-assisted HF/H_2O_2 chemical etching process [23]. The microreactors were first cleaned using piranha solution (a mixture of 1:1 concentrated H_2SO_4 to 30% H_2O_2) for 20 min. To define the porous silicon area in the reaction channel, a shadow mask with a window of 6 mm × 12 mm was aligned to the microreactor. A thin layer of silver (4–5 nm) was then deposited in this window using a sputter coater (K675XD; Emitech, Kent, UK). The silver in this step played the role of catalyst for the etching chemistry. HF etching was carried out in a PTFE container in an etching solution with a volume ratio of Ethanol:HF(49%):H_2O_2(30%) = 1:1:1. The silver patterned microreactors were immersed into the etching solution and were etched for different time periods (e.g., 30 and 45 min). Afterwards, the microreactors were transferred into an ethanol bath for 30 min and then washed in a 30% HNO_3 solution for 30 min to remove the silver residue in the silicon. The microreactors were then rinsed thoroughly with DI water and dried under nitrogen stream.

2.1.2. Catalyst Deposition

The next stage of the process is the deposition of the silver catalyst on the porous silicon structure. Prior to its deposition, the microreactors were cleaned again using piranha solution. The same shadow mask used to define the porous silicon structure was used to define the catalytic reaction area by covering the reactor side walls. A layer of silver (equivalent to a thickness of 250 nm for flat geometry) was deposited onto the reaction channel by the sputter coater, which was operated with multi-time cycles, a procedure based on a prior calibration. The amount of silver deposited on the defined catalyst area was checked by weighing the silicon reactors before and after the sputter coating and was found to be ~2×10^{-4} g. This value was very close to that calculated based on the flat geometric area and the thickness of the silver layer (1.9×10^{-4} g).

2.1.3. Anodic Bonding

The silicon microreactor with the silver catalyst was then bonded with a glass wafer (Corning 7740; Corning, NY, USA) cleaned using piranha solution. The anodic bonding was carried out at 450 °C and 500–1000 V. The microreactors with porous silicon were named based on the HF etching time: Psi-Ag-30 for etching time of 30 min and Psi-Ag-45 for etching time of 45 min. Film-Ag was the microreactor with the flat non-porous silicon. The bonded microreactor with silver catalyst is shown in Figure 2b.

2.2. Characterization of Porous Silicon and Silver Catalyst

To characterize the pore structure of the porous silicon formed, flat silicon wafers were etched separately by HF solution following the procedure described above. The surface area was determined using N_2 adsorption-desorption isotherm (BET) measurement (Tristar 3000; Micromeritics Instrument Corporation, Norcross, GA, USA). In order to load the porous silicon sample into the glass measurement tube, the substrates were diced in pieces of 6 × 10 mm. The samples were degassed at 135 °C in

helium overnight before BET measurement. The surface morphology of the porous silicon was examined by SEM (Jeol JSM-6480LV; JEOL Ltd., Tokyo, Japan). The composition of the silver catalyst deposited on the porous silicon layer was also examined by SEM (Jeol JSM-6480LV; JEOL Ltd., Tokyo, Japan), using an Electron Backscattered Diffraction Detector (EBSD). An SEM (Jeol JSM-7401; JEOL Ltd., Tokyo, Japan) equipped with an upper secondary electron in-lens detector (SEI), a lower secondary electron detector (LEI), and a backscattered electron detector (BEI) was used for observation of the cross-section. For observation of the cross-section structure, the substrates were cleaved manually.

2.3. Experimental Set-Up and Procedure

The microreactor was first assembled with an inlet/outlet connector and a heating unit, as shown in Figure 3A. The inlet and outlet were sealed using O-rings (Perlast® G80A; O Rings Ltd., Chichester, UK) and a stainless steel housing/connector (Figure 3A). The microreactor was heated on both sides using two ceramic heaters (Ultramic™ 600; Watlow Ltd., Nottingham, UK), with a spacer made of 1.5 mm thick graphite sheet (Figure 3B). The assembled microreactor system, including a liquid evaporator, thermal insulation, a flow switching valve box and the line insulation is shown in Figure 3C. The schematic diagram of the setup is shown in Figure 4. A syringe pump (Cole Parmer 79400 series; Cole Parmer Instrument Co. Ltd., London, UK) was used to deliver the liquid alcohol to an evaporator where the vaporized alcohol was carried away by helium flow regulated by a mass flow controller. Oxygen was mixed with the alcohol-helium mixture at the outlet of the evaporator. At the outlet of the reactor, the reaction mixture was directed to a condenser/gas-liquid separator which was kept in an ice-water bath. The non-condensable gas was directed to a GC (Trace GC; ThermoQuest, Rodano, Italy) with Carboxen 1006 column and a thermal conductivity detector to determine the amount of CO_2 formed. Flow rate of the non-condensable gas was measured after the GC using a soap bubble flow meter. The liquid sample collected was analyzed using another GC (Agilent 6890; Agilent technologies Ltd., Cheshire, UK) with a HP-INNOWax column and a flame ionization detector. The oxidation of rosalva on silver catalyst could lead to several other decenal isomers. Pure 9-decenal was not available but a mixture was obtained from Givaudan (90% decenal isomers, containing >50% of 9-decenal). Cis-4-decenal, cis-7-decenal and a mixture of decenal isomers all had a same GC retention time and same peak areas when their concentrations were the same. GC calibration for 9-decenal was carried out using cis-4-decenal as a standard. Identification of the aldehyde in reaction product was carried out using NMR analysis: ä$_H$ (500 MHz, $CDCl_3$) 1.23–1.42 (8H, m, 4× CH_2), 1.58–1.67 (2H, m, C^3H_2), 1.95–2.08 (2H, m, C^8H_2), 2.40 (2H, td, *J* 1.9 and 7.4, C^2H_2), 4.91 (1H, m, $C^{10}H_2$-*cis*), 4.94–5.02 (1H, m, $C^{10}H_2$-*trans*), 5.73–5.85 (1 H, m, C^9H), 9.74 (1 H, t, *J* 1.9, C^1HO); (Bruker 500 MHz; Bruker, Coventry, UK). The flow rate of the non-condensable gas was measured using a soap bubble meter. The carbon balance from the analysis was within ±3%.

The oxidation of rosalva was carried out under atmospheric pressure with oxygen as the oxidant and helium as the diluent gas. The residence time was calculated at reaction temperature. A blank test was carried out at 450 °C with a reaction mixture containing 1.75% rosalva and 17.5% oxygen with a residence time of 20 ms. Trace costenal was detected but was confirmed to be from the reactant

rosalva. The activation of silver catalyst was carried out by repeated oxidation and reaction cycles at 450 °C. Oxygen was first passed through the microreactor for 1 h (oxidation) and then a standard inlet mixture (1.75% rosalva, 5.25% oxygen) for 1–2 h (reaction). The procedure was repeated until a stable activity (or the conversion of rosalva) was obtained. Between experiments (*i.e.*, overnight), the microreactor system was kept at 250 °C under a flow of 10% oxygen. A standard run was carried out each day at 450 °C and residence time 18 ms with the standard inlet mixture to check the catalyst activity. The reactor was replaced when the decrease in conversion in the standard run was larger than 10%.

Figure 3. Microreactor inserted in stainless steel housing/connector (**A**), ceramic heater system disassembled (**B**) and assembled microreactor-heater system (**C**).

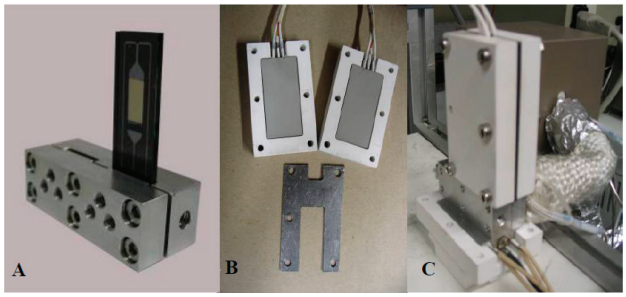

Figure 4. Experimental setup for the gas-phase oxidation of rosalva.

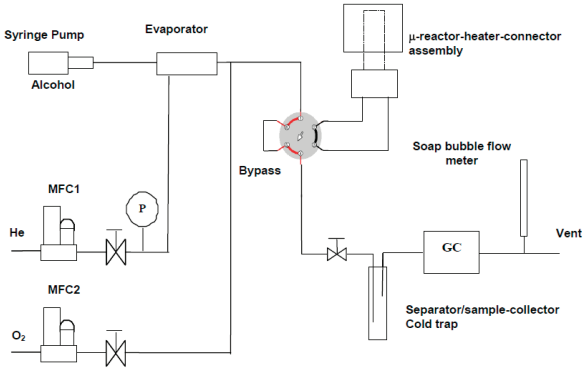

3. Results and Discussion

3.1. Characterisation of Porous Silicon and Silver Catalyst

The BET surface area was measured to be 0.30 and 0.38 m^2 g^{-1} for Psi-30 and Psi-45, respectively, and was based on the mass of the whole sample, including the porous and the solid layer. The actual porous areas were 0.023 and 0.029 m^2 for Psi-Ag-30 and Psi-Ag-45, respectively. The BET surface area measured in this work is comparable to those reported by Tiggelaar *et al.* [31] for porous silicon obtained by anodic oxidation, showing that the thicker the porous layer the larger the surface area.

SEM images of the top view of the porous silicon samples are shown in Figure 5. Both samples showed tortuous pores extending in the bulk of the Si wafer. Silver was deposited on the above samples with the procedure described in Section 2. The silver coated samples were treated in air at

450 °C. SEM images of the silver coated Psi-30 before and after heating treatment are shown in Figure 6. The silver coated porous surfaces look smoother, probably due to silver deposition covering/bridging small features of the porous silicon structure (Figure 6A). After thermal treatment, the silver coated porous surfaces do not show significant change (Figure 6B). Silver crystals with a diameter of ~1 μm are observed on top of the porous layer. The silver crystals and the silver on porous silicon were confirmed by SEM-EBSD analysis which gave a composition of 85% of Ag on the silver crystal and 65% of Ag on silver-porous silicon areas. Other elements detected were oxygen (11% on the silver crystal and 22% on silver-porous silicon area) and Si.

Figure 5. SEM images (top view) of porous silicon formed on n-type<100> silicon wafer etched in Ethanol/HF/H_2O_2 (volume ratio 1:1:1). (**A**) Psi-30 and (**B**) Psi-45.

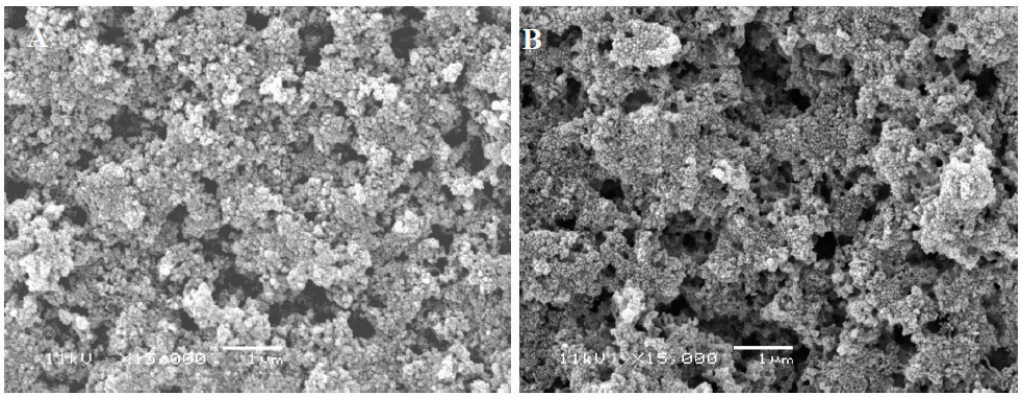

Figure 6. SEM images of Psi-Ag-30: (**A**) before and (**B**) after heating in an oven at 450 °C for 1 h.

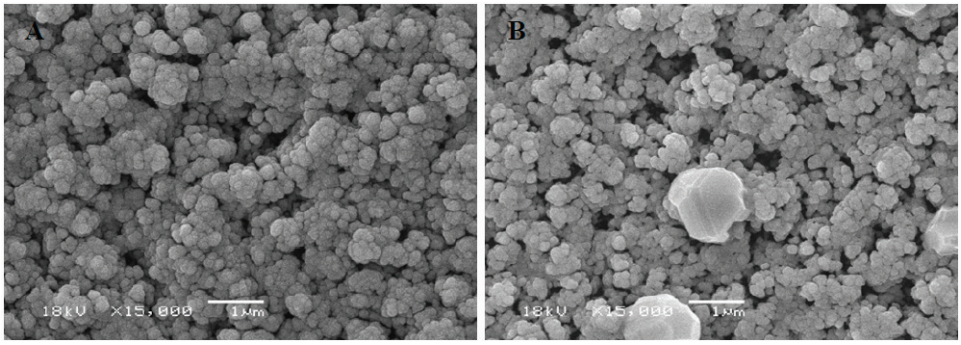

SEM images of the cross-section from SEM-LEI are shown in Figure 7. It can be seen from the top images of Figure 7A,B that the porosity of porous silicon along the depth of the layers is not uniform, with larger and more open pores on the upper part of the layer and smaller pores deeper in it. This leads to a porous silicon layer structure without a clear boundary between porous and solid silicon. However, the thickness of the porous silicon layer may be estimated to be 1–2 μm for Psi-30 and 2–3 μm for Psi-45, judged by the density of the porous structure, as seen in the top images in Figure 7. From the bottom images in Figure 7, which are obtained from SEM-COMPO analysis, the shining parts correspond to silver conformally coating the exposed cauliflower-like porous structure (Figure 6B). The scattered shining spots are silver particles which penetrated through the pores during sputter coating and deposited into a thin section beneath the conformal silver layer with

particle sizes of 6–30 nm observed also by TEM (images not shown). On the contrary, flat silver films have been known to undergo restructuring upon heating and reaction; when a film is subjected to biaxial stress, local areas relax to different degrees generating a gradient between a relaxed grain and the surrounding film. Consequently, mass flow between the film and the substrate takes place. This results in the relaxed area growing out from the base as a hillock, which is more energetically favourable [32] and results in larger size particles. SEM images of thin Ag films on silicon before and after heat treatment show break-up of the granular film and agglomeration of some of the silver particles from a particle size of a few hundred nanometres to a few micrometers [33,34]. From our previous work on a thin Ag film catalyst, an average Ag particle size of ~1 μm after heat treatment was observed [30]. Thus, the porous structure stabilised the Ag coating and prevented agglomeration to a certain extent.

Figure 7. Side view SEM images of porous silicon supported silver: (**A**) Psi-Ag-30 and (**B**) Psi-Ag-45. Top: SEM-LEI, bottom: SEM-BEI.

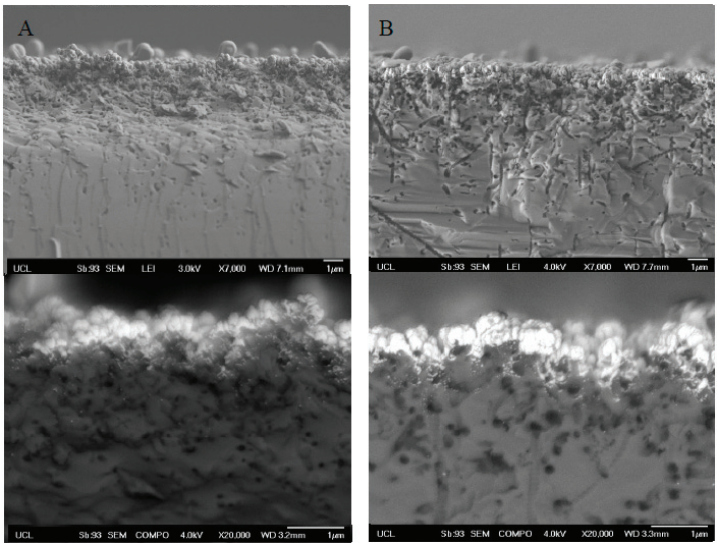

3.2. Rosalva Oxidation on Silver Catalyst

3.2.1. Effect of Reaction Temperature

The effect of reaction temperature on the oxidation of rosalva was first studied in the reactor Psi-Ag-30 over a temperature range of 375–475 °C with the standard inlet mixture (1.75% rosalva, 5.25% oxygen) at a residence time of 18 ms. To examine performance enhancement by using the porous silicon as catalyst support, the same experiment was also carried out in a microreactor with thin film silver catalyst. The main product of the reaction was 9-decenal which was confirmed by performing NMR analysis; total alternative aldehyde content was ~1%. CO and H_2 were not detected when the non-condensable gas was analysed using a third GC (Agilent, 7890; Agilent technologies Ltd., Cheshire, UK) with a molecular sieve column. Decenoic acid and CO_2 were the only side products detected. The results are presented in Table 1 showing the effect of temperature on the conversion of rosalva and the selectivity to costenal, 9-decenoic acid and CO_2. In the reactor Psi-Ag-30, the conversion of rosalva increases with temperature significantly, while the selectivity

to costenal is less affected by reaction temperature and slightly decreases from 98.7%–96.2% with temperature increases from 375–475 °C. The selectivity to CO_2 and the acid together is about 2%–4% in the temperature range studied. The selectivity to CO_2 increases slightly with temperature which is just detectable at 375 °C and increases to ~2.5% at 475 °C; while the selectivity to the acid is less affected by the reaction temperature. In the reactor Film-Ag, the dependency of conversion and selectivity of the reaction on temperature is the same as those in Psi-Ag-30. However, the performance of the film silver catalyst is poorer than that of the silver supported on porous silicon. Conversions of rosalva are 7.7% at 425 °C and 35% at 475 °C compared to 66% and 91% obtained in Psi-Ag-30 at the same reaction temperatures.

Table 1. Conversion and selectivity at different reaction temperatures on two forms of silver catalyst: the porous silicon supported silver Psi-Ag-30 and the thin film silver catalyst Film-Ag (Inlet mixture: 1.75% rosalva, 5.25% oxygen with helium as balance; residence time: 18 ms).

T, °C	Psi-Ag-30				Film-Ag			
	X, %	Selectivity, %			X, %	Selectivity, %		
		9-decenal	9-decenoic acid	CO_2		9-decenal	9-decenoic acid	CO_2
375	23.3	98.7	1.3					
400	43.2	98.2	1.6	0.2				
425	66.3	97.6	1.7	0.7	7.7	100		
450	81.8	96.9	1.2	1.9	14.4	98.9		1.1
475	91.4	96.2	1.2	2.5	35.1	95.3	3.0	1.7

The enhanced performance of the oxidation of rosalva on the porous silicon supported silver catalyst is clearly demonstrated by the data in Table 1. Turnover frequencies (TOF) (based on moles of Ag) for the consumption of rosalva at 450 °C is calculated to be 225 h^{-1} on Psi-Ag-30 which is about 5.6 times higher than that on Film-Ag (40 h^{-1}). The enhancement could be attributed to the increase of catalyst surface area and different catalyst morphology. The rough porous structure (Figures 5 and 6) increased the dispersion of the silver catalyst and produced a conformal layer contrary to the silver deposited on flat silicon wafer surface [30]. Oxygen diffusion in silver occurs via both grain boundary and interstitial diffusion at temperatures below 900 K [35]. The importance of oxygen diffusion along grain boundaries and related structural faults for silver-catalysed oxidation reactions has been demonstrated by Waterhouse *et al.* [36]. The catalyst surface morphology can also influence the state of the chemisorbed oxygen, which can have an impact on the reaction performance [35,37]. Restructuring of the catalyst surface also takes place with heating and reaction, and is dependent on a variety of factors, including temperature, partial pressure of oxygen and the initial morphology of the silver substrate.

The results can be compared with those reported by Gallezot *et al.* for the same reaction on 4.5 wt% Ag/SiC in a 75 cm^3 cylindrical Pyrex reactor [29]. The best results reported were 70% conversion of rosalva with selectivity to costenal of 73% at 450 °C at a contact time of 28 ms. Low selectivity to costenal in their work could be due to the experimental set-up, where total oxidation might take place in the gas phase or on the walls of vaporiser and in the reactor heated at 450 °C.

Inefficient heat transfer in the catalyst bed giving rise to hot spots might also be a contribution to the total oxidation for such highly exothermic reaction. Hence, increasing reaction temperature above 450 °C might have caused an adverse effect on the selectivity because total oxidation was favoured [29]. In our work, the inertness of the microreactor was confirmed as there was no gas phase oxidation reaction detected during blank experiments. The low CO_2 selectivity and high selectivity to costenal observed here can be attributed to the highly isothermal behaviour of the microstructured reactor.

Figure 8. Dependence of conversion and selectivity on oxygen concentration. Reactor, Psi-Ag-30. Reaction temperature, 450 °C; inlet mixture, 1.75% rosalva, varying oxygen with helium as balance; residence time, 18 ms.

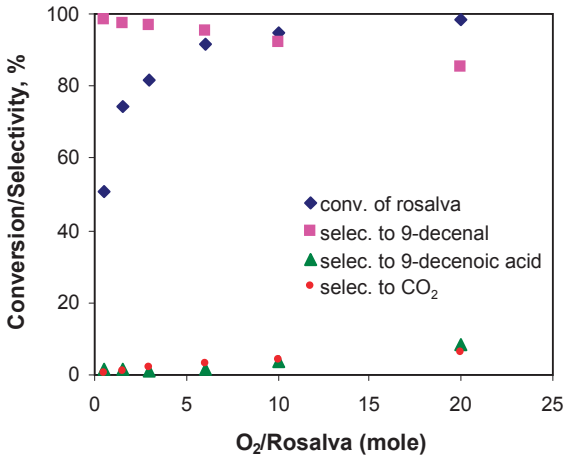

3.2.2. Effect of Inlet Oxygen Concentration

Effect of O_2 concentration on the reaction was studied at 450 °C with reactor Psi-Ag-30. The inlet rosalva concentration was kept at 1.75% while oxygen concentration was varied to adjust the ratio of O_2/rosalva from 0.5–20 with helium as balance. Residence time was kept at 18 ms. Results are shown in Figure 8. It can be seen that conversion of rosalva increases significantly with an increase in the ratio of O_2 to rosalva from 0.5–6. Further increasing O_2 leads to limited increase in conversion, as the reaction is close to completion. The selectivity to costenal decreases with the increase of O_2 concentration but not dramatically, from ~98%–~85% with the ratio of O_2/rosalva increasing from 0.5–20. The formation of 9-decenoic acid and CO_2 is favoured by increasing O_2 concentration, with selectivity to the acid and CO_2 of 8.6% and 6%, respectively, at an O_2/rosalva mole ratio of 20. The increased formation of CO_2 could be due to total oxidation of the aldehyde with higher O_2 concentration [12]. It is worth noting that the selectivity to costenal was maintained at a relatively high value even at the ratio of O_2/rosalva of 20, while in a glass tube packed bed reactor an optimum ratio of 1.5 was observed [29].

3.2.3. Effect of Inlet Rosalva Concentration

Effect of rosalva concentration on the reaction was studied at 425 °C with reactor Psi-Ag-45. Rosalva concentration increased from 1.17%–3.43% while O_2 concentration was kept constant at 5.1%. The total inlet flow was balanced by helium and kept constant which produced a residence time of 18 ms. Results presented in Figure 9 show a decrease in conversion with increasing inlet rosalva concentration from 99.1%–79.2% in the range of concentrations studied. Selectivity to costenal increases slightly from 94.6%–96.8%. Selectivity to CO_2 was seen decreasing with the inlet rosalva concentration (4.2%–1.2%); selectivity to 9-decenoic acid was at ~1.2%–3.2%. It is noted that the ratio of O_2 to rosalva varied from 4.5–1.5 with the inlet concentration of rosalva changing from 1.17–3.41% due to the fixed O_2 inlet concentration (5.1%). The decrease in selectivity to CO_2 may also reflect the effect of the decreased O_2/rosalva ratio; the lower the O_2/rosalva ratio the less CO_2 formed by total oxidation. The average reaction rate on the silver catalyst increased with the inlet rosalva concentration (Figure 9) almost linearly. This might be an indication of a reaction order with respect to rosalva concentration close to one.

Figure 9. Dependence of conversion and selectivity on rosalva inlet concentration. Reactor, Psi-Ag-45. temperature, 425 °C; inlet mixture, 5.1% oxygen with helium as balance; residence time, 18 ms.

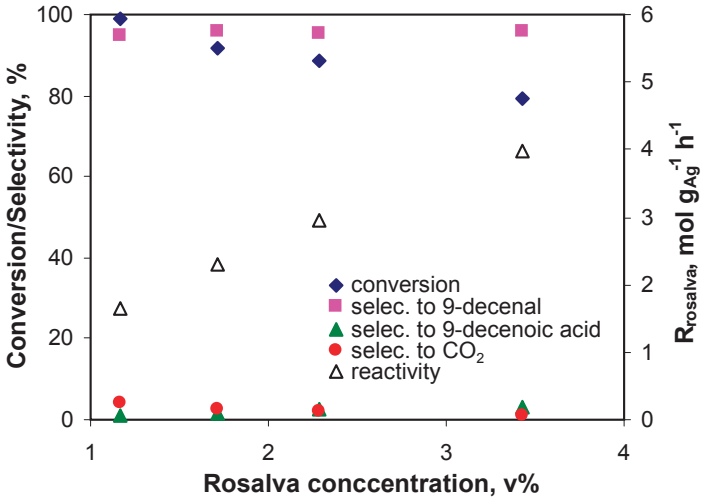

3.2.4. Effect of Residence Time

The effect of residence time was studied with the Psi-Ag-30 reactor at 450 °C by changing the total gas flow rate but keeping the concentration of the inlet mixture unchanged. The residence time varied from 0.009–0.027 s and the results are plotted in Figure 10. It can be seen that conversion of rosalva increases with residence time, having close to a first order dependence on rosalva concentration. Selectivity is practically unaffected by residence time, changing from 97.3% at residence time of 9 ms to 96.5% at residence time of 27 ms. Selectivity to 9-decenoic acid and CO_2 was not significantly affected by the residence time and was at only 2.5%–3.5% in total.

Figure 10. Dependence of conversion and selectivity on residence time. Reactor, Psi-Ag-30; temperature, 450 °C; inlet mixture, 1.75% rosalva, 5.25% O_2 with helium as balance.

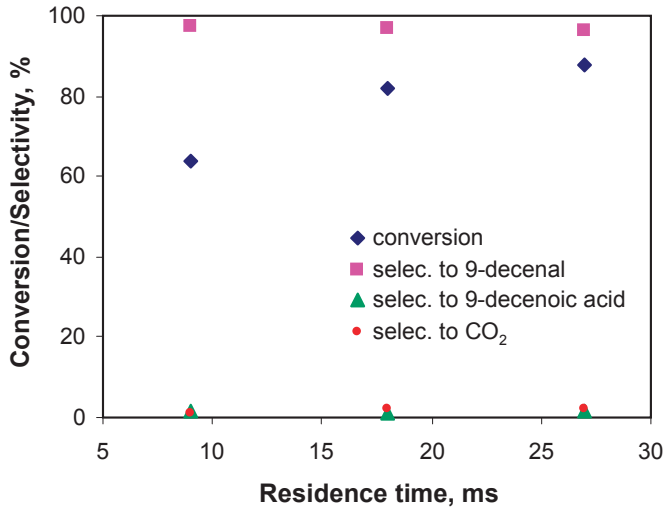

3.2.5. Effect of the Porous Silicon Layer Structure

Effect of the porous layer structure on the reaction was further examined by using the reactor Psi-Ag-45 which was etched longer in HF/H_2O_2 solution and had a thicker porous silicon layer and higher surface area. The reaction was carried out at a temperature range of 375–450 °C with the standard inlet mixture at a residence time of 18 ms. Results are plotted in Figure 11 together with the results from Psi-Ag-30 and Film-Ag for comparison. It can be seen from Figure 11 that the reaction showed higher conversion in Psi-Ag-45 than in Psi-Ag-30, with a conversion of 61% at 375 °C and close to complete (97% conversion) at 450 °C compared to 23% and 82% in Psi-Ag-30, respectively. Selectivity to costenal was not significantly affected by the reaction temperature in all three microreactors and was higher than 95% even at the highest reaction temperature (475 °C). The total selectivity to 9-decenoic acid and CO_2 was around 1%–5% in the same range of the reaction temperature. TOF for rosalva on Psi-Ag-45 at 450 °C is 268 h^{-1} compared to 225 h^{-1} on Psi-Ag-30 and 40 h^{-1} on Film-Ag.

To understand these results, a simple kinetic analysis was performed. For the standard inlet conditions (1.75% rosalva, 5.25% oxygen), the oxidation of rosalva on the porous silicon-supported silver shows approximately first order dependence on rosalva concentration (Figure 9). By assuming that the O_2 concentration was approximately constant during the reaction, which can be justified by the excess O_2 concentration in the inlet (ratio of O_2/rosalva of 3) and very low selectivity to CO_2, the reaction rate constants are estimated with a plug-flow reactor model from the data in Figure 11. An Arrhenius analysis was performed and the results are plotted in Figure 12. The activation energy is estimated to be 75.6, 77.3 and 130 kJ mol^{-1} for the reactions on Psi-Ag-30, Psi-Ag-45 and Film-Ag, respectively. The activation energy on the film catalyst is almost double to these on the porous-supported silver.

Figure 11. Effect of porous structure on reaction performance (Inlet mixture: 1.75% rosalva, 5.25% oxygen with helium as balance; residence time: 18 ms).

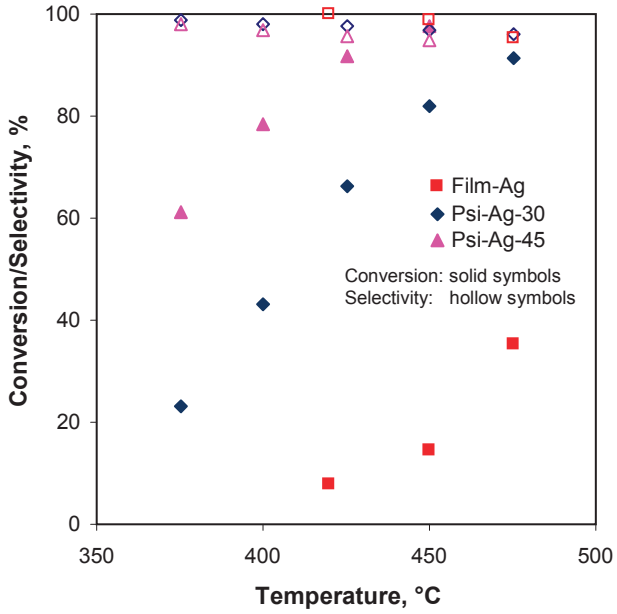

Figure 12. Arrhenius plot from data of Figure 10.

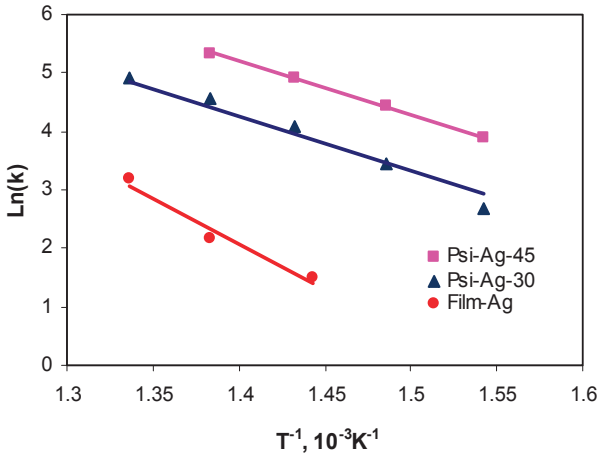

The activation energy values obtained in the three microreactors are within the range of typical catalytic reactions. However, a reduction in apparent activation energy for the porous silicon-supported catalysts, as compared to the flat silicon catalyst, may suggest the existence of mass transfer resistance for the former. In order to check for diffusion limitations in the porous layer, the Thiele modulus (φ) was calculated based on a first order reaction assumption:

$$\varphi = d\sqrt{\frac{k}{D_{eff}}}$$

where d is the thickness of porous layer, k is the reaction rate constant, D_{eff} is the effective diffusivity. The diffusivity of rosalva in air was estimated using Fuller's correlation [38]. The

effective diffusivity was then approximated by one 10th of the bulk diffusivity. For the reaction in Psi-Ag-45 at 450 °C, k and D_{eff} were estimated to be 207 s^{-1} and 3×10^{-6} m^2 s^{-1}, respectively. With a thickness of the porous silicon layer of 3×10^{-6} m, φ was estimated to be 0.009, indicating absence of diffusion limitation.

Particle size and shape can significantly influence catalyst performance for structure sensitive reactions [39]. Nanoparticles with different sizes and shapes have different surface properties that can affect both selectivity and reactivity for various catalytic reactions. Such size effects are often observed in the size range of ~1–10 nm [40,41]. This particle size effect is unlikely in our work since most of the silver seems to be in the form of a conformal layer, while small particles would sinter at the high reaction temperature used. On the other hand, the physical and chemical properties of the flat silicon and the porous silicon surfaces could be different. As the porous silicon is formed in an HF solution, the exposed surface becomes terminated with hydrogen atoms and will typically oxidize in air at room temperature producing different types of surface species (Si-H, Si-O_x) [42,43]. Furthermore, porous silicon has a significantly different morphology as compared to flat silicon. These characteristics may result in different morphology, surface facets, electronic properties, non-equilibrium surface structures and metal-support interactions of the deposited catalytic layer/particles, which have been shown to affect catalyst (and, in particular, Ag) reactivity [36,44–47].

4. Conclusions

The application of metal-assisted HF chemical etching as a simple method of producing porous structures in silicon microreactor channels has been demonstrated. The oxidation of rosalva to its aldehyde (costenal) on silver catalyst was successfully performed in silicon/glass microstructured reactors at temperatures of 375–475 °C. Significant performance enhancement was achieved by the porous silicon in the reaction channel, which increased the catalytic surface area. TOF for the rosalva consumption on the porous silicon supported silver was *ca.* six times that of flat silicon at 450 °C. Different activation energies were found for the porous silicon supported silver and for the thin film silver which could be due to different properties of the silver catalyst induced by the different chemical and physical properties of the support. Isothermal conditions in the microreactors allowed high conversions and selectivities to be achieved in a wide range of temperatures and oxygen concentrations. A selectivity of 95% even at 97% conversion levels was achieved in this work, which is higher than those reported in the literature for conventional laboratory packed bed reactors.

Acknowledgments

Financial support from EPSRC is gratefully acknowledged. We thank Chris Newman from Givaudan for supplying the costenal sample.

Conflicts of Interest

The authors declare no conflict of interest.

References

1. Sheldon, R.A.; van Bekkum, H. *Fine Chemicals through Heterogeneous Catalysis*; WILEY-VCH: Weinhein, Germany, 2001.
2. Della Pina, C.; Falletta, E.; Prati, L.; Rossi, M. Selective oxidation using gold. *Chem. Soc. Rev.* **2008**, *37*, 2077–2095.
3. Mallat, T.; Baiker, A. Oxidation of alcohols with molecular oxygen on solid catalysts. *Chem. Rev.* **2004**, *104*, 3037–3058.
4. Biella, S.; Rossi, M. Gas phase oxidation of alcohols to aldehydes or ketones catalysed by supported gold. *Chem. Commun.* **2003**, *9*, 378–379.
5. Han, D.; Xu, T.; Su, J.; Xu, X.; Ding, Y. Gas-Phase selective oxidation of benzyl alcohol to benzaldehyde with molecular oxygen over unsupported nanoporous gold. *ChemCatChem* **2010**, *2*, 383–386.
6. Della Pina, C.; Falletta, E.; Rossi, M. Highly selective oxidation of benzyl alcohol to benzaldehyde catalyzed by bimetallic gold-copper catalyst. *J. Catal.* **2008**, *260*, 384–386.
7. Shen, J.; Shan, W.; Zhang, Y.; Du, J.; Xu, H.; Fan, K.; Shen, W.; Tang, Y. Gas-phase selective oxidation of alcohols: In situ electrolytic nano-silver/zeolite film/copper grid catalyst. *J. Catal.* **2006**, *237*, 94–101.
8. Yadav, G.D.; Mewada, R.K. Selectivity engineering in the synthesis of value added chemicals: Oxidation of 1-octanol to 1-octanal over nano-fibrous Ag-OMS-2 catalysts. *Chem. Eng. Res. Des.* **2012**, *90*, 86–97.
9. Yamamoto, R.; Sawayama, Y.S.; Shibahara, H.; Ichihashi, Y.; Nishiyama, S.; Tsuruya, S. Promoted partial oxidation activity of supported Ag catalysts in the gas-phase catalytic oxidation of benzyl alcohol. *J. Catal.* **2005**, *234*, 308–317.
10. Hoelderich, W.F.; Kollmer, F. Oxidation reactions in the synthesis of fine and intermediate chemicals using environmentally benign oxidants and the right reactor system. *Pure Appl. Chem.* **2000**, *72*, 1273–1287.
11. Hessel, V.; Hardt, S.; Löwe, H. *Chemical Micro Process Engineering*. Weiley-VCH: Weinheim, Germany, 2004.
12. Cao, E.; Gavriilidis, A.; Motherwell, W.B. Oxidative dehydrogenation of 3-methyl-2-buten-1-o1 in microreactors. *Chem. Eng. Sci.* **2004**, *59*, 4803–4808.
13. Haas-Santo, K.; Fichtner, M.; Schubert, K. Preparation of microstructure compatible porous supports by sol-gel synthesis for catalyst coatings. *Appl. Catal. A* **2001**, *220*, 79–92.
14. Meille, V. Review on methods to deposit catalysts on structured surfaces. *Appl. Catal. A* **2006**, *315*, 1–17.
15. Losey, M.W.; Jackman, R.J.; Firebaugh, S.L.; Schmidt, M.A.; Jensen, K.F. Design and fabrication of microfluidic devices for multiphase mixing and reaction. *J. Microelectromech. Syst.* **2002**, *11*, 709–717.
16. Schilke, K.F.; Wilson, K.L.; Cantrell, T.; Corti, G.; McIlroy, D.N.; Kelly, C. A novel enzymatic microreactor with aspergillus oryzae β-galactosidase immobilized on silicon dioxide nanosprings. *Biotechnol. Prog.* **2010**, *26*, 1597–1605.

17. Huang, Z.; Geyer, N.; Werner, P.; de Boor, J.; Gösele, U. Metal-assisted chemical etching of silicon: A review. *Adv. Mater.* **2011**, *23*, 285–308.
18. Drott, J.; Lindström, K.; Rosengren, L.; Laurell, T. Porous silicon as the carrier matrix in microstructured enzyme reactors yielding high enzyme activities. *J. Micromech. Microengineer.* **1997**, *7*, 14–23.
19. Stewart, M.P.; Buriak, J.M. Chemical and biological applications of porous silicon technology. *Adv. Mater.* **2000**, *12*, 859–869.
20. Pichonat, T.; Gauthier-Manuel, B. A new process for the manufacturing of reproducible mesoporous silicon membranes. *J. Membrane Sci.* **2006**, *280*, 494–500.
21. Clicq, D.; Tjerkstra, R.W.; Gardeniers, J.G.E.; van den Berg, A.; Baron, G.V.; Desmet, G. Porous silicon as a stationary phase for shear-driven chromatography. *J. Chromatogr. A* **2004**, *1032*, 185–191.
22. De Malsche, W.; Clicq, D.; Verdoold, V.; Gzil, P.; Desmet, G.; Gardeniers, H. Integration of porous layers in ordered pillar arrays for liquid chromatography. *Lab Chip* **2007**, *7*, 1705–1711.
23. Li, X.; Bonn, P.W. Metal-assisted chemical etching in HF/H_2O_2 produces porous silicon. *Appl. Phys. Lett.* **2000**, *77*, 2572–2574.
24. Chern, W.; Hsu, K.; Chun, I.; Azeredo, B.; Fang, N.; Ferreira, P.; Li, X. Non-lithographic patterning and metal-assisted chemical etching for manufacturing of tunable light-emitting silicon nanowire arrays. In Proceedings of Lasers and Electro-Optics/Quantum Electronics and Laser Science Conference: 2010 Laser Science to Photonic Applications, San Jose, CA, USA, 16–21 May 2010; IEEE: Piscataway, NJ, USA, 2010.
25. Banwell, M.G.; McRae, K.J. Chemoenzymatic synthesis of (+)-aspicilin from chlorobenzene. *Org. Lett.* **2000**, *2*, 3583–3586.
26. Bortolini, O.; Campestrini, S.; di Furia, F.; Modena, G.; Valle, G. Metal catalysis in oxidation by peroxides. Anionic molybdenum-picolinate *N*-oxido-peroxo complex: An effective oxidant of primary and secondary alcohols in nonpolar solvents. *J. Org. Chem.* **1987**, *52*, 5467–5469.
27. McErlean, C.S.P.; Proisy, N.; Davis, C.J.; Boland, N.A.; Sharp, S.Y.; Boxall, K.; Slawin, A.M.Z.; Workman, P.; Moody, C.J. Synthetic ansamycins prepared by a ring-expanding Claisen rearrangement. Synthesis and biological evaluation of ring and conformational analogues of the Hsp90 molecular chaperone inhibitor geldanamycin. *Org. Biomol. Chem.* **2007**, *5*, 531–546.
28. Uyanik, M.; Akakura, M.; Ishihara, K. 2-iodoxybenzenesulfonic acid as an extremely active catalyst for the selective oxidation of alcohols to aldehydes, ketones, carboxylic acids, and enones with oxone. *J. Amer. Chem. Soc.* **2009**, *131*, 251–262.
29. Gallezot, P.; Ceroni, L.; Perrard, A. Oxidative dehydrogenation of rosalva to costenal on supported silver catalysts. *J. Mol. Catal. A* **1998**, *129*, L127–L130.
30. Cao, E.; Gavriilidis, A. Oxidative dehydrogenation of methanol in a microstructured reactor. *Catal. Today* **2005**, *110*, 154–163.
31. Tiggelaar, R.M.; Verdoold, V.; Eghbali, H.; Desmet, G.; Gardeniers, J.G.E. Characterization of porous silicon integrated in liquid chromatography chips. *Lab Chip* **2009**, *9*, 456–463.

32. Chaudhari, P. Hillock growth in thin films. *J. Appl. Phys.* **1974**, *45*, 4339–4346.
33. Sharma, S.K.; Spitz, J. Hillock growth and agglomeration in thin silver films. *Thin Solid Films* **1979**, *61*, L13–L15.
34. Sharma, S.K.; Spitz, J. Hillock formation, hole growth and agglomeration in thin silver films. *Thin Solid Films* **1980**, *65*, 339–350.
35. Waterhouse, G.I.N.; Bowmaker, G.A.; Metson, J.B. Oxygen chemisorption on an electrolytic silver catalyst: A combined TPD and Raman spectroscopic study. *Appl. Surface Sci.* **2003**, *214*, 36–51.
36. Waterhouse, G.I.N.; Bowmaker, G.A.; Metson, J.B. Influence of catalyst morphology on the performance of electrolytic silver catalysts for the partial oxidation of methanol to formaldehyde. *Appl. Catal. A* **2004**, *266*, 257–273.
37. Waterhouse, G.I.N.; Bowmaker, G.A.; Metson, J.B. Mechanism and active sites for the partial oxidation of methanol to formaldehyde over an electrolytic silver catalyst. *Appl. Catal. A* **2004**, *265*, 85–101.
38. Hayes, R.E.; Kolaczkowski, S.T. *Introduction to Catalytic Combustion*; Gordon & Breach Science Publishers: Amsterdam, The Netherlands, 1997.
39. van Santen, P.A.; Neurock, M. *Molecular Heterogeneous Catalysis-A Conceptual and Computational Approach*; WILEY-VCH: Weinheim, Germany, 2006.
40. Che, M.; Bennett, C.O. The influence of particle size on the catalytic properties of supported metals. In *Advances in Catalysis*; H.P.D.D., Eley, Paul, B.W., Eds.; Academic Press: New York, NY, USA, 1989; Volume 36, pp. 55–172.
41. Musselwhite, N.; Somorjai, G. Investigations of structure sensitivity in heterogeneous catalysis: From single crystals to monodisperse nanoparticles. *Top. Catal.* **2013**, *56*, 1277–1283.
42. Anderson, R.C.; Muller, R.S.; Tobias, C.W. Chemical surface modification of porous silicon. *J. Electrochem. Soc.* **1993**, *140*, 1393–1396.
43. Michael, J.S. *Porous silicon in Practice: Preparation, Characterization and Applications*, First ed.; Wiley-VCH: Weinheim, Germany, 2012.
44. Tsybulya, S.V.; Kryukova, G.N.; Goncharova, S.N.; Shmakov, A.N.; Balzhinimaev, B.S. Study of the real structure of silver supported catalysts of different dispersity. *J. Catal.* **1995**, *154*, 194–200.
45. Mastikhin, V.M.; Goncharova, S.N.; Tapilin, V.M.; Terskikh, V.V.; Balzhinimaev, B.S. Effect of particle size upon catalytic and electronic properties of supported Ag catalysts: Combined catalytic, 109Ag NMR and quantum chemistry studies. *J. Mol. Catal. A* **1995**, *96*, 175–179.
46. Zuburtikudis, I.; Saltsburg, H. Linear metal nanostructures and size effects of supported metal catalysts. *Science* **1992**, *258*, 1337–1339.
47. Christopher, P.; Linic, S. Shape- and size-specific chemistry of Ag nanostructures in catalytic ethylene epoxidation. *ChemCatChem* **2010**, *2*, 78–83.

Absorption and Chemisorption of Small Levitated Single Bubbles in Aqueous Solutions

Alexander Tollkötter and Norbert Kockmann

Abstract: The absorption and chemisorption of small bubbles with N_2 or CO_2 were investigated experimentally in aqueous and alkaline solutions. Different bubble sizes were studied ranging from 0.1 to 2.5 mm in alkaline concentrations of 0.1 mM to 1 M NaOH. The experiments were conducted in a device consisting of a converging microchannel with a down flowing liquid. Levitation positions of single bubbles were optically characterized. A correlation was developed for the drag force coefficient, C_D, including wall effects based on the force equilibrium. A linear decrease of bubble diameters was identified with and without chemical reaction, which is referred to as a rigid bubble surface area. Measured Sherwood numbers agree well with the literature values for the investigated Reynolds number range.

Reprinted from *Processes*. Cite as: Tollkötter, A.; Kockmann, N. Absorption and Chemisorption of Small Levitated Single Bubbles in Aqueous Solutions. *Processes* **2014**, *2*, 200-215.

1. Introduction

Multiphase reactions are of major importance in chemical engineering and in many cases limited by mass transfer and mixing. Chemical reactions at fluid interfaces often occur, including the first contact of the involved phases and the generation of lamellae, bubbles and droplets. A large specific interface of the phases intensifies chemical reactions between the phases. Stitt describes conventional technologies of multiphase equipment in a comprehensive review [1], including trickle bed reactors, stirred and bubble columns and jet loop reactors. The major purpose of the devices is to generate a large fluid interface, where the reaction can take place.

Microchannels can handle mixing sensitive chemical reactions, due to their excellent mixing conditions and superior mass transfer characteristics in a homogeneous liquid [2] or gaseous systems [3], as well as for heterogeneous gas-liquid-solid systems [4,5]. While homogeneous systems are basically understood [6], multiphase transport phenomena with chemical reactions in microchannels are still a wide field in research and design. Microreactors offer short diffusions lengths and good transport characteristics, but capillary forces gain importance on the micro-scale. The state-of-the-art of multiphase flow, transport and transformation are reviewed by Günther and Jensen [7], Doku *et al*. [8], Hessel *et al*. [9], as well as Kashid and Kiwi-Minsker [10] for chemical reactions in microreactors. Exothermic reactions in microchannels can be treated with increased safety [11]. Nevertheless, the proper description and understanding of bubble flow, transport processes and reaction kinetics are essential for the successful application of microstructured devices [12].

An essential part is the determination of the mass transfer of a single microbubble before transition to the complex flow of bubble swarms in microstructured devices. An important

parameter here is the liquid-side mass transfer coefficient, k_L, represented in dimensionless form as the Sherwood number, *Sh*. Mass transfer depends on the surface of dissolving gas bubbles [13]. The surface attains different shapes according to the bubble's size and rising velocity [14]. Additionally, the inner motion of the bubble improves the mass transfer [15]. This motion is influenced by the bubble size itself and its surface contamination. Air bubbles in water with diameters smaller than 0.2 mm act as solid spheres without any motion, due to dominant surface tension, generally [14,16,17]. Contamination is affected by the liquid purity in terms of salt and ion concentration. High electrical conductivity or low resistance favors contamination. In water purified by an ion exchanger bubbles with diameters up to 1.6 mm showed a rigid behavior [18]. The constant decay of the bubble radius due to absorption was observed for several gases in tap water with a low solubility in this range of bubble sizes. A lower liquid saturation resulted in a higher rate [19]. In tap water, too, comparable values of diameter decay were found for air bubbles with diameters of 8 mm. Two different sections of decreasing radii instead were identified using clean water for several gases with a low solubility. This rate change was related to impurities in the water acting as surfactants and creating a stagnant cap at the bubble's back, which hinders inner motions, due to Marangoni convection [20]. The absorption of highly soluble gas bubbles, especially carbon dioxide, was observed in different liquids and concentrations. For water, an initially high mass transfer coefficient was observed followed by a constant period of a reduced value. The change occurred in a bubble diameter range of 1.0 to 1.5 mm. This was also related to surface contamination and transition to a rigid bubble behavior [21]. Only one regime could be observed for diameters from 0.2 to 1.0 mm in contaminated water [22]. Bubbles with radii from 0.1 to 0.5 mm decrease faster in sodium hydroxide solutions with concentrations of 0.01 to 1 M by chemical reaction. Sherwood numbers were calculated and show 10% deviations from a non-equilibrium reaction model [23]. The reduction of linear radius decay with time at a larger diameter was related to a shrinking surface, due to contamination [24]. The relation between motion and bubble size is also affected by the bubble age. Hence, the exact transition point from a rigid to a mobile surface is not identified clearly [20]. For low soluble gases, this point appeared after minutes, which exceeds the residence time of most classical devices, such as stripping columns. Two approaches are established to capture bubbles and to increase the observation time: a rotary chamber [18] or using a conical tube with down flowing liquid [20].

In this paper, a device is presented to capture and levitate bubbles with diameters of 0.1 to 2.5 mm by downward flow in a conical tube. A drag force model, including wall effects, is developed to determine the rising velocity of the bubble. Hence, levitation positions were studied in more detail. Further absorption and chemisorption of N_2 and CO_2 bubbles were analyzed in various liquids to investigate the mass transfer concerning the difference between a mobile and a rigid bubble surface.

2. Theory

2.1. Bubble Rising Velocity and Drag Models

In liquids, several forces act on bubbles determining their rising velocity and position in the flow field. A differentiation between vertical and horizontal forces is possible. Bubbles behave as solid particles when a rigid surface and, consequently, no-slip boundary condition on their surface exist [15]. Non-uniform shear stresses cause solid particles to move away from the middle of the channel, due to different velocities on each bubble side. Wall interaction induces solid particle movement toward the middle of the channel. The balance of both forces results in an equilibrium radius, r_{eq}, mainly dependent on size, which lets larger solid particles stay closer to the center line. This radius represents the distance between the solid particle center and the central axis [25].

Regarding the vertical direction, the drag force consists of a pressure and a friction part. Friction originates from the viscous forces of the surrounding liquid and dominates for small Reynolds numbers. The pressure part becomes more important for flow detachment from the bubble and resultant eddies, due to the higher velocities. Both parts are combined using the drag force coefficient, C_D [26]. Furthermore, buoyancy force gives a vertical force balance, written as:

$$C_D \rho_l \frac{u^2}{2} A_b = (\rho_l - \rho_g) g \frac{d_b^3 \pi}{6} \tag{1}$$

or in non-dimensional form:

$$C_D = \frac{4}{3} \frac{\rho_l - \rho_g}{\rho_l} \frac{g d_b}{u^2} = \frac{4}{3} \frac{Ar}{\mathrm{Re}^2} \tag{2}$$

Here, ρ_l and ρ_g are liquid and gas densities, u the liquid velocity, A_b the bubble surface normal to the flow, g the gravitational acceleration, d_b the bubble diameter and Re the Reynolds number. Ellipsoids are described by their main diameters, a and b, due to the arrangement to the flow, also known as Feret diameters. The diameter of a volume-equivalent sphere, d_e, is then calculated by Equation (3). For low aspect ratios, the deviation from an ideal sphere is negligible [20].

$$d_e = \sqrt[3]{a^2 b} \tag{3}$$

Many correlations describe drag coefficients for different condition in various devices. Beside the Stokes range for very small Re, bubbles and solid particles behave differently [15]. Most of these correlations are only valid for an infinite flow field. Two approaches consider wall effects with an additional correction factor, K. The first one was developed for particles [26]. For both, all constants are summed up to constants K_i.

$$C_{D,I} = C_{D,\infty} + \frac{K_I}{\mathrm{Re}} \quad \wedge \quad C_{D,II} = C_{D,\infty} K_{II} \tag{4}$$

Here, $C_{D,\infty}$ is the drag force coefficient for an infinite flow field. Some empirical correlations modeling K_i are listed in [26,27]. Most of these correlations have the same form as a division of two polynomials, where the denominator has a higher order. Each polynomial depends on the ratio of bubble diameter to channel width λ.

2.2. Mass Transfer of Single Bubbles

When gas and liquid are in contact, mass transport occurs over the interface between the phases driven by concentration gradients. Transfer from the gas to the liquid is termed absorption and depends mainly on the liquid's loading of the gas component. Generally, the gas-side resistance is several orders of magnitude lower than the one on the liquid side. Hence, the first one is neglected in most cases. The general equation for mass transfer from a bubble to a liquid is expressed as follows:

$$-\frac{dn}{dt} = k_L A(c_0 - c_l) \tag{5}$$

Here, n is the amount of a substance, k_L the liquid side mass transfer coefficient, A the contact surface and c_0 and c_l the mole concentrations at the gas-liquid interface and in the liquid bulk. If c_l is negligibly small, Equation (5) can be transformed into the following using the ideal gas and Henry's law.

$$k_L = -\frac{1}{A}\left(\frac{H}{RTp_b}\right)\frac{d}{dt}(p_b V_b) \tag{6}$$

H is the Henry constant, p_b and V_b the pressure and volume of the gas bubble, R the universal gas constant and T the temperature in K. The Henry constant for electrolyte solutions is calculated with Equation (7) [28].

$$\log\left(\frac{H}{H_w}\right) = \sum h_i \cdot 0.5 \sum c_j z_j^2 \tag{7}$$

Here, H_w is the Henry constant for water calculated by the method given in [29], h the contribution referring to positive and negative ions and to the gas and z the valence electrons. Differentiation of Equation (6) gives (corresponding to [30]):

$$k_L = -\frac{1}{A}\left(\frac{H}{RT}\right)\left(\frac{d}{dt}V_b + \frac{V_b}{p_b}\frac{d}{dt}p_b\right) \tag{8}$$

If the bubble volume, V_b, of a sphere and the bubble surface, A, are inserted into Equation (8), it can be rewritten using the definition of Sh to:

$$Sh = \frac{k_L d_b}{D} = -\frac{1}{6}\left(\frac{Hd_b}{DRT}\right)\left(3\frac{d}{dt}d_b + \frac{d_b}{p_b}\frac{d}{dt}p_b\right) \tag{9}$$

Here, D is the diffusion coefficient calculated by the method given in [31]. Other physical properties were drawn from [32]. The bubble's internal pressure consists of atmospheric pressure, hydrostatic pressure and surface tension pressure according to Equation (10).

$$p_b = p_{atm} + \rho_l g h + 4\sigma / d_b \tag{10}$$

Here, p_{atm} is the atmospheric pressure, h the height of the water head and σ the surface tension. If bubbles are levitated at the same position and the fluid properties stay constant, pressure change in the bubble depends only on variation of d_b. In the range of diameters from 2.0 to 0.05 mm, the surface tension pressure change can be calculated to differences of 58 mbar for a

water/air-system and is therefore negligibly small. This result is valid for all aqueous solutions in this work. Hence, Equation (9) can be written as follows:

$$Sh = \frac{k_L d_b}{D} = -\frac{1}{2}\frac{H}{DRT} d_b \frac{d}{dt} d_b \tag{11}$$

In a more general form, *Sh* is only a function of *Re*, in which Equation (11) can be transformed to:

$$Sh = C_1 \mathrm{Re} \tag{12}$$

With:

$$C_1 = -\frac{1}{2}\frac{\upsilon_l}{u}\frac{H}{DRT}\frac{d}{dt} d_b \tag{13}$$

Sh for bubbles with mobile surfaces can be calculated according to Higbie's theory as follows:

$$Sh = 1.13 \mathrm{Re}^{1/2} Sc^{1/2} \tag{14}$$

or, for bubbles with a rigid surface, after Froessling [13] with:

$$Sh = 0.6 \mathrm{Re}^{1/2} Sc^{1/3} \tag{15}$$

Here, *Sc* is the Schmidt number as the ratio of υ and *D*.

If a chemical reaction is superimposed, the absorption changes to chemisorption. Chemisorption proceeds more quickly, generally, regarding a steeper concentration gradient at the phase boundary. The enhancement factor, *E*, classifies the acceleration of the absorption and is therefore defined as the ratio of chemisorption to the absorption rate.

$$E = \frac{\dot{n}_{chemsorption}}{\dot{n}_{absorption}} \tag{16}$$

3. Experimental Methods

3.1. Apparatus and Procedure

Experiments were performed in an in-house build device consisting of a glass channel with an expanding quadratic cross-section, as shown in Figure 1. The channel is vertically positioned between two polyacrylic cubes, with the smaller cross-section facing toward the top. This cross-section has an inner width of 0.88 mm, while the larger cross-section at the bottom has a width of 3.0 mm. A correlation of channel width over height was measured and is given in Figure 1 for later calculation of the mean velocity. The bottom cube is connected to a three-way valve with standard Teflon tubing and fittings, which were used as the connection type of choice, generally. The top polyacrylic cube contains an inner T-junction. One side is connected to a three-way valve similar to the bottom valve. A stainless steel needle with an outer diameter of 0.4 mm is placed in the middle of the glass channel to generate bubbles with a diameter from 0.1 to 2.5 mm. The needle itself is connected to a micro three-way valve, which is connected to the gas bottle on one side and to a 50 µL syringe series 800 from Hamilton Messtechnik GmbH, Germany, on the other side. This valve has an inner volume of 16 µL only to improve the bubble generation with the syringe. The

other three-way valves are used to control the flow direction. Syringe pumps (HLL200, Landgraf Laborsysteme HLL GmbH, Germany) feed the liquid flow in a range from 0.5 to 10 mL/min. Syringe pumps are connected to check valves for filling and delivery. Glass flasks with three connections are used as liquid reservoirs. Two of them are used for the liquid flow, while one is connected to the gas line or vacuum pump. Water and alkaline solutions of different concentrations and purities are used in terms of pH value (C3010 and SK20T probe, Consort bvba, Belgium) and electrical conductivity (741 probe with the conductivity meter SevenEasy S30, Mettler-Toledo GmbH, Germany). Tap water (0.0034 MΩ·cm), deionized water (0.34 MΩ·cm) and Merck Millipore (Merck KGaA, Germany) treated water (5.0 MΩ·cm) are used. Sodium hydroxide is purchased from Merck KGaA, Germany. Nitrogen (5.0, 99.999% pure) and carbon dioxide (technical grade, 99.5% pure; 4.5, 99.995% pure) from Messer Group GmbH, Germany, as well as pressurized air are investigated in the set-up. An Advance ICD (10×)–(160×) transmitted-light microscope from Bresser GmbH, Germany, is used for visualization with a length scale mounted next to the glass channel. A D7000 digital camera from Nikon GmbH, Germany, with an AF Nikkor 24–85 mm f/2.8-4D IF macro-objective and a MotionXtra NR4 Speed 2 high-speed camera from ImagingSolutions GmbH, Germany, are connected to the microscope for documentation.

Figure 1. Drawing of the experimental device with details of one polyacrylic cube, the microvalve and a sketch of the inside of the glass channel with all the forces acting on the bubble.

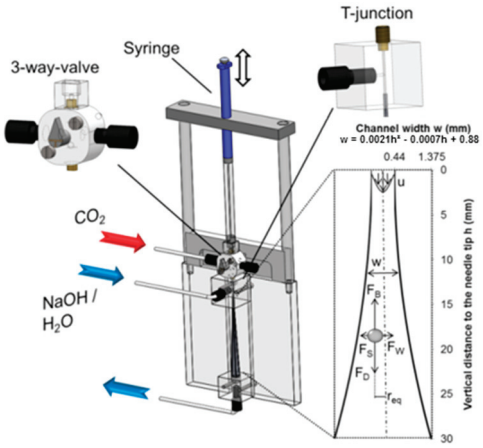

All glass flasks are rigorously cleaned with acetone and Millipore water several times. Afterwards, they are dried using nitrogen and filled with the studied liquid. Conductivity is measured directly in the flasks and at the end of the experimental set-up to ensure the removal of all surfactants.

For degassing a vacuum of 80 mbar absolute pressure is applied to the flasks for thirty minutes while being stirred in an ultrasonic bath. Temperature is held constant at 20 °C. The liquid is circulated through the experimental set-up during the entire investigation. Pre-saturated solution is generated with an alternated operation of degassing and pressurization with the desired gas. The gas side of the set-up is purged for 10 min to ensure that the same gas quality in the syringe is as in the bottle. Then, the microliter syringe is filled with gas.

Deionized water and air are used to study the drag force coefficient. Bubbles are injected into the liquid. A bubble is generated at the needle tip, while pressing the syringe. The bubble detachment is controlled by the flow rate and, hence, by the momentum force of the liquid. The bubble position after levitation is recorded with the digital camera. Several bubble diameters and flow rates are studied in combination. Limitations exist, because of the channel dimensions. Too high of a flow rate flushes the bubbles out of the channel, while too small of a flow rate lets the bubbles rise back to the needle tip. Because of this, a narrow range of *Re* was studied for each λ. For absorption experiments, bubble growth at the tip is shortened to rapidly ensure steady flow around the whole bubble surface. Therefore, higher flow rates are used, resulting in only small bubbles for these experiments. The absorption of larger diameters and bubble age are studied by generating bubbles in a saturated solution and switching afterwards to a degassed solution.

3.2. Bubble Diameter Determination with ImageJ

The recorded images are analyzed using the software tool, ImageJ (Wayne Rasband, National Institutes of Health, USA, 2012). At the beginning of each experiment, a reference value is measured from the analyzed image with the length scale next to the glass channel. Furthermore, bubble-wall and bubble-needle tip distances are determined. Afterwards, the image is transformed to binary data according to a set threshold, while all irrelevant details are filtered. The Feret diameters of the bubbles are measured and transferred into a size using the reference distance. An equivalent diameter is calculated with Equation (3). The transformation into a binary picture removes 5 pixel of the bubble diameter at the maximum and only 2 as an average. This results in a maximal total error of 10% for the smallest and 0.1% for the largest bubbles, with a typical pixel size of approximately 2 µm.

4. Results and Discussion

4.1. Levitation Position

Levitation was observed for air bubbles of the same diameter for different volumetric flow rates, due to the diverging channel width and wall interaction. The same tendency is valid *vice versa*. Figure 2a shows the horizontal levitation positions over the vertical positions of decreasing bubble diameters for different volumetric flow rates. The vertical position is measured in the flow direction and shown in the diagram, too. The displayed points represent the bubble center. Additionally, the inner wall of the glass channel is shown. The stabilizing position of the bubble moves downward for smaller bubbles, generally, as a consequence of the reduced buoyancy forces. In addition, the radius, r_{eq}, of the equilibrium position increases, as seen in Figure 2b. Higher flow rates imply the same tendency regarding larger drag forces. Bubbles stay in the middle of the channel for $\lambda > 0.5$. Differences to this central position are identified for smaller ratios in an increasing manner; thus, each equilibrium radius is larger for smaller bubbles. This general trend corresponds with the solid particles studied in [33]; even equilibrium radii are notably smaller here.

Figure 2. (**a**) The horizontal levitation position with the vertical levitation position of the bubbles; (**b**) The non-dimensional equilibrium radius with the non-dimensional bubble diameter for the levitated bubbles.

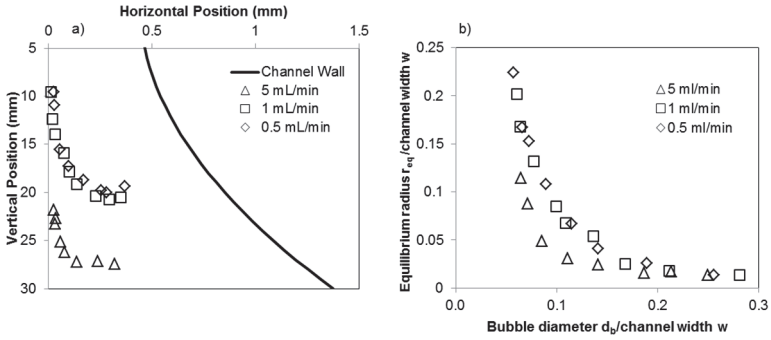

4.2. Modeling Drag Force Coefficient C_D

If wall effects are neglected and a uniform velocity profile is assumed, *Re* is calculated with bubble rising speed or flow velocity in the stagnation point. In this work, acceleration of the liquid flow around a bubble is higher with increasing λ, due to the growing blockage of the cross-section by the bubble. Here, an average difference between mean velocities of 30% occurs in the stagnation point and the center point of the bubble. Furthermore, the flow velocity changes in the radial direction, due to the small channel dimensions. The calculated drag force coefficients with simplified velocity integration over the bubble surface similar to [26] differ from those using the mean velocity in the stagnation point in the same order. Deviations for drag force coefficients are less than 1% by the mean velocity at the center of the bubble considering the cross-section blockage. For that reason, reference velocities are calculated from the known volume flow rates and the free cross-section at the bubble's midpoint height as a simplified modeling approach similar to [34].

Figure 3d shows drag force coefficients calculated by Equation (2) as points based on experimental results. Different values for the same Reynolds numbers occur because of wall effects. In contrast to a free rising bubble, not just one curve is applicable for the drag force coefficient. Higher ratios of λ increase the coefficient and lead the curves away from the axis, as is shown by [26], too. The comparison of the given correlations show the high deviations of the drag force coefficients in infinite flow fields. According to both approaches, including wall effects, Mei's equation [15] is valid for $C_{D\infty}$ and offers the best results in the investigated bubble range. Constants K_I and K_{II} are calculated by the least-squares method. Figure 3a,b shows the determined values and their correlations. An exponential and a double-linear approach are used as the best-fitting curves for each constant. The intersection points of the straight lines are $\lambda = 0.62$ and $\lambda = 0.648$. The walls have to be considered for $r_{eq} < 2d_b$ [35], which is equivalent to λ larger than 0.2. No elongation of the bubbles was observed for these λ values. Therefore, larger constants and, hence, drag force coefficients are shown for higher values of λ, but further investigations have to clarify this observation. Deviations are smaller than 0.5% for all four fits, so similar results are given using either the exponential or linear modeling. In Figure 3c, good conformity is shown for the experimental results and the two modeling approaches according to Equation 4 for three λ exemplarily. The

second approach multiplying K_{II} with $C_{D\infty}$ approximates the calculated drag force coefficients even better. Thus, in Figure 3d, five modeled drag force coefficient curves with this approach are shown additionally to the experimental results mentioned before. The maximum deviations are lower than 8% for each λ in total, which involves an accurate correlation.

Figure 3. (**a**,**b**) Constants K_I and K_{II} with λ; (**c**) Calculated and correlated drag coefficients C_D with Re for three λ values; (**d**) Calculated and correlated drag coefficients C_D with Re for λ values from 0.1 to 0.9.

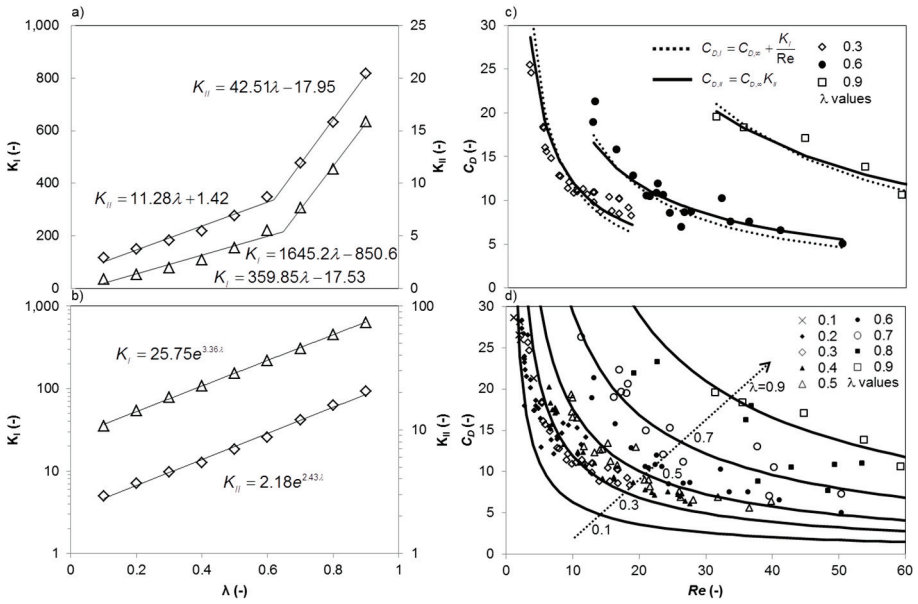

4.3. Absorption of N_2 and CO_2

Figure 4 shows the decreasing bubble diameters, due to the absorption of single nitrogen bubbles in degassed water of different purities. Bubble diameters decrease linearly independent of the starting diameters. The lines have a constant, nearly identical negative slope of 0.003 ± 0.0002 mm/s for all water purities considering the measuring inaccuracy. This indicates a similar dissolving speed of all bubble diameters and water purities. The determined value is comparable to that given in [19] and the second regime in [20], which was explained by a rigid bubble surface. Two different regimes are not identified in this work, even for the same range of bubble diameters as was observed by Vasconcelos *et al*. [20]. The accelerated absorption in their first regime was referred to as a mobile bubble surface. No water specifications were given by the authors. It can be assumed that very pure water was used, because the mobile surfaces were only observed by Duineveld [16]. Concerning our own experimental results, a generally immobilized bubble surface can be extended to water with an electrical resistance of 5.0 MΩ·cm and bubble diameters of 2.0 mm.

Figure 4b shows the decreasing bubble diameters, due to the absorption of carbon dioxide of different gas qualities in saturated and degassed deionized water. Bubble diameters stay constant after a rapid decrease from the start for saturated water. The final diameter has a distinct smaller value for a gas quality of 4.5 (>99.995 *vol*%) compared to the technical grade carbon dioxide. Both curves have an approximately identical slope; hence, the decrease refers to the absorption of carbon

dioxide only. The calculated bubble diameter based on the impurities in the gas bottle and the start diameters corresponds to smaller values, as were observed in the experiments. In each bubble, the partial pressures of other gases are very low, since the purity of carbon dioxide is very high. The dissolved gases, mainly nitrogen, in the liquid diffuse into the gas bubble [20] and enlarge its volume. This desorption explains the larger diameter compared to the calculated values assuming only the gas feed composition. The bubble diameter still decreases, due to the higher absorption rate of carbon dioxide. A constant value is reached with a concentration equilibrium of saturated solution and identical partial pressures of the impurities in the bubble.

Figure 4. (**a**) The nitrogen bubble diameter with time in water of different purities; (**b**) The carbon dioxide bubble diameter with time. Technical (techn.) grade and quality 4.5.

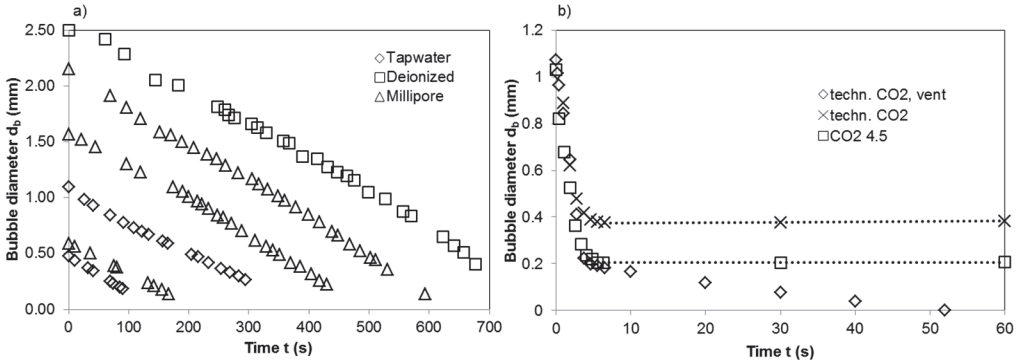

In degassed deionized water, two regimes are identified. The first regime is nearly identical to the absorption of carbon dioxide in untreated water. The second regime is consistent with the absorption of nitrogen shown in Figure 4a, which confirms the explanation above. Calculation of the transition point of both regimes shows similar deviations concerning the gas composition in the gas bottle and the diffusion of dissolved gases in the liquid. During degassing, the vacuum pump reaches approximately 80 mbar absolute pressure, hence, the rest of the impurities stay in the solution and diffuse into the bubble.

The absorption of carbon dioxide 4.5 in degassed pure water was studied according to the experiments with nitrogen, too. For each starting diameter, similar curves were determined. The absorption of carbon dioxide occurs rapidly followed by a slower absorption of nitrogen. In each case, the bubbles disappear completely. For small start diameters, the transition point is located at a diameter below 0.2 mm, which means a constant diameter decrease below the transition point from the rigid to the mobile surface in the purest water. Absorption in tap water shows the same tendency. Schulze and Schlünder [21] observed two regimes of carbon dioxide absorption in different pre-saturated aqueous solutions. The transition point was located at diameters between 1.0 and 1.5 mm. They explained the two regimes by the bubble surface condition change. The measured diameter decreasing rate in their first regime has a value of approximately 0.3 mm/s. This is similar to the rate measured in this work. No gas or water qualities are given by the authors. Therefore, it cannot be verified if the two regimes belong to a surface condition change or to gas qualities, as discussed before. Takemura and Yabe [22] also observed two linear regimes, which were explained

by a mobile and a rigid bubble surface. The value of their first regime is slightly larger than the value given by [21] and from this work. The authors observed this value for the first 0.15 s. The bubble formation enhances the initial mass transfer [36], which might be a reason for these differences, due to the fact that Takemura and Yabe used a pipe with a bubble generator at the bottom. Their second regime deviates notably from Schulze's and the values observed in this work. Finally, no consistent absorption rate exists for carbon dioxide in water. Since absorption shows a similar dependency as nitrogen, mentioned above, it is concluded that a rigid bubble surface occurs generally for water qualities lower than 5 MΩ·cm.

4.4. Chemisorption of CO_2

Chemisorption of carbon dioxide was studied in alkaline solutions, too. Figure 5a shows the bubble diameter change over time. One curve of the absorption in water is also included. All curves show similar trends in terms of two regimes. Higher concentrations of alkaline solutions result in steeper slopes of the curves. For 1 M NaOH, the second regime was reached after less than 1 s. The chemisorption of carbon dioxide was too quick to adequately document this behavior. High variations were measured between single experiments in the range of −1.0 to −1.4 mm/s. The absorption rate is the same for NaOH with a concentration of 0.1 mmol/L and water, due to the very low concentration. Both lines run parallel considering a larger starting diameter of the bubble in water.

Figure 5. (**a**) The carbon dioxide bubble diameter with time in sodium hydroxide solutions of different concentrations; (**b**) The mass transfer coefficient depending on the flow rate and the bubble diameter, represented by *Sh* and *Re*.

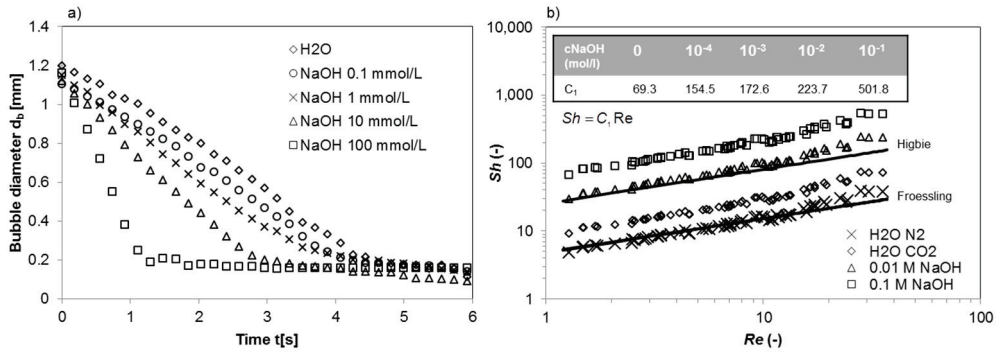

In Figure 5b, the Sherwood numbers are shown for different alkaline solutions and water according to Equation (12). The calculated values of C_1 are presented in the figure, too. For comparison, Equation (14) and Equation (15) of Higbie and Froessling are also given. *Sh* values for N_2 in water align to the Froessling curves with only a low deviation. *Sh* values of CO_2 in water are located between Higbie and Froessling with a minor tendency to Froessling's equation. This confirms the observation of a rigid surface area. Regarding Equation (11), the Sherwood numbers are calculated with several parameters dependent on the concentration. The diffusion coefficient, density and Henry constant vary only slightly up to a concentration of 1 M; hence, the Sherwood numbers and k_L increase, due to the steeper bubble decrease. The determined values are in the same

order as the values from Takemura and Matsumoto [23], even for a smaller range of *Re*. The differences in the Reynolds numbers are refer to the device used in their work, since the rising velocities of free bubbles and, hence, the Reynolds numbers are larger due to a smaller drag force coefficient compared to this work. Madhavi *et al*. [24] determined *E* as a function of time in the range from 13 to 19 for 1 M NaOH. *E* can be calculated with k_L assuming a negligible concentration in the bulk and an identical surface and concentration in the bubble. The ratio of the mass transfer coefficient with chemisorption to the one without depends on the bubble diameter decrease. For a value of −1.0 mm/s, *E* is determined to be 13, and for a value of −1.4 mm/s, *E* is 18, which corresponds to the data of Madhavi *et al*. very well.

5. Conclusions

Gas bubble flow without and with chemical reactions was investigated for the system of N_2/CO_2 in aqueous and alkaline solutions. Different bubble sizes ranging from 0.1 to 2.5 mm and concentrations from 0.1 mM to 1 M NaOH were studied. The experiments were conducted in a novel device consisting of a converging microchannel according to the design of Vasconcelos *et al*. [20] to increase the observation time of single bubbles. The device is more than one order of magnitude smaller compared to existing devices. Therefore, the inner volume of the complete set-up only has a few milliliters, which make this set-up favorable for very costly substances. A special feature is an inserted needle into the smallest cross-section of the channel to generate single, very small bubbles.

The levitation positions of the air bubbles were optically characterized in saturated water. A displacement from the center axis occurred, which was larger for smaller bubbles, corresponding to solid particles. Drag force coefficients, including wall effects, were determined based on two modeling approaches by a curve fitting dependent on the ratio of the channel width to the bubble diameter. Model data and experimental data deviate less than 8% from each other.

The absorption of N_2 showed a linear decreasing bubble diameter with time until complete extinction of the bubbles. The range of an immobilized bubble surface was enlarged in terms of water purity and bubble diameters. Absorption and chemisorption of CO_2 bubbles showed two linear regimes of diameter decreases independent of the gas composition. The first regime was related to pure CO_2 and the second regime to impurities in the initial gas, mainly N_2. Larger concentrations of NaOH result in faster bubble decreases. Mass transfer coefficients represented by the Sherwood numbers in correlation with Reynolds numbers and the enhancement factor were calculated showing comparable values from the literature. Comparison of *Sh* with the Froessling equation indicates a rigid bubble surface area for N_2 and CO_2.

In summary, this study shows the successful implementation of the absorption and chemisorption processes of microbubbles for a new device with an internal volume smaller than 1 mL for studying mass transport phenomena. Furthermore, other phenomena at the interface of a two-phase system can be investigated with extremely short, up to very long necessary observation times.

Acknowledgments

We want to thank Matthias Beck, Martin Matuschek and Thomas Patzer for their valuable lab work and contribution to this article. Special thanks go to Roland Schröder for building the device.

Nomenclature

a	maximum Feret diameter, mm
A	surface area, m^2
Ar	Archimedes number, −
b	minimum Feret diameter, mm
c	concentration, $mol \cdot m^{-3}$
C_1	constant, −
C_D	drag force coefficient, −
d	diameter, mm
D	diffusion coefficient, $m^2 \cdot s^{-1}$
E	enhancement factor, −
h	Henry constant model parameter, −
h	height, mm
H	Henry constant, $bar \cdot m^3 \cdot mol^{-1}$
k	mass transfer coefficient, $m \cdot s^{-1}$
K	drag force model constant, −
n	amount of substance, mol
p	pressure, barg (gauge)
r	radius, mm
R	universal gas constant, $J \cdot mol^{-1} \cdot K^{-1}$
Re	Reynolds number, −
Sc	Schmidt number, −
Sh	Sherwood number, −
t	time, s
T	temperature, K
u	channel flow velocity, $m \cdot s^{-1}$
V	volume, m^3
z	valence electrons, −

Greek symbols

λ	ratio of bubble diameter to channel width, −
ρ	density, $kg \cdot m^{-3}$
σ	surface tension, $N \cdot m^{-1}$
ν	kinematic viscosity, $m^2 \cdot s^{-1}$

Variable index nomenclature

atm	atmosphere
b	bubble
D	drag

e	volume equivalent
eq	equilibrium
g	gas
l	liquid
L	liquid
w	water
0	gas-liquid interface
∞	infinite flow field

Conflicts of Interest

The authors declare no conflict of interest.

References

1. Stitt, E.H. Alternative multiphase reactors for fine chemicals—A world beyond stirred tanks? *Chem. Eng. J.* **2002**, *90*, 47–60.
2. Schneider, M.-A.; Maeder, T.; Ryser, P.; Stoessel, F. A microreactor-based system for the study of fast exothermic reactions in liquid phase: Characterization of the system. *Chem. Eng. J.* **2004**, *101*, 241–250.
3. Stefanidis, G.D.; Vlachos, D.G.; Kaisare, N.S.; Maestri, M. Methane steam reforming at microscales: Operation strategies for variable power output at millisecond contact times. *AIChE J.* **2009**, *55*, 180–191.
4. Crespo-Quesada, M.; Grasemann, M.; Semagina, N.; Renken, A.; Kiwi-Minsker, L. Kinetics of the solvent-free hydrogenation of 2-methyl-3-butyn-2-ol over a structured Pd-based catalyst. *Catal. Today* **2009**, *147*, 247–254.
5. Grasemann, M.; Renken, A.; Kashid, M.N.; Kiwi-Minsker, L. A novel compact reactor for three-phase hydrogenations. *Chem. Eng. Sci.* **2010**, *65*, 364–371.
6. Kockmann, N.; Roberge, D.M. Harsh reaction conditions in continuous-flow microreactors for pharmaceutical production. *Chem. Eng. Technol.* **2009**, *32*, 1682–1694.
7. Günther, A.; Jensen, K.F. Multiphase microfluidics: From flow characteristics to chemical and materials synthesis. *Lab Chip* **2006**, *6*, 1487–1503.
8. Doku, G.N.; Verboom, W.; Reinhoudt, D.N.; van den Berg, A. On-microchip multiphase chemistry—A review of microreactor design principles and reagent contacting modes. *Tetrahedron* **2005**, *61*, 2733–2742.
9. Hessel, V.; Angeli, P.; Gavriilidis, A.; Löwe, H. Gas-liquid and gas-liquid-solid microstructured reactors: Contacting principles and applications. *Ind. Eng. Chem. Res.* **2005**, *44*, 9750–9769.
10. Kashid, M.N.; Kiwi-Minsker, L. Microstructured reactors for multiphase reactions: State of the art. *Ind. Eng. Chem. Res.* **2009**, *48*, 6465–6485.

11. Kockmann, N.; Gottsponer, M. Heat transfer limitations of gas-liquid exothermic reactions in microchannels. In Proceedings of the ASME 2010 8th International Conference on Nanochannels, Microchannels, and Minichannels Collocated with 3rd Joint US-European Fluids Engineering Summer Meeting, Montreal, QC, Canada, 1–5 August 2010; Paper No. FEDSM-ICNMM 2010–30389, pp. 193–199.
12. Kockmann, N. Sicherheitsaspekte bei der Prozessentwicklung und Kleinmengenproduktion mit Mikroreaktoren. *Chemie Ingenieur Technik* **2012**, *84*, 715–726.
13. Lochiel, A.C.; Calderbank, P.H. Mass transfer in the continuous phase around axisymmetric bodies of revolution. *Chem. Eng. Sci.* **1964**, *19*, 471–484.
14. Peebles, F.N.; Garber, H.J. Studies of the motion of gas bubbles in liquids. *Chem. Eng. Prog.* **1953**, *49*, 88–97.
15. Kulkarni, A.A.; Joshi, J.B. Bubble formation and bubble rise velocity in gas-liquid systems: A review. *Ind. Eng. Chem. Res.* **2005**, *44*, 5873–5931.
16. Duineveld, P.C. The rise velocity and shape of bubbles in pure water at high reynolds number. *J. Fluid Mech.* **1995**, *292*, 325–332.
17. Garner, F.H.; Hammerton, D. Circulation inside gas bubbles. *Chem. Eng. Sci.* **1954**, *3*, 1–11.
18. Peters, F.; Biermann, S. Streulichtuntersuchungen an einem kleinen, levitierten Bläschen. In Proceedings of the Fachtagung der Deutschen Gesellschaft für Laser-Anemometrie, Karlsruhe, Germany, 7–9 September 2004.
19. Nüllig, M.; Peters, F. Diffusion of small gas bubbles into liquid studied by the rotary chamber technique. *Chemie Ingenieur Technik* **2013**, *85*, 1074–1079.
20. Vasconcelos, J.M.T.; Orvalho, S.P.; Alves, S.S. Gas-liquid mass transfer to single bubbles: Effect of surface contamination. *AIChE J.* **2002**, *48*, 1145–1154.
21. Schulze, G.; Schlünder, E.U. Absorption von einzelnen gasblasen in vorbeladenem wasser. *Chemie Ingenieur Technik* **1985**, *57*, 233–235.
22. Takemura, F.; Yabe, A. Rising speed and dissolution rate of carbon dioxide bubble in slightly contaminated water. *J. Fluid Mech.* **1999**, *378*, 319–334.
23. Takemura, F.; Matsumoto, Y. Dissolution rate of spherical carbon dioxide bubbles in strong alkaline solutions. *Chem. Eng. Sci.* **2000**, *55*, 3907–3917.
24. Madhavi, T.; Golder, A.K.; Samanta, A.N.; Ray, S. Studies on bubble dynamics with mass transfer. *Chem. Eng. J.* **2007**, *128*, 95–104.
25. Matulka, P. Partikelbewegung und Trennung in laminar durchströmten Rohren mit nachfolgender Strömungsaufweitung. Ph.D. Thesis, Dortmund University, Dortmund, Germany, 2013.
26. Clift, R.; Grace, J.R.; Weber, M.E. *Bubbles, Drops and Particles*; Academic Press: New York, NY, USA, 1978.
27. Wham, R.M.; Basaran, O.A.; Byers, C.H. Wall effects on flow past solid spheres at finite reynolds number. *Ind. Eng. Chem. Res.* **1996**, *35*, 864–874.
28. Danckwerts, P.V. *Gas-Liquid Reactions*; McGraw-Hill: New York, NY, USA, 1963.
29. Carroll, J.J.; Slupsky, J.D.; Mather, A.E. The solubility of carbon dioxide in water at low pressure. *J. Phys. Chem. Ref. Data* **1991**, *20*, 1201–1209.

30. Calderbank, P.H.; Lochiel, A.C. Mass transfer coefficients, velocities and shapes of carbon dioxide bubbles in free rise through distilled water. *Chem. Eng. Sci.* **1964**, *19*, 485–503.
31. Vas Bhat, R.D.; Kuipers, J.A.M.; Versteeg, G.F. Mass transfer with complex chemical reactions in gas-liquid systems: Two-step reversible reactions with unit stoichiometric and kinetic orders. *Chem. Eng. J.* **2000**, *76*, 127–152.
32. Perry, R. *Perry's Chemical Engineers Handbook*, 7th ed.; McGraw-Hill: New York, NY, USA, 1997.
33. Matas, J.-P.; Morris, J.F.; Guazzelli, E. Lateral force on rigid sphere in large-inertia laminar pipe flow. *J. Fluid Mech.* **2009**, *621*, 59–67.
34. Haberman, W.L.; Sayre, R.M. Motion of rigid and fluid spheres in stationary and moving liquids inside cylindrical tubes. *David Taylor Model Basin Report* **1958**, 1143.
35. Büchner, E.-W. Experimentelle Untersuchung über Strömungskräfte auf ruhend und bewegten Kugeln in einer ebenen Poiseuille-Strömung. Ph.D. Thesis, University Fridericiana Karlsruhe, Karlsruhe, Germany, 1987.
36. Sakai, M.; Kusakabe, K. Gas absorption during the burst of an individual bubble on the water surface. *J. Chem. Eng. Jpn.* **2004**, *37*, 1117–1121.

Rapid Determination of Optimal Conditions in a Continuous Flow Reactor Using Process Analytical Technology

Michael F. Roberto, Thomas I. Dearing, Charles W. Branham, Olav Bleie and Brian J. Marquardt

Abstract: Continuous flow reactors (CFRs) are an emerging technology that offer several advantages over traditional batch synthesis methods, including more efficient mixing schemes, rapid heat transfer, and increased user safety. Of particular interest to the specialty chemical and pharmaceutical manufacturing industries is the significantly improved reliability and product reproducibility over time. CFR reproducibility can be attributed to the reactors achieving and maintaining a steady state once all physical and chemical conditions have stabilized. This work describes the implementation of a smart CFR with univariate physical and multivariate chemical monitoring that allows for rapid determination of steady state, requiring less than one minute. Additionally, the use of process analytical technology further enabled a significant reduction in the time and cost associated with offline validation methods. The technology implemented for this study is chemistry and hardware agnostic, making this approach a viable means of optimizing the conditions of any CFR.

Reprinted from *Processes*. Cite as: Roberto, M.F.; Dearing, T.I.; Branham, C.W.; Bleie, O.; Marquardt, B.J. Rapid Determination of Optimal Conditions in a Continuous Flow Reactor Using Process Analytical Technology. *Processes* **2014**, *2*, 24-33.

1. Introduction

Currently, the majority of pharmaceutical and specialty chemical manufacturing is performed in large volume batch reactors. These reactors are limited by a number of challenges: Poor mixing, large temperature gradients, potentially inaccurate serial additions, safety and pressure hazards, and resource-intensive validation procedures requiring man-hours, time, and manual sampling for quality assurance and control. Many of these challenges are mitigated using continuous flow reactors (CFRs). CFRs are small volume flow cells optimized for continuous, consistent production of a target compound. The volumes and channels of CFRs can range from milliliter to microliter scale [1]. Milliliter-scale CFRs typically employ reaction plates designed for turbulent mixing (Figure 1a). Reaction plates are typically manufactured with millimeter-wide channels and a high surface-to-volume interface for a multi-fold reduction in the average distance to temperature control channels (Figure 1b). The design results in a reduction of temperature gradients and improved homogeneity in CFRs [2–4]. It has also been shown that parallel addition of reagents removes variation introduced by operators, and a closed system is less affected by environmental variation [5]. Roberto *et al*. have previously demonstrated a 75% reduction in reaction time in continuous flow when compared to a batch reactor [6].

Figure 1. (**a**) Side view of continuous flow reactor mixing chip showing heat exchange and mixing areas. Each area has a width of 1.5 mm, and are separated by 1 mm of glass; (**b**) Top view of continuous flow reactor mixing chip. Heart-shaped mixers are employed to ensure turbulent mixing throughout.

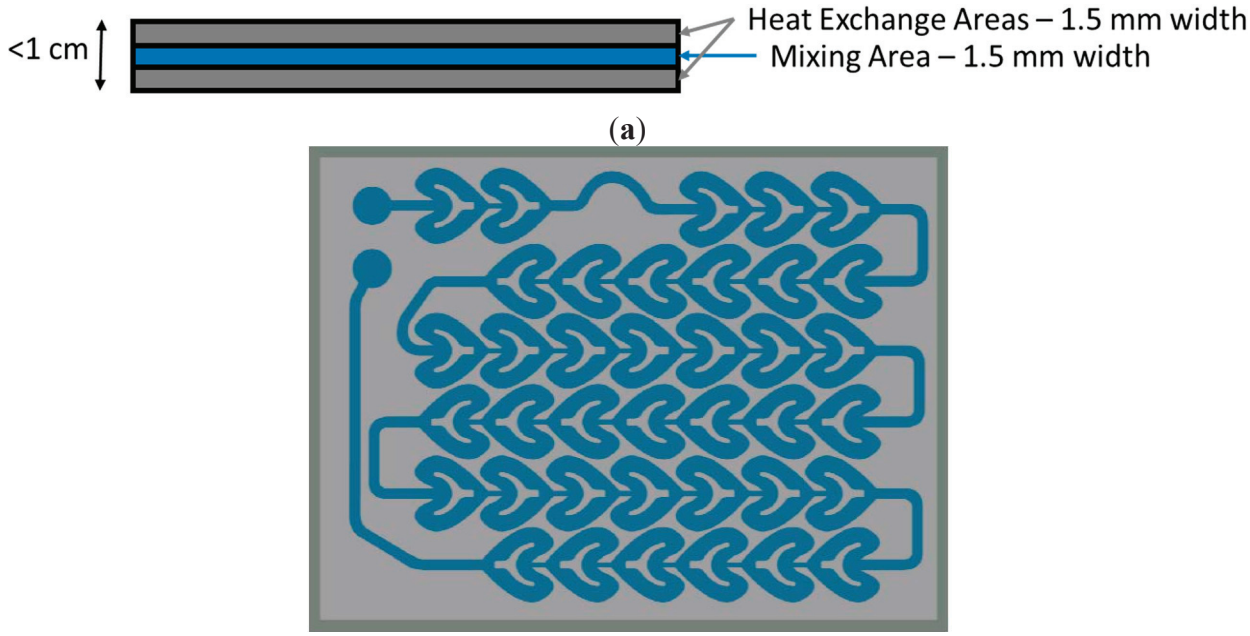

All of these advantages assume that a reactor system is in steady state. A steady state continuous flow system is one that is physically stable with regards to the variables of pressure, flow rate, mixing, and temperature. This results in controlled chemical production with reproducible results. Such a system offers significant advantages over batch reactors that fluctuate between different production runs. Currently, CFRs are determined to be at steady state by either a univariate method detecting physical stability in the reactor or a multivariate method determining the stability of chemical output [1,5,7–9]. Chemical measurements frequently require aliquots for offline validation to determine steady state. Uncertainty in reactor steady state requires multiple measurements, further extending analysis time. This can be especially problematic when attempting to determine optimal reactor conditions that require the exploration of a large design space. Physical measurements, while rapid, cannot effectively detect problems associated with product quality. Reactor systems are not currently constructed with interfaces to accommodate process analytical technology (PAT). Instead, current physical stability detection methods largely rely on feedback from the temperature or flow controllers without dedicated analytics.

A continuous flow system was designed that expands traditional physical monitoring while implementing real-time chemical monitoring to accurately and rapidly determine steady state. Monitoring of any process requires a reproducible sampling interface for reliable results. New Sampling/Sensor Initiative (NeSSI) sampling systems have previously been shown to be effective tools for enabling process monitoring in fluid and gas systems [6,10], and as interfaces for continuous flow reactor analytics [6]. NeSSI is a modular platform allowing for simple expansion or rearrangement of a sampling platform. This enables rapid prototyping and development of

continuous flow reactor systems. The coupling of NeSSI with appropriate sensors creates a dependable interface for the sampling of a flow channel [10,11].

Chromatographic methods are the most frequently used validation methods to determine chemical steady state and conversion in CFRs [5,7–9,12,13]. These methods yield reproducible results but can have analysis times in excess of fifteen minutes after sample collection. Confirmation of chemical steady state in a CFR over multiple aliquots requires an hour or more using chromatographic methods. A design of experiments (DoE) with 25 points would require more than a day to determine optimal conditions. Raman spectroscopy has previously been applied and proven effective for in-line process monitoring of flow systems [9,14–16]. Recent work by Roberto *et al*. has shown that Raman spectroscopy is a viable method for monitoring chemical yield in a CFR [6]. Deconvolution of Raman spectral data is challenging in complex chemical systems. Chemometric tools such as principal component analysis (PCA) are often used to process and analyze this spectral data quickly and effectively [17,18]. Used in tandem, Raman spectroscopy and PCA allow for robust process monitoring and effective process control [18–21].

Figure 2. The Swern oxidation. The center column (green background) shows the desired chemical path, with added reagents shown in black boxes. The outer columns (red background) show the potential chemical pathways for side-product formation (**8** and **9**).

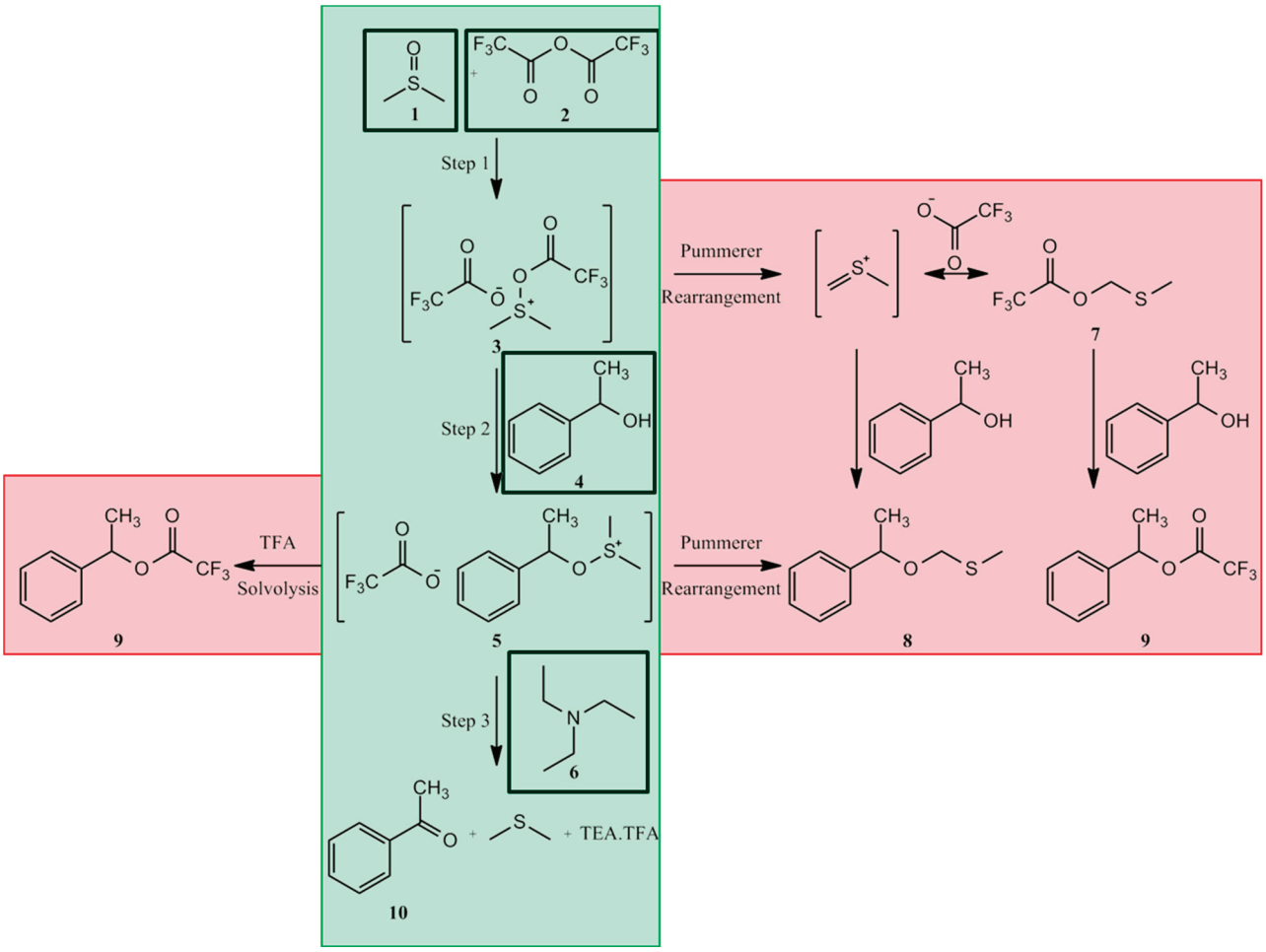

The focus of this investigation was to demonstrate that the combination of NeSSI with PAT and multivariate chemical monitoring offers significant advantages for optimizing chemical design space when compared with systems that employ physical or chemical techniques alone. Additionally, methods developed show potential for quality control and upset detection in production-scale facilities. Critical to the success of this project was the construction and design of a smart reactor system for monitoring and control of a defined chemistry with PAT. To demonstrate the smart reactor system, the Moffatt-Swern oxidation of 1-phenylethanol (Figure 2) was investigated. The formation of the highly unstable intermediates **3** and **5** is highly exothermic, requiring accurate temperature control [12,13]. The overall results demonstrate that the application of PAT to accurately detect physical and chemical stability in CFRs improved the time required to determine steady state by more than an order of magnitude. This reduced the time required to process the DoE and determine optimal reactor conditions. The final goal of this project was to develop a procedure for optimizing CFRs independent of the chemistry performed.

2. Experimental Section

The continuous flow reactor (CFR) was comprised of 4 main components: The Intraflow NeSSI sampling system, the analytics and controllers, the chemical mixers, and the control software. The Intraflow sampling system, provided by Parker Hannifin (Cleveland, OH, USA), consisted of four identical reagent lines and a product line. Four reagents: 1.0 M trifluoroacetate anhydride (Sigma-Aldrich, St. Louis, MO, USA), 1.1 M DMSO (Sigma-Aldrich, St. Louis, MO, USA), 1.0 M *S*-1-phenylethanol (Sigma-Aldrich, St. Louis, MO, USA), and 2.4 M triethylamine (Sigma-Aldrich, St. Louis, MO, USA) all in dichloromethane (Sigma-Aldrich, St. Louis, MO, USA) are pumped into the system by HPLC Pumps (two FLOM FS10A HPLC pumps, FLOM USA, San Diego, CA, USA, and two SSI Series I HPLC pumps, SSI, State College, PA, USA). These pumps actively controlled the residence time and stoichiometry of the reactor system. Pressure relief valves were installed on each line to ensure that the reactor did not overpressurize. Temperature was controlled by a Huber Tango heat-exchanger (Huber USA, Northport, NY, USA) and was pumped across three sequential Corning LF Reactor plates (Corning Glass, Avon, France), each with a reactor volume of 1 mL, that included 38 heart-shaped mixers per plate (Figure 1b) to ensure turbulent mixing throughout.

The analytics on each of the four reagent line were as follows: A pressure transducer (HEISE, Stratford, CT, USA), a flow meter (FCI Incorporated, San Marcos, CA, USA), and a 0.5” O.D. Raman ball-probe (Marqmetrix, Seattle, WA, USA) were interfaced to NeSSI via a fiber optic cable. The heat exchange lines were equipped with a thermocouple (Omega Engineering, Stamford, CT, USA) before and after the reactor plates to determine the temperature loss across the reactor. The product line NeSSI system contained a thermocouple and a 0.5” O.D. Raman ball-probe. A four-channel 785 nm Raman system, supplied by Kaiser Optical Systems (Ann Arbor, MI, USA) was used to collect Raman spectra from the four ball-probes mounted on the reactor sequentially. The sensors and controllers, with the exception of the Raman instrument, were all monitored and controlled via an in-house designed LabVIEW 7.5 (National Instruments Corporation, Austin, TX, USA) GUI environment. All of the analytics were interfaced to the reaction flow via NeSSI sampling

system. The sensors and digital controllers were queried once per second; the GUI reported temperature, pressure, and flow information in real-time.

Raman investigation of the reaction chemistry was performed prior to exploring the full temperature and flow rate design space. Spectra were collected by performing chemistry at a constant flow rate of 4 mL/min from −20 °C to 20 °C at 10 °C intervals. Five Raman spectra were recorded; each consisting of five one-second exposures, for a total of 25 calibration spectra. All calibration samples were validated on an Agilent 1100 Series HPLC (Agilent Technologies, Santa Clara, CA, USA) using a reverse-phase column (Agilent C18 Column, Santa Clara, CA, USA). The liquid chromatography was performed using two mobile phases: 0.1% acetic acid in water and acetonitrile. A constant flow of 5% acetonitrile for 2 min, then a gradient of 5% acetonitrile to 95% acetonitrile over 5.5 min, followed by 2 min constant flow resulted in clearly defined peaks for *S*-1-phenylethanol (**4**), acetophenone (**10**), and side-products **8** and **9**. Acetophenone peak area was used to determine reaction progress.

Raman spectra were imported into MATLAB 7.5 (Mathworks, Natick, MA, USA) for analysis and modeling. All spectra were preprocessed using a 1st order baseline removal to remove variations between spectra. PCA was performed with PLS Toolbox 5.0 (Eigenvector Research, Inc., Wenatchee, WA, USA) using mean-centered, background corrected spectra to monitor reactor steady state via changes in the multivariate scores. After establishing a system for accurately detecting chemical steady state, the full 25 point design space of flow rate (2–10 mL/min at 2 mL/min increments) and temperature (−20 °C to 20 °C at 10 °C intervals) was explored via the control software.

3. Results and Discussion

A system was developed using a CFR, NeSSI sampling system, and PAT to monitor chemical and physical variation in real-time (Figure 3). The PAT served two purposes: To determine reaction steady state, and to detect process upsets in the reactor. The variables temperature, pressure, and flow were recorded at one second intervals at specific locations in the reactor (Figure 3). When the lowest deviation of each physical measurement had been obtained the reactor was considered physically stable.

Upon reaching physical stability the reactor requires a lead time in order for the physical changes to be reflected in the chemical output downstream. Lead time is dependent upon the flow rate and the total volume of the reactor system by the equation:

$$Time\ \boldsymbol{\alpha}\ \frac{Reactor\ Volume}{Flow\ Rate} \tag{1}$$

A Raman ball probe on the product line (Figure 3) performed spectral acquisitions every 15 s. Raman spectroscopy is particularly suitable for monitoring the Swern oxidation due to the strength of the C=O band at 1691 cm^{-1} (Figure 4). Upon exiting the final reactor plate, all chemicals rapidly reached room temperature in the NeSSI sampling system prior to Raman analysis. This was confirmed by a thermocouple upstream of the Raman ball-probe on the product line. Chemical stability was determined via monitoring of the first PCA score from the Raman spectra in real-time. Four sequential scores within an acceptable statistical confidence established chemical steady state

(approximately 1 min of sample time). Upon attaining chemical steady state, a single HPLC sample was extracted and analyzed to quantitatively determine the yield of product.

Figure 3. Schematic of continuous flow reactor system. Each of the four reagent lines have the same analytics present: Flow meter, pressure sensor, Raman probe, and valves for operator safety. The first two reagent lines combine in the first reactor, with each subsequent line adding a reagent to the next reactor. The product line contains a Raman probe, a pressure regulator, and a pneumatic valve that is able to send the chemical output to either product collection or waste.

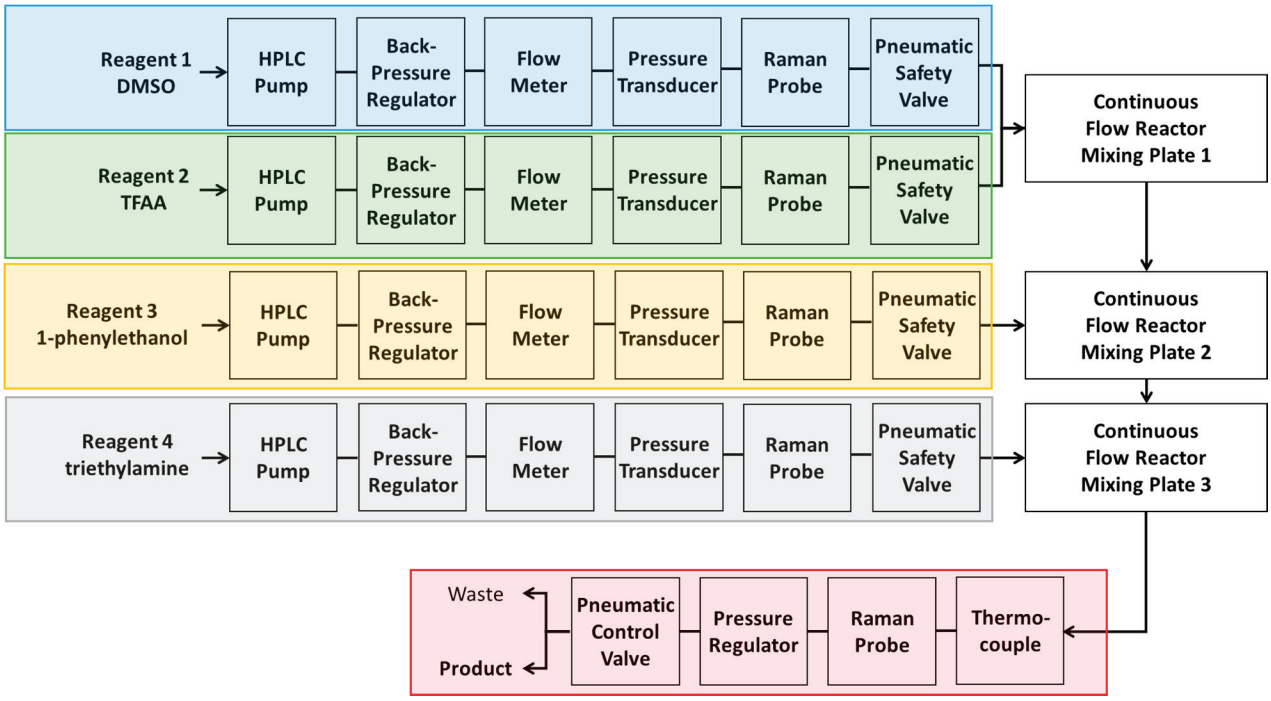

An example of how physical stability and chemical steady state relate to each other is shown in Figure 5. The dark dotted line shows the measured pressure in one of the four reagent lines. At 3 min, the flow rates of the four reagents were doubled from 2 to 4 mL/min. Physical stability is established in less than one minute. The first change in the PCA scores is observed at 4 min, shown in the lighter dotted line. Chemical steady state is reached by 13 min, 10 min after the change in physical conditions. Determining chemical steady state using HPLC would have significantly increased the time to complete reactor optimization. Four consecutive HPLC measurements require an analysis cycle of one hour. This is 60 times longer than Raman monitoring to determine steady state. The real-time Raman information enabled a more effective use of HPLC for validation. Using this technique to rapidly and accurately determine steady state, a 25-point design space was explored in under four hours.

Figure 4. Wavelength subset of Raman spectra at five different temperatures. While the entire spectrum was used for PCA modeling, this region in particular shows the temperature dependence of the production of acetophenone, with peaks at 1691 cm^{-1} and 1602 cm^{-1}.

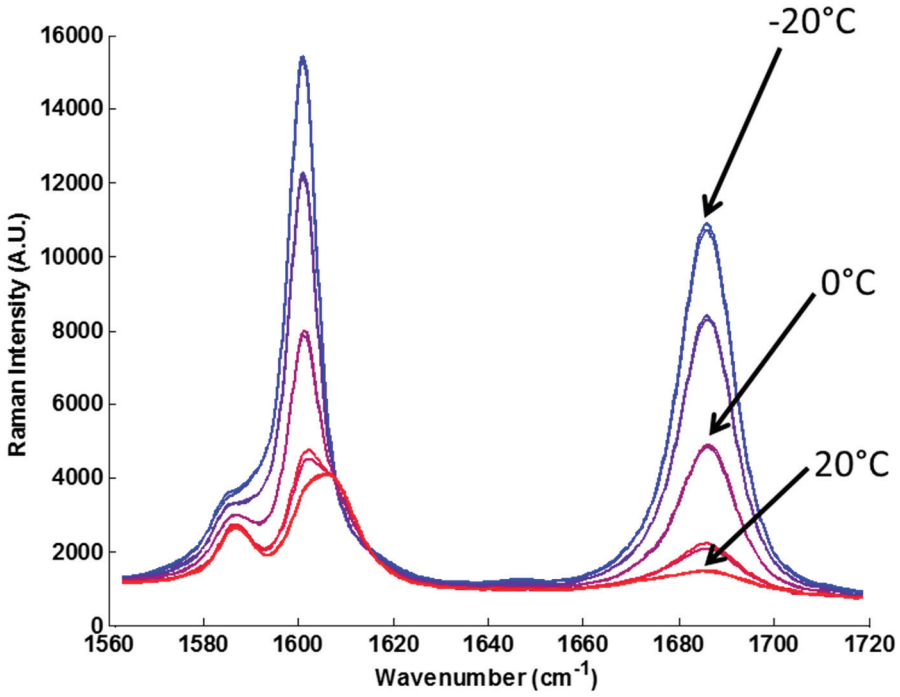

Figure 5. Pressure response in a reagent line (**dark dotted line**) and chemical yield information (**light dotted line**) that demonstrate physical and chemical steady states and changes in the system. At 3 min, the flow rates of the four reagent lines were doubled. The pressure sensor indicates physical steady state occurring in the reactor at 4 min, and the chemical yield response demonstrates chemical steady state occurring in the reactor at 13 min.

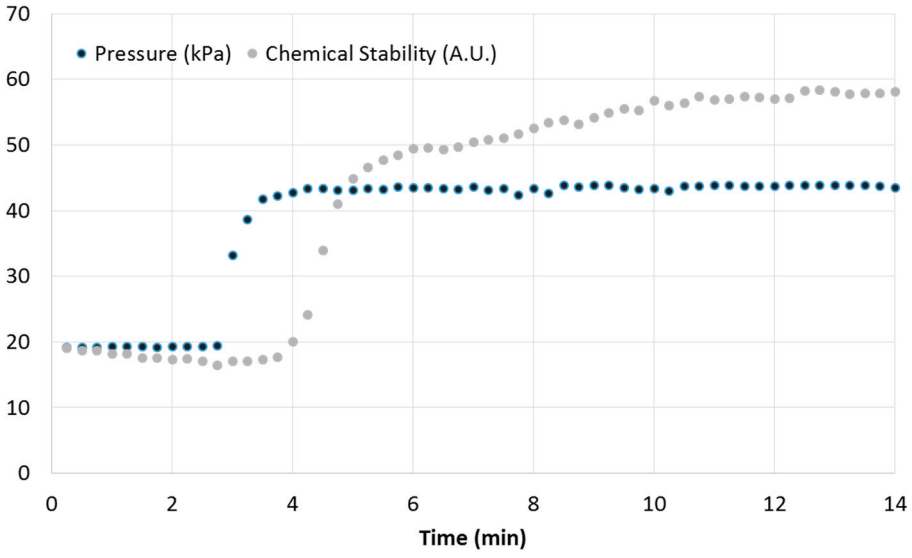

The chemical yield results obtained by using offline HPLC are shown in Table 1. In batch, at temperatures above −30 °C, no significant product yield was detected (<2%) [13]. Within the CFR at temperatures above −30 °C the Moffat Swern oxidation had yields ranging from 81% at −20 °C to 37% at 0 °C. As expected due to the exothermic nature of the reaction, yield decreases with increasing temperature. The unstable nature of intermediates **3** and **5** also resulted in lower chemical yield at slower flow rates (Table 1). This effect has been previously reported by Yoshida *et al*. [12] and Kemperman *et al*. [13].

Table 1. Chemical yield in % product of acetophenone, determined by off-line HPLC.

Flow Rate (mL/min)	Temperature				
	−20 °C	−10 °C	0 °C	10 °C	20 °C
2	34	17	15	4.5	1
4	73	58	31.5	7.5	2.28
6	80	68.5	32.5	8.5	3
8	81	73	37	14	5
10	81	74	37	14.5	5

The information from physical and chemical sensors allowed for rapid exploration of a design of experiments in the CFR in less than four hours. Using HPLC to validate chemical steady state would have required at least 30 h of experiment time. These results demonstrate that the real-time monitoring of physical and chemical steady state in a CFR offers significant advantages for optimizing a reactor system when compared with systems that employ either physical or chemical techniques. This was accomplished through the construction of a reactor designed for PAT implementation using NeSSI sampling systems and Raman spectroscopy. The fast optimization technique is chemistry and hardware agnostic, making this approach a viable means of optimizing any CFR for any suitable chemical reaction.

4. Conclusions

On-line analytics, providing information on physical stability combined with Raman spectroscopy and multivariate modeling, allowed for real-time detection of steady state in a CFR. The investigation of a design space to optimize reactor conditions was improved through the rapid detection of steady state. The design of experiments was explored in under four hours, with improved confidence in the reproducibility of quality product. In addition, the optimization was achieved via a chemistry agnostic platform that allows for determination of optimum parameters for future production based on quality, volume, and energy needs, regardless of chemistry. Application of advanced chemometrics methods coupled with HPLC information enables a quantitative real-time approach to chemical conversion and could have a broad impact on many process development, optimization, and control methodologies.

Acknowledgments

The authors of this paper would like to acknowledge William Cost at Parker Hannefin and Brian Phillips at University of Washington for their contributions. This project was supported in part by an appointment to the Research Participation Program at the Center for Drug Evaluation and Research administered by the Oak Ridge Institute for Science and Education through an interagency agreement between the U.S. Department of Energy and the U.S. Food and Drug Administration.

Conflicts of Interest

The authors declare no conflict of interest.

References

1. Wiles, C.; Ngamsom, B. *Continuous Flow Esterifications*; Application Note: chemtrix.com, 2010.
2. Roberge, D.M.; Ducry, L.; Bieler, N.; Cretton, P.; Zimmermann, B. Microreactor technology: A revolution for the fine chemical and pharmaceutical industries? *Chem. Eng. Technol.* **2005**, *28*, 318–323.
3. Roberge, D.M.; Bieler, N.; Mathier, M.; Eyholzer, M.; Zimmermann, B.; Barthe, P.; Guermeur, C.; Lobet, O.; Moreno, M.; Woehl, P. Development of an industrial multi-injection microreactor for fast and exothermic reactions—Part II. *Chem. Eng. Technol.* **2008**, *31*, 1155–1161.
4. Roberge, D.M.; Zimmermann, B.; Rainone, F.; Gottsponer, M.; Eyholzer, M.; Kockmann, N. Microreactor technology and continuous processes in the fine chemical and pharmaceutical industry: Is the revolution underway? *Org. Process Res. Dev.* **2008**, *12*, 905–910.
5. Watts, P.; Wiles, C. Recent advances in synthetic micro reaction technology. *Chem. Commun.* **2007**, doi:10.1039/B609428G.
6. Roberto, M.F.; Dearing, T.I.; Martin, S.; Marquardt, B.J. Integration of continuous flow reactors and online raman spectroscopy for process optimization. *J. Pharm. Innov.* **2012**, *7*, 69–75.
7. Wiles, C.; Watts, P.; Haswell, S.J.; Pombo-Villar, E. The aldol reaction of silyl enol ethers within a micro reactor. *Lab Chip* **2001**, *1*, 100–101.
8. Wiles, C.; Watts, P.; Haswell, S.J.; Pombo-Villar, E. 1,4-addition of enolates to α,β-unsaturated ketones within a micro reactor. *Lab Chip* **2002**, *2*, 62–64.
9. Leung, S.A.; Winkle, R.F.; Wootton, R.C.R.; deMello, A.J. A method for rapid reaction optimisation in continuous-flow microfluidic reactors using online raman spectroscopic detection. *Analyst* **2005**, *130*, 46–51.
10. Pawliszyn, J. *Comprehensive Sampling and Sample Preparation: Analytical Techniques for Scientists*; Elsevier: Amsterdam, The Netherlands, 2012; Volume 1.34.
11. Undey, K.; Low, D.; Menezes, J.; Koch, M. *Pat Applied in Biopharmaceutical Process Development and Manufacturing: An Enabling Tool for Quality-by-Design*; CRC Press: Boca Raton, FL, USA, 2012.
12. Kawaguchi, T.; Miyata, H.; Ataka, K.; Mae, K.; Yoshida, J. Room-temperature swern oxidations by using a microscale flow system. *Angew. Chem. Int. Ed.* **2005**, *44*, 2413–2416.

13. Van der Linden, J.J.M.; Hilberink, P.W.; Kronenburg, C.M.P.; Kemperman, G.J. Investigation of the moffatt-swern oxidation in a continuous flow microreactor system. *Org. Process Res. Dev.* **2008**, *12*, 911–920.
14. Mozharov, S.; Nordon, A.; Littlejohn, D.; Wiles, C.; Watts, P.; Dallin, P.; Girkin, J.M. Improved method for kinetic studies in microreactors using flow manipulation and noninvasive raman spectrometry. *J. Am. Chem. Soc.* **2011**, *133*, 3601–3608.
15. Cao, E.; Sankar, M.; Firth, S.; Lam, K.F.; Bethell, D.; Knight, D.K.; Hutchings, G.J.; McMillan, P.F.; Gavriilidis, A. Reaction and raman spectroscopic studies of alcohol oxidation on gold-palladium catalysts in microstructured reactors. *Chem. Eng. J.* **2011**, *167*, 734–743.
16. Mechtilde, S.; Eduard, S.; Andreas, F. Computer controlled chemical micro-reactor. *J. Phys. Conf. Ser.* **2006**, *1*, 115.
17. Misra, M.; Yue, H.H.; Qin, S.J.; Ling, C. Multivariate process monitoring and fault diagnosis by multi-scale pca. *Comput. Chem. Eng.* **2002**, *26*, 1281–1293.
18. Chen, J.; Liu, K.-C. On-line batch process monitoring using dynamic PCA and dynamic PLS models. *Chem. Eng. Sci.* **2002**, *57*, 63–75.
19. Dearing, T.I.; Thompson, W.J.; Rechsteiner, C.E., Jr.; Marquardt, B.J. Characterization of crude oil products using data fusion of process raman, infrared, and nuclear magnetic resonance (NMR) spectra. *Appl. Spectrosc.* **2011**, *65*, 181–186.
20. Szostak, R.; Mazurek, S. Quantitative determination of acetylsalicylic acid and acetaminophen in tablets by FT-Raman spectroscopy. *Analyst* **2002**, *127*, 144–148.
21. Shah, R.B.; Tawakkul, M.A.; Khan, M.A. Process analytical technology: Chemometric analysis of raman and near infra-red spectroscopic data for predicting physical properties of extended release matrix tablets. *J. Pharm. Sci.* **2007**, *96*, 1356–1365.

Stability Analysis of Reactive Multiphase Slug Flows in Microchannels

Alejandro A. Munera Parra, Nicolai Antweiler, Rachit Nagpal and David W. Agar

Abstract: Conducting multiphase reactions in micro-reactors is a promising strategy for intensifying chemical and biochemical processes. A major unresolved challenge is to exploit the considerable benefits offered by micro-scale operation for industrial scale throughputs by numbering-up whilst retaining the underlying advantageous flow characteristics of the single channel system in multiple parallel channels. Fabrication and installation tolerances in the individual micro-channels result in different pressure losses and, thus, a fluid maldistribution. In this work, an additional source of maldistribution, namely the flow multiplicities, which can arise in a multiphase reactive or extractive flow in otherwise identical micro-channels, was investigated. A detailed experimental and theoretical analysis of the flow stability with and without reaction for both gas-liquid and liquid-liquid slug flow has been developed. The model has been validated using the extraction of acetic acid from *n*-heptane with the ionic liquid 1-Ethyl-3-methylimidazolium ethyl sulfate. The results clearly demonstrate that the coupling between flow structure, the extent of reaction/extraction and pressure drop can result in multiple operating states, thus, necessitating an active measurement and control concept to ensure uniform behavior and optimal performance.

Reprinted from *Processes*. Cite as: Parra, A.A.M.; Antweiler, N.; Nagpal, R.; Agar, D.W. Stability Analysis of Reactive Multiphase Slug Flows in Microchannels. *Processes* **2014**, *2*, 371-391.

1. Introduction

An effective exploitation of the advantages of microscale operation for industrial production processes requires a reliable and robust numbering-up procedure. For multiphase systems, one must not only ensure uniform flow rates of each phase but also similar flow structures [1] and residence time distributions [2,3] in the individual microchannels, if the optimal performance is to be achieved [4]. Furthermore, in reactive systems, multiplicities can arise, leading to drastic differences in the behavior between otherwise identical microchannels [5]. The problem is compounded by the greater significance of fabrication tolerances at the microscale, since even slight discrepancies can give rise to considerable changes in volumetric flow rates, which scale with the fourth power of the channel diameter [6,7].

Passive distribution strategies thus necessitate high-precision machining, usually entail large upstream pressure drops and are unable to adapt to changing operating conditions, such as fouling [8]. An active approach, in which the flow in each microchannel is monitored and regulated using simple non-invasive probes and actuators overcome these shortcomings [9].

Even so, the multiplicities in reactive flows still represent a particularly severe challenge, since they can not only diminish performance but may also lead to hazardous runaway situations or reactor failure. In polymerizations, for instance, the reaction and hydrodynamics are strongly coupled

through the viscosity of the reaction medium. Should, for whatever reason, the flow in one channel be less than that in the others, the resulting increase in the residence time will yield higher conversion and thus viscosities, increasing the resistance to flow and lowering the flow rate still further. If no remedial action is taken, this self-reinforcing mechanism amplifies any flow divergence and can ultimately cause the channel concerned to plug.

Of course, such multiplicities are by no means confined to microscale systems. In multiphase flow in microchannels, on the other hand, certain reactive hydrodynamic multiplicities can arise which are unlikely or even impossible in macroscale equipment, due to the intensified interaction in the biphasic flow. In an alternating gas-liquid slug flow with absorption, for example, the gas uptake reduces the size of the gas slugs, thus, changing the pressure drop characteristics of the flow, raising the channel residence time and thus enhancing the absorption still further. Conversely, reactions that generate gas or decrease viscosity exert a stabilizing influence on the uniformity of the flow distribution over parallel microchannels.

The objective of the work presented here was to elucidate the relevance of such microscale-specific phenomena in the parallelization of multiphase flows in microchannels and to establish if it might be feasible to utilize self-regulating behavior in order to ameliorate irregularities in flow distribution.

2. Experimental Extraction

A liquid-liquid extraction was used to validate the results obtained after adapting the gas-liquid model presented in Section 3. The chemical, analytics and the experimental set up are described in the following sections.

2.1. Chemicals and Analytics

The chemicals *n*-heptane and acetic acid were supplied from VWR prolab with a purity of 99.7% *w*/*w* and 99% *w*/*w*. The ionic liquid 1-ethyl-3-methylimidazolium ethylsulfate [EMIM][$EtSO_4$] was obtained from Io-Li-Tec (Ionic Liquids Technology, Tuscsaloosa, AL, USA) with a purity of 99% *w*/*w*. The most significant properties of the chemicals used are shown in Table 1. The viscosities were measured by means of a capillary viscosimeter (KPG Ubbelohde capillary viscosimeter, Schott AG, Mainz, Germany) and the concentration of acetic acid in *n*-heptane was analyzed by an Agilent 7890A gas chromatograph using an autosampler Agilent 7693 and a flame-ionization detector (FID) from Agilent Technologies (Agilent Technologies, Böblingen, Germany). A capillary column HP-05 (Agilent Technologies, Böblingen, Germany) with a length of 30 m and an inner diameter of 320 μm was employed and helium used as carrier gas with a flow rate of 1.22 mL/min at a temperature of 250 °C.

Table 1. Physical properties of extractive system at 25 °C and 1 atm.

Property	Unit	*n*-Heptane [10]	Acetic acid [10]	[EMIM][$EtSO_4$] [11]
Molecular weight	g/mol	100.21	60.05	236.29
Surface tension	N/m	----	----	0.004879
Density	g/cm^3	0.6787	1.043	1.2423
Dynamic viscosity	mPa.s	0.43	1.22	95 [11]/69 (measured)

2.2. Experimental Setup

The experimental set-up is shown in Figure 1. *n*-Heptane containing 10% *w*/*w* acetic acid and EMIM $EtSO_4$ were introduced by two syringe pumps (LA-100 Landgraf Laborsysteme HLL GmbH, Langenhagen, Germany) into a "Mixer-Valve" where the slug flow of the immiscible phases was generated. This special valve enables the slug length to be manipulated whilst keeping all other parameters, for example flow rates and the physical properties of components, constant. The outlet of the mixer was connected to a Polytetrafluoroethylene-capillary (PTFE-capillary) with an inner diameter of 800 µm. To achieve well-defined extraction times a union T-separator was installed downstream of the contacting section to implement an instantaneous liquid-liquid phase separation by virtue of their different wetting properties. One of the separator outlets consists of a steel capillary, with an inner diameter of 750 µm, and the other comprises a PTFE-capillary with an inner diameter of 800 µm. The dispersed EMIM $EtSO_4$ phase, which does not wet the PTFE capillary wall, leaves via the steel outlet while the continuous *n*-heptane phase exits through the PTFE branch.

Figure 1. (**a**) Flowsheet schematic of the experimental setup; (**b**) Pressure drop measurement technique.

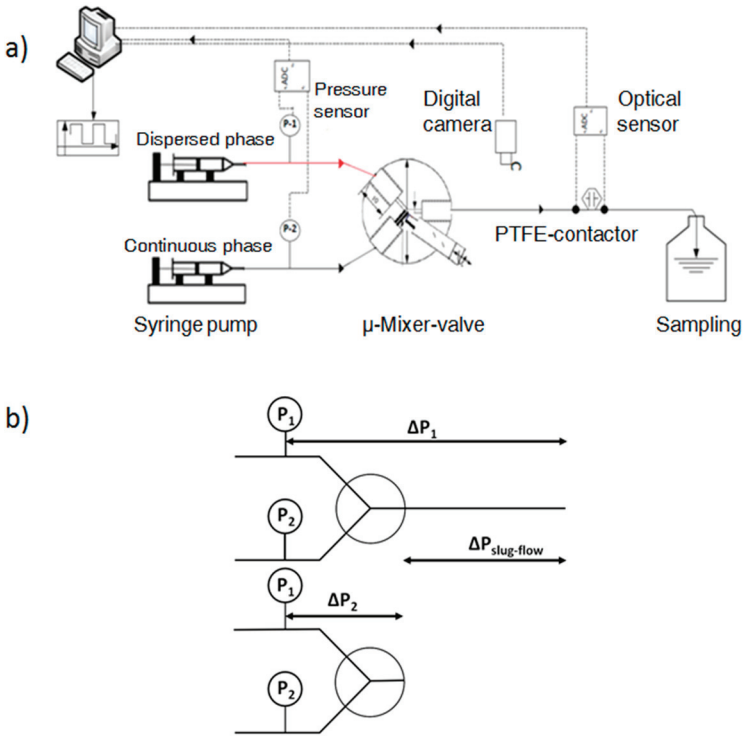

The pressure drop measurement technique is depicted in Figure 1b. The pressure drop of interest is that in the reaction capillary denoted $\Delta P_{slugflow}$. To avoid the pressure sensor influencing the multiphase flow structure, the pressure sensors are placed upstream of the mixing point. The pressure drop ΔP_2 was measured without the separator and ΔP_1 following removal of the capillary from the mixer. The pressure drop of the mass transfer contacting section is then calculated as:

$$\Delta P_{slugflow} = \Delta P_1 - \Delta P_2 \quad (1)$$

In order to describe the mass transfer for a liquid-liquid system, the extraction efficiency was used:

$$h = \frac{C_{out} - C_{in}}{C_{Eq} - C_{in}} \tag{2}$$

where C_{Eq} is the equilibrium concentration at a phase ratio EMIM $EtSO_4$:*n*-heptane of 0.2. This concentration was measured at room temperature in a 20 mL batch reactor. C_{in} and C_{out} are the inlet and outlet concentrations of acetic acid in the extract phase, *i.e.*, EMIM $EtSO_4$, respectively.

The phase ratio (α) was defined via a snapshot with a camera and an optical sensor. For this case, the volume fraction of the film was considered negligible. The phase ratio can then be defined as:

$$\alpha = \frac{L_{disp}}{L_{UC}} \tag{3}$$

Observed flow structures and unit cells under different conditions are presented in Figure 2.

Figure 2. Observed flow structure and unit cell for a superficial velocity of 0.044 m/s and (**a**) phase ratio 1; (**b**) phase ratio 2.

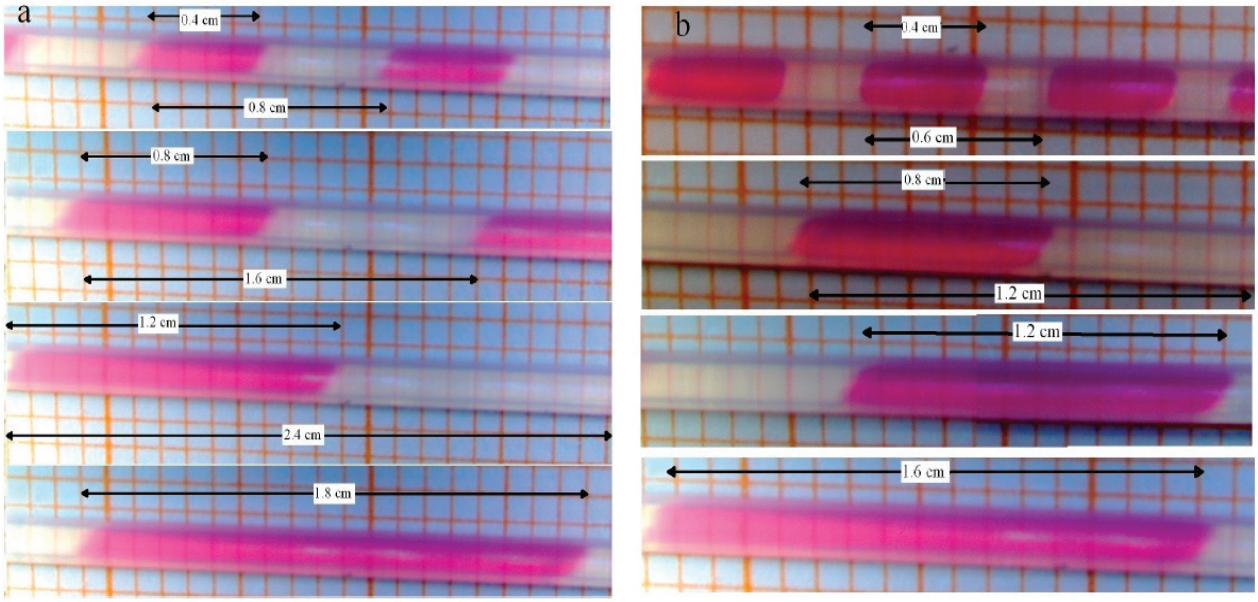

3. Gas-Liquid Model Equations

As shown in previous work, bubble length and bubble velocity play an important role for hydrodynamics and the mass transfer in the slug-flow regime. Even though some studies have focused on the possibility of the expansion of the bubble due to the inherent pressure drop [12,13], and in more recent studies [14,15] due to mass transfer from the liquid into the gas phase, none of them has considered the fact that, for very reactive systems, the effect of the consumption may well exceed that of the expansion of the bubble or the case where the mass transfer occurs from the gas to the liquid phase. The model presented in this work couples hydrodynamics with mass transfer and thus accounts for the change in the size of the bubble as a result of chemical absorption.

When the length of the bubble alters, several parameters are affected, starting with the superficial velocity. Since the volume of the unit cell comprising a single bubble and the associated slug is changing along the channel length, the two-phase superficial velocity will be a function of the position as given in Equation (4). This entails that all parameters that are velocity-dependent are also location-dependent, *i.e.*, capillary and Reynolds numbers, film thickness and mass transfer coefficients.

$$U_{TP}(z) = \frac{V_{slug}^{0} + V_{B}(z)}{V_{slug}^{0} + V_{B}^{0}} U_{TP}^{0} \tag{4}$$

In slug flow, it is known that bubbles travel faster than the nominal superficial velocity due to the presence of a thin liquid wall film surrounding the bubble. The true velocity can be approximated by a simple mass balance in round capillaries, as expressed in Equation (5) (a deviation of no more than 5% was reported by [3]). In this equation, δ represents the film thickness and can be obtained by the expression found by Aussillous and Quéré [16], describing the extent of significant films in micro-channels (Equation (6)).

$$U_{B}(z) \cong U_{TP}(z)\left(1 + \frac{4\delta}{d_{c}}\right) \tag{5}$$

$$\frac{\delta}{d_{c}} = \frac{0.67 Ca_{b}^{2/3}}{1 + 3.34 Ca_{b}^{2/3}} \tag{6}$$

As can be seen, the film thickness is a function of the capillary number, $Ca = {}^{\mu U}/_{\sigma}$ which in turn is a function of the velocity and therefore also of the location as stated earlier.

To describe the hydrodynamics, the pressure drop must be defined. In this work, the pressure drop is taken according to the unit cell based model presented by Warnier *et al.* [13]. In this model the pressure drop across a unit cell (presented in Figure 3) is defined by the individual contributions of the liquid slug and the pressure drop generated by the presence of the bubble.

$$\Delta P_{UC} = \Delta P_{Ls} + \Delta P_{B} \tag{7}$$

Figure 3. Unit cell representation. L_b represents the length of the bubble, L_s represents the slug length R_b is the bubble diameter and ζ accounts for the liquid in the cap region.

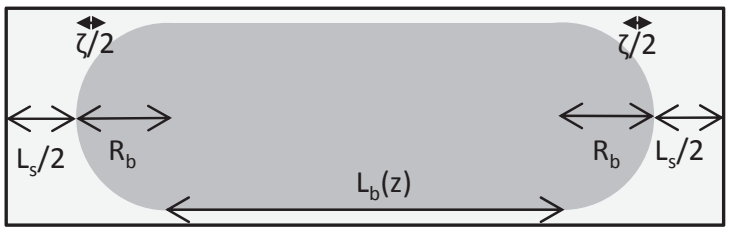

The individual bubble pressure is described by the corrected Bretherton's approximation, and the liquid slug pressure drop is described by the fully developed Hagen-Poiseuille with a correction for the amount of liquid in the domed bubble cap region (ζ).

$$\Delta P_B = 7.16 \frac{\sigma}{d_C} \frac{\left(3 \cdot Ca_B\right)^{2/3}}{\left(1 + 3.34 Ca_B{}^{2/3}\right)} \tag{8}$$

$$\Delta P_s = \frac{32 \cdot \mu \cdot U \cdot \left(L_s + \zeta\right)}{d_c^2} \tag{9}$$

The differential pressure drop can then be obtained as:

$$-\frac{dP}{dz} = \frac{\Delta P_{UC}}{L_{UC}} = \frac{\Delta P_{UC}}{L_B + L_S + d_B} \tag{10}$$

However, the length of the bubble is not constant along the channel length. In the case of gas absorption into the liquid phase, for instance, it is necessary to couple the mass transfer with the pressure drop in order to determine how the bubble contracts along the channel length.

The change in the number of moles for the absorbed component with respect to the residence time can be given by:

$$\frac{dN_A}{d\tau} = -\Delta \dot{n}_A \tag{11}$$

$$\frac{dN_A}{d\tau} = \frac{dy_A N_T}{d\tau} = N_T \frac{dy_A}{d\tau} + y_A \frac{dN_T}{d\tau} = N_T \frac{dy_A}{d\tau} + y_A \frac{d(N_A + N_I)}{d\tau} \tag{12}$$

since the number of moles of the inert is not changing with time Equation (12) becomes:

$$\frac{dN_A}{d\tau} = N_T \frac{dy_A}{d\tau} + y_A \frac{dN_A}{d\tau} \tag{13}$$

yielding:

$$\frac{dy_A}{d\tau} = \frac{1}{N_T}(1 - y_A)\frac{dN_A}{d\tau} \tag{14}$$

The residence time for the bubble is given by the bubble velocity yielding:

$$\frac{dy_A}{dz} = -\frac{1}{U_B N_T}(1 - y_A)\Delta \dot{n}_A \tag{15}$$

The chemical system used for this study was the widely studied chemical absorption of CO_2 in NaOH [17]. First a pseudo 1st order reaction was assumed, but since the reaction was found to be fast enough, the chemical absorption was then simply accounted for by the inclusion of the enhancement factor. Finally, the change in the molar flow due to chemical absorption can be given by:

$$\Delta \dot{n}_A = k_L A_T E (C_A^g - C_A^l) \tag{16}$$

As for determining the mass transfer coefficient, several studies conducted on mass transfer in gas-liquid slug flow [18–21] were considered. In this work most of the available models were examined, with particular emphasis on the models of Vandu *et al.* [18] and Yue *et al.* [19], as they allow the introduction of changes in the parameters along the length of the channel. Vandu's model treats the cap and wall film contributions separately according to:

$$k_{L,cap} = 2\frac{\sqrt{2}}{\pi}\sqrt{\frac{DU_B}{d_c}} \tag{17}$$

$$k_{L,film} = \frac{2}{\sqrt{\pi}}\sqrt{\frac{DU_B}{L_B}} \tag{18}$$

$$A_{caps} = 4\pi \cdot \left(\frac{d_B}{2}\right)^2 \tag{19}$$

$$A_{film} = \pi d_B L_B \tag{20}$$

$$k_L A = k_{L,cap} A_{cap} + k_{L,film} A_{film} \tag{21}$$

Yue's model, on the other hand, considers the overall mass transfer across the entire interface:

$$k_L A = \frac{2}{d_h}\left(\frac{DU_B}{L_B + L_S}\right)^{0.5}\left(\frac{L_B}{L_B + L_S}\right)^{0.3} V_B \tag{22}$$

Finally, the link between the mass transfer and the pressure drop is given by the bubble length, since a relationship between bubble length and the total number of moles can be expressed as:

$$L_B(z) = \frac{V_B(z) - V_{caps}}{A_B(z)} = \frac{\frac{N_T(z)RT}{P(z)} - V_{caps}}{A_B(z)} \tag{23}$$

the total number of moles is linked to the molar fraction by the relationship:

$$N_T(z) = \frac{N_I}{1 - y_A(z)} \tag{24}$$

yielding the influence of all parameters on the bubble length:

$$L_B(z) = \frac{\frac{\left(\frac{N_I}{1 - y_A(z)}\right)RT}{P(z)} - V_{caps}}{A_B(z)} \tag{25}$$

It is important to notice that the expansion due to the pressure drop presented in previous works is included in this model as well, since the volume of the bubble is calculated by using the pressure at each location.

4. Results and Discussion

4.1. Simulations

For the simulations, as mentioned before, the absorption of carbon dioxide (CO_2) into sodium hydroxide (NaOH) was studied. For the modeling the resistance to mass transfer in the gas phase was neglected. The diffusion and Henry coefficients as well as the surface tension were taken for the system H_2O/CO_2. The system was considered to be isothermal at room temperature (298 K). The parameter values are summarized in Table 2.

Table 2. Parameter values for simulations.

Parameter	Value	Units
σ	0.072	N/m
μ	1	mPa.s
ρ	1000	kg/m^3
H	3.85×10^{-4}	mol/m^3/Pa
T	298	K
P	101,325	Pa
D	2×10^{-9}	m^2/s

4.1.1. Gas-Liquid Model Validation

In order to validate the model, the results obtained were compared with those obtained by previous simulation and experimental studies. First of all, the effect of the mass transfer model on the hydrodynamics was evaluated. The parameters used in this study are presented in Table 3 and the results given in Figure 4.

Table 3. Parameters for mass transfer validation.

Parameter	Value	Units
d_c	400	μm
$L_{B,0}$	$4 \cdot d_c$	μm
$L_{S,0}$	d_c	μm
k_{OH^-}	8.5	m^3/mol/s
C_{OH^-}	0.1	M
y_{CO2}	0.4	-----
L_R	0.1	m

Figure 4. Pressure drop for different mass transfer models.

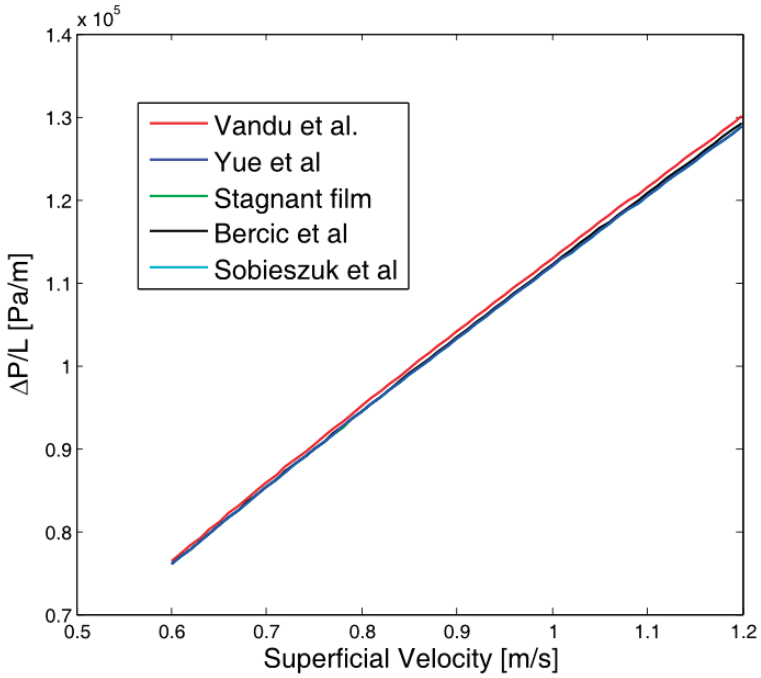

The results show that the choice of mass transfer model shows little or no influence on the hydrodynamics, only Vandu's Model yields slightly different behavior, due to the overestimation of the mass transfer coefficients and hence a faster contraction of the bubble. It can also be seen that the range of pressure drop per unit length is of the same order of magnitude as in previous studies.

The model was also used to calculate the mass transfer coefficients and good agreement was obtained between the simulations and the experimental values presented by Yue *et al.* [19] and Sobieszuk *et al.* [20] (Figure 5). Since this model allows for the change in velocity, a more realistic residence time is calculated for the bubble and hence the expansion behavior present in the experiments is also captured.

Figure 5. Mass transfer coefficients (**a**) Theoretical (Adapted from [20]) (**b**) Obtained from our simulations (using both Yue *et al.* model [19] and Sobieszuk *et al.* model [20]).

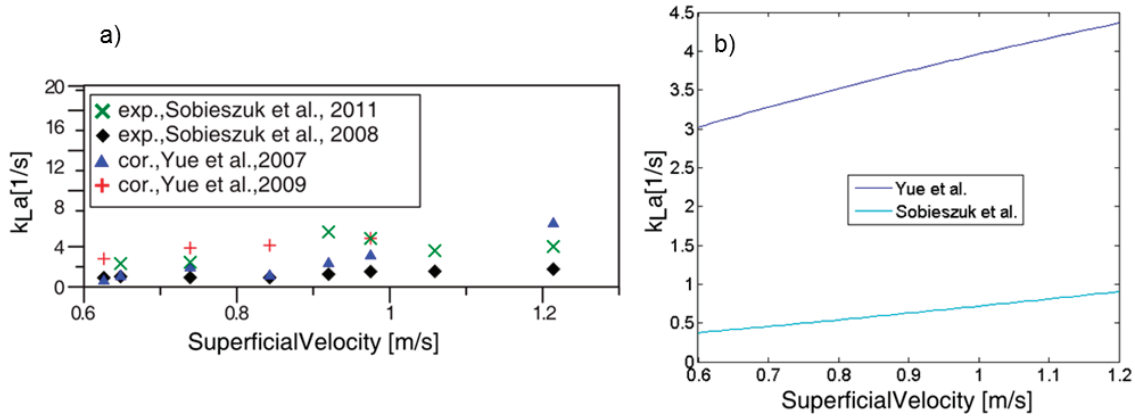

For the final validation, the pressure drop model considered was compared to those previously presented in the literature (Figure 6). It can be seen that the unit cell based pressure drop model yields lower values for the pressure drop in comparison to Kreutzer's model [22]. However, the results are in agreement with the values presented by Warnier *et al.* [13].

Figure 6. Pressure drop models comparison. The unit cell model is based in Warnier *et al.* [13] and the Kreutzer model is used as presented in [22].

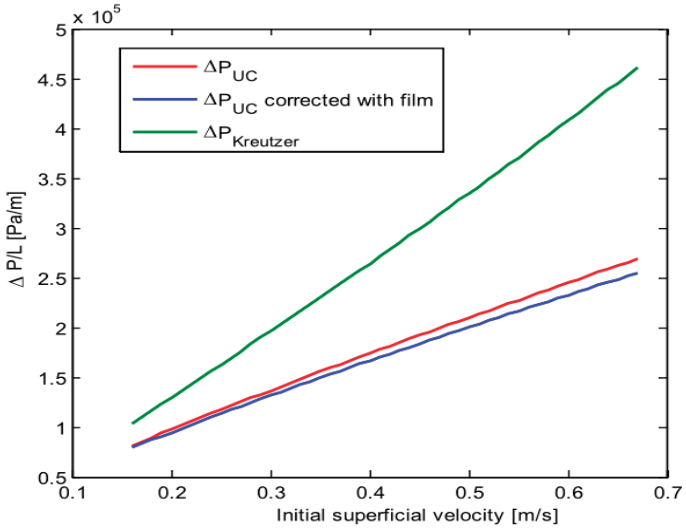

4.1.2. Hydrodynamic Multiplicity

A hydrodynamic multiplicity has already been found in vertically operated monoliths by Kreutzer *et al.* [3]. However, it was due to the hydrostatic pressure in comparison to the coupling of parameters presented in this study.

Once the model had been validated, the stability of the system was studied. Since the contribution to the pressure drop in the gas phase is small for long slugs, a short slug was taken as the basis for this study. The pressure drop was then calculated by varying the bubble length; the length of the reactor was taken as 10 cm and its diameter as 800 μm. For simplicity the calculations were first performed neglecting the film.

For short bubbles (Figure 7) the pressure rises as expected at a higher velocity. However, upon increasing the bubble length, this effect tends to become smaller indicating to the hydrodynamic instability sought.

Figure 7. Pressure drop for small bubbles.

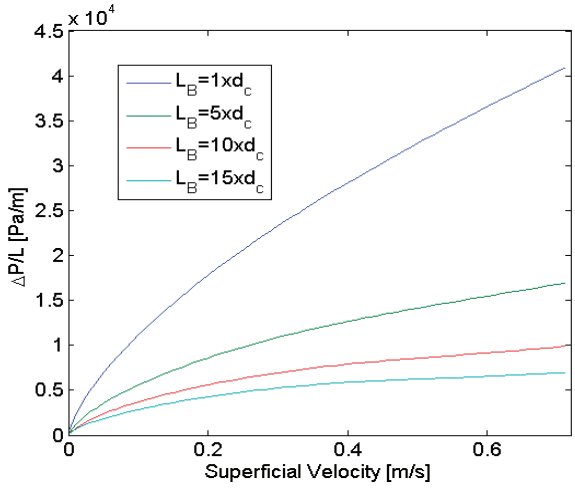

When bubble size was increased further, the multiplicity effect due to the increased pressure of the number of interfaces generated for higher conversions was found as illustrated in Figure 8.

Figure 8. Pressure drop for long bubbles.

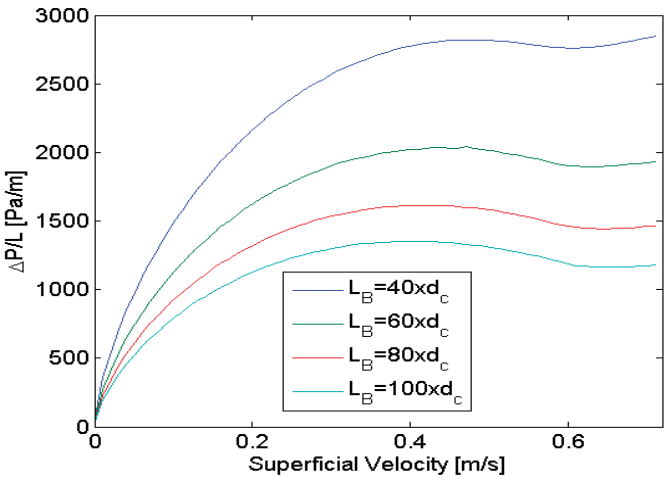

This effect can be explained as follows: at a low velocity, the bubble will spend more time inside the channel therefore the conversion will be high, resulting in an increase of the number of interfaces and the average viscosity of the unit cells. At a higher velocity, conversion will be lower leading to a system with a lower average viscosity a lower number of interfaces and hence an equal pressure drop to the case with lower initial velocity. This effect is depicted in Figure 9.

Figure 9. Two cases for hydrodynamic multiplicity.

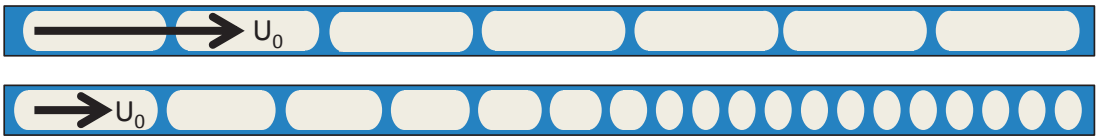

4.1.3. Film Effect

Since the results were obtained for the model without film, the next step was to calculate the complete model to check whether the discrepancy due to this simplification was significant. The results are presented in Figure 10. It can be seen that the inclusion of the film has a slight influence on the behavior, especially in the regions of higher superficial velocity. This can be explained by the wall film being thicker at higher velocities film since it depends on the capillary number. However, this effect was considered to be not large enough to affect the results qualitatively and therefore the subsequent calculations were performed without considering the film, since the computational effort was considerably smaller (with the film an iteration is required for each single step in order to establish the bubble velocity).

Figure 10. Film effect on pressure drop.

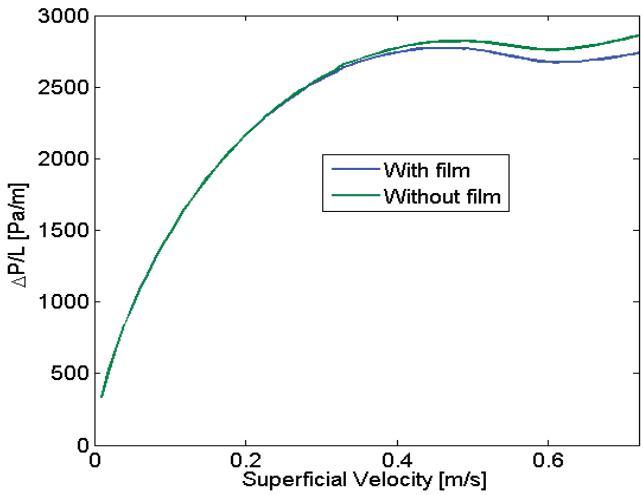

4.1.4. Interfacial Geometry

It has been found in some studies that the interfacial curvature factor used to calculate the interfacial pressure drop can change as a function of the velocity [23]. The value of 7.16 normally used (as in Equation (6) was proposed initially by Bretherton for hemispherical caps. Jovanovic *et al.*

found that these values can actually range between 3 and 10. Since the instabilities arise from the bubble pressure drop, as shown previously, this effect also had to be considered. To account for this phenomenon, the values from Jovanovic *et al.* were correlated using a simple linear regression (Equation (26)). The results are presented in Figure 11.

$$C = -4.17 \cdot U_{TP} + 10.04 \tag{26}$$

Figure 11. Effect of the curvature.

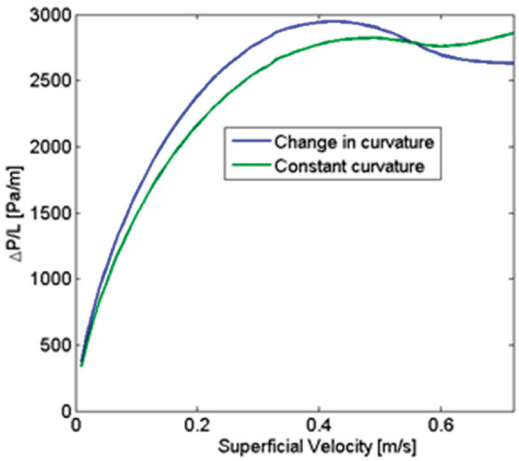

It can be seen that the effect of the curvature exerts a noticeable effect on the pressure drop characteristics, making the region of the multiplicity more pronounced. The higher curvature for lower velocities increases the influence of the remaining caps at the end of the channel where the lowest velocities are found, and as explained earlier, the effect of these extra interfaces is the source of the multiplicity.

4.1.5. Effect of Viscosity Changes

In the Section 4.1.2, a hydrodynamic multiplicity was identified, albeit for systems with unrealistic bubble lengths. A factor playing a major role in this phenomenon was the average viscosity in the unit cell. It is, thus, intuitively obvious to imagine that if the average viscosity changes along the channel length, the hydrodynamic multiplicity could be present in a wider range of systems in comparison with the case presented in Section 4.1.2. One possible case where this behavior can occur is in the case where viscosity changes with the progress of a reaction/extraction/absorption. For such systems, a general formula for the viscosity as a function of the conversion could be represented as:

$$\mu(x) = a\mu_0 x^b + \mu_0 \tag{27}$$

where a would represent the net increase in viscosity, and b the mechanism.

Using this behavior, multiplicities can be found even for systems with short bubbles. Figure 12 depicts the results for an initial bubble five times larger than the channel diameter and a value for a of 4 for various values of b.

Figure 13 presents the results for an initial bubble five times larger than the channel diameter and a value for *b* of 3 for different values of *a*.

As can be seen in both figures, any change increase viscosity leads to major changes in the pressure drop characteristics of the system and yielding instances of hydrodynamic multiplicity.

This leads to the question as to whether for systems with decreasing viscosity, the behavior would be the opposite, *i.e.*, result in more stable systems with more uniform distribution. These results are presented in the same fashion as for increasing viscosity: first a fixed value of *b* of 3, and then for a fixed value of *a* of −0.5 in Figure 14.

Figure 12. Pressure drop for system with viscosity changes ($L_{b,0} = 5d_c$).

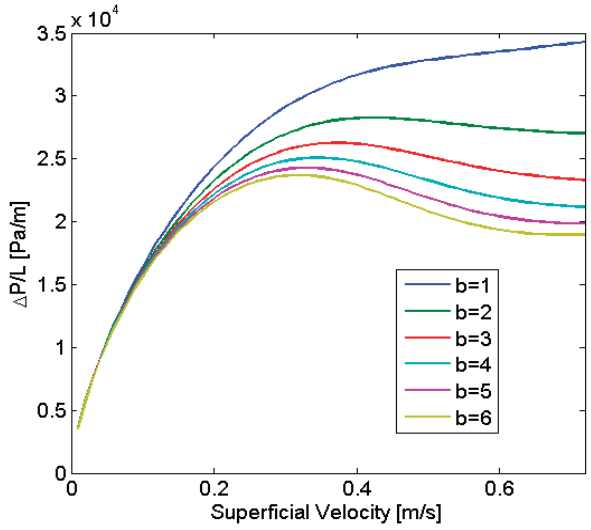

Figure 13. Pressure drop for systems with viscosity changes ($L_{b,0} = 5d_c$).

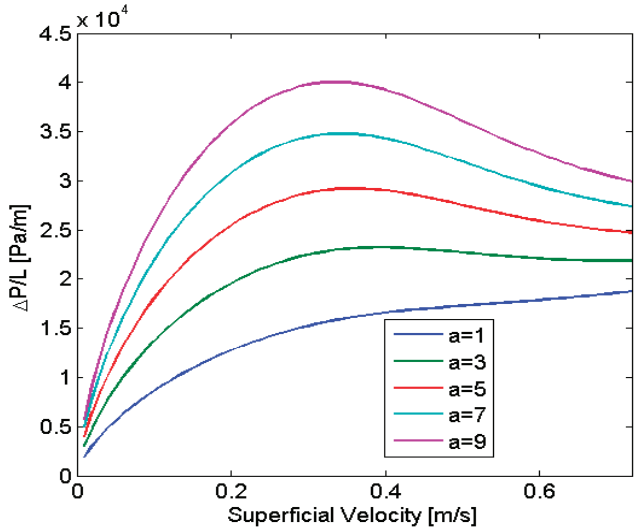

As it can be seen, no signs of instability were detected for this system, which exhibits self-regulating behavior. Experiments with a liquid-liquid extraction system in which the solvent viscosity diminishes with solute concentration were performed in an attempt to try and validate these results.

Figure 14. Pressure drop for systems with decreasing viscosity (**a**) Fixed *a* value (**b**) Fixed *b* value.

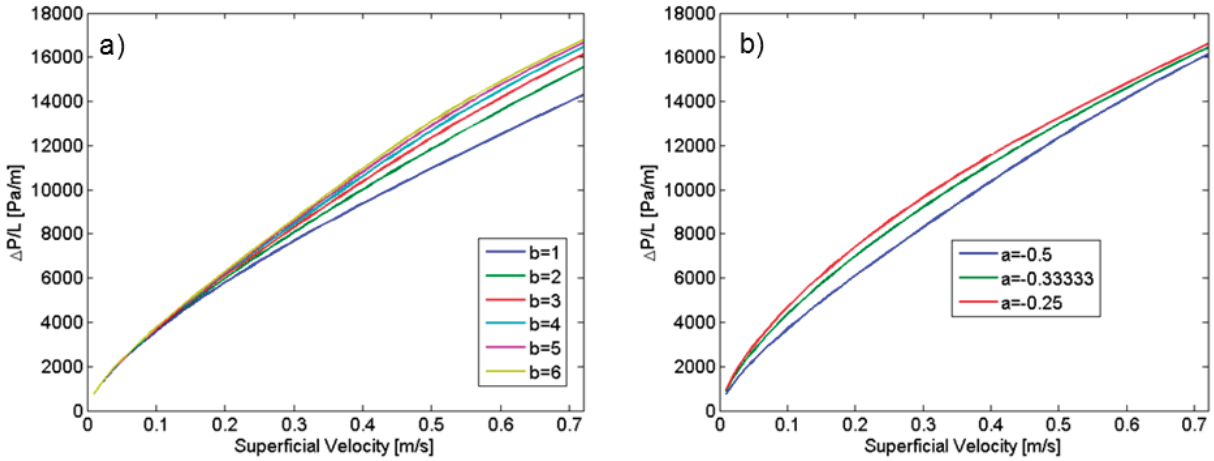

4.1.6. Model Adaptation to the Liquid-Liquid Case

Experiments were performed with a liquid-liquid system due to its relative simplicity in comparison to the gas-liquid case. The gas-liquid model was therefore adapted to an extractive aqueous-ionic liquid system. Conceptually the modifications were:

- The pressure drop model was changed to that of a stagnant film model as presented by Jovanovic *et al.* [23].

$$\Delta P = \frac{32\mu_{disp}\alpha L_c}{d_c^2} + \frac{32\mu_{cont}(1-\alpha)L_c}{d_c^2} + C(3Ca)^{2/3}\frac{\sigma}{d_c}\frac{L_c}{L_{UC}} \tag{28}$$

- The extraction phenomenon (extraction of acetic acid from *n*-heptane into an ionic liquid) replaces the chemical absorption (absorption of CO_2 in NaOH). The equation representing the concentration change along the channel is the following:

$$\frac{dC_{EMIM}}{dz} = \frac{k_L a}{U}(C_{EMIM}^{Eq} - C_{EMIM}) \tag{29}$$

With this adaptation, it is implied that the unit cell length will remain unchanged for both of the two phases and therefore no change in velocity will occur. However, the coupling of the mass transfer presented in the gas-liquid system is still present. Additionally, the viscosity change presented in Section 4.1.5 will be supplied by the change in viscosity of the ionic liquid. The experimental results are presented in the following section.

The hydrodynamic parameters for this system can be found in Table 1.

4.2. Experimental Validation: Liquid-Liquid System

The adapted model describing the coupling between fluid dynamics and the change in viscosity through mass transfer or reaction via the pressure drop and the residence time was validated through the extraction of acetic acid from *n*-heptane into the ionic liquid EMIM $EtSO_4$. In this system, the viscosity of the ionic liquid changes considerably as a result of mass transfer, although the underlying

behavior dictating the pressure drop interactions are the same whether mass transfer, reaction or gas slug contraction is involved. Two sets of experiments were carried out: one at a constant micro-channel length whilst varying the velocity and the other at constant velocity, varying the channel length. The pressure drop, the viscosity and the extraction efficiency were measured at each operating point as described in Section 2.2 and the results illustrated in Figure 15.

Figure 15. (**a**) Pressure drop, extraction efficiency and dynamic viscosity for different superficial velocities in slug flow regime. The capillary length was 100 cm, the phase ratio 0.2 and the number of unit cells 80; (**b**) Pressure drop, extraction efficiency and dynamic viscosity for different capillary lengths in slug flow regime. The superficial velocity was 0.022 m/s, the phase ratio 0.2 and the number of unit cells 80.

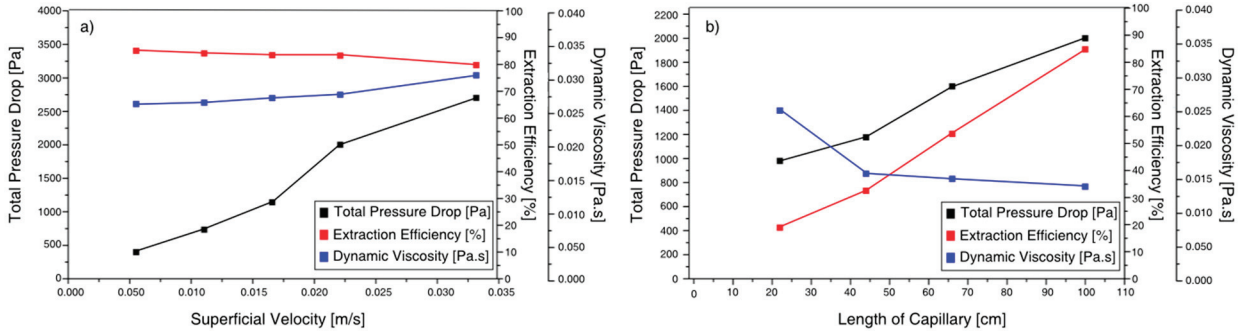

The viscosity of EMIM $EtSO_4$ falls with increasing acetic acid concentration and thus causes a decrease in the pressure drop. In both cases, the pressure drop is mainly influenced by the change in viscosity due to extraction. The pressure drop increases with increasing capillary length, while the dynamic viscosity decreases because of the extraction. With increasing velocity, the pressure drop increases because of the hydrodynamic pressure loss. The extraction efficiency and the viscosity at the outlet of the capillary were constant but the average values along the capillary vary.

4.2.1. Validation

In order to validate the model for the liquid-liquid system, simulations were carried out for different configurations. The parameters used are listed in Table 4.

Table 4. Parameter values for liquid-liquid simulations.

Parameter	Value	Units
d_c	800	µm
$L_{cont,0}$	$3.75 \cdot d_c$	µm
$L_{disp,0}$	$1.25 \cdot d_c$	µm
L_c	0.2–1	m
σ	0.0048	N/m
$\mu_{disp,0}$	0.069	Pa.s
U	0.005–0.035	m/s
C	2.385	-
$C_{EMIM,0}$	1171	mol/m^3
$C_{EMIM,eq}$	521	mol/m^3

Additionally, Equation (27) was modified to replace the conversion with the extraction efficiency h (defined in Equation (2)). The viscosity can now be described as:

$$\mu(h) = a\mu_0 h^b + \mu_0 \tag{30}$$

The model parameter a = −0.67 and b = 0.3 of the viscosity equation (Equation (30)) were taken from experimental results by fitting the dynamic viscosity of the ionic liquid at different levels of extraction efficiency (as presented in Figure 15) and performing a regression minimizing the least squares error (LSE), these parameter yielded a LSE of 0.001. The results from this procedure are presented in Figure 16.

Figure 16. Measured values for the dynamic viscosity as a function of extraction efficiency and the fitting based on Equation (30).

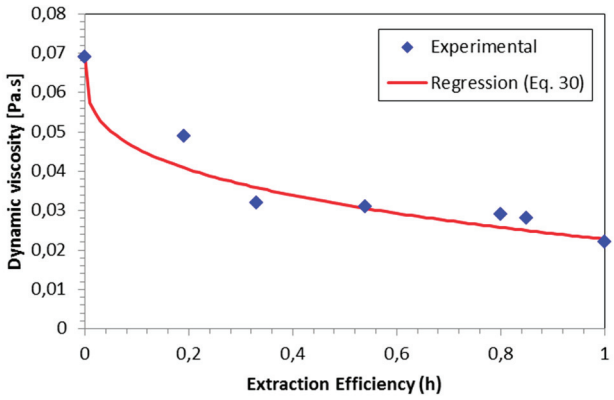

A comparison between experimental and model results shown in Figure 17 indicates the coupling between pressure drop, change in viscosity due to reaction or mass transfer and hydrodynamics is described in a correct way. It also can be seen that the pressure drop of the experiments fitted well with the prediction of the model.

Figure 17. Comparison between pressure drop calculated by the model and the experimental values obtained for different velocities and capillary lengths. (**a**) Pressure drop as a function of velocity (fixed capillary length 1 m); (**b**) Pressure drop as a function of capillary length (fixed superficial velocity 0.022 m/s).

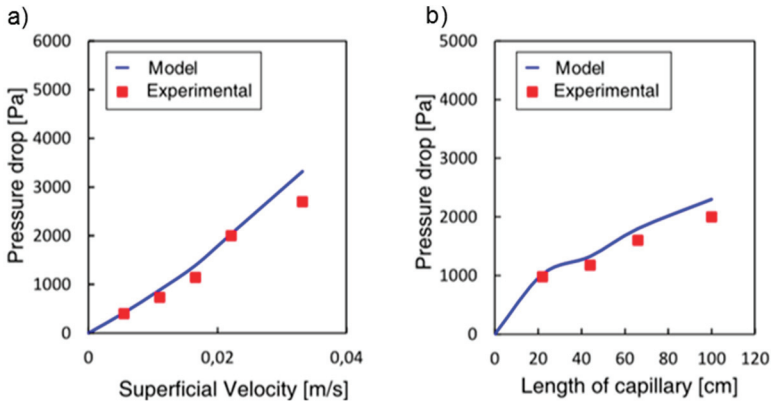

The mean relative error between model and experiment for various flow rates is about 13% and for changing capillary length 11% and therefore simulations results can also be taken as valid.

5. Conclusions

In this paper, a model has been developed to describe the behavior of a multiphase slug flow in circular microchannels. The model couples the hydrodynamics, reaction and mass transfer phenomena, and for gas-liquid systems, it accounts for both the contraction of the gas phase due to reactive absorption and the inherent change in volume linked to the pressure drop.

The model was first validated by comparing the results obtained with results from other researchers yielding results of the same order of magnitude. For the pressure drop it gave results consistent with those obtained by Warnier *et al.* [13], and to a lesser extent, Kreutzer *et al.* [22]. For the mass transfer characteristics, the model predicted mass transfer coefficient values in close agreement with those from the most recent publications, like the experimental results of Sobieszuk *et al.* [20] and Yue *et al.* [19]. Furthermore, the model was tested to get an idea of how large the effect of the film surrounding the bubble is on the hydrodynamics, showing only a slight deviation from the case without film. Finally, the effect of the slug geometry was studied, as it was found that this could play an important role for instabilities, and the work of Jovanovic *et al.* [23] has shown that it was not constant but a function of the velocity.

The model was used to analyze the stability of the flow for a gas-liquid system establishing that multiplicities can arise in particular cases, such as long bubbles, or for systems with changes in viscosity. These results led to the study of systems with decreasing viscosity, since this can enable one to achieve a better distribution in parallelized microchannels. Experimental results obtained for an aqueous-ionic liquid-system found a good agreement between the experimental and predicted values (11% and 13% error, depending on the parameter varied).

The results demonstrate that the coupling between flow structure, the extent of reaction/extraction and pressure drop can result in multiple operating states, thus, making an active measurement and control strategy to ensure uniform behavior and optimal performance essential.

Nomenclature

Symbol	Description	Units
A	Area	m^2
a	Interfacial area	m^2/m^3
a,b	Viscosity fitting factors	
C	Concentration	mol/m^3
C	Curvature factor	
d	Diameter	μm
D	Diffusion coefficient	
E	Enhancement factor	-
h	Extraction efficiency	-
k	Mass transfer coefficient	m/s

L	Length	μm
N	Number of mol	mol
$\dot{n}$	Molar flow	mol/s
Symbol	**Description**	**Units**
P	Pressure	Pa
R	Ideal gas constant	
T	Temperature	K
U	Velocity	-
V	Volume	
x	Conversion	-
y	Molar fraction	mol/mol
z	Axial coordinate	m

Greek Symbols

Symbol	Description	Units
α	Liquid phase ratio	
μ	Viscosity	Pa.s
Δ	Difference	
δ	Film Thickness	μm
ζ	Correction factor for liquid volume in the bubble cap zone	μm
ρ	Density	kg/m^3
σ	Surface tension	N/m
τ	Mean residence time	s

Indexes

Symbol	Description
0	Initial
A	Related to component A
B	Bubble
C	Channel
Cap	Cap of the bubble
Cont	Continuous phase
Disp	Dispersed phase
EMIM	Related to EMIM-$EtSO_4$
Eq	Equilibrium
Film	Liquid film
G	Gas
I	Inert
In	Inlet
L	Liquid
Out	Outlet

S	Slug
T	Total
TP	Two phase
UC	Unit cell

Conflicts of Interest

The authors declare no conflict of interest.

References

1. Leclerc, A.; Philippe, R.; Houzelot, V.; Schweich, D.; de Bellefon, C. Gas-liquid Taylor flow in square micro-channels: New inlet geometries and interfacial area tuning. *Chem. Eng. J.* **2010**, *165*, 290–300.
2. Wibel, W.; Wenka, A.; Brandner, J.J.; Dittmeyer, R. Reprint of: Measuring and modeling the residence time distribution of gas flows in multichannel microreactors. *Chem. Eng. J.* **2013**, *227*, 203–214.
3. Kreutzer, M.T.; Bakker, J.J.W.; Kapteijn, F.; Moulijn, J.A.; Verheijen, P.J.T. Scaling-up multiphase monolith reactors: Linking residence time distribution and feed maldistribution. *Ind. Eng. Chem. Res.* **2005**, *44*, 4898–4913.
4. Berčič, G.; Pintar, A. The role of gas bubbles and liquid slug lengths on mass transport in the Taylor flow through capillaries. *Chem. Eng. Sci.* **1997**, *52*, 3709–3719.
5. Mendorf, M.; Moenter, A.; Moll, T.; Agar, D.; Tiller, J. Polymerisation of butyl acrylate in the two phase slug flow regime of parallel microcapillary reactors. *Macromol. Symp.* **2011**, *302*, 245–256.
6. Amador, C.; Gavriilidis, A.; Angeli, P. Flow distribution in different microreactor scale-out geometries and the effect of manufacturing tolerances and channel blockage. *Chem. Eng. J.* **2004**, *101*, 379–390.
7. Yue, J.; Boichot, R.; Luo, L.; Gonthier, Y.; Chen, G.; Yuan, Q. Flow distribution and mass transfer in a parallel microchannel contactor integrated with constructal distributors. *AIChE J.* **2010**, *56*, 298–317.
8. Al-Rawashdeh, M.; Fluitsma, L.; Nijhuis, T.; Rebrov, E.; Hessel, V.; Schouten, J. Design criteria for a barrier-based gas–liquid flow distributor for parallel microchannels. *Chem. Eng. J.* **2012**, *181–182*, 549–556.
9. Mendorf, M.; Nachtrodt, H.; Mescher, A.; Ghaini, A.; Agar, D.W. Design and control techniques for the numbering-up of capillary microreactors with uniform multiphase flow distribution. *Ind. Eng. Chem. Res.* **2010**, *49*, 10908–10916.
10. Perry, R.H.; Green, D.W.; Maloney, J.O. *Perry's Chemical Engineers' Handbook: Physical and Chemical Data*, 8th ed.; McGraw-Hill: New York, NY, USA, 2008; pp. 1–517.
11. Yang, J.-Z.; Lu, X.-M.; Gui, J.-S.; Xu, W.-G. A new theory for ionic liquids? The interstice model: Part 1. The density and surface tension of ionic liquid EMISE. *Green Chem.* **2004**, *6*, 541.

12. Molla, S.; Eskin, D.; Mostowfi, F. Pressure drop of slug flow in microchannels with increasing void fraction: Experiment and modeling. *Lab Chip* **2011**, *11*, 1968.
13. Warnier, M.J.F.; Croon, M.H.J.M.; Rebrov, E.V.; Schouten, J.C. Pressure drop of gas–liquid Taylor flow in round micro-capillaries for low to intermediate Reynolds numbers. *Microfluid Nanofluid* **2010**, *8*, 33–45.
14. Eskin, D.; Mostowfi, F. A model of a bubble train flow accompanied with mass transfer through a long microchannel. *Int. J. Heat Fluid Flow* **2012**, *33*, 147–155.
15. Molla, S.; Eskin, D.; Mostowfi, F. Two-phase flow in microchannels: The case of binary mixtures. *Ind. Eng. Chem. Res.* **2013**, *52*, 941–953.
16. Aussillous, P.; Quéré, D. Quick deposition of a fluid on the wall of a tube. *Phys. Fluids* **2000**, *12*, 2367.
17. Zanfir, M.; Gavriilidis, A.; Wille, C.; Hessel, V. Carbon dioxide absorption in a falling film microstructured reactor: Experiments and modeling. *Ind. Eng. Chem. Res.* **2005**, *44*, 1742–1751.
18. Vandu, C.; Liu, H.; Krishna, R. Mass transfer from Taylor bubbles rising in single capillaries. *Chem. Eng. Sci.* **2005**, *60*, 6430–6437.
19. Yue, J.; Chen, G.; Yuan, Q.; Luo, L.; Gonthier, Y. Hydrodynamics and mass transfer characteristics in gas–liquid flow through a rectangular microchannel. *Chem. Eng. Sci.* **2007**, *62*, 2096–2108.
20. Sobieszuk, P.; Pohorecki, R.; Cygański, P.; Grzelka, J. Determination of the interfacial area and mass transfer coefficients in the Taylor gas–liquid flow in a microchannel. *Chem. Eng. Sci.* **2011**, *66*, 6048–6056.
21. Shao, N.; Gavriilidis, A.; Angeli, P. Mass transfer during Taylor flow in microchannels with and without chemical reaction. *Chem. Eng. J.* **2010**, *160*, 873–881.
22. Kreutzer, M.T.; Kapteijn, F.; Moulijn, J.A.; Kleijn, C.R.; Heiszwolf, J.J. Inertial and interfacial effects on pressure drop of Taylor flow in capillaries. *AIChE J.* **2005**, *51*, 2428–2440.
23. Jovanović, J.; Zhou, W.; Rebrov, E.V.; Nijhuis, T.; Hessel, V.; Schouten, J.C. Liquid-liquid slug flow: Hydrodynamics and pressure drop. *Chem. Eng. Sci.* **2011**, *66*, 42–54.

Microflow Photochemistry—Photodecarboxylations in Microformats

Michael Oelgemöller, Sonia Gallagher and Kevin McCarthy

Abstract: This article summarizes selected examples of intra- and intermolecular photodecarboxylations involving phthalimides in a commercially available dwell device. Compared to batch conditions in a larger chamber reactor, the investigated transformations in the microreactor furnished higher conversions and yields after significantly shorter reaction times. The product qualities were commonly higher under flow conditions thus avoiding the need for further purifications.

Reprinted from *Processes*. Cite as: Oelgemöller, M.; Gallagher, S.; McCarthy, K. Microflow Photochemistry—Photodecarboxylations in Microformats. *Processes* **2014**, *2*, 158-166.

1. Introduction

Microflow photochemistry combines the advantageous features of microreactors, flow operation and organic photochemistry [1–3]. The microscopic dimensions within micro-structured devices allow for an efficient penetration of light and subsequently yield high energy and quantum efficiencies [4,5]. In addition, continuous flow operation reduces photodecompositions of light-sensitive products [6] and avoids the accumulation of potentially hazardous materials in larger amounts, the latter especially problematic for heterogeneous gas-liquid reactions [7]. Likewise, irradiation enables the synthesis of complex molecules with ease and numerous examples of highly effective photochemical transformations have been reported [8–10]. Of these, the photodecarboxylation of phthalimides has been developed as an efficient access to macrocycles or Grignard-type addition products [11,12]. As a result, the reaction has been used for the synthesis of known and potentially bioactive target compounds [13,14]. Examples of these reactions in meso- and micro-formats have also been reported [15–17].

2. Experimental Section

A UV panel (Luzchem, Ottawa, Canada) was selected as light source. The panel was fitted with 5 × 8 W UVB fluorescent tubes ($\lambda = 300 \pm 25$ nm). The microreactor, a dwell device manufactured by mikroglass chemtech (Mainz, Germany), was placed underneath the panel. Its body is fabricated from Foturan™ glass and possesses two separate channels; the bottom reaction channel is 500 μm in depth, 2000 μm in width and 1.15 m in length with a volume of 1.68 mL, while the top channel was used for cooling during operations. The photoreactor module was enclosed on the sides with reflective tinfoil sheets and at the front with a UV shield to contain the UV light during irradiation. A small fan was placed in the back for cooling. The reaction channel inlet was connected to a programmable syringe pump (Harvard apparatus 11 plus, Holliston, MA, USA) via a shut-off valve and the outlet to a round bottom flask outside the irradiated area. The cooling channel was attached to a rotary piston pump (ISMATEC REGLO-CPF Digital, Wertheim, Germany), which drew cooling

water in a loop from a reservoir. The complete reaction set-up incorporating the dwell device is shown in Figure 1.

Figure 1. Dwell device set-up.

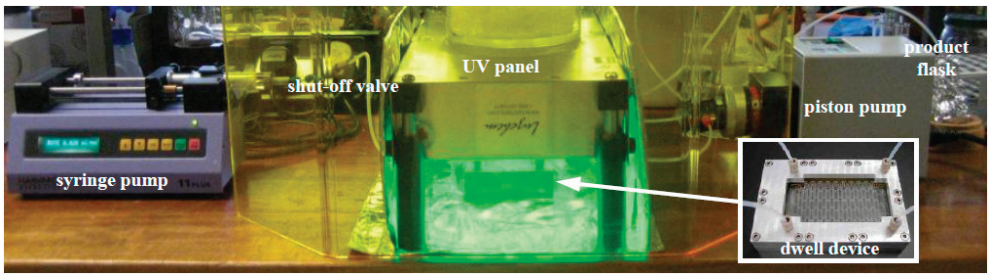

2.1. General Procedure for Photodecarboxylative Cyclizations

A solution of **1** or **3a**,**b** (0.15 mmol) in an acetone/water mixture (1:1 vol%, 10 mL) was purged with nitrogen and loaded into a gas-tight syringe. The dwell device was prepared by pumping approximately 10 mL of the solvent mixture through its reaction channel. The shut-off valve was closed and the syringe containing the reaction mixture was loaded. The UV panel was ignited and ran for 2 min to achieve optimal light output. The cooling water flow and fan were subsequently started. After about 1 min, the shut-off valve was opened and the syringe pump started. The reaction mixture was pumped through a microreactor while irradiated with UVB light. Once the entire 10 mL of reaction mixture was pumped through the reactor system, the UV panel and syringe pump were both turned off simultaneously. The shut-off valve was closed and a syringe containing 10 mL of the plain solvent mixture was attached. The valve was once again opened and the syringe pump and the light source were turned on in unison to flush the residual reaction mixture out of the channel. The washings and product mixture were collected together and subjected to work-up. Most of the acetone was evaporated and the crude product mixture was extracted with CH_2Cl_2 (3 × 10 mL). The combined organic layer was washed with saturated $NaHCO_3$ (2 × 10 mL), brine (2 × 10 mL) and dried over $MgSO_4$. Filtration and evaporation gave pure **2** or **4a**,**b** as colorless solids.

Selected physical and spectral data for 9b-hydroxy-1, 2, 3, 9b-tetrahydro-pyrrolo[2,1-a]isoindol-5-one (**2**) [18]: Melting point = 125–127 °C. R_f (SiO_2, ethyl acetate:*n*-hexane = 1:1) = 0.35. ^{1}H-NMR: (400 MHz, acetone-d_6): δ (ppm) = 1.54 (m; 1H; CH_2), 2.30 (m; 2H; CH_2), 2.57 (m; 1H; CH_2), 3.35 (m; 1H; CH_2), 3.61 (m; 1H; CH_2), 5.26 (br.s; 1H; OH), 7.50 (m; 1H; CH_{arom}), 7.60 (m; 3H; CH_{arom}). ^{13}C-NMR: (100 MHz, acetone-d_6): δ (ppm) = 28.2 (1C; CH_2), 36.0 (1C; CH_2), 42.0 (1C; CH_2), 96.7 (1C; C–OH), 123.5 (1C; CH_{arom}), 123.5 (1C; CH_{arom}), 129.9 (1C; CH_{arom}), 132.9 (1C; Cq_{arom}), 133.0 (1C; CH_{arom}), 149.3 (1C; Cq_{arom}), 170.0 (1C; C=O).

2.2. General Procedure for Photodecarboxylative Additions to N*-methylphthalimide*

N-Methylphthalimide (**5**; 0.38 mmol) was dissolved in 5 mL of acetone. The addition partner **6a**–**f** or **8a**–**e** (1.13 mmol) was added to K_2CO_3 (0.57 mmol) and dissolved in 5 mL of distilled water. These solutions were then added together in a conical flask and made up to 25 mL using a mixture of acetone/water (50:50). The solution was sonicated for 5 min and then degassed with a

slow stream of nitrogen. The microreactor was operated and the reaction mixture treated as described above in Section 2.1. Conversion rates of **5** and, for compounds **9a**–**e**, diastereoselectivities were determined by comparison of baseline-separated signals in the ^{1}H-NMR spectrum of the crude product. Whenever necessary, pure products were isolated by column chromatography using silica gel and ethyl acetate/*n*-hexane mixtures.

Selected physical and spectral data for 3-benzyl-3-hydroxy-2-methylisoindolin-1-one (**7a**) [19]: Melting point = 148–152 °C. R_f (SiO_2, ethyl acetate:*n*-hexane = 1:1) = 0.28. ^{1}H-NMR: (400 MHz, $CDCl_3$): δ (ppm) = (s; 3H; NCH_3), 3.09 (d; ^2J = 14.0 Hz; 1H; CH_2), 3.46 (d; ^2J = 14.0 Hz; 1H; CH_2), 3.67 (br.s; 1H; OH), 6.86 (m; 2H; CH_{arom}), 7.10 (br.m; 3H; CH_{arom}), 7.25 (d; ^3J = 7.6 Hz; 1H; CH_{arom}), 7.32 (ddd; ^3J = 7.6, ^4J = 1.0 Hz; 1H; CH_{arom}), 7.41 (d; ^3J = 7.6 Hz; 1H; CH_{arom}), 7.45 (ddd; ^3J = 7.6 Hz, ^4J = 1.0 Hz; 1H; CH_{arom}). ^{13}C-NMR: (100 MHz, $CDCl_3$): δ (ppm) = 24.2 (s, 1C, NCH_3), 42.7 (s, 1C, CH_2), 90.9 (s, 1C, COH), 123.0 (s, 1C, CH_{arom}), 123.2 (s, 1C, CH_{arom}), 127.3 (s, 1C, CH_{arom}), 128.3 (s, 2C, CH_{arom}), 129.8 (s, 1C, CH_{arom}), 130.3 (s, 2C, CH_{arom}), 131.4 (s, 1C, CH_{arom}), 132.0 (s, 1C, Cq_{arom}), 134.7 (s, 1C, Cq_{arom}), 146.5 (s, 1C, Cq_{arom}), 167.4 (s, 1C, C=O).

3. Results and Discussion

A set of intra- and intermolecular photodecarboxylations involving phthalimides was chosen as model reactions to investigate the effectiveness of the microreactor setup. For comparison, batch reactions were performed using a conventional Rayonet (Branford, CT, USA) chamber photoreactor (RPR-200) equipped with 16 × 8 W UVB fluorescent tubes (λ = 300 ± 25 nm) [18,19]. A Pyrex Schlenk flask (inner diameter: 32 mm) with an inserted cooling-finger (outer diameter: 24 mm) and an approximate volume of 150 mL was used as reaction vessel. Irradiations were performed on 100 mL scales.

3.1. Intramolecular Photodecarboxylative Cyclization Reactions

The photodecarboxylative cyclization of the L-glutamic acid derived compound **1** furnished the tricyclic product **2** (Scheme 1) via a cascade of α- and ω-decarboxylations [20,21]. Under batch conditions, prolonged irradiation for several hours is typically required to reach high conversion. Consequently, irradiation of **1** for 2 h furnished compound **2** in an isolated yield of 42%. To evaluate the efficiency of the microreactor platform, the irradiation time was shortened to 21 min instead. When using the traditional chamber reactor, the isolated yield of **2** was low with 17%. The comparison reaction carried out in the microreactor with a residence time of 21 min resulted in a significantly improved yield of **2** of 33%. ^{1}H-NMR-analysis of the crude product obtained under flow conditions furthermore showed no signs of impurities, thus avoiding the need for further purification.

Scheme 1. Photodecarboxylative cyclizations of phthaloly-L-glutamic acid **1**.

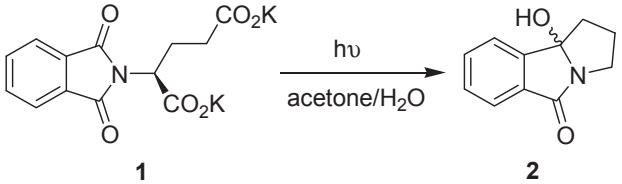

1 **2**

The photocyclization of the anthranilic acid-linked dipeptide models **3a** and **3b** is known to proceed with memory of chirality and exclusively yields the *trans*-diastereoisomers of the polycyclic (1,4)-benzodiazepines **4a** and **4b** (Scheme 2; Table 1) [22]. Upon extended irradiation under conventional conditions for a period of 4 h and 2.5 h, the corresponding cyclization products **4a** and **4b** were isolated in yields of 40% and 58%, respectively. When the reactions were transferred to the microreactor, residence times were shortened to allow for more reasonable operation times and to avoid clogging of the reaction channel due to product precipitation. The L-alanine-derived product **4a** was formed in a yield of 35% with a residence time of less than 3 h. The result obtained for the L-leucine-derived compound **3b** showed a marked improvement with an enhanced yield of **4b** of 87% being achieved after an irradiation period of just under 1 h. The differences in performances for both compounds may be due to alterations in conformational folding, with the leucine-containing compound **3b** preferentially populating a reactive conformation responsible for successful photocyclization [23,24]. Noteworthy, no further purifications were again required for the crude products obtained under microflow conditions. Flow operation thus increases product qualities and avoids time- and resource-demanding purification steps.

Scheme 2. Photodecarboxylative cyclizations of the dipeptide models **3a** and **3b**.

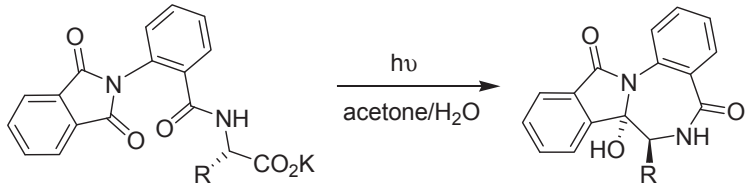

3a (R = Me)
b (R = *i*-Bu)

4a,b

Table 1. Comparison of microreactor *versus* batch reactor performances.

Entry	Batch Reactor		μ-Reactor	
	Time (h)	Yield of 4 (%)	Time (min)	Yield of 4 (%)
3a	4	40	168 [a]	35
3b	2.5	58	56 [a]	87

[a] Shortened residence time to avoid clogging by precipitation.

3.2. Intermolecular Photodecarboxylative Addition Reactions

The merits of using the microreactor were further investigated by attempting various benzylation reactions of *N*-methylphthalimide (**5**) with phenylacetates (**6a**–**f**) (Scheme 3; Table 2) [19]. For direct comparison reasons, the irradiation times were kept the same or similar in almost all cases. Simple decarboxylations (–CO_2H/–H exchange) are commonly observed for these benzylations, resulting in incomplete conversions and yielding the corresponding toluene derivatives of **6a**–**f** as by-products. For the parent phenylacetate **6a**, irradiation under batch conditions for 1 h furnished the desired product **7a** in a good yield of 80% after column chromatography. When conducted in the dwell device with a residence time of just 42 min, ^{1}H-NMR analysis of the crude product obtained showed only the presence of **7a**. No further purification of the product was needed, thus resulting in an

improved yield of **7a** of 98%. The reactions involving phenylacetates **6b** and **6f** proceeded similarly but required prolonged reaction times of 4 h and 3 h, respectively. In the larger chamber reactor, the benzylated products **7b** and **7f** were both obtained after purification in yields of 53%. Under microflow conditions, the same transformations furnished pure products **7b** and **7f** directly in yields of 93% each. All other reactions involving the mono-halogenated phenylacetates **6c**–**e** showed incomplete conversions of **5** due to competing simple decarboxylations. Differences in return electron transfer rates [25] or radical stabilities [26–28] of the corresponding benzyl radicals may have caused this drop in chemoselectivity. Purification was thus required for both, batch and microflow operation modes. In the conventional Rayonet reactor, isolated yields of 39% (**7c**), 35% (**7d**) and 51% (**7e**) were achieved despite prolonged irradiation periods after 4–5 h. In case of the para-fluoro compound **6c**, the reaction in the microreactor with a residence time of 4 hours gave the desired product **7c** in 53% yield. Due to the limitations of the syringe pump employed, the residence time of the transformation involving carboxylate **6d** was kept below 5 h. Nevertheless, the benzylation product **7d** was isolated in a compared to the batch reaction increased yield of 60%. The photoreaction employing the ortho-iodo derivative **6e** was conducted with a residence time of less than 3 h due to precipitation of the product at lower flow rates and thus the danger of clogging. As a result, the corresponding addition product **7e** was obtained in a somewhat lower yield of 23%.

Scheme 3. Photodecarboxylative benzylations of *N*-methylphthalimide (**5**).

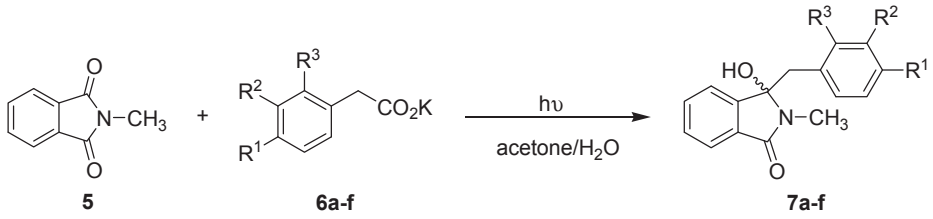

Table 2. Comparison of microreactor *versus* batch reactor performances.

Entry	R^1	R^2	R^3	Batch Reactor		μ-Reactor	
				Time (h)	Yield of 7 (%)	Time (min)	Yield of 7 (%)
6a	H	H	H	1	80	42	98 [a]
6b	CH_3	H	H	4	53	240	93 [a]
6c	F	H	H	4	39	240	53
6d	H	H	Br	5	35	280	60
6e	H	H	I	4	51	168 [b]	23
6f	Cl	Cl	H	3	53	180	93 [a]

[a] Pure product, no purification required. [b] Shortened residence time to avoid clogging by precipitation.

Scheme 4. Photodecarboxylative addition of *N*-protected amino acids (**8a**–**e**) to *N*-methylphthalimide (**5**).

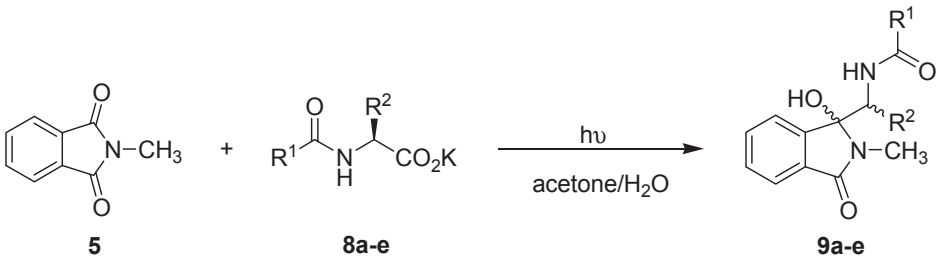

Table 3. Comparison of microreactor *versus* batch reactor performances.

Entry	R^1	R^2	Batch reactor		μ-Reactor	
			Time (h)	Yield of 9 (%)	Time (min)	Yield of 9 (%)
8a	CH_3	*i*-Pr	3.5	52	210	58
8b	CH_3	*i*-Bu	3	26	42 [a]	18
8c	CH_3	*sec*-Bu	3	78	21 [a]	27
8d	*t*-BuO	CH_3	3	65	168 [a]	93
8e	*t*-BuO	Bn	3	34	168 [a]	53

[a] Shortened residence times to avoid clogging by precipitation.

N-Acyl protected amino acids successfully undergo photodecarboxylative additions with **5** (Scheme 4) [29]. A selection of these reactions was thus performed with the amino acid derivatives **8a**–**e** in the microreactor and compared to analogue reactions conducted in the conventional chamber reactor (Table 3). To avoid precipitation of photoproducts within the microchannel and thus clogging, high flow rates had to be maintained for some of the reactions, thus causing reduced residence times. Even after prolonged irradiations, conversions of **5** were incomplete, suggesting consumption of **8a**–**e** due to alternative photoreactions [30]. Yields and conversions varied depending on the amino acid utilized, thus supporting electronic [31] as well as steric effects [32]. The isoleucine derived product **9c** was formed as a mixture of four stereoisomers. For all other amino acids, diastereoselectivities (*d.e.*) were moderate and ranged from 22% to 38% [33]. Under batch conditions, the corresponding addition products **9a**–**e** were formed in acceptable to good yields of 26%–78% after 3–3.5 h of irradiation. When conducted in the dwell device, the amounts of **9a**–**e** naturally varied depending on residence times. For amino acids **8a**, **d** and **e**, yields were significantly higher than for the batch counterparts. Despite the much shorter residence times of 42 min and 21 min, compounds **9b** and **9c** were generated in reasonable amounts of 18% and 27%, respectively. The results demonstrate once again that photodecarboxylative additions progress more efficiently in the microreactor and this observation is strengthened by the fact that the product quality was generally improved compared to operations in the chamber reactor.

4. Conclusions

A range of photodecarboxylation cyclization and addition reactions has been transferred successfully to microflow conditions. Despite the larger light power of the Rayonet chamber reactor

with its sixteen UVB fluorescent tubes, the smaller dwell device utilized the light emitted from its five fluorescent tubes more efficiently. As a result, the chosen microreactor repeatedly enabled a decrease in reaction time compared to the conventional batch reactor. In addition, higher yields and better product qualities were typically observed, thus minimizing or completely avoiding the need of purification steps. These performance features make microflow photochemistry a green chemical synthesis tool [34]. A current drawback of microflow devices is the lengthy operation time and subsequently their low productivity. However, microreactors offer interesting applications in early research and development processes, where only small amounts of materials are needed [35]. Small-scale manufacturing plants have also been realized using automated and parallel microflow photochemical reactors, for example the innovative Heraeus Noblelight process for the synthesis of anti-cancer precursors [36]. In conclusion, microflow photochemistry represents a sustainable technology with a bright future.

Acknowledgments

This work was financially supported by the Environmental Protection Agency (EPA, 2008-ET-MS-2-S2), the Department of Environment, Heritage and Local Government (DEHLG, 2008-S-ET-2), the Science Foundation Ireland (SFI, 07/RFP/CHEF817) and the Australian Research Council (ARC, Discovery Project DP130100794). Kevin McCarthy thanks the SFI for a Secondary Teacher Assistant Researchers (STARs) award in 2008. The authors thank Oksana Shydkiv (Dublin City University, Dublin, Ireland) for technical assistance.

Conflicts of Interest

The authors declare no conflict of interest.

References

1. Oelgemöller, M. Highlights of photochemical reactions in microflow reactors. *Chem. Eng. Technol.* **2012**, *35*, 1144–1152.
2. Oelgemöller, M.; Shvydkiv, O. Recent advances in microflow photochemistry. *Molecules* **2011**, *16*, 7522–7550.
3. Coyle, E.E.; Oelgemöller, M. Micro-photochemistry: Photochemistry in microstructured reactors. The new photochemistry of the future? *Photochem. Photobiol. Sci.* **2008**, *7*, 1313–1322.
4. Sugimoto, A.; Fukuyama, T.; Sumino, Y.; Takagi, M.; Ryu, I. Microflow photo-radical reaction using a compact light source: Application to the Barton reaction leading to a key intermediate for myriceric acid A. *Tetrahedron* **2009**, *65*, 1593–1598.
5. Aillet, T.; Loubiere, K.; Dechy-Cabaret, O.; Prat, L. Photochemical synthesis of a “cage” compound in a microreactor: Rigorous comparison with a batch photoreactor. *Chem. Eng. Proc.* **2013**, *64*, 38–47.

6. Maeda, H.; Nashihara, S.; Mukae, H.; Yoshimi, Y.; Mizuno, K. Improved efficiency and product selectivity in the photo-Claisen-type rearrangement of an aryl naphthylmethyl ether using a microreactor/flow system. *Res. Chem. Intermed.* **2013**, *39*, 301–310.
7. Terao, K.; Nishiyama, Y.; Tanimoto, H.; Morimoto, T.; Oelgemöller, M.; Kakiuchi, K. Diastereoselective [2 + 2] photocycloaddition of a chiral cyclohexenone with ethylene in a continuous flow microcapillary reactor. *J. Flow Chem.* **2012**, *2*, 73–76.
8. Bach, T.; Hehn, J.P. Photochemical reactions as key steps in natural product synthesis. *Angew. Chem. Int. Ed.* **2011**, *50*, 1000–1045.
9. Hoffmann, N. Photochemical reactions as key steps in organic synthesis. *Chem. Rev.* **2008**, *108*, 1052–1103.
10. Iriondo-Alberdi, J.; Greaney, M.F. Photocycloaddition in natural product synthesis. *Eur. J. Org. Chem.* **2007**, 4801–4815.
11. Griesbeck, A.G.; Kramer, W.; Oelgemöller, M. Synthetic applications of photoinduced electron transfer decarboxylation reactions. *Synlett* **1999**, *1999*, 1169–1178.
12. Kramer, W.; Griesbeck, A.G.; Nerowski, F.; Oelgemöller, M. Synthetic potential of the PET-decarboxylation of ω-phthalimido carboxylic acids. *J. Inf. Rec.* **1998**, *24*, 81–85.
13. Belluau, V.; Noeureuil, P.; Ratzke, E.; Skvortsov, A.; Gallagher, S.; Motti, C.A.; Oelgemöller, M. Photodecarboxylative benzylations of phthalimide in pH 7 buffer: A simple access to 3-arylmethyleneisoindolin-1-ones. *Tetrahedron Lett.* **2010**, *51*, 4738–4741.
14. Hatoum, F.; Engler, J.; Zelmer, C.; Wißen, J.; Motti, C.A.; Lex, J.; Oelgemöller, M. Photodecarboxylative addition of carboxylates to phthalimides: A concise access to biologically active 3-(aryl and alkyl)methylene-1*H*-isoindolin-1-ones. *Tetrahedron Lett.* **2012**, *53*, 5573–5577.
15. Griesbeck, A.G.; Kramer, W.; Oelgemöller, M. Photoinduced decarboxylation reactions. Radical chemistry in water. *Green Chem.* **1999**, *1*, 205–207.
16. Shvydkiv, O.; Gallagher, S.; Nolan, K.; Oelgemöller, M. From conventional to microphotochemistry: Photodecarboxylation reactions involving phthalimides. *Org. Lett.* **2010**, *12*, 5170–5173.
17. Shvydkiv, O.; Nolan, K.; Oelgemöller, M. Microphotochemistry—4,4'-dimethoxybenzophenone mediated photodecarboxylation reactions involving phthalimides. *Beilstein J. Org. Chem.* **2011**, *7*, 1055–1063.
18. Griesbeck, A.G.; Henz, A.; Kramer, W.; Lex, J.; Nerowski, F.; Oelgemöller, M.; Peters, K.; Peters, E.-M. Synthesis of medium- and large-ring compounds initiated by photochemical decarboxylation of ω-phthalimidoalkanoates. *Helv. Chim. Acta* **1997**, *80*, 912–933.
19. Hatoum, F.; Gallagher, S.; Baragwanath, L.; Lex, J.; Oelgemöller, M. Photodecarboxylative benzylations of phthalimides. *Tetrahedron Lett.* **2009**, *50*, 6335–6338.
20. Sato, Y.; Nakai, H.; Mizoguchi, T.; Kawanishi, M.; Kanaoka, Y. Photochemistry of the phthalimide system. I. Photodecarboxylation of *N*-phthaloyl-α-amino acids. *Chem. Pharm. Bull.* **1973**, *21*, 1164–1166.

21. Griesbeck, A.G.; Henz, A.; Peters, K.; Peters, E.-M.; von Schnering, H.G. Photo electron transfer induced macrocyclization of *N*-phthaloyl-ω-amino-carboxylic acids. *Angew. Chem. Int. Ed.* **1995**, *34*, 474–476.
22. Griesbeck, A.G.; Kramer, W.; Lex, J. Stereoselective synthesis of 1,4-benzodiazepins via photoinduced decarboxylation of *N*-phthaloylanthranilic acid amides. *Synthesis* **2001**, 1159–1166.
23. Wagner, P.J. Conformational flexibility and photochemistry. *Acc. Chem. Res.* **1983**, *16*, 461–467.
24. Huang, F.; Nau, W.M. A conformational flexibility scale for amino acids in peptides. *Angew. Chem. Int. Ed.* **2003**, *42*, 2269–2272.
25. Yokoi, H.; Nakano, T.; Fujita, W.; Ishiguro, K.; Sawaki, Y. In-cage formation of carbanions in photoinduced electron-transfer reaction of carboxylate ions. *J. Am. Chem. Soc.* **1998**, *120*, 12453–12458.
26. Jackson, R.A.; Sharifi, M. Stabilization of benzylic radicals by substituents: An EPR study of para-substituted benzyl radicals. *J. Chem. Soc. Perkin Trans.* **1996**, *2*, 775–778.
27. Singh, N.K.; Popelier, P.L.A.; O'Malley, P.J. Substituent effects on the stability of para substituted benzyl radicals. *Chem. Phys. Lett.* **2006**, *426*, 219–221.
28. Suryan, M.M.; Stein, S.E. Stabilities of substituted benzyl radicals: Dissociation rates of amino-, hydroxy-, and cyanoethylbenzenes. *J. Phys. Chem.* **1989**, *93*, 7362–7365.
29. Gallagher, S.; Hatoum, F.; Zientek, N.; Oelgemöller, M. Photodecarboxylative additions of *N*-protected α-amino acids to *N*-methylphthalimide. *Tetrahedron Lett.* **2010**, *51*, 3639–3641.
30. Schaich, K.M. Free radical initiation in proteins and amino acids by ionizing and ultraviolet radiations and lipid oxidation—Part II: Ultraviolet radiation and photolysis. *CRC Critical Rev. Food Sci. Nutr.* **1980**, *13*, 131–159.
31. Ho, J.; Coote, M.L.; Easton, C.J. The distal effect of *N*-electron-withdrawing groups on the stability of peptide carbon radicals. *Aust. J. Chem.* **2011**, *64*, 403–408.
32. White, D.P.; Anthony, J.C.; Oyefeso, A.O. Computational measurement of steric effects: The size of organic substituents computed by Ligand Repulsive Energies. *J. Org. Chem.* **1999**, *64*, 7707–7716.
33. Gallagher, S. From conventional to microphotochemistry: A study of phthalimide and phthalonitrile derivatives. Ph.D. Thesis, Dublin City University, Dublin, Ireland, April 2011.
34. Newman, S.G.; Jensen, K.F. The role of flow in green chemistry and engineering. *Green Chem.* **2013**, *15*, 1456–1472.
35. Chin, P.; Barney, W.S.; Pindzola, B.A. Microstructured reactors as tools for the intensification of pharmaceutical reactions and processes. *Curr. Opin. Drug Dis. Dev.* **2009**, *12*, 848–861.
36. Werner, S.; Seliger, R.; Rauter, H.; Wissmann, F. Quarzglas-mikrophotoreaktor und synthese von 10-hydroxycamptothecin und 7-alkyl-10-hydroxycamptothecin. EP-2065387A2, 2009.

Scale-up of the Reversible Addition-Fragmentation Chain Transfer (RAFT) Polymerization Using Continuous Flow Processing

Nenad Micic, Alan Young, Julien Rosselgong and Christian H. Hornung

Abstract: A controlled radical polymerization process using the Reversible Addition-Fragmentation Chain Transfer (RAFT) approach was scaled up by a factor of 100 from a small laboratory scale of 5 mL to a preparative scale of 500 mL, using batch and continuous flow processing. The batch polymerizations were carried out in a series of different glass vessels, using either magnetic or overhead stirring, and different modes of heating: Microwave irradiation or conductive heating in an oil bath. The continuous process was conducted in a prototype tubular flow reactor, consisting of 6 mm ID stainless steel tubing, fitted with static mixers. Both reactor types were tested for polymerizations of the acid functional monomers acrylic acid and 2-acrylamido-2-methylpropane-1-sulfonic acid in water at 80 °C with reaction times of 30 to 40 min. By monitoring the temperature during the exothermic polymerization process, it was observed that the type and size of reactor had a significant influence on the temperature profile of the reaction.

Reprinted from *Processes*. Cite as: Micic, N.; Young, A.; Rosselgong, J.; Hornung, C.H. Scale-up of the Reversible Addition-Fragmentation Chain Transfer (RAFT) Polymerization Using Continuous Flow Processing. *Processes* **2014**, *2*, 58-70.

1. Introduction

The Reversible Addition-Fragmentation Chain Transfer (RAFT) method is arguably the most convenient and versatile approach to controlled free radical polymerizations, as it is compatible with most monomers amenable to free radical polymerization [1–6]. With appropriate selection of reaction conditions the RAFT process takes on most of the characteristics of a living polymerization, and it allows the synthesis of polymers with narrow molecular weight distributions and well defined end groups, as well as complex polymer architectures, such as blocks, stars and others [2–6].

In recent years, microreactor technology has transformed the way chemical synthesis is conducted in research laboratories [7–20], replacing batch reactions classically carried out in laboratory glassware by continuous flow processes using tubular [21–24] or chip/plate based [25–27] reactor designs. A continuous flow reactor can offer a range of benefits over batch processing; as one example, flow reactors have better heat and mass transfer properties, leading to increased control over the process and often to improvements in product quality [7–9].

The advantageous heat transfer performance of micro-structured flow reactors for use in exothermic solution phase polymerization reactions was first described by Iwasaki *et al*. [28]. The authors described the free radical polymerization of five different monomers in a steel reactor system containing capillaries with 500 μm inner diameter (ID). The results were compared to a macro-scale batch process resulting in an improved control over the molecular weight distribution

of the polymer product in the microreactor, especially for the highly exothermic reactions of (meth)acrylate monomers. Later work by the same group demonstrated the numbering-up of this continuous flow microreactor system to the pilot plant scale for the use in free radical polymerization of methyl methacrylate [29]. Here, a stainless steel shell and tube microreactor was developed consisting of 94 microtubes (500 μm ID) with a total volumetric hold up 9.6 mL. The shell was divided into two sections accounting for the different temperatures in the two stages of the process. Hot oil was introduced in the first section of the shell in order to carry out the polymerization at 100 °C, and coolant in the second for fast termination. The authors concluded that precise temperature control by effective heat transfer, which is an inherent advantage of microreactor systems, was responsible for the effective control of the molecular weight distribution of the polymer. Since then, several other research groups have investigated continuous flow polymerizations in micro- and meso-structured flow reactors [27,30–36]. Over the past three years, our group has undertaken extensive research in the area of continuous flow RAFT polymerizations, including post-polymerization steps such as RAFT end group removal or modification [37–42]. In this paper, we report the scale-up of exothermic RAFT polymerizations of acid functional monomers in water. The reactions were performed in a prototype tubular continuous flow reactor containing static mixer arrays and compared to batch reactions performed at different scales and in different reaction vessels.

2. Experimental Section

2.1. Materials and Analysis

The initiator 4,4'-azobis(4-cyanovaleric acid), supplied by Fluka (Buchs, Switzerland), was used without further treatment. The RAFT agent 2-(2-carboxyethylsulfanylthiocarbonylsulfanyl)propionic acid was synthesized in our group, using the experimental protocol described by Wang *et al*. [43]. The monomers acrylic acid (AAc) and 2-acrylamido-2-methylpropane-1-sulfonic acid (AMPS) were pre-treated using polymer resin (for removal of hydroquinone and monomethyl ether hydroquinone, Sigma Aldrich, St. Louis, MO, USA, Cat. No: 31,133-2) in order to remove the radical inhibitor. The solvent diethyl ether was obtained from Merck KGaA and was used without further purification. Reaction conversions were calculated from ^{1}H-NMR spectra. In some cases the conversion was calculated using 1,3,5-trioxane as an internal standard, a method successfully applied and described in previous work [37–39]. Average molecular weight of the polymer, M_n and its dispersity, $Đ$, were measured using size exclusion chromatography (SEC). An aqueous SEC system was used, the different components were: a Waters E2695 separation module running at a flow rate of 1 mL/min, two PL aquagel-OH 8 μm mixed columns (300 × 7.5 mm) and a PL aquagel-OH 8 mm guard column (50 × 7.5 mm), water as the eluent (containing 0.2 M $NaNO_3$, 0.01 M NaH_2PO_4, pH adjusted to 8.2) and a differential refractive index detector calibrated with linear poly(ethylene oxide) standards (M_p = 6 × 10^2 to 435 × 10^3 g·mol^{-1}).

2.2. RAFT Polymer Synthesis in Batch Using a Microwave Reactor—Scale: Up to 20 mL

Small, discovery scale RAFT polymerization experiments in batch were conducted on a laboratory microwave (MW) reactor (Biotage Initiator; Biotage AB, Uppsala, Sweden) [44]. The following procedure is typical. A starting material solution of 3.60 g (50 mmol) monomer (AAc), 14.0 mg initiator (0.05 mmol), 63.6 mg RAFT agent (0.25 mmol), in 16.6 mL of deionised water, was premixed and deoxygenated for 20 min using nitrogen purging. The polymerization was carried out at 80 °C with a reaction time of 40 min. This reactor uses magnetic stirring to agitate the solution during reaction. At the end of the heating cycle, the glass vial was cooled down by blowing a stream of cold air or nitrogen around it. The product was a yellow viscous polymer solution, from which conversion was determined by ^{1}H-NMR. For a 20 mL reaction a small aliquot of the polymer solution was purified by precipitation, for 3 and 5 mL reactions the entire product solution was purified: Following solvent removal and re-dissolving in DCM, the product, polyacrylic acid (pAAc), was precipitated in Et_2O, resulting in a yellow polymer powder, after filtration and drying.

2.3. RAFT Polymer Synthesis in Batch Using an Oil Bath—Scale: Up to 500 mL

Scale-up RAFT polymerization experiments of AAc in batch were performed using an oil bath. The following procedure is typical. Two starting material solution were prepared: the first one consisted of 90.1 g (1.25 mol) monomer (AAc) and 1590 mg RAFT agent (6.25 mmol) in 380 mL of deionised water; the second contained 350 mg initiator (1.25 mmol) in 34.3 mL of deionised water. Both solutions were deoxygenated separately for 40 min using nitrogen purging. The polymerization was conducted in a 1 L, 3-neck round bottom flask (RBF) at 80 °C with a reaction time of 40 min. The reaction vessel was heated by an oil bath and the reaction mixture was stirred using an overhead stirrer (IKA, Eurostar power control-visc; IKA-Werke GmbH & Co. KG, Staufen, Germany) with a PTFE blade type impeller. During the reaction, the stirrer speed was set to 200 rpm. The photograph in Figure 1 gives a comparison between the four different batch glass vessels used.

Figure 1. Photo of batch glass reaction vessels for 5 mL, 20 mL, 100 mL and 500 mL reaction scale; the insert on the top left shows an image taken during the 500 mL reaction.

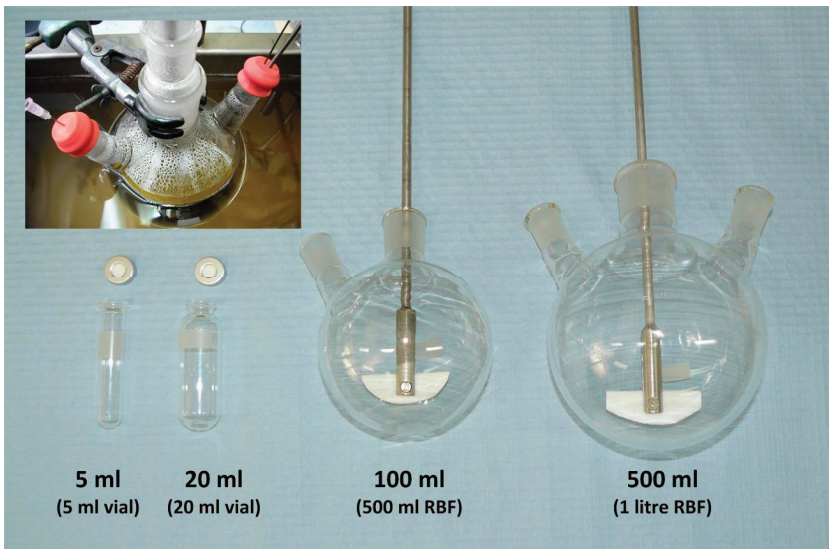

A yellow viscous polymer solution was obtained after reaction, from which conversion was determined by ^{1}H-NMR. A small aliquot of the polymer solution was purified by precipitation; following solvent removal and re-dissolving in DCM, the pAAc product was precipitated in Et_2O, resulting in a yellow polymer powder, after filtration and drying.

2.4. RAFT Polymer Synthesis in Continuous Flow—Scale: 500 mL

Scale-up RAFT polymerization experiments in continuous flow were performed using a prototype tubular flow reactor from Cambridge Reactor Design Ltd., (Cambridge Reactor Design Ltd., Cottenham, UK) [45], the Salamander Flow Reactor. The reactor chamber is a 4 m long stainless steel tube (8 mm OD, 6 mm ID), which is arranged in a serpentine fashion and housed in a metal heating block. The heating is provided by a series of electrical cartridge heaters which are controlled with custom built software coded in LabVIEW (National Instruments Co., Austin, TX, USA) via a graphical user interface (GUI). Temperature and pressure measurements are automatically recorded and plotted on the GUI. The reactor temperature can be set between room temperature and 150 °C on the GUI, while pressure is manually adjusted by an inline backpressure regulator, situated at the outlet of the reactor. The maximum operation pressure of the reactor is 20 bar. In order to enhance mixing of the reagent solution inside the reactor, the straight sections of the pipe were fitted with static mixer units, which in turn reduced the total reactor volume to 108 mL. The flow through the reactor was provided with a Gilson 305 dual piston pump, which can operate at flow rates between 0.5 mL/min and 50 mL/min. Deoxygenation of the stock solutions was provided by nitrogen purging and an inline degasser (Uniflows Degasys DG-1310, Uniflows Co. Ltd., Tokyo, Japan), situated before the pump. Figure 2 shows a flow diagram of the continuous flow polymerization process, with a photograph of the tubular flow reactor on the top right, highlighting the flow path through it in red.

The following procedure is typical. A starting material solution of 90.1 g (1.25 mol) monomer (AAc), 350 mg initiator (1.25 mmol), 1590 mg RAFT agent (6.25 mmol), in 414 mL of deionised water, was premixed and deoxygenated for 40 min using nitrogen purging. The washing solvent (water) was also deoxygenated using nitrogen. After the reactor was flushed with deoxygenated water and brought up to the reaction temperature of 80 °C, the 3-way valve was switched and the monomer solution was pumped into the reactor as a continuous stream (see Figure 1). Polymerization was conducted at a flow rate of 2.7 mL/min resulting in a reaction time of 40 min. At the end of the reaction, deoxygenated water was used to flush the reactor. In order to obtain concentration and conversion profiles over the entire duration of the reaction, small samples of the product solution were collected at predetermined time intervals at the outlet of the reactor and analyzed by ^{1}H-NMR. The yellow viscous solution, obtained at the outlet of the reactor was collected in several fractions. A small aliquot of the main fraction of the polymer solution (processed under steady state conditions) was purified by precipitation. Following solvent removal and re-dissolving in DCM, the pAAc product was precipitated in Et_2O, resulting in a yellow polymer powder, after filtration and drying.

Figure 2. Flow diagram of the continuous Reversible Addition-Fragmentation Chain Transfer (RAFT) polymerization of water-soluble monomers; the magnified photograph on the top right shows the tubular flow reactor, highlighting the flow path through it in red.

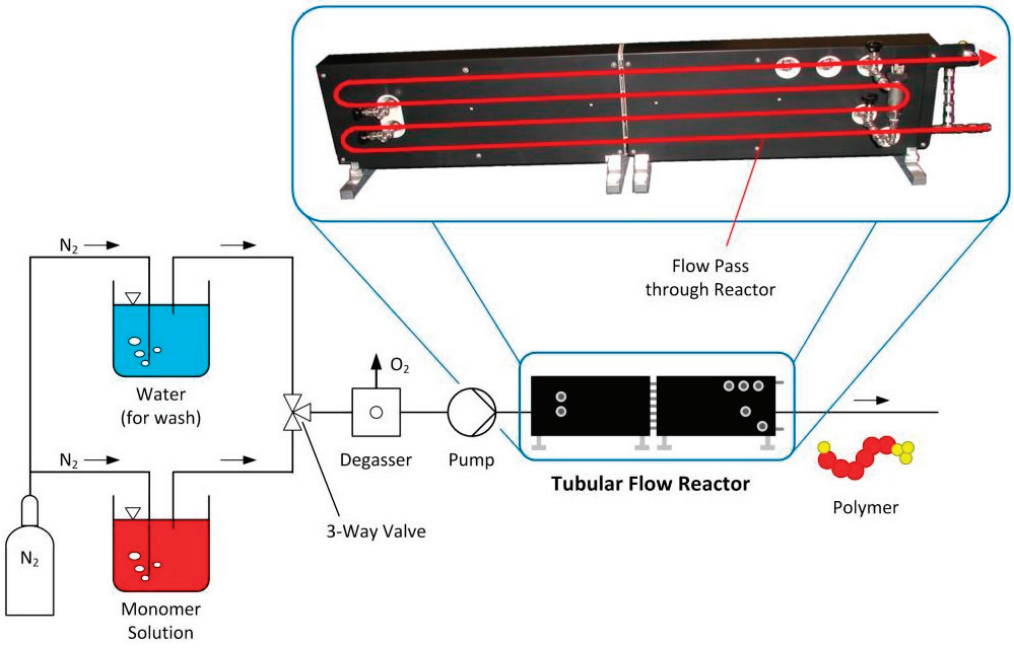

3. Results and Discussion

The herein presented solution phase RAFT polymerizations of the acid functional monomers AAc and AMPS follow the general reaction pathway shown in Scheme 1. A series of different reactors in batch and continuous mode using different heating mechanisms were compared as well as different reaction scales ranging from 3 mL to 500 mL. The reaction conditions, temperature and time, as well as the composition of the monomer stock solution were kept constant for all experiments, so performance of the reactors could be compared directly. Experimental conditions and results are listed in Table 1.

Scheme 1. RAFT polymerization of water-soluble monomers acrylic acid (AAc) and 2-acrylamido-2-methylpropane-1-sulfonic acid (AMPS).

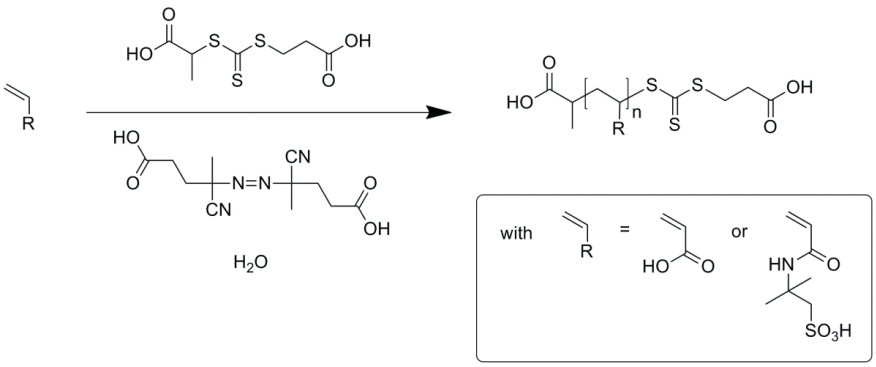

Table 1. Experimental conditions and results for RAFT polymerizations in batch and continuous flow.

Polymer	Process	Scale (mL)	Monomer wt-% [c]	*T* (°C)	*t* (min)	Conversion (%)	M_n (g/mol)	*Đ*
pAAc-1	batch [a]	3	17.7	80	30	95.4	22,700 [f]	1.35 [f]
pAAc-2	batch [a]	5	17.7	80	40	95.5	20,200	1.37
pAAc-3	batch [a]	20	17.7	80	40	96.7	27,000	1.45
pAAc-4	batch [b]	100	17.7	80	40 [d]	94.2 [d]	24,900	1.36
pAAc-5	batch [b]	500	17.7	80	40 [e]	97.4 [e]	21,600	1.45
pAAc-6	cont.	500	17.7	80	40	94.7	23,200	1.53
pAMPS-1	batch [a]	5	30.0	80	30	96.3	32,200 [f]	1.44 [f]
pAMPS-2	cont.	500	30.0	80	40	92.6	31,500	1.50

[a] reaction performed in a batch microwave reactor (see section 2.2); [b] reaction performed in batch in a round bottom flask using an oil bath (see section 2.3); [c] for all reactions the ratio of monomer to RAFT agent to initiator was 200:1:0.2; [d] an ^{1}H-NMR sample of this reaction was taken at 20 min reaction time, resulting in a conversion of 86.1%; [e] an ^{1}H-NMR sample of this reaction was taken at 20 min reaction time, resulting in a conversion of 95.5%; [f] SEC samples of **pAAc-1** and **pAMPS-1** were taken from the dried product after precipitation, all other SEC samples were taken from the crude product solution.

When comparing the batch polymerizations of AAc, **pAAc-1** to **pAAc-5**, with the continuous flow experiment, **pAAc-6**, it can be observed that the polymerization in all these cases was near complete, with conversions varying between 94% and 97%. For the two experiments conducted in the round bottom flask, **pAAc-4** and **pAAc-5**, an ^{1}H-NMR sample was also taken at 20 min, revealing that the 500 mL reaction had progressed already significantly further than the 100 mL reaction: the conversion in the 100 mL reaction at 20 min was 86.1%, in the 500 mL reaction it was 95.5%. The reason for faster reaction on the larger scale is due to the exothermic chain reaction of the radical polymerization (see for example Saldivar-Guerra and Vivaldo-Lima [46]) and the fact that the bigger round bottom flask was not as efficient in cooling this excess heat as the smaller system was. This development becomes very apparent when looking at the temperature curves, taken for reactions **pAAc-2** to **pAAc-5**, which are plotted in Figure 3. Here the temperatures for the three different reactor types are shown: (1) batch microwave reactor (5 mL and 20 mL scale), using microwave irradiation to heat, and a nitrogen stream to cool down the vial after reaction; (2) batch round bottom flask reactor (100 mL and 500 mL scale), using an oil bath to heat up the vessel and regulate the temperature; the reaction was cooled by lifting the flask out of the reactor (no active cooling mechanism); (3) the continuous flow reactor (500 mL scale), using electrical cartridge heaters, embedded within a metal heating block alongside the reactor tubing. These three reactor types resulted in fundamentally different temperature profiles for the RAFT polymerization process. It also needs to be noted that the temperature measurements in these three cases were taken at different points in the system. While for the round bottom flask reactions, the temperature of the reaction solution was measured directly using a thermocouple submersed in it, the microwave reactor measures the temperature of the glass vial via an infrared sensor [44], and the continuous flow reactor measures the temperature of the metal heating mantel via a set of thermocouples [45].

Therefore, the latter two temperature profiles are only an approximation of the bulk fluid temperature during polymerization.

Figure 3. Temperature profiles of RAFT polymerizations of AAc in various batch reactors (MW = Biotage microwave reactor, RBF = round bottom flask) and in the continuous flow reactor; for the MW reactions $t = 0$ corresponds to the point where the temperature of the solution reaches ~80 °C; for the RBF reactions $t = 0$ corresponds to the addition of initiator to the previously heated up monomer solution; for the continuous flow reaction $t = 0$ corresponds to the change-over from pumping solvent to pumping monomer solution into the reactor (see also text below).

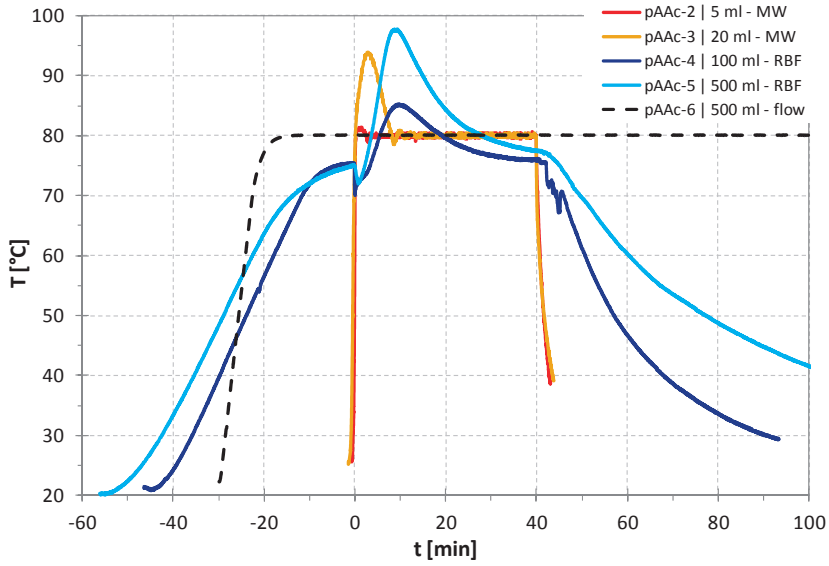

As Figure 3 shows, the temperature in the microwave reactor rises rapidly in the matter of a few seconds at the start of the heating cycle from room temperature to the set value of 80 °C. The temperature stays very close to this value for the entire 40 min in the case of the 5 mL reaction (**pAAc-2**). In the case of the 20 mL reaction (**pAAc-3**), the microwave reactor is not capable of compensating for the exothermic process; hence the temperature rises to 94 °C over the first 5 min before stabilizing at 80 °C for the remaining reaction time. The cooling profile for both reactions is similarly rapid and takes less than 2 min. This shows very clearly the effect of reaction scale on the temperature performance of a batch reactor. A similar observation can be made when comparing the 100 mL and 500 mL reactions in the round bottom flask (**pAAc-4** and **pAAc-5**). Firstly, it can be observed that the transient regimes before the start and after the end of the reaction are many times longer than in the microwave reactor, taking up to 60 min and longer to heat up the reaction mixture or cool it down again. Other than in the microwave and continuous flow reactions, where a stock solution containing all components including the initiator was heated up, for the experiments in the round bottom flask a solution containing only the monomer and RAFT agent were heated up first to near reaction temperature and by adding degassed initiator solution, the reaction was started. This was necessary because of the long heating up time, during which initiation would otherwise already have occurred. Because the initiator solution was injected into the vessel at room temperature, the

temperature traces show a small drop at $t = 0$, but rise very quickly afterwards to 85 °C (100 mL reaction, **pAAc-4**) or 98 °C (500 mL reaction, **pAAc-5**). Similar to the microwave reactor experiments, the trend for these two reactions is non-ambiguous: the larger the reaction scale, the higher the maximum temperature, because the reactor set-up is less efficient in compensating for the exothermic process. For comparison, the temperature trace recorded by the thermocouples of the continuous flow reactor is plotted for reaction **pAAc-6**. As in the case of the 5 mL microwave batch reaction, the continuous flow reactor does not show a measurable deviation from the set temperature value of 80 °C over the entire reaction time, despite the fact that 100 times the amount of material were processed. This demonstrates the efficiency of the continuous flow reactor for the scale-up of exothermic reactions, especially in comparison to batch reactors.

The SEC results show similar performance between comparable batch and continuous flow experiments. All polyacrylic acids had an average molecular weight around 23,000 g/mol, with the only major deviation being **pAAc-3** with 27,000 g/mol. The continuous flow experiment resulted in similar, but slightly higher $Đ$ than the corresponding large scale batch experiment, which was not expected given the difference in temperature profile between batch and flow. One possible explanation could be that $Đ$ was higher because of axial dispersion inside the tubular reactor, leading to a residence time distribution (RTD) profile which deviates significantly from plug flow behavior. Preliminary RTD experiments, currently ongoing, suggest that axial dispersion might have an impact on $Đ$. The lowest $Đ$ in all experiments was 1.35 and was observed in the small scale microwave experiment, using 3 mL of reagent solution. The higher $Đ$ values of **pAAc-3** and **pAAc-5** also confirm the results from the temperature measurements, as it was these two experiments that showed the highest temperature spike. It is believed that during this overheating period large amounts of radicals are formed by the thermal initiator, which leads to a loss of control of the polymerization process in comparison to a reaction that is kept at a constant temperature of 80 °C.

In order to quantify the consistency of the product solution exiting the continuous flow reactor, a set of ^{1}H-NMR samples were taken at the reactor outlet, over the entire duration of the experiment. Weight fractions of monomer and polymer as well as reaction conversions were calculated from these samples: the resulting profiles are plotted in Figure 4. Both the monomer and polymer weight fraction profiles rise sharply at early times and have a tail at long times, which can also be called a "wash out curve". It can further be observed that the monomer profile rises faster than the polymer profile and has a small peak around 50 min, while at the end of the profile the opposite is the case; the monomer profile drops faster than the polymer profile. This suggests that the monomer flows through the reactor faster than the polymer. It is believed that this is due to a stronger physical interaction of the polymer with the tubing wall and the static mixer inserts, which could potentially be a result of the difference in surface charge density between polymer and monomer. This effect is reflected even more in the conversion profile, which is derived from the same set of ^{1}H-NMR data as the monomer and polymer weight fraction values. At the beginning the conversion rises steeply before stabilizing around 95% at steady state conditions, and then drops off lightly after 240 min. The conversion past this time is still relatively high, meaning that significantly more polymer was being washed out of the reactor than monomer, but the total concentration of both was low. This means that the conversion data past 240 min cannot be regarded as such, and its relatively high values are more

likely to be an artifact of the polymer retention phenomena within the tubular reactor, as described above. In a similar way than the pAAc process the polymerization of AMPS was also successfully scaled up from 5 mL in the microwave to 500 mL in the continuous flow reactor, with only small differences in conversion, M_n and $Đ$ (see Table 1). Here the average molecular weight was around 32,000 g/mol and $Đ$ was around 1.5. In general, it was feasible to produce pAAc and pAMPS continuously in the flow reactor, with a similarly good quality than in the batch experiments.

Figure 4. Polymer and monomer weight fraction profiles (to be read on the left y-axis) and conversion profile (to be read on the right y-axis) for the 500 mL RAFT polymerization of AAc in the continuous flow reactor, **pAAc-6**.

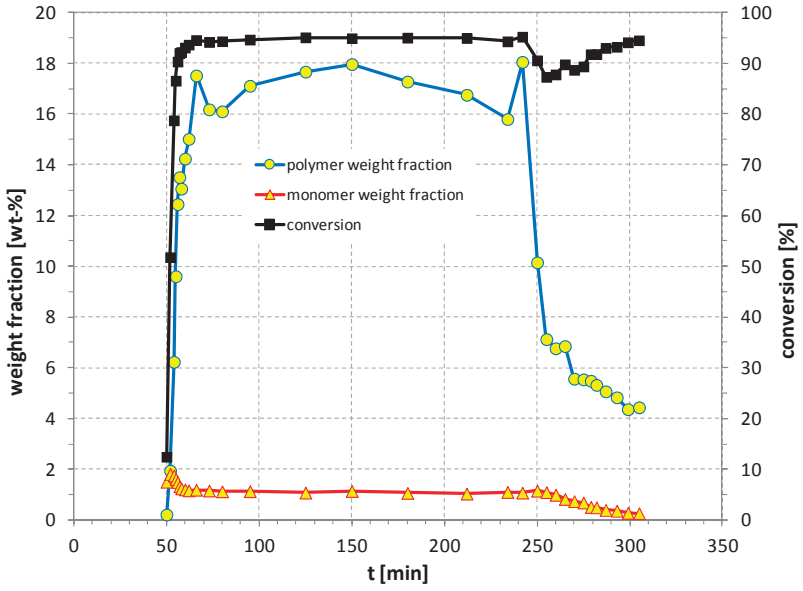

With the current reactor configuration, it was not possible to measure the temperature of the bulk fluid inside the flow reactor. In future work we are planning to reconfigure our equipment, so that the bulk fluid temperature can be measured at various points along the length of the tubular reactor. We are also planning further investigations looking at the residence time performance and fluid characteristics of the reactor, which might resolve the question why the flow reactor produced polymers with higher $Đ$ than the corresponding batch experiments.

4. Conclusions

We have successfully demonstrated the scale-up of aqueous RAFT polymerizations in a continuous flow reactor, using the monomers AAc and AMPS. The reactions were carried out on a 500 mL scale at 80 °C and concentration profiles at the outlet of the reactor were taken over time. The reactor produced high conversions in excess of 90% and the recorded temperature was stable at 80 °C throughout the entire duration of the experiments. In comparison, a series of batch reactions were conducted at different scales, ranging from 3 to 500 mL and in different reactor vessels; temperature profiles were taken during the course of the reactions. A strong dependence of temperature with scale was observed for these experiments, with the larger scales resulting in a higher temperature rise at the start of the reaction (up to 98 °C), as well as a longer overheating period. During this

overheating period more radicals are formed by the thermal initiator than in a system which is kept constant at 80 °C, resulting in a loss of control over the polymerization process. The SEC data confirmed these findings. The polymerization process is also simplified in the continuous flow reactor, where the premixed stock solution can be pumped into the reactor directly. In comparison, processing the same amount of material in a round bottom flask, requires a long heating up period first, where the monomer and solvent are brought up to temperature over one hour (which is 1.5 times longer than the reaction time), before the reaction is started by adding the initiator.

Acknowledgments

The authors thank Bradley Ladewig from Monash University and John Tsanaktsidis, Simon Saubern and San Thang from CSIRO for helpful discussions. Thank you to Bashir Harji from Cambridge Reactor Design Ltd. for technical support. The authors also wish to acknowledge the post-doctoral fellowship awarded to Julien Rosselgong by the CSIRO's Office-of-the-Chief Executive.

Conflicts of Interest

The authors declare no conflict of interest.

References

1. Chiefari, J.; Chong, Y.K.; Ercole, F.; Krstina, J.; Jeffery, J.; Le, T.P.T.; Mayadunne, R.T.A.; Meijs, G.F.; Moad, C.L.; Moad, G.; *et al*. Living free-radical polymerization by reversible addition—Fragmentation chain transfer: The RAFT process. *Macromolecules* **1998**, *31*, 5559–5562.
2. Moad, G.; Rizzardo, E.; Thang, S.H. Living radical polymerization by the RAFT process. *Aust. J. Chem.* **2005**, *58*, 379–410.
3. Moad, G.; Rizzardo, E.; Thang, S.H. Living radical polymerization by the RAFT process—A first update. *Aust. J. Chem.* **2006**, *59*, 669–692.
4. Moad, G.; Rizzardo, E.; Thang, S.H. Living radical polymerization by the RAFT process—A second update. *Aust. J. Chem.* **2009**, *62*, 1402–1472.
5. Moad, G.; Rizzardo, E.; Thang, S.H. Living radical polymerization by the RAFT process—A third update. *Aust. J. Chem.* **2012**, *65*, 985–1076.
6. Barner-Kowollik, C. *Handbook of RAFT Polymerization*; Wiley-VCH: Weinheim, Germany, 2008.
7. Hessel, V.; Renken, A.; Schouten, J.C.; Yoshida, J. *Micro Process Engineering: A Comprehensive Handbook, 3 Volume Set*; Wiley-VCH: Weinheim, Germany, 2009.
8. Hessel, V.; Hardt, S.; Löwe, H.; Müller, A.; Kolb, G. *Chemical Micro Process Engineering, 2 Volume Set*; Wiley-VCH: Weinheim, Germany, 2005.
9. Ehrfeld, W.; Hessel, V.; Löwe, H. *Microreactors: New Technology for Modern Chemistry*; Wiley-VCH Verlag GmbH: Weinheim, Germany, 2000.
10. Wirth, T. *Microreactors in Organic Synthesis and Catalysis*; Wiley-VCH: Weinheim, Germany, 2008.

11. Deal, M. Continuous Flow Chemistry in Medicinal Chemistry. In *RSC Drug Discovery*; Farrant, E., Ed.; Royal Society of Chemistry: Cambridge, UK, 2012; Chapter 5, pp. 90–125.
12. Fukuyama, T.; Ryu, I. Radical Chemistry by Using Flow Microreactor Technology. In *Encyclopedia of Radicals in Chemistry, Biology and Materials*; Chatgilialoglu, C., Studer, A., Eds.; John Wiley & Sons Inc.: Hoboken, NJ, USA, 2012; pp. 1243–1258.
13. Baxendale, I.R.; Hornung, C.; Ley, S.V.; de Mata Muñoz Molina, J.; Wikström, A. Flow microwave technology and microreactors in synthesis. *Aust. J. Chem.* **2013**, *66*, 131–144.
14. Mawatari, K.; Kazoe, Y.; Aota, A.; Tsukahara, T.; Sato, K.; Kitamori, T. Microflow systems for chemical synthesis and analysis: Approaches to full integration of chemical process. *J. Flow Chem.* **2012**, *1*, 3–12.
15. Wiles, C.; Watts, P. Continuous flow reactors: A perspective. *Green Chem.* **2012**, *14*, 38–54.
16. Hartman, R.L.; McMullen, J.P.; Jensen, K.F. Deciding whether to go with the flow: Evaluating the merits of flow reactors for synthesis. *Angew. Chem. Int. Ed.* **2011**, *50*, 7502–7519.
17. Oelgemöller, M.; Shvydkiv, O. Recent advances in microflow photochemistry. *Molecules* **2011**, *16*, 7522–7550.
18. Valera, F.E.; Quaranta, M.; Moran, A.; Blacker, J.; Armstrong, A.; Cabral, J.T.; Blackmond, D.G. The flow's the thing...or is it? Assessing the merits of homogeneous reactions in flask and flow. *Angew. Chem. Int. Ed.* **2010**, *49*, 2478–2485.
19. Ley, S.V.; Baxendale, I.R. The changing face of organic synthesis. *CHIMIA Int. J. Chem.* **2008**, *62*, 162–168.
20. Hessel, V.; Löb, P.; Löwe, H. Industrial and Real-life Applications of Micro-reactor Process Engineering for Fine and Functional Chemistry. In *New Development and Application in Chemical Reaction Engineering*; Proceedings of the 4th Asia-Pacific Chemical Reaction Engineering Symposium (APCRE '05), Gyeongju, Korea, 12–15 June 2005; Elsevier: Amsterdam, The Netherlands, 2006; Volume 159, pp. 35–46.
21. Seyler, H.; Haid, S.; Kwon, T.-H.; Jones, D.J.; Bäuerle, P.; Holmes, A.B.; Wong, W.W.H. Continuous flow synthesis of organic electronic materials—Case studies in methodology translation and scale-up. *Aust. J. Chem.* **2013**, *66*, 151–156.
22. Browne, D.L.; Wright, S.; Deadman, B.J.; Dunnage, S.; Baxendale, I.R.; Turner, R.M.; Ley, S.V. Continuous flow reaction monitoring using an on-line miniature mass spectrometer *Rapid Commun. Mass Spectrom.* **2012**, *26*, 1999–2010.
23. Hornung, C.H.; Hallmark, B.; Baumann, M.; Baxendale, I.R.; Ley, S.V.; Hester, P.; Clayton, P.; Mackley, M.R. Multiple microcapillary reactor for organic synthesis. *Ind. Eng. Chem. Res.* **2010**, *49*, 4576–4582.
24. Hornung, C.H.; Mackley, M.R.; Baxendale, I.R.; Ley, S.V. A microcapillary flow disc reactor for organic synthesis. *Org. Process Res. Dev.* **2007**, *11*, 399–405.
25. Van Rens, L.; van Dijk, H.; Mulder, J.; Nieuwland, P. Using a web application to conduct and investigate syntheses of methyl orange remotely. *J. Chem. Educ.* **2013**, *90*, 574–577.
26. McMullen, J.P.; Jensen, K.F. Rapid determination of reaction kinetics with an automated microfluidic system. *Org. Process Res. Dev.* **2011**, *15*, 398–407.

27. Serra, C.A.; Chang, Z. Microfluidic-assisted synthesis of polymer particles. *Chem. Eng. Technol.* **2008**, *31*, 1099–1115.
28. Iwasaki, T.; Yoshida, J.-I. Free radical polymerization in microreactors. Significant improvement in molecular weight distribution control. *Macromolecules* **2005**, *38*, 1159–1163.
29. Iwasaki, T.; Kawano, N.; Yoshida, J. Radical polymerization using microflow system: Numbering-up of microreactors and continuous operation. *Org. Process Res. Dev.* **2006**, *10*, 1126–1131.
30. Rosenfeld, C.; Serra, C.; Brochon, C.; Hadziioannou, G. High-temperature nitroxide-mediated radical polymerization in a continuous microtube reactor: Towards a better control of the polymerization reaction. *Chem. Eng. Sci.* **2007**, *62*, 5245–5250.
31. Wilms, D.; Klos, J.; Frey, H. Microstructured reactors for polymer synthesis: A renaissance of continuous flow processes for tailor-made macromolecules? *Macromol. Chem. Phys.* **2008**, *209*, 343–356.
32. Schork, F.J.; Guo, J. Continuous miniemulsion polymerization. *Macromol. React. Eng.* **2008**, *2*, 287–303.
33. Kessler, D.; Löwe, H.; Theato, P. Synthesis of defined poly(silsesquioxane)s: Fast polycondensation of trialkoxysilanes in a continuous-flow microreactor. *Macromol. Chem. Phys.* **2009**, *210*, 807–813.
34. Enright, T.E.; Cunningham, M.F.; Keoshkerian, B. Nitroxide-mediated bulk and miniemulsion polymerization in a continuous tubular reactor: Synthesis of homo-, di- and triblock copolymers. *Macromol. React. Eng.* **2010**, *4*, 186–196.
35. Nagaki, A.; Takahashi, Y.; Akahori, K.; Yoshida, J.-I. Living anionic polymerization of tert-butyl acrylate in a flow microreactor system and its applications to the synthesis of block copolymers. *Macromol. React. Eng.* **2012**, *6*, 467–472.
36. Vandenbergh, J.; de Moraes Ogawa, T.; Junkers, T. Precision synthesis of acrylate multiblock copolymers from consecutive microreactor RAFT polymerizations. *J. Polym. Sci. A* **2013**, *51*, 2366–2374.
37. Hornung, C.H.; Guerrero-Sanchez, C.; Brasholz, M.; Saubern, S.; Chiefari, J.; Moad, G.; Rizzardo, E.; Thang, S.H. Controlled RAFT polymerization in a continuous flow microreactor. *Org. Process Res. Dev.* **2011**, *15*, 593–601.
38. Hornung, C.H.; Postma, A.; Saubern, S.; Chiefari, J. A continuous flow process for the radical induced end group removal of RAFT polymers. *Macromol. React. Eng.* **2012**, *6*, 246–251.
39. Hornung, C.H.; Nguyen, X.; Dumsday, G.; Saubern, S. Integrated continuous processing and flow characterization of RAFT polymerization in tubular flow reactors. *Macromol. React. Eng.* **2012**, *6*, 458–466.
40. Hornung, C.H.; Nguyen, X.; Kyi, S.; Chiefari, J.; Saubern, S. Synthesis of RAFT block copolymers in a multi-stage continuous flow process inside a tubular reactor. *Aust. J. Chem.* **2013**, *66*, 192–198.
41. Chiefari, J.; Hornung, C.H.; Saubern, S. Continuous Flow Polymerisation Process. WO2012037596, 22 September 2010.

42. Chiefari, J.; Hornung, C.H.; Postma, A.; Saubern, S. RAFT Polymers. WO2013086585, 14 December 2011.
43. Wang, R.; McCormick, C.L.; Lowe, A.B. Synthesis and evaluation of new dicarboxylic acid functional trithiocarbonates: RAFT synthesis of telechelic poly(n-butyl Acrylate)s. *Macromolecules* **2011**, *38*, 9518–9525.
44. Biotage. Available online: http://www.biotage.com/ (accessed on 7 November 2013).
45. Cambridge Reactor Design Ltd. Available online: http://www.cambridgereactordesign.com/ (accessed on 7 November 2013).
46. Saldivar-Guerra, E.; Vivaldo-Lima, E. *Handbook of Polymer Synthesis, Characterisation and Processing*; John Wiley & Sons, Inc.: Hoboken, NJ, USA, 2013.

Microreactor-Assisted Solution Deposition for Compound Semiconductor Thin Films

Chang-Ho Choi, Brian K. Paul and Chih-Hung Chang

Abstract: State-of-the-art techniques for the fabrication of compound semiconductors are mostly vacuum-based physical vapor or chemical vapor deposition processes. These vacuum-based techniques typically operate at high temperatures and normally require higher capital costs. Solution-based techniques offer opportunities to fabricate compound semiconductors at lower temperatures and lower capital costs. Among many solution-based deposition processes, chemical bath deposition is an attractive technique for depositing semiconductor films, owing to its low temperature, low cost and large area deposition capability. Chemical bath deposition processes are mainly performed using batch reactors, where all reactants are fed into the reactor simultaneously and products are removed after the processing is finished. Consequently, reaction selectivity is difficult, which can lead to unwanted secondary reactions. Microreactor-assisted solution deposition processes can overcome this limitation by producing short-life molecular intermediates used for heterogeneous thin film synthesis and quenching the reaction prior to homogeneous reactions. In this paper, we present progress in the synthesis and deposition of semiconductor thin films with a focus on CdS using microreactor-assisted solution deposition and provide an overview of its prospect for scale-up.

Reprinted from *Processes*. Cite as: Choi, C.-H.; Paul, B.K.; Chang, C.-H. Microreactor-Assisted Solution Deposition for Compound Semiconductor Thin Films. *Processes* **2014**, *2*, 441-465.

1. Introduction

Compound semiconductors play an important role for generating, emitting and manipulating energy. State-of-the-art techniques for the fabrication of compound semiconductors are mostly vacuum-based physical vapor or chemical vapor deposition (CVD) processes. These vacuum-based techniques typically operate at high temperatures and normally require higher capital costs. Solution-based techniques offer opportunities to fabricate compound semiconductors at lower temperatures and lower capital costs. Other additional advantages of the solution-phase routes are the availability of large resources of synthetic strategies and the compatibility with soft organic materials. A variety of solution-based techniques, including electrodeposition, successive ionic-layer adsorption and reaction, spray pyrolysis and chemical bath deposition (CBD) have been developed for the fabrication of compound semiconductors [1–3]. Among these, CBD is an attractive technique owing to its low temperature, low cost and large area deposition capability [4,5]. Many semiconductor thin films have been successfully deposited using this technique, and it has already been proven to be a very useful method for fabricating large area devices, such as high efficiency $CuInSe_2$ and CdTe solar cells. CBD processes are mainly performed using batch reactors, where all reactants are fed into the reactor and products are removed after the processing is finished. These batch

processes can suffer from slow heat and mass transfer, which can result in large temperature, concentration and solution pH gradients. Microreactor-assisted nanomaterial deposition (MAND) processes can overcome some of the limitations of conventional batch processes and lead to large-scale manufacturing of uniform nanomaterials and nanostructured thin films [6–9]. MAND processes provide the solution-phase nanomaterial synthesis, purification, functionalization and deposition with the use of microreaction technology. The MAND process allows the control of reactants ranging from small molecules, macromolecules to nanoclusters, nanoparticles and assemblies of nanoparticles. To date, two MAND strategies have been reported: microreactor-assisted solution deposition (MASD) and microreactor-assisted nanoparticle deposition (MANpD). The MASD process is able to produce reactive fluxes of short-life, intermediate molecules for heterogeneous growth on a temperature-controlled substrate. Alternatively, the MANpD process utilizes nanoparticles or nanoparticle assemblies for the fabrication of nanostructured surfaces with various morphologies.

2. Chemical Bath Deposition (CBD)

Chemical bath deposition (CBD), also known as chemical solution deposition, has been known for more than a hundred years. This process can be easily implemented by immersing a substrate into a beaker, filled with an aqueous solution of chemical precursors, sitting on top of a hot plate (Figure 1a). Usually carried out as a batch process, CBD has received a great deal of attention, due to its low temperature and low cost nature. It has been used for the deposition of buffer layers in both CdTe and Cu(In,Ga)Se_2-based photovoltaics. Historically, the first application of CBD was the fabrication of lead sulfide photoconductive detectors in 1884 by James Emerson-Reynolds [10]. CBD is an aqueous analogue of CVD. The constituent ions are dissolved in a water solution, and the thin films are produced through a heterogeneous surface reaction. Many compound semiconductors, including II-VI, IV-VI, V-VI, and I-III-VI material systems, have been successfully fabricated by CBD processes [4].

Figure 1. (**a**) Scheme of a typical batch chemical bath deposition (CBD) process; and (**b**) photograph of a CdS-coated beaker wall.

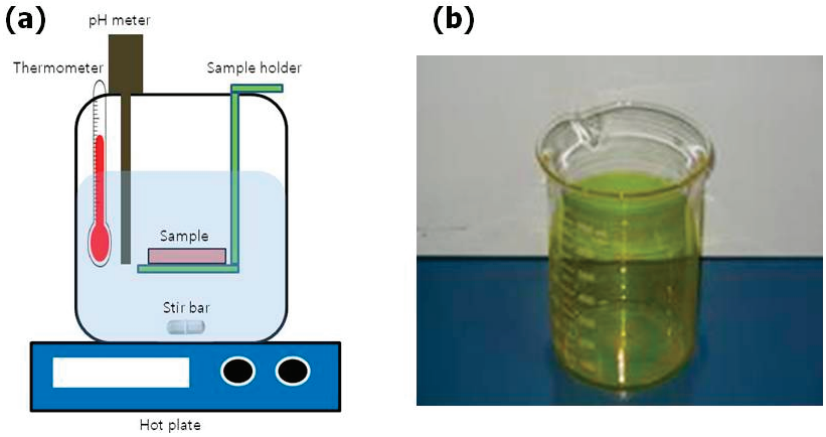

A typical growth curve of CBD measured by using quartz crystal microbalance (QCM) is shown in Figure 2 [11]. Four regimes can be identified from the QCM curve. The first one is an induction

regime, where the reaction rate is slow and no clear deposition is observed. This regime corresponds to short reaction times and is marked by the beginning of nucleation. The second one is the compact layer growth regime through the molecular heterogeneous surface reactions. High quality and tightly adhering film is grown in this regime. When the growth process begins, it is characterized by a linear variation, and any minute deviation in this process can be attributed to a coalescence period. The third one is the porous layer growth regime. When the reaction time gradually increases, a clear increase in the growth rate can be observed, which corresponds to the growth of a porous layer. The appearance of this porous layer is due to the colloidal settling and sticking on the substrate created by homogeneous particle formation. However, this layer, unlike those compact layers, is weakly bonded to the substrate surface and, hence, can be removed easily, either by sonication using an ultrasonic bath or mechanical rubbing. After this, the growth rate will reach saturation and eventually stop due to the limited reagent concentration. A key issue of the batch CBD process is its difficulty in controlling the rate of the reaction once it starts. The compound is deposited from a super-saturated solution continuously everywhere in the solution, including the container wall. Figure 1b shows a CdS-coated beaker after performing a CBD growth experiment. The homogeneous reaction in which nanoparticles form in the solution result in a lower yield of reactant conversion to film, which is a significant problem of the batch CBD process. The depletion of reactants from the homogeneous particle formation would also limit the achievable terminal thickness by batch CBD processes. One remedy to slow down the homogeneous precipitation in the batch CBD process is to add complexing agents or a buffer reagent, which will also slow down the surface deposition reaction.

Figure 2. A typical growth curve and the growth mechanism of film prepared by a CBD process.

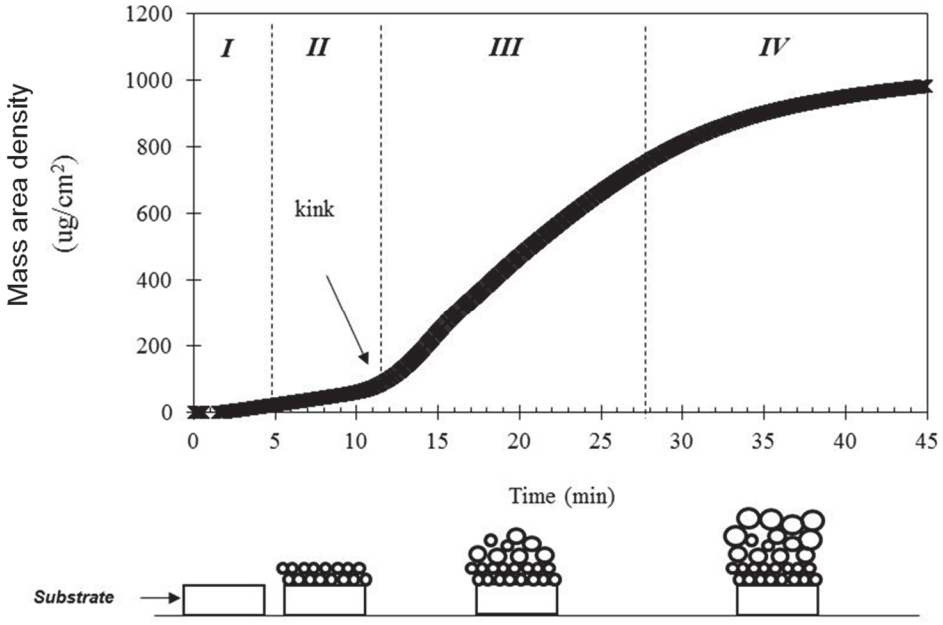

3. Microreactor-Assisted Solution Deposition (MASD)

MASD processes were first developed with the intent to de-couple the homogeneous particle formation and deposition from the molecular level heterogeneous surface reaction [12]. The MASD

system has the capability to selectively produce intermediate, short-life molecules that are essential for the heterogeneous surface reaction on substrates, while avoiding the homogeneous particle formation reaction. This capability provides a better control of film growth and enhances the conversion of reactants into desired products (thin films). Many compound semiconductor thin films, including CdS, ZnS, CdTe, Cu_xSe, $CuInS_2$, $CuInSe_2$ and ZnO, have been fabricated by MASD [13–17].

The MASD process was used to fabricate the $CuInS_2$ film on glass substrates by Park *et al.* [16]. Copper indium disulfide ($CuInS_2$) is one of the most promising ternary chalcopyrite materials, as an absorber in thin film solar cells, due to its direct band gap value (1.3–1.5 eV) [18–20]. For the deposition of the ternary $CuInS_2$ compound, indium solution was first coated on the temperature-controlled substrate to form an indium precursor layer, and subsequently, a homogeneous mixture of copper and sulfur precursor solution from a micromixer was delivered onto the indium precursor-coated substrate. As-deposited $CuInS_2$ film was annealed at 200 °C for 1h in a vacuum furnace to generate a dense, crystalline thin film. It was found that the control of the thiourea concentration is critical in obtaining a single-phase $CuInS_2$ film. The molar concentration of thiourea also affects the morphology of $CuInS_2$ film. Polycrystalline $CuInSe_2$ film was deposited using the MASD process by Kim *et al*. [17]. It was found that the crystallinity of the film was affected by the composition of indium. Their work demonstrated the feasibility of fabricating smooth $CuInSe_2$ films with a large grain size, which is promising in solar cell applications.

ZnO, a transparent, wide bandgap semiconductor material, is one of the most studied materials among various metal oxides, because of the wide variety of nanostructure shapes, easier crystal growth and earth abundance [21–23].

McPeak *et al.* implemented the chemical bath deposition using a micro-flow cell to fabricate well-aligned ZnO nanowire arrays [24]. They employed the spatial resolution of the microreactor to allow direct correlation of nanowire properties to process conditions. The results reveal that the lengths of nanowire decreased along the length of the flow cell, due to the depletion of precursors, morphology change from pyramidal tops to flat tops and the transition of growth mechanism from two-dimensional nuclei to spiral growth, as shown in Figure 3.

Han *et al.* reported the deposition of biomimetic nanostructured ZnO films using the MASD process, exhibiting anti-reflection on textured pyramidal silicon surfaces [25]. The pyramidal silicon substrate was prepared by a wet chemical etching process. Ag nanoparticles (Ag NPs) were separately synthesized in a solution-based process and deposited on the pyramidal silicon substrate as the seed layer for the uniform deposition of ZnO nanostructures. Ag NPs also provided the nucleation sites for the initial formation of ZnO nanostructures, leading to the well-aligned orientation of the nanostructures. ZnO nanorods with a length of 400 to 500 nm were densely grown onto the Ag NP-coated pyramidal silicon substrate. Dense and uniform nanostructures are attributed to the heterogeneous surface reaction that is available by controlling the residence time, reaction temperature and precursor concentration in the MASD process. The deposition rate of nanostructures was measured to be around 125 $nm \cdot min^{-1}$, which is highly efficient in comparison to the conventional hydrothermal reaction. The comparison of reflectance measurement reveals that the reflectance is significantly reduced as ZnO nanostructures are deposited onto the pyramidal silicon surface.

Figure 3. Cross-sectional SEM images of ZnO nanowires prepared at flow rates of 0.72 mL/h (**top row**); and 2.88 mL/h (**bottom row**) with an equimolar inlet concentration of zinc nitrate and Hexamethylenetetramine (HMT) Dimensions in each panel present the position where images were taken downstream from the inlet. The scale bar applies to all image. Reproduced from [24].

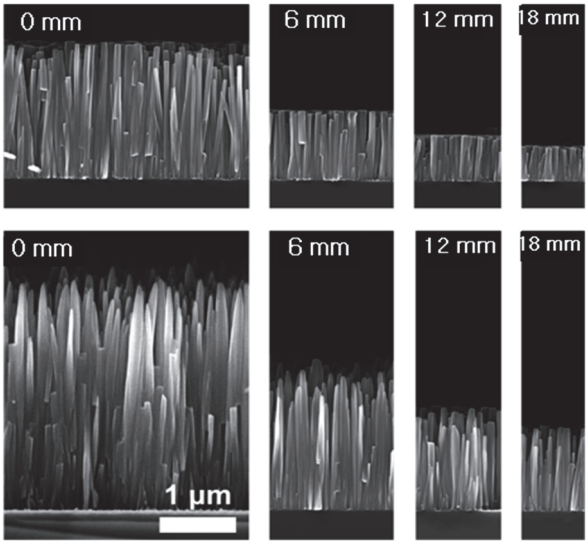

In the following section, investigations of CdS thin films prepared by the MASD system are discussed in detail to illustrate its underlying principles and benefits.

Cadmium sulfide (CdS) is an important II-VI semiconductor that is finding applications in thin film transistor, photodetector and thin film solar cells [26–28]. CdS is being used to create the p/n junctions in $Cu(In,Ga)Se_2$ and CdTe thin film solar cells. Among various synthetic approaches, chemical bath deposition (CBD) is a commonly used technique for the fabrication of CdS film, due to its simple manufacturing and large area fabrication.

The MASD technique was first reported by Chang *et al.* to deposit CdS thin film for the fabrication of thin film transistors at low temperature [6,12]. The reported MASD process, illustrated in Figure 4, consisted of a micromixer, a digital pump, a heat exchanger and a hot plate. Solution 1 (a mixture of $CdCl_2$, NH_4Cl and NH_4OH) and Solution 2 ($SC(NH_2)_2$) are introduced into the mixing element and countercurrently enter the interdigital channels (30 µm), where they are spilt into many interpenetrated substreams. The substreams exit the interdigital channel perpendicular to the direction of the feed flows, initially with a multilayered structure. Rapid mixing through diffusion follows, due to the small thickness of the individual layer. The solution mixture of 1 and 2 pass a heat exchanger that supplies the constant reaction temperature and then are delivered onto the preheated substrate. This reactor provides the advantage of introducing constant flux of reactant solutions to the system (continuous process), which allows control over the homogeneous reaction of the chemical bath solution before the solution is delivered onto the substrate. This reactor successfully generated a reactant flux that is particle free by controlling the residence time. Using this particle-free flux, the authors were able to promote the molecule-by-molecule heterogeneous growth mechanism and prevent particle-by-particle growth [6]. Enhancement-mode CdS metal insulator semiconductor field-effect transistors (MISFETs) (Figure 5) was fabricated using this reactor

at low temperature (80–90 °C) without any post-deposition annealing. An effective mobility, $\mu_{eff} \approx$ 1.46 cm^2/V-sec, and a field-effect mobility, $\mu_{FE} \approx$ 1.4 cm^2/V-sec, were obtained from this device [12]. Arreola-Jardon *et al.* reported that the as-deposited CdS-based thin film transistors fabricated from batch CBD show a field effect mobility in the range of 0.12–0.16 cm^2/V-sec [27].

Figure 4. Scheme of the microreactor-assisted solution deposition (MASD) technique for CdS film deposition. Reproduced from [6].

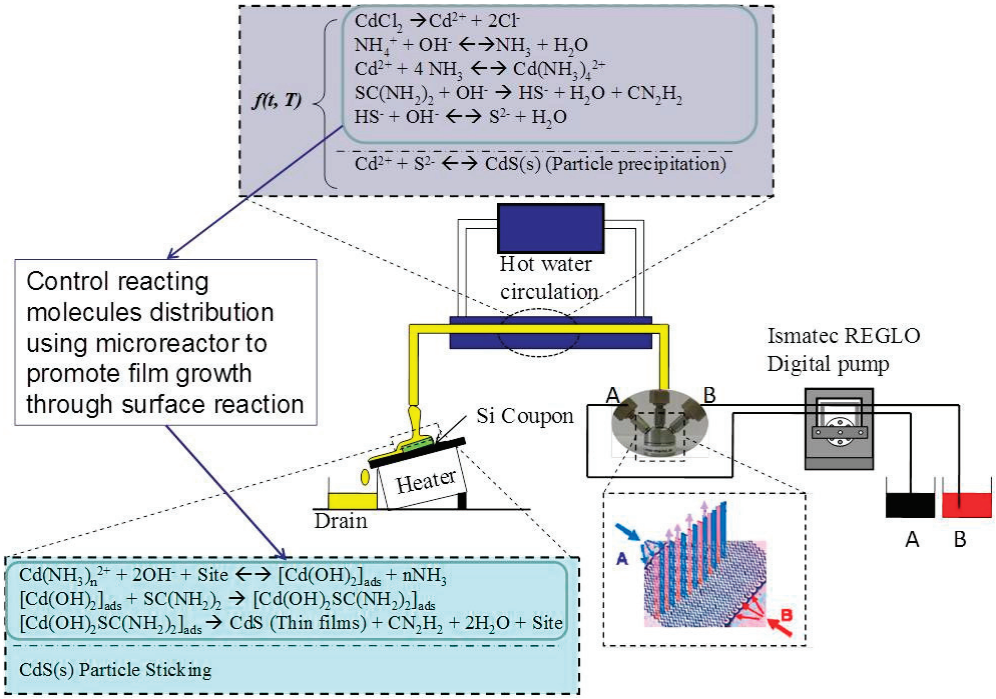

Figure 5. Structure, device performance and output characteristic curves of CdS metal insulator semiconductor field-effect transistors (MISFETs). Reproduced from [12].

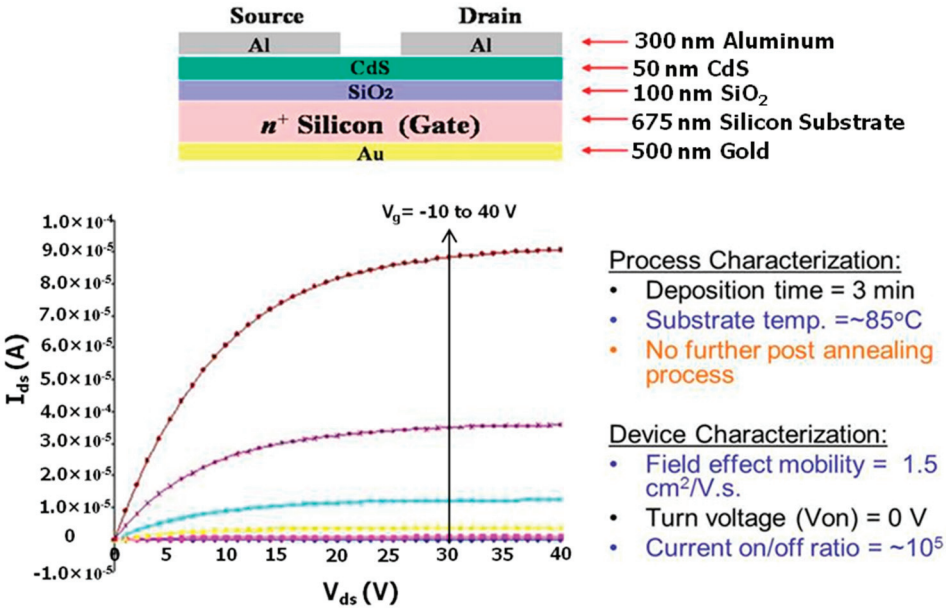

A comparison study of CdS thin film deposition by the MASD technique with the batch CBD was performed and reported by Mugdur *et al.* [29]. Having the same starting precursor concentration, reaction temperature and deposition time as the CBD, the CdS deposition by the MASD technique was carried out. AFM analysis of CdS film prepared by the MASD technique was compared with that prepared by the CBD (Figure 6a,b). Dense and continuous film was obtained by the MASD technique, whereas discontinuous film was obtained by the CBD with the same deposition time. The RMS value of the roughness of the film by the MASD technique is 11.75 nm with a mean roughness of 9.61 nm. In contrast, the RMS value of film roughness by the batch CBD technique is 19.592 nm with a mean roughness of 15.795 nm. Two diffractogram peaks are shown in the XRD spectrum, corresponding to the (111) and (222) planes, respectively, from the cubic (zinc blends) phase (Figure 6c). It is indicated that the film is strongly oriented along (111) with another small peak at (222) orientation. The presence of only (111) and (222) peaks indicates the highly oriented nature of CdS films deposited by MASD, which must grow as successive alternative planes composed of only either Cd or S atoms parallel to the substrate surface, as this corresponds to the (111) planes of the cubic crystalline structure. This type of growth is in good agreement with the molecular-level growth mechanism. In contrast, Figure 6d shows a relatively broad XRD peak from the as-deposited CdS thin films by a batch CBD process that indicates its lower crystallinity. Figure 7 shows a cross-sectional SEM image of a dense CdS thin film with a thickness of around 500 nm deposited by MASD. The terminal thickness of the batch CBD CdS is normally limited, due to the depletion of reactants. Thus, multiple depositions are required to deposit thicker and high quality CdS films by batch CBD. Previous results indicated that for CBD CdS deposition, small particles were forming and growing even at the beginning of the deposition process, as supported by real-time dynamic light scattering measurements and TEM characterization. We have observed a similar result using MASD (Figure 8) [6]. Experiments were carried out by pre-heating the precursor solutions (stream A and B) at 80 °C. At this temperature, thiourea releases more sulfide ions through hydrolysis. Free sulfide ions react with free cadmium ions to form CdS particles at these operation conditions. In order to obtain a solution without the homogeneous particle formation, the source chemicals have to be maintained at room temperature before they enter the micromixer. The mixed reactants are then maintained at 80 °C using heat exchanging fluid from a constant temperature circulator. TEM samples were obtained by collecting drops of hot solution from the Polyether ether ketone (PEEK) tube on the lacey carbon-coated TEM copper grid. TEM images (Figure 8d) indicate that at very short residence times (e.g., 1 s), there was no evidence of particle formation on the surface of the grid under these processing conditions.

Figure 6. Comparison study of CdS film grown by the MASD with CBD: AFM image of the film by (**a**) the MASD and (**b**) the CBD, respectively; the XRD spectrum of the film by (**c**) the MASD and (**d**) the CBD, respectively. Reproduced from [29].

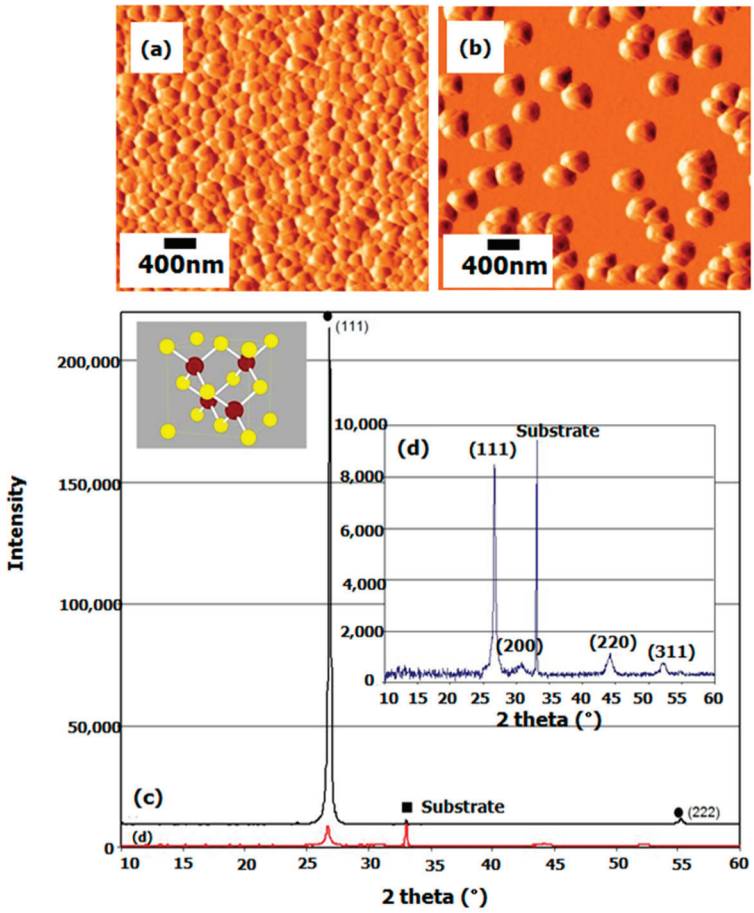

Figure 7. Cross-sectional SEM image of the CdS film grown by the MASD.

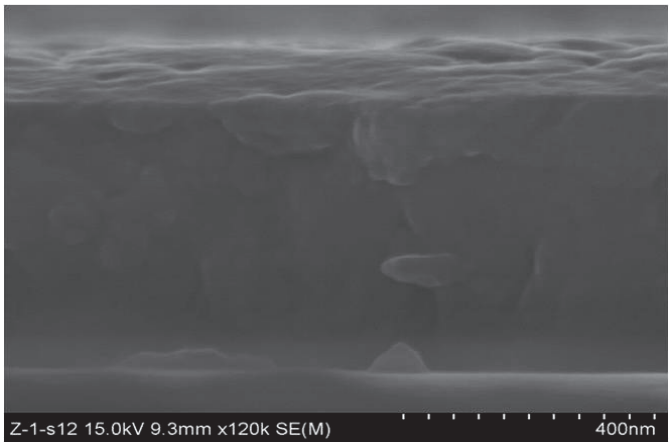

Figure 8. TEM image of CdS nanoparticles generated from the continuous flow microreactor with a residence time of (**a**) 1, (**b**) 3.5 and (**c**) 70 s by preheating the precursor solutions and with a residence time of (**d**) 1 s for the precursor at room temperature. Reproduced from [6].

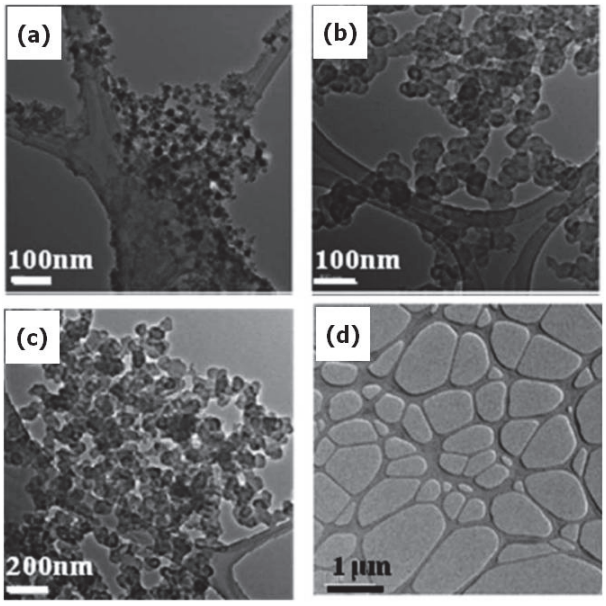

Using a particle-free flux study of the CdS deposition kinetics via the heterogeneous surface reaction by a molecule-by-molecule growth mechanism could be realized. A series of CdS thin film deposition experiments at different residence times (1, 3.5, 7, 35 and 70 s) were performed. The film thickness was determined by a surface profiler (Veeco, Plainview, NY, USA, 3D Dektak 8). Figure 9a shows the deposited CdS thin film thickness *versus* the deposition time at different residence times. The fitted linear regression lines were also plotted to obtain growth rate values. These growth rate results in Figure 9b clearly indicate that a lower CdS thin film growth rate was obtained (~77 Å/min) when a 1-s residence time was used. The growth rate increases significantly (about four times higher) when a 3.5-s residence time was used compared to a 1-s time. The thin film growth rate increases gradually from a 3.5-s to a 35-s residence time. However, when a 70-s residence time was used, the growth rate decreased. These results clearly demonstrate the capability of MASD to control the reaction kinetics of chemical solution deposition beyond the batch process. In addition, these results also demonstrate the utility of MASD as a valuable tool to investigate the chemical solution deposition processes. The pioneering studies by Ortega-Borges and Lincot and Doña and Herrero suggest that thiourea reacts with either cadmium hydroxide or dihydroxo-diammino-cadmium complex to form different adsorbed metastable complexes for CBD CdS deposition [5,30]. The proposed molecular-level heterogeneous reaction mechanism is given in Equations (1) to (3).

$$Cd(NH_3)_4^{2+} + 2OH^- + site \underset{k_{-1}}{\overset{k_1}{\rightleftharpoons}} Cd(OH)_{2\ ads} + 4NH_3 \quad (1)$$

$$Cd(OH)_{2\ ads} + SC(NH_2)_2 \xrightarrow{k_2} \{Cd[SC(NH_2)_2](OH)_2\}_{ads} \quad (2)$$

$$\{Cd[SC(NH_2)_2](OH)_2\}_{ads} \xrightarrow{k_3} CdS + CN_2H_2 + 2H_2O + site \quad (3)$$

The CdS growth rates should be proportional to the concentration of thiourea, according to this reaction mechanism. The initial thiourea concentrations are the same for all of the MASD experiments. The thiourea concentration should decrease as a function of residence time, due to the hydrolysis Reaction 4:

$$SC(NH_2)_2 + OH^- \longrightarrow HS^{-1} + CN_2H_2 + 2H_2O \quad (4)$$

One would expect a slight reduction of the deposition rate at a longer residence time. The observed results suggest that the dominant reacting sulfur molecule that is responsible for CdS thin film deposition is not thiourea, but HS^-. At the short residence time of 1 s, the concentration of sulfide ions formed through the thiourea hydrolysis reactions and is lower than the concentration of sulfide ions at a longer residence time, thus resulting in a lower growth rate of CdS thin film. Between 35 and 70 s of residence time, nanoparticles start to form in the solution and to reduce the reacting molecular species. The proposed reaction mechanism is illustrated in Figure 10 [31].

Figure 9. Fabrication of CdS thin film using MASD process: (**a**) CdS thin film thickness *versus* deposition time and (**b**) growth rate as a function of different residence times. Reproduced from [6].

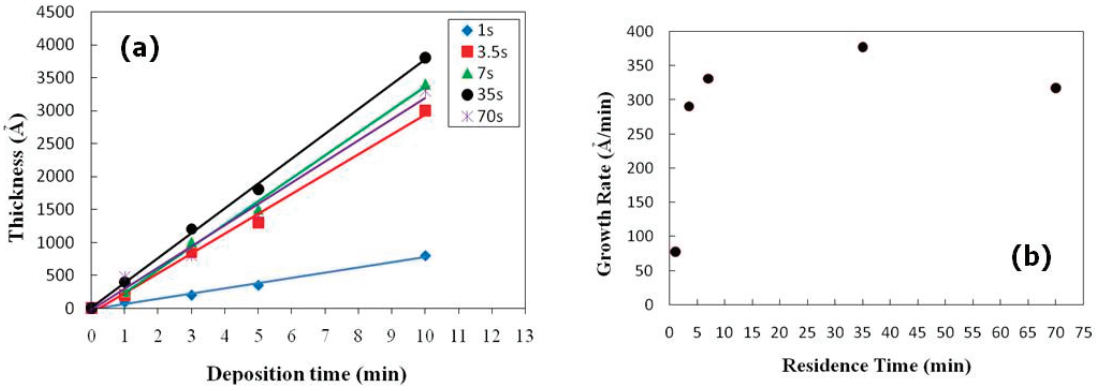

Figure 10. Growth mechanism of CdS thin film in the batch CBD process.

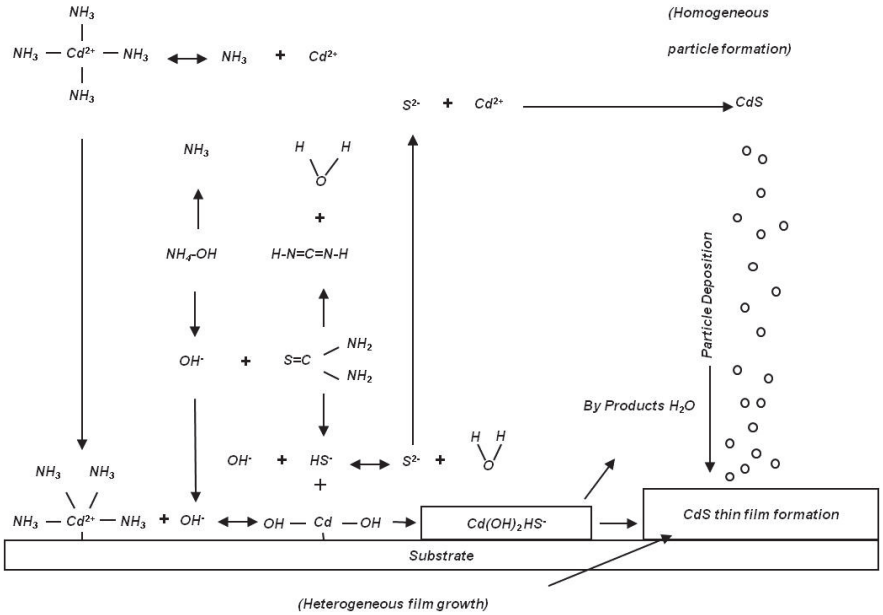

In a conventional batch CBD process, the heat needed for chemical reaction is supplied from the solution bath to the sample surface, resulting in both heterogeneous CdS nucleation at the surface, as well as homogeneous CdS formation in the bath. Hence, for baths involving a thermal jacket (glass beaker, *etc.*) or water bath, significant CdS deposition also occurs on the walls of the vessels. A significant amount of chemical precursors were converted into the formation of CdS particles in the solution. Normally, the bath was stirred continuously to ensure uniform thermal and chemical mixing and to minimize the sticking of CdS particles to the growing film surface. Moreover, the unequal volumes of the bath used to form the desired CdS film generates a lot of waste and creates defects in devices. Several groups of researchers have found ways to increase the precursor conversion yield [32]. Boyle *et al.* reported a modified CBD process that incorporate a filtration unit with the potential for continuous reaction by replenishment, treatment and purification of reagents within a recirculating closed-loop CBD reactor [33]. Nair *et al.* reported a technique to improve thin-film yield in the chemical bath deposition of semiconductor thin films [32]. The concept is to use a very small substrate separation, 0.1 mm, to eliminate the passive layer of the bath, which contributes solely to precipitation. In small substrate separation, a thin layer of the bath mixture is held by surface tension between pairs of substrates. The thin-film yield obtained in their work approaches 100% for CuS, $Cu_{2-x}Se$, CdS and CdSe thin films. The final thickness estimated for the films is about 40–50 nm after a deposition time of 6 to 16 h. The combination of MASD with these innovative approaches should result in achieving an optimum film quality, growth rate and precursor by controlling the reacting chemical flux, the bath-to-surface volume and reaction temperatures.

4. Scale-Up of MASD Processes

To achieve reasonable volumetric flows, microchannel components are scaled-up by numbering-up *i.e.*, scaling-up by repeating microchannel unit operations in parallel to increase the cross-section of flow [34,35]. Numbering-up may be accomplished either internally or externally [36]. Internal numbering-up involves arraying an original microchannel as an array of parallel microchannels within a single reactor component. An internal flow distribution system must be designed and implemented as part of the component to ensure equivalent reaction conditions in each channel. However, when scaling-up a process, the size of a single reactor component can be limited by either the size of the raw material available or the size of the work envelope for the fabrication processes used to produce the component [35]. Consequently, external numbering-up can be used to scale-up the process further by putting a number of reactor components in parallel, allowing the original flow to be split evenly between the components. External numbering-up has the advantage that clogged components can be replaced without throwing away the remaining reaction capacity. However, external numbering-up can suffer from poor flow distribution between components and is logistically more difficult and expensive to implement.

Theoretically, the scale-up of microreactors is made easier by maintaining equivalent thermal, chemical and temporal reaction conditions within an array of microchannel unit operations. However, maintaining equivalent reaction conditions through channels of varying sizes and between components having different dimensions can be difficult, due to the effect on flow conditions. Saber *et al.* investigated the effects of flow maldistribution on microreactor performance and found that for mass

transfer-limited reactions, flow maldistribution had a more pronounced negative effect on reaction selectivity than for kinetic-limited reactions [37]. Further, the researchers distinguished flow maldistribution due to poor manifolding during external numbering-up from that due to internal clogging. Internal clogging was found to have little effect on flow distribution, yet a relatively larger effect on the sensitivity of the reaction selectivity, due to reasons other than hydrodynamic effects. Tonomura *et al.* performed numerical and experimental studies showing that pressure drop control is superior to total flow control for managing internal blockage between externally numbered-up components [38]. The team validated these findings by implementing pressure drop control across four parallelized microchannel heat exchangers.

However, external numbering-up can be expensive, due to the amount of process control equipment required for each added device. Efforts have been made to simplify external numbering-up through the use of flow splitters that efficiently distribute a single flow into several uniform subflows, reducing the number of pumps [36,39]. Kashid *et al.* demonstrated the external numbering-up of a two-phase capillary reactor using two six-channel polytetrafluoroethylene (PTFE) flow distributors (one for gas and one for liquid), six Y-shaped mixing elements and six glass capillaries [40]. Though no reactions were conducted, the mass transfer characteristics for the six channel unit were found to track with those of a single capillary.

The technical literature provides various demonstrations for scaling the production of various chemistries using microchannel reactor technology. Iwasaki *et al.* demonstrated six days of operation of a microchemical pilot plant consisting of a static T-micromixer followed by eight microtube reactors in a tube-and-shell arrangement for the numbering-up of a radical polymerization reaction [41]. Results showed that at eight-fold the flow rate, a similar yield, molecular weight and molecular weight distribution were produced in the numbered-up reactor compared to the single microtube reactor. Deshmukh *et al.* demonstrated the ability to scale-up the Fischer–Tropsch synthesis of synthetic fuels from a single microchannel to 276 parallel process microchannels at a production rate of 1.5 gallons per day [42]. The process was found to provide equivalent outcomes, including syngas conversion and selectivity to a byproduct, across three orders of magnitude. Mae *et al.* (2004) introduced two types of splitting and recombination micromixers that enabled the rapid aqueous extraction of phenol from dodecane within one second under a flow rate of 5–20 liters per hour [43]. Kockmann *et al.* demonstrated the numbering-up of a two-step organo-metallic reaction operated at two temperature levels [44]. The final reactor contained 1 mm in diameter mixing channels and supported overall production rates of 700 grams per minute, leading to the production of more than two tons of isolated material. Bally *et al.* discussed the design of a 2000 metric tons per year pilot plant with 28 interdigitated micromixers to mix the inlet flow of four tubular reactors to avoid precipitation in homogeneous polymerization reactions, which formed the basis of a patent [45,46]. Many additional examples of microreactor pilot plants for organic syntheses are provided by Wirth [47]. Fox *et al.* describe a numbered-up pulsed electric field reactor design for use in pasteurization [48].

CBD is relatively easy to scale-up across large surfaces. However, as a batch process, CBD can offer low material utilization for chemistries involving competing reactions. MASD techniques are capable of providing the reaction selectivity and a short-life, intermediate chemistry unattainable in

CBD. Other benefits include reduced energy requirements and processing times for long synthesis reactions and characteristically small reaction volumes, which can reduce human exposure to hazardous chemistries. The benefits of using microchannel reactors are primarily realized in diffusion-limited processes. An estimate for the mean time needed for molecules to diffuse in mass transfer is to the square of the channel radius over the diffusivity coefficient of the chemistry. Therefore, a tenfold reduction in tube diameter results in a one hundred-fold reduction in the residence time. The accelerated heat and mass transfer provides better process control, while reducing the size and weight of reactors. For diffusion-limited reactions, the use of microchannel components reduces the size and weight of the reactor apparatus, making implementation of MASD easier. Through the use of microchannel reactor components, temporal control of the chemistry enables the reactant stream to be introduced to the reaction surface at the peak of its reaction potential. Conceptually, a continuous flow MASD reactor for producing thin films from reactive chemistry will include a micromixer, a heat exchanger, a residence time unit and a flow cell for controlling deposition onto a substrate (see Figure 11). A scale-up study of MASD using a flow cell was reported by Paul *et al.* [9,49,50].

Figure 11. A typical MASD setup. Reproduced from [49].

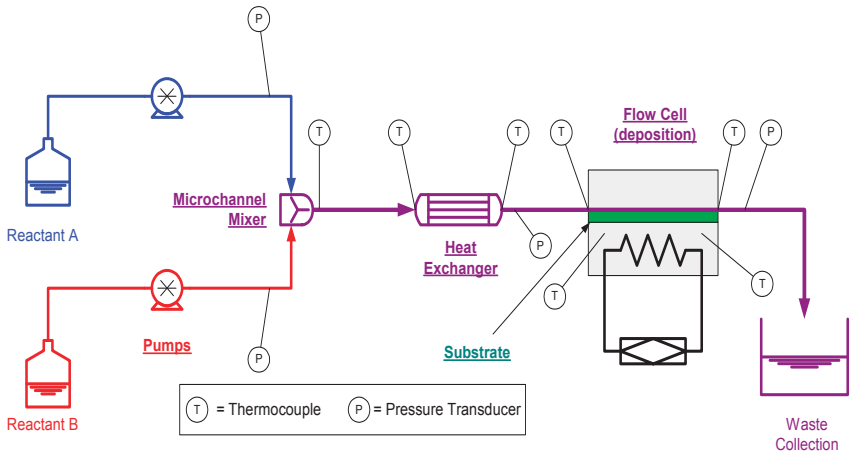

While the numbering-up of pilot plants have been demonstrated for many chemistries, a key to enabling MASD is the use of small, lightweight reactors capable of providing the distributed production of solution chemistries. The size and weight of microchannel reactors was envisioned early in the development of microreactor technology for enabling the distributed production of chemical products [51]. A key component of MASD is a micromixer. Micromixers offer features that cannot be easily achieved by macroscopic devices, such as ultrafast mixing on the microscale. For example, Bökenkamp *et al.* fabricated a micromixer as a quench-flow reactor to study fast reactions (millisecond time resolution) [52]. A variety of micromixers have been reported in the literature, including static and dynamic mixers [53,54]. A simple T-mixer was used in the 6" MASD system reported by Paul *et al.* [48]. T-mixers are relatively cheap and simple to fabricate; however, they might face a limitation to further scaling up. Other micromixers, such as oscillatory flow mixers and interdigital micromixers, could be used for the higher flow requirement. Oscillatory flow mixers fall into two categories. Pressure-driven oscillatory mixers have been shown to be capable of sustaining

the largest production rates of nanoparticle chemistries reported to date, while piezo-driven ones, being compact and precise, have not been shown to provide adequate production rates [55,56]. Interdigital micromixers seem to provide the smallest format at a reasonable production volume. In the case of numbering-up the synthesis of phosphine-stabilized undecagold nanoclusters, Jin *et al.* used an interdigital micromixer to demonstrate a production rate 500 times greater and a yield over 3.5 times higher than that of a conventional batch process [57]. To demonstrate the ability to internally number-up the reaction, the number of plates in the mixer was doubled (double the flow cross-section) and the overall flow rate was quintupled, leading to a five-fold increase in the production rate to 7.1 kg per week, while maintaining a constant material conversion rate. The largest micromixer used was just under 1.7 cm^3 in volume.

Ramprasad *et al.* developed an adjustable residence time heat exchanger, suitable for MASD, comprised of two sections integrated in a single device; a rapid heating zone (HZ) and an adjustable residence time (RT) section, as shown in Figure 12 [9]. The heat exchanger is a composite unit consisting of copper plates at the top and bottom, to seal the polycarbonate channels, which are interposed between silicone gaskets. Copper was chosen because of its high thermal conductivity. An ESI (Portland, OR, USA) Laser 5330 was used for machining of the micro-channels in polycarbonate and silicone. This entire unit was bolted together to provide a leak-proof system. The HZ is the initial section of the polycarbonate channel in which the mixed reagents enter at room temperature and are heated to the set-point temperature in roughly one second. The hot fluid exiting from the heating zone enters the RT unit of the heat exchanger. The function of the RT unit is to maintain the fluid at the HZ exit temperature, while providing the specific additional residence time of the hot fluid before deposition onto the substrate (Figure 13). The residence time in the heat exchanger is contingent on the number of polycarbonate plates in the heat exchanger assembly. The heat exchanger is designed such that the first polycarbonate plate is an integrated device consisting of both the HZ and the RT unit. This integrated unit of the HZ and RT polycarbonate plate is sandwiched between two silicone gaskets. However, the option of exclusively augmenting only the polycarbonate RT plates may be utilized to achieve the desired higher residence time. The schematic of the residence time configuration is shown in Figure 11. Two silicone strip heaters are overlaid onto the RT units both on the top and bottom to provide sufficient heat to maintain the fluid at the desired temperature. A total of four ceramic heaters were used, with two heaters on each face of the HZ section.

A key challenge for scaling up MASD is the requirement for film uniformity over large substrates, which requires that reaction conditions are uniform over the target substrate. Surface reaction kinetics are highly dependent on the reactant concentration and temperature at the reactive surface. In the case of reactants supplied as a continuously flowing fluid, the velocity at which the fluid travels determines the residence time over which the reactants have access to the deposition surface. For large substrates 150 mm-wide or more, it can be difficult to maintain constant fluid residence time across the entire surface. Further, faster flowing fluid results in a thinner boundary layer through which reactants diffuse. This difference in residence time and boundary layer thickness produces a variable film thickness, which is undesirable for the final cell functionality.

Figure 12. A schematic representation of residence time configurations available in the adjustable residence time heat exchanger (**a**) 1×; (**b**) 5×; (**c**) 10×. Reproduced from [9].

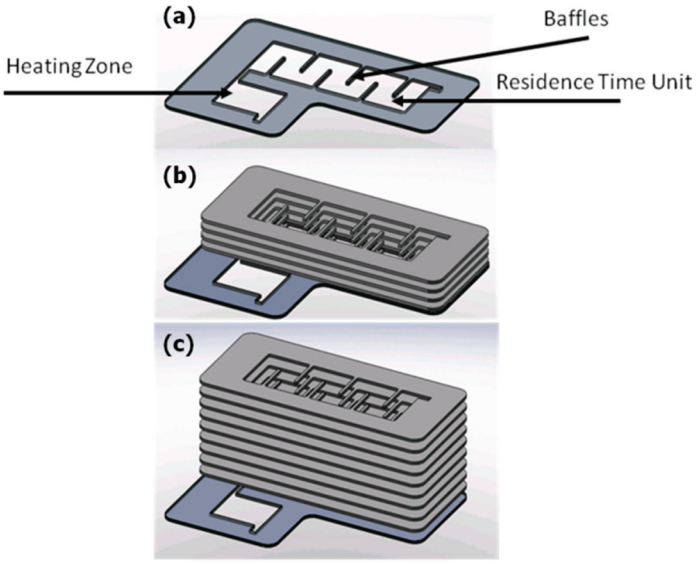

Figure 13. The temperature variation as a function of the residence time in a comparison of a micro-channel heat exchanger with conventional chemical bath deposition. Reproduced from [9].

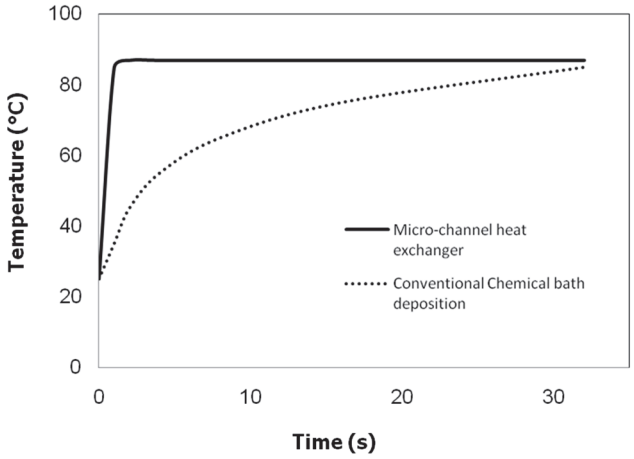

In a pressure gradient-driven system, a challenge arises when transforming a virtual "point source" fluid supply from tubing to a uniform velocity front across a comparatively large surface area and then back to tubing for collection. In this chapter, the function of a flow cell is to manage flow distribution across the thin film substrate. Little has been published regarding flow cell designs used in scaling up liquid-phase continuous flow deposition.

The basic flow cell design consists of a fluid cavity between two parallel plates with an inlet and an outlet. Efforts have been made in adjacent fields to manage flow distribution within various types of flow cell arrangements. Chung *et al.* presented a flow cell design for cell culture cultivation having over-sized inlet and outlet reservoirs designed as long plenums, as shown in Figure 14 [58]. The long plenums have a low pressure drop, which helps to distribute the fluid laterally prior to flowing over the parallel plate region, effectively managing the lateral variation of fluid velocity.

In a similar manner, PDMS flow cells were developed by Hung *et al.* to provide nutrients to a cell culture system in a uniform and controlled manner [59]. An outer plenum was connected to the flow cell using small perfusion channels, which have greatly reduced cross-sectional areas and much larger pressure drops than the plenum (Figure 15). The size of the perfusion channels can be used to effectively manage the fluid velocity across the flow cell (Figure 16).

Figure 14. Schematic of flow chamber with inlet/outlet reservoirs. Reproduced from [58].

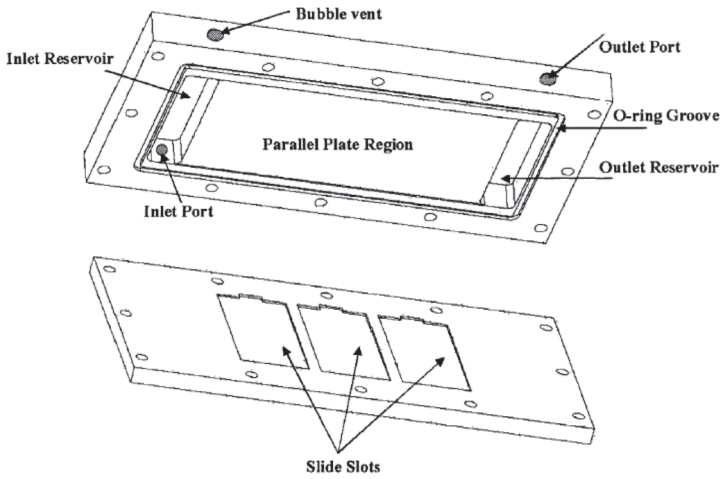

Figure 15. (**a**) Magnified view of the cell chamber; (**b**) magnified view of the perfusion channels. Reproduced from [59].

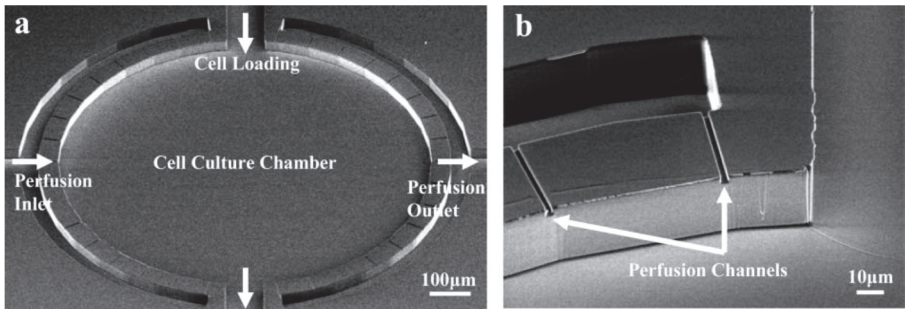

Figure 16. (**a**) Time-stepped computational fluid dynamics (CFD) simulation of fluid velocity; (**b**) time-stepped colored dye observation. Reproduced from [59].

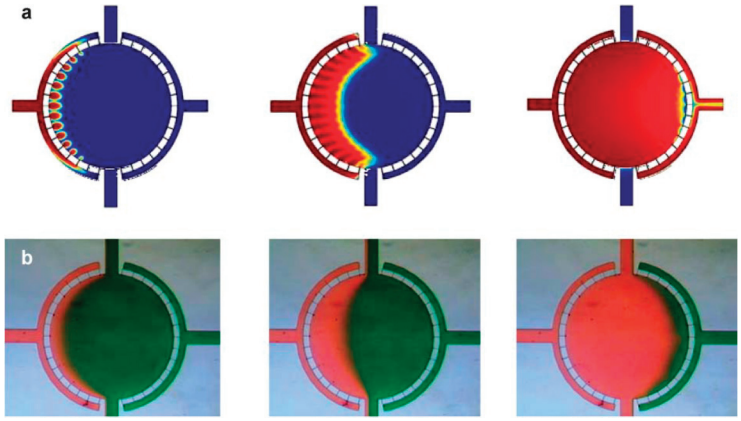

However, fluid flow analysis of these types of flow cells shows that the large plenums contain "dead" zones, where fluid stagnates, causing a larger residence time distribution within the flow cell. For systems containing reactive species, precipitates may form in dead zones, which inherently reduces the material utilization and can lead to clogging, which would alter the flow field across the flow cell.

Jones *et al.* investigated the flow distribution effects of the flow geometry in the plane parallel to the fluid plane of a microchannel heat sink [60]. Figure 17 depicts the change in the velocity profile between two flow geometries; one with a constricted geometry around the inlet and outlet *versus* a design with unconstrained flow from the inlet and outlet. Experimental analysis showed a much better flow distribution in the case of the unconstrained flow with a 4.7% difference between the maximum and minimum mass flux across the channel array for the unconstrained design *versus* a 33.5% difference for the constrained design. The unconstrained design also realized a significantly lower pressure drop.

Figure 17. Velocity contours of circular top down inlets. (**a**) Constrained design around the inlet/outlet; (**b**) Unconstrained design. Reproduced from [60].

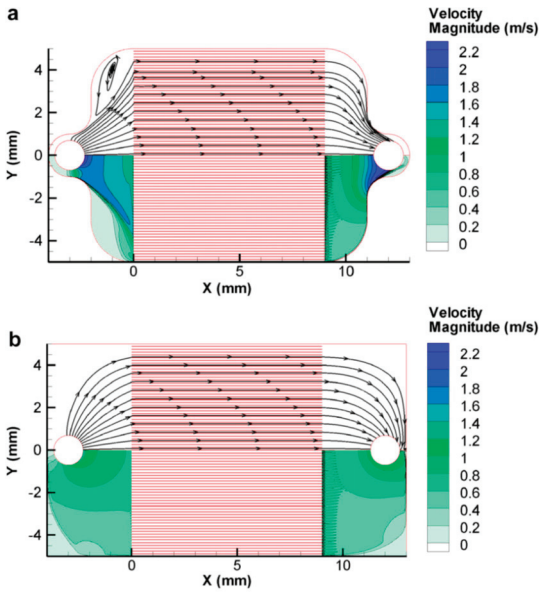

Pan *et al.* characterized a microscale flow chamber composed of several parallel rectangular channels and used an electrical network parody to describe the system (Figure 18) [61].

Figure 18. Microdevice design and analytical model. Reproduced from [61].

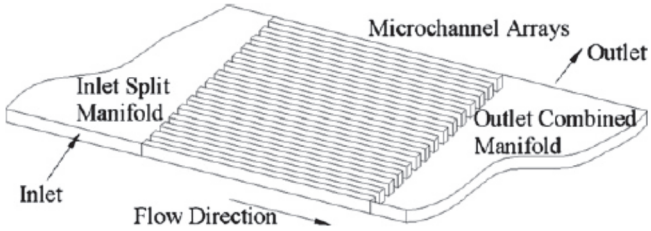

Figure 18. *Cont.*

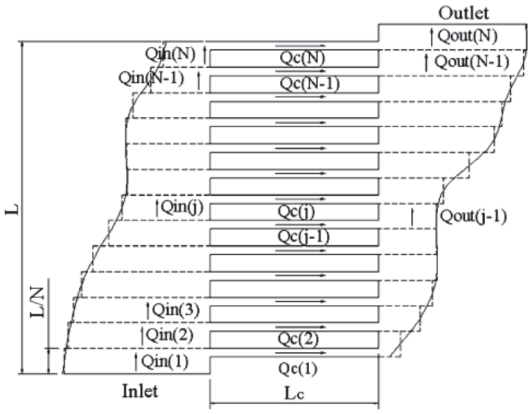

Operating under laminar flow conditions, the pressure drop of each channel using the Hagen–Poiseuille equation for rectangular channels is:

$$\Delta P = \frac{32\mu L\lambda_{NC}}{D_H^2}U = \frac{32\mu L\lambda_{NC}}{D_H^2 A}Q \tag{5}$$

where A is the channel cross-sectional area, L is the channel length, U is the velocity, D_H is the hydraulic diameter, $D_H = 2HW/(H + W)$; and λ_{NC} is a non-circular correction coefficient of $(3/2)/((1 - 0.351(E/W))^2(1 + H/W)^2)$ for $W > H$. In the model, the "loop rule" of $V = IR$ used for electrical circuits was made analogous to the Hagen–Poiseuille equation for fluidic circuits by replacing the voltage, current and electrical resistance with pressure drop, volumetric flow rate and the following term for flow resistance:

$$R = \frac{32\mu L\lambda_{NC}}{D_H^2 A} \tag{6}$$

The basic overall resistance model assumes each channel is associated with its own unique inlet (R_{in}) and outlet (R_{out}) region, resulting in a unique potential difference (ΔP) across each channel. This leads to a system of flow resistances in both series and in parallel, as shown in Figure 19. Varying the length, depth and number of channels allowed the optimization of the inlet and outlet geometries for uniform a flow distribution between each channel.

Figure 19. Microdevice design and the equivalent electrical resistance model. Reproduced from [61].

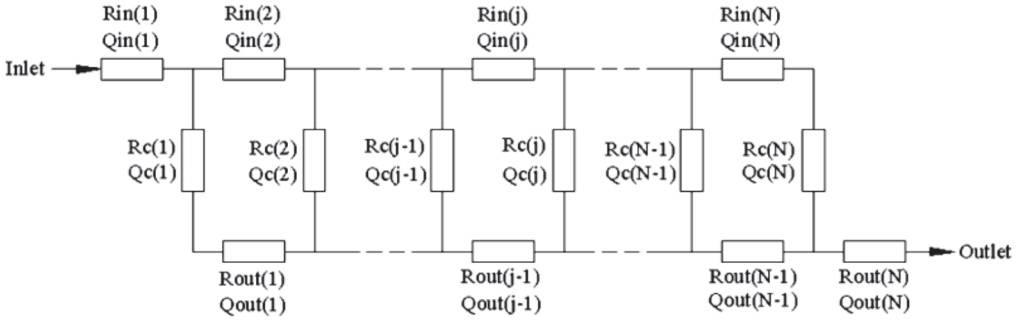

Paul *et al.* developed a MASD flow cell with a more uniform fluid residence time for depositing CdS buffer layers for thin film photovoltaics over a 150 mm-sized glass substrate coated with fluorine-doped tin oxide (Figure 20) [49]. The geometry of the flow cell in the flow plane reflects efforts to minimize drag and stagnant flow regions within the flow cell. Similar to other flow cell designs, the height of the flow cell was controlled between 100 and 1000 μm by the distance between two parallel plates. However, in this design, the top plate was deflected into the flow cell, as shown in Figure 20. The shape of the deflected channel profile was used to control the pressure drop of the fluid across the width of the flow channel, providing for a uniform flow front. Dye injection evaluations of flow fields within an 800 μm-high parallel plate and a deflected plate flow cell are shown in Figure 21. The parallel plate flow cell shows a distinctive parabolic flow profile, while the deflected plate profile shows a much more uniform flow front both at the inlet and middle of the flow cell. The flow cell was used to produce CdS films between 20 and 40 nm in thickness with variations down to 10% across a 150 × 150-mm glass substrate. The thickness of the film deposited was found to be between three and five times more uniform than films produced using the parallel-plate flow cell. This level of film uniformity compared favorably with prior continuous reactor flow cells for solution deposition, showing over fivefold more variation in chemical product (nanowire) dimensions over a 30-mm dimension [24].

Figure 20. (**a**) Top view of the MASD flow cell design and (**b**) the deflected channel profile from the equivalent channel heights. Reproduced from [49].

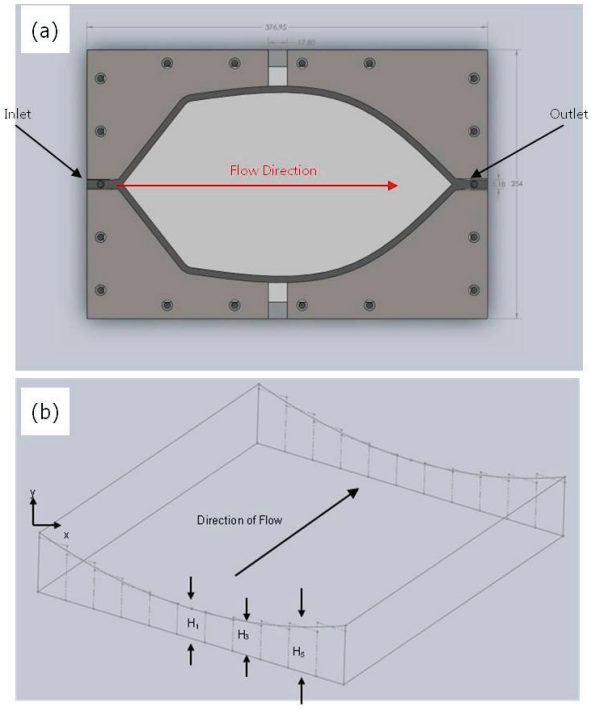

Figure 21. Flow distributions at the beginning (**top**) and middle (**bottom**) of the flow cell for the parallel plate (**left**) and the deflected plate (**right**) flow cells. Reproduced from [49].

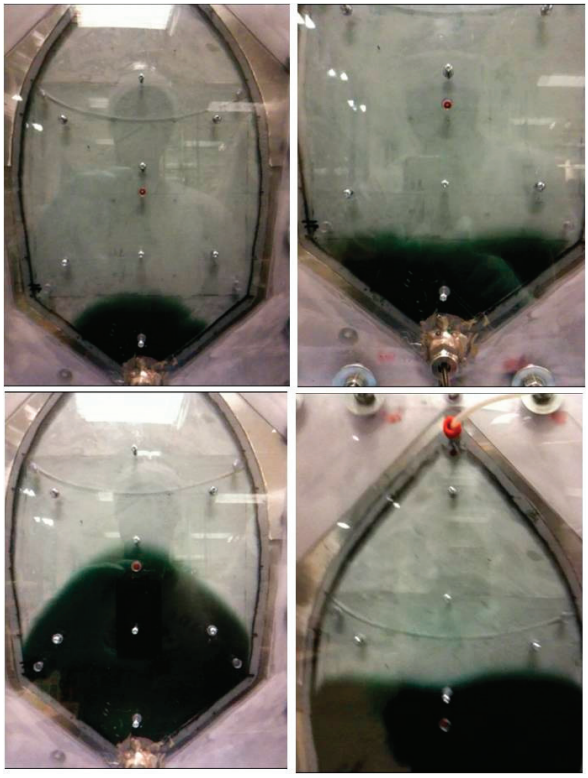

5. Conclusions and Future Directions

The microreactor-assisted solution deposition (MASD) process combines the benefits of microreaction technology and solution-based deposition processes for the fabrication of semiconductor thin films. MASD is a new approach that could be adopted for many chemical solution deposition processes to enable the low-temperature deposition of many compound semiconductor thin films for the manufacturing of functional devices. In particular, it is able to produce reactive fluxes of short-life, intermediate molecules to promote heterogeneous growth and alleviate the drawbacks of the conventional batch chemical solution deposition process. MASD provides opportunities to fabricate high quality compound semiconductor thin films using low-cost capital equipment along with the scalability for numbering-up the process towards an industrial production scale.

There are some challenges associated with MASD. One fundamental challenge is the depletion of reactants along with the residence time of the chemical solution. A beautiful example reported by McPeak *et al.* clearly illustrates this issue [62]. In their study, the deposition of ZnCdS thin films by CBD using a continuous flow microreactor was performed. As shown in Figure 22, over the length of a single substrate, films showed an increasing Zn:Cd ratio, a resultant monotonic increase in the band gap from 2.42 to 2.75 eV and significant thickness variation.

Figure 22. (**a**) Plug flow reactor model showing the Zn and Cd bath concentration as a function of the position (thick lines), the laminar flow profile (thin line) and the temperature profile (color gradation indicates a change from 70 to ~60 °C) in the continuous flow microreactor; (**b**) CdZnS deposition on a Si wafer showing the interference pattern arising from the spatial variation in the film thickness; (**c**) The CdZnS film thickness as a function of the distance from the inlet. Reproduced from [62].

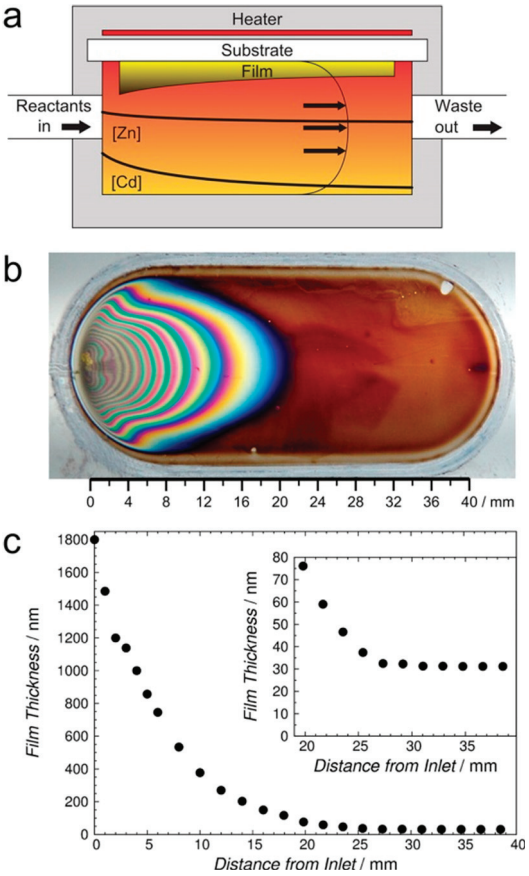

The MASD process opens up several opportunities that are difficult to achieve by the conventional chemical bath deposition process. The temporal control offered by MASD provides the capability to deposit tailored thin films, such as functional gradient thin films. Some examples of thin films with a compositional gradient and that are layer-by-layer are illustrated in Figure 23. The possibility of continuously generating reactive species by MASD should also expand the material spaces that were previously not covered by the conventional batch chemical bath deposition processes, due to the tendency of many reactive species towards particle formation instead of film formation. It will be exciting to see some examples demonstrating some of these capabilities by MASD in the near future.

Figure 23. Tailored thin films potentially fabricated by MAND: (**a**) three different layers on a substrate; and (**b**) compositional gradients.

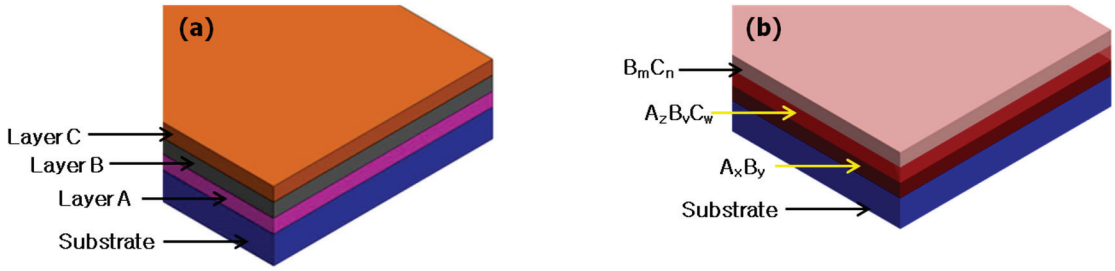

Acknowledgments

The authors are grateful for the fruitful collaboration with Curtis Voss, Yu-Jen Chang, Seung-yeol Han, Prakash Mugdur, Si Ok Ryu, Sudhir Ramprasad and Daniel Palo. The authors would like to acknowledge the financial support from the National Science Foundation CAREER CTS-0348723, CBET-0654434, the Department of Energy's Office of Energy Efficiency and Renewable Energy (EERE), the Industrial Technology Program (ITP), the Nanomanufacturing Activity through award number NT08847 DOE ITP, the Oregon Nanoscience and Microtechnology Institute (ONAMI) and Oregon Built Environment & Sustainable Technologies (Oregon BEST).

Conflicts of Interest

The authors declare no conflict of interest.

References

1. Schlesinger, T.E. *Electrodepostion of Semiconductors*; John Wiley and Sons, Inc.: Hoboken, NJ, USA, 2000; Volume 14.
2. Mane, R.S.; Lokhande, C.D. Chemical deposition method for metal chalcogenide thin films. *Mater. Chem. Phys.* **2000**, *65*, 1–31.
3. Mwakikunga, B.W. Progress in ultrasonic spray pyrolysis for condensed matter sciences developed from ultrasonic nebulization theories since michael faraday. *Crit. Rev. Solid State Mater. Sci.* **2014**, *39*, 46–80.
4. Hodes, G. *Chemical Solution Deposition of Semiconductor Films*; Marcel Dekker: New York, NY, USA, 2003.
5. Ortegaborges, R.; Lincot, D. Mechanism of chemical bath deposition of cadmium-sulfide thin-films in the ammonia-thiourea system—*In-situ* kinetic-study and modelization. *J. Electrochem. Soc.* **1993**, *140*, 3464–3473.
6. Chang, Y.J.; Su, Y.W.; Lee, D.H.; Ryu, S.O.; Chang, C.H. Investigate the reacting flux of chemical bath deposition by a continuous flow microreactor. *Electrochem. Solid State Lett.* **2009**, *12*, H244–H247.
7. Han, S.Y.; Chang, Y.J.; Lee, D.H.; Ryu, S.O.; Lee, T.J.; Chang, C.H. Chemical nanoparticle deposition of transparent zno thin films. *Electrochem. Solid State Lett.* **2007**, *10*, K1–K5.

8. Liu, S.; Chang, C.-H.; Paul, B.K.; Remcho, V.T. Convergent synthesis of polyamide dendrimer using a continuous flow microreactor. *Chem. Eng. J.* **2008**, *135*, S333–S337.
9. Ramprasad, S.; Su, Y.-W.; Chang, C.-H.; Paul, B.K.; Palo, D.R. Cadmium sulfide thin film deposition: A parametric study using microreactor-assisted chemical solution deposition. *Sol. Energy Mater. Sol. Cells* **2012**, *96*, 77–85.
10. Reynolds, J.E. On the synthesis of galena by means of thiocarbamide, and the deposition of lead sulphide as a specular film. *J. Chem. Soc.* **1884**, *45*, 162–165.
11. Voss, C.; Chang, Y.J.; Subramanian, S.; Ryu, S.O.; Lee, T.J.; Chang, C.H. Growth kinetics of thin-film cadmium sulfide by ammonia-thiourea based CBD. *J. Electrochem. Soc.* **2004**, *151*, C655–C660.
12. Chang, Y.J.; Mugdur, P.H.; Han, S.Y.; Morrone, A.A.; Ryu, S.O.; Lee, T.J.; Chang, C.H. Nanocrystalline CdS MISFETs fabricated by a novel continuous flow microreactor. *Electrochem. Solid State Lett.* **2006**, *9*, G174–G177.
13. Lee, D.H.; Jung, J.Y.; Bae, E.J.; Lee, T.J.; Ryu, S.O.; Chang, C.H. Highly uniform ZnS thin film through the continuous flow reaction process. *J. Korean Phys. Soc.* **2008**, *53*, 102–105.
14. Lee, J.Y.; Park, M.S.; Lee, T.J.; Ryu, S.O.; Chang, C.H.; Ryu, S.O. Synthesis of CdTe thin films for solar cell using solution-based deposition methods at low temperature. *Mol. Cryst. Liq. Cryst.* **2011**, *551*, 181–190.
15. Kim, C.R.; Han, S.Y.; Chang, C.H.; Lee, T.J.; Ryu, S.O. A study on copper selenide thin films for photovoltaics by a continuous flow microreactor. *Mol. Cryst. Liq. Cryst.* **2010**, *532*, 455–463.
16. Park, M.S.; Han, S.Y.; Bae, E.J.; Lee, T.J.; Chang, C.H.; Ryu, S.O. Synthesis and characterization of polycrystalline $CuInS_2$ thin films for solar cell devices at low temperature processing conditions. *Curr. Appl. Phys.* **2010**, *10*, S379–S382.
17. Kim, C.R.; Han, S.Y.; Chang, C.H.; Lee, T.J.; Ryu, S.O. Synthesis and characterization of $CuInSe_2$ thin films for photovoltaic cells by a solution-based deposition method. *Curr. Appl. Phys.* **2010**, *10*, S383–S386.
18. Yamamoto, Y.; Yamaguchi, T.; Tanaka, T.; Tanahashi, N.; Yoshida, A. Characterization of $CuInS_2$ thin films prepared by sputtering from binary compounds. *Sol. Energy Mater. Sol. Cells* **1997**, *49*, 399–405.
19. Peng, S.; Cheng, F.; Liang, J.; Tao, Z.; Chen, J. Facile solution-controlled growth of $CuInS_2$ thin films on FTO and TiO_2/FTO glass substrates for photovoltaic application. *J. Alloys Compd.* **2009**, *481*, 786–791.
20. Peza-Tapia, J.M.; Sanchez-Resendiz, V.M.; Albor-Aguilera, M.L.; Cayente-Romero, J.J.; de Leon-Gutierrez, L.R.; Ortega-Lopez, M. Electrical and optical characterization of Na: $CuInS_2$ thin films grown by spray pyrolysis. *Thin Solid Films* **2005**, *490*, 142–145.
21. Ozgur, U.; Alivov, Y.I.; Liu, C.; Teke, A.; Reshchikov, M.A.; Dogan, S.; Avrutin, V.; Cho, S.J.; Morkoc, H. A comprehensive review of ZnO materials and devices. *J. Appl. Phys.* **2005**, *98*, doi:10.1063/1.1992666.
22. Tian, Z.R.R.; Voigt, J.A.; Liu, J.; McKenzie, B.; McDermott, M.J.; Rodriguez, M.A.; Konishi, H.; Xu, H.F. Complex and oriented ZnO nanostructures. *Nat. Mater.* **2003**, *2*, 821–826.

23. Wang, X.; Liao, M.; Zhong, Y.; Zheng, J.Y.; Tian, W.; Zhai, T.; Zhi, C.; Ma, Y.; Yao, J.; Bando, Y.; *et al*. ZnO hollow spheres with double-yolk egg structure for high-performance photocatalysts and photodetectors. *Adv. Mater.* **2012**, *24*, 3421–3425.
24. McPeak, K.M.; Baxter, J.B. ZnO nanowires grown by chemical bath deposition in a continuous flow microreactor. *Cryst. Growth Des.* **2009**, *9*, 4538–4545.
25. Han, S.-Y.; Paul, B.K.; Chang, C.-H. Nanostructured ZnO as biomimetic anti-reflective coatings on textured silicon using a continuous solution process. *J. Mater. Chem.* **2012**, *22*, 22906–22912.
26. Nair, P.K.; Campos, J.; Nair, M.T.S. Opto-electronic characteristics of chemically deposited cadmium sulphide thin films. *Semicond. Sci. Technol.* **1988**, *3*, doi:10.1088/0268-1242/3/2/010.
27. Arreola-Jardon, G.; Gonzalez, L.A.; Garcia-Cerda, L.A.; Gnade, B.; Quevedo-Lopez, M.A.; Ramirez-Bon, R. Ammonia-free chemically deposited CdS films as active layers in thin film transistors. *Thin Solid Films* **2010**, *519*, 517–520.
28. Birkmire, R.W.; McCandless, B.E. Cdte thin film technology: Leading thin film PV into the future. *Curr. Opin. Solid State Mater. Sci.* **2010**, *14*, 139–142.
29. Mugdur, P.H.; Chang, Y.J.; Han, S.Y.; Su, Y.W.; Morrone, A.A.; Ryu, S.O.; Lee, T.J.; Chang, C.H. A comparison of chemical bath deposition of CdS from a batch reactor and a continuous-flow microreactor. *J. Electrochem. Soc.* **2007**, *154*, D482–D488.
30. Dona, J.M.; Herrero, J. Chemical bath deposition of CdS thin-films—Electrochemical *in situ* kinetic-studies. *J. Electrochem. Soc.* **1992**, *139*, 2810–2814.
31. Chang, Y.J.; Munsee, C.L.; Herman, G.S.; Wager, J.F.; Mugdur, P.; Lee, D.H.; Chang, C.H. Growth, characterization and application of US thin films deposited by chemical bath deposition. *Surface Interface Anal.* **2005**, *37*, 398–405.
32. Nair, P.K.; Garcia, V.M.; Gomez-Daza, O.; Nair, M.T.S. High thin-film yield achieved at small substrate separation in chemical bath deposition of semiconductor thin films. *Semicond. Sci. Technol.* **2001**, *16*, 855–863.
33. Boyle, D.S.; Bayer, A.; Heinrich, M.R.; Robbe, O.; O'Brien, P. Novel approach to the chemical bath deposition of chalcogenide semiconductors. *Thin Solid Films* **2000**, *361*, 150–154.
34. Lerou, J.J.; Harold, J.; Ryley, J.; Ashmead, J.; O'Brien, T.C.; Johnson, M.; Perrotto, J.; Blaisdell, C.T.; Rensi, T.A.; Nyquist, J. Microfabricated mini-chemical systems: Technical feasibility. In *Microsystem Technology for Chemical and Biological Microreactors, Dechema Monographs*; Ehrfeld, W., Ed.; Verlag Chemie: Weinheim, Germany, 1996; Volume 132, pp. 51–69.
35. Chang, C.-H.; Paul, B.K.; Remcho, V.T.; Atre, S.; Hutchison, J.E. Synthesis and post-processing of nanomaterials using microreaction technology. *J. Nanopart. Res.* **2008**, *10*, 965–980.
36. Schenk, R.; Hessel, V.; Hofmann, C.; Lowe, H.; Schonfeld, F. Novel liquid-flow splitting unit numbering-up of liquid/liquid specifically made for chemical microprocessing. *Chem. Eng. Technol.* **2003**, *26*, 1271–1280.

37. Saber, M.; Commenge, J.M.; Falk, L. Microreactor numbering-up in multi-scale networks for industrial-scale applications: Impact of flow maldistribution on the reactor performances. *Chem. Eng. Sci.* **2010**, *65*, 372–379.
38. Tonomura, O.; Tominari, T.; Kano, M.; Hasebe, S. Operation policy for micro chemical plants with external numbering-up structure. *Chem.Eng. J.* **2008**, *135*, S131–S137.
39. Schenk, R.; Hessel, V.; Hofmann, C.; Kiss, J.; Lowe, H.; Ziogas, A. Numbering-up of micro devices: A first liquid-flow splitting unit. *Chem. Eng. J.* **2004**, *101*, 421–429.
40. Kashid, M.N.; Gupta, A.; Renken, A.; Kiwi-Minsker, L. Numbering-up and mass transfer studies of liquid-liquid two-phase microstructured reactors. *Chem. Eng. J.* **2010**, *158*, 233–240.
41. Iwasaki, T.; Kawano, N.; Yoshida, J.-I. Radical polymerization using microflow system: Numbering-up of microreactors and continuous operation. *Org. Process. Res. Dev.* **2006**, *10*, 1126–1131.
42. Deshmukh, S.R.; Tonkovich, A.L.Y.; Jarosch, K.T.; Schrader, L.; Fitzgerald, S.P.; Kilanowski, D.R.; Lerou, J.J.; Mazanec, T.J. Scale-up of microchannel reactors for fischer-tropsch synthesis. *Ind. Eng. Chem. Res.* **2010**, *49*, 10883–10888.
43. Mae, K.; Maki, T.; Hasegawa, I.; Eto, U.; Mizutani, Y.; Honda, N. Development of a new micromixer based on split/recombination for mass production and its application to soap free emulsifier. *Chem. Eng. J.* **2004**, *101*, 31–38.
44. Kockmann, N.; Gottsponer, M.; Roberge, D.M. Scale-up concept of single-channel microreactors from process development to industrial production. *Chem. Eng. J.* **2011**, *167*, 718–726.
45. Bally, F.; Serra, C.A.; Hessel, V.; Hadziioannou, G. Micromixer-assisted polymerization processes. *Chem. Eng. Sci.* **2011**, *66*, 1449–1462.
46. Pysall, D.; Wachsen, O.; Bayer, T.; Wulf, S. Method and Device for Continuous Production of Polymers. U.S. Patent 20140011914, 9 January 2014.
47. Wirth, T. *Microreactors in Organic Synthesis and Catalysis*; Wiley-VCH: Weinheim, Germany, 2008.
48. Fox, M.B.; Esveld, D.C.; Boom, R.M. Conceptual design of a mass parallelized PEF microreactor. *Trends Food Sci. Technol.* **2007**, *18*, 484–491.
49. Paul, B.K.; Hires, C.L.; Su, Y.W.; Chang, C.H.; Rarnprasad, S.; Palo, D. A uniform residence time flow cell for the microreactor-assisted solution deposition of CdS on an FTO-glass substrate. *Cryst. Growth Des.* **2012**, *12*, 5320–5328.
50. Ramprasad, S.; Su, Y.-W.; Chang, C.-H.; Paul, B.K.; Palo, D.R. Continuous microreactor-assisted solution deposition for scalable production of CdS films. *Ecs J. Solid State Sci. Technol.* **2013**, *2*, P333–P337.
51. Benson, R.S.; Ponton, J.W. Process miniaturization—A route to total environmental acceptability. *Chem. Eng. Res. Des.* **1993**, *71*, 160–168.
52. Bokenkamp, D.; Desai, A.; Yang, X.; Tai, Y.C.; Marzluff, E.M.; Mayo, S.L. Microfabricated silicon mixers for submillisecond quench-flow analysis. *Anal. Chem.* **1998**, *70*, 232–236.

53. Nguyen, N.T.; Wu, Z.G. Micromixers—A review. *J. Micromech. Microeng.* **2005**, *15*, R1–R16.
54. Löwe, H.; Ehrfeld, W.; Hessel, V.; Richter, T.; Schiewe, J. Micromixing Technology. In Proceedings of the 4th International Conference on Microreaction Technology (IMRET), Atlanta, GA, USA, 5–9 March 2000; pp. 31–47.
55. Peterson, D.A.; Chandran, P.; Paul, B.K. A reverse oscillatory flow microreactor system for the synthesis of uniformly-size CdS nanoparticles. In Proceedings of the IEEE International Conference on Nanotechnology, Portland, OR, USA, 15–18 August 2011; pp. 666–670.
56. Sugano, K.; Yoshimune, H.; Nakata, A.; Hirai, Y.; Tsuchiya, T.; Tabata, O. High-speed pulsed mixing with high-frequency switching of micropump driving and its application to nanoparticle synthesis. In Proceedings of the 16th International Solid-State Sensors, Actuators and Microsystems Conference (Transducers), Beijing, China, 5–9 June 2011; pp. 1773–1776.
57. Jin, H.D.; Garrison, A.; Tseng, T.; Paul, B.K.; Chang, C.-H. High-rate synthesis of phosphine-stabilized undecagold nanoclusters using a multilayered micromixer. *Nanotechnology* **2010**, *21*, doi:10.1088/0957-4484/21/44/445604.
58. Chung, B.J.; Robertson, A.M.; Peters, D.G. The numerical design of a parallel plate flow chamber for investigation of endothelial cell response to shear stress. *Comput. Struct.* **2003**, *81*, 535–546.
59. Hung, P.J.; Lee, P.J.; Sabounchi, P.; Aghdam, N.; Lin, R.; Lee, L.P. A novel high aspect ratio microfluidic design to provide a stable and uniform microenvironment for cell growth in a high throughput mammalian cell culture array. *Lab. Chip* **2005**, *5*, 44–48.
60. Jones, B.J.; Lee, P.-S.; Garimella, S.V. Infrared micro-particle image velocimetry measurements and predictions of flow distribution in a microchannel heat sink. *Int. J. Heat Mass Transf.* **2008**, *51*, 1877–1887.
61. Pan, M.; Tang, Y.; Pan, L.; Lu, L. Optimal design of complex manifold geometries for uniform flow distribution between microchannels. *Chem. Eng. J.* **2008**, *137*, 339–346.
62. McPeak, K.M.; Opasanont, B.; Shibata, T.; Ko, D.-K.; Becker, M.A.; Chattopadhyay, S.; Bui, H.P.; Beebe, T.P., Jr.; Bunker, B.A.; Murray, C.B.; *et al*. Microreactor chemical bath deposition of laterally graded $Cd_{1-x}Zn_xS$ thin films: A route to high-throughput optimization for photovoltaic buffer layers. *Chem. Mater.* **2013**, *25*, 297–306.

MDPI AG
Klybeckstrasse 64
4057 Basel, Switzerland
Tel. +41 61 683 77 34
Fax +41 61 302 89 18
http://www.mdpi.com/

Processes Editorial Office
E-mail: processes@mdpi.com
http://www.mdpi.com/journal/processes

MDPI • Basel • Beijing
ISBN 978-3-03842-039-2
www.mdpi.com